Wave limitations for floating AWES

A method for determining effects of wave induced motions on horizontally landing Airborne Wind Energy Systems on floating foundations

S. Drenth

TU Delft

ampyx power

Wave limitations for floating AWES

A method for determining effects of wave induced motions on horizontally landing Airborne Wind Energy Devices on floating foundations

by

S. Drenth

in partial fulfilment of the requirements for the degree of

Master of Science
in Marine Technology

at the Delft University of Technology,
to be defended publicly on Thursday November 2, 2017 at 11:00 AM.

Student number:	4064127	
Project duration:	February 13, 2017 – November 2, 2017	
Thesis committee:	Prof. dr. ir. A.P. van ‘t Veer,	TU Delft, Supervisor
	Dr. ir. R. Schmehl,	TU Delft
	ir. B. van Hemert,	Ampyx Power

This thesis is confidential and cannot be made public until November 2, 2022.

Abstract

Airborne Wind Energy (AWE) is a field of engineering that utilizes tethered aircraft for the generation of electrical power. The potential for the application of AWE in deep-water offshore environments on top of floating foundations is enormous. Where conventional wind turbines would require a very stable platform to reduce motions at the nacelle, AWE requires just enough stability to survive extreme conditions, take-off and land horizontally, and not negatively affect cross-wind performance. The requirements scale well with increasing capacity of AWE systems, which mostly influences the mooring configuration instead of the steel structure. That is why Ampyx Power started an investigative study into the floating offshore application of AWE in collaboration with Mocean Offshore, MARIN and ECN.

A driving factor in the design of the floating foundations is the maximum allowed motions in different sea states. The objective of this research is to determine the relative magnitude of the effect of platform motions on the landing performance. This will result in more clearly defined design requirements for both the floating platform and the aircraft. The method used in this research can be extended to more advanced numerical models at a later stage of the design to obtain quantified motion constraints or operational limits.

It is assumed that standard deviations of several parameters at the end of the landing approach serve as good indicators of successful landings. A numerical model of a tethered aircraft (RPA) making a horizontal landing in time domain is developed to determine these parameters in a multitude of wind conditions. By performing a Monte-Carlo analysis, the standard deviations of these parameters can be acquired. Especially symmetric motions (X, Z and RY) are expected to affect landing performance, which is why a 3DOF model is used. Then harmonic platform motions are included in the model in order to investigate what type of platform motions are most critical. Finally, the platform designed by Mocean Offshore is examined. By combining the motion response of this platform with metocean data at a reference location, the standard deviation of critical parameters is obtained in comparison to an onshore application. The motion response of the platform is determined using a numerical model that combines potential theory with semi-empirical drag formulations. This model is validated with basin tests at MARIN.

Simulations with harmonic platform motions indicate that both frequency and amplitude of platform motions are critical for the landing performance. The landing performance appear to be mainly related to the platform motion velocities. Therefore, increasing

damping and added mass of the platform will both have a positive effect on the landing of the RPA.

When looking further at the results of the simulations with platform motions based on metocean data and the hydrodynamic, numerical model, it was found that the current design of the floating platform by Mocean Offshore leads to an expected decrease in landing performance compared to the onshore application. The performance decrease is not insurmountable, and multiple methods of reducing the negative effects on landing performance are presented.

Acknowledgments

To conclude my MSc with a project that combines Aerospace Engineering and Marine Technology, is a beautiful way to finish my studies. I am therefore forever grateful for the support and guidance of my supervisors Riaan van ‘t Veer, Bernard van Hemert and Roland Schmehl. Without their insights this project would not have been possible. I would also like to thank Ampyx Power for giving me the trust to execute this research.

During the project I was able to build on the knowledge and technical expertise of many people. At Ampyx Power I would like to give my special thanks to Paul Williams, Giovanni Licitra and Jonas Koenemann for their support on numerical modelling of aircraft. Thanks to Daniel Biggot I was able to use a beautiful render of the floating AWES for the cover page of this report.

I would like to acknowledge the partners of the Sea Air Farm project as well. René Lindeboom of MARIN and Willem van Schoten and Mark Paalvast of Mocean Offshore, provided me with valuable advice on the numerical modelling of floating structures, as well as the experimental validation using basin tests.

My thanks go out to all other colleagues at Ampyx Power too, who helped to create a work environment that I enjoyed very much.

Finally, I am grateful for my family and friends, and especially my parents and Jet for supporting me, not only during this project, but in all endeavors I have embarked on in the past and will in the future.

Delft University of Technology,
October 2017

Sil Drenth

Acronyms

A1	Nonlinearly Damped Hydrodynamic Decay Response from Simulation
A2	Nonlinearly Damped Hydrodynamic Decay Response from Simulation
AFT	Aft
AR	Autoregressive
ARMA	Autoregressive Moving Average
ARMAX	Autoregressive Moving Average with Exogenous Input
ARX	Autoregressive with Exogenous Input
ASDS	Autonomous Spaceport Drone Ship
AWE	Airborne Wind Energy
AWEC	Airborne Wind Energy Conference
AWES	Airborne Wind Energy System
B	Linearly Damped Hydrodynamic Decay Response from Simulation
CFD	Computational Fluid Dynamics
CL	Centerline
DARPA	Defense Advanced Research Projects Agency
DOF	Degree Of Freedom
DUT	Delft University of Technology
DWA	Deep Water Assumption
E	Hydrodynamic Decay Response from Experiment
ECN	Energy Center Netherlands
FP	Floating Platform
FWT	Floating Wind Turbine
FWD	Forward
GBAS	Ground Based Augmentation System
GNSS	Global Navigation Satellite System
GPS	Global Positioning System
ILS	Instrument Landing System
IMU	Inertial Measurement Unit
JONSWAP	JOint North Sea WAve Project
JPALS	Joint Precision Approach and Landing System
LAAS	Local Area Augmentation System
LCG	Longitudinal Center of Gravity
LCOE	Levelized Cost Of Energy

LLA	Launch and Land Apparatus
MARIN	Maritime Research Institute Netherlands
MSL	Mean Sea Level
MSS	Marine Systems Simulator
NASA	National Aeronautics and Space Administration
NED	North East Down
O	Original Hydrodynamic Decay Response from Simulation
OWME	On board Wave and Motion Estimator
ODE	Ordinary Differential Equation
PID	Proportional Integral Differential
PS	Portside
RAO	Response Amplitude Operator
RPA	Remotely Piloted Aircraft
SAF	Sea Air Farm
SB	Starboard
SB-JPALS	Sea Based – Joint Precision Approach and Landing System
TCG	Transversal Center of Gravity
TKIWoZ	Topconsortium Kennis en Innovatie Wind op Zee
UAV	Unmanned Arial Vehicle
VCG	Vertical Center of Gravity
WNN	Wavelet Neural Network

List of symbols

Greek Symbols

α	Angle of attack
α_t	Tether angle in inertial frame
γ	Flight path angle
γ	Peakedness factor of JONSWAP spectrum
δ	Elongation of tether
δ_e	Elevator deflection
$\delta_{e,com}$	Elevator deflection command
$\delta_{ii,ini}$	Initial deflection of decay variable
Δ	Cylinder surface roughness
ε	Error (PID controller input)
ζ	Water surface elevation
ζ_a	Wave amplitude
ζ	Damping coefficient
θ	Wave phase angle shift
κ	Damping ratio
λ	Wave length
ξ	Position vector FP (6DOF)
$\dot{\xi}$	Velocity vector FP (6DOF)
$\ddot{\xi}$	Acceleration vector FP (6DOF)
ρ	Water density
ρ_a	Air density
σ	Standard deviation
τ_*	Exciting forces and moments vector
ϕ	Space-dependent term of linear fluid velocity potential
Φ	Linear fluid velocity potential
ψ	Wake amplification factor
ψ	Wave direction
ω	Wave frequency
ω	Angular velocity winch drum
$\dot{\omega}$	Angular acceleration winch drum
ω_0	Undamped natural frequency
ω_d	Damped natural frequency

ω_p	Wave peak frequency
∇	Volumetric displacement of FP

Latin symbols

a_τ	Exciting force and moment amplitude
a_{FP}	Acceleration vector FP (3DOF)
a_{RPA}	Acceleration vector RPA (3DOF)
a_{rel}	Relative acceleration vector between FP and RPA (3DOF)
A	Cross-sectional area of tether
A	Hydrodynamic added mass matrix of FP
A_c	Convolution state space representation system matrix
b	Wing span RPA
B	Hydrodynamic damping matrix of FP
B_c	Convolution state space representation input matrix
$\bar{c}$	Mean wing chord length RPA
C_c	Convolution state space representation output matrix
C_D	Drag coefficient (hydrodynamic)
C_D	Drag coefficient (aerodynamic)
C_{DS}	Drag coefficient for steady flow
C_L	Aerodynamic lift coefficient
C_M	Aerodynamic pitching moment coefficient
C_X	Aerodynamic body load coefficient in x-direction
C_Z	Aerodynamic body load coefficient in z-direction
d	Deviation from glide slope
dA	Projected area of discretized drag element
dT	Tether tension differential
dt_{fin}	Reference value time to landing for pitch control phase
dy	Distance between FP columns (center to center)
dz	Discretized drag element length
D	FP column diameter
D	Differential gain
E	Young’s modulus
FB	Freeboard
F_D	Local drag force vector
Fr	Froude number
g	Gravitational acceleration

gs	Glide slope angle command
G	Hydrodynamic stiffness matrix of FP
GM_L	Longitudinal metacentric height
GM_T	Transversal metacentric height
h	Water depth
h_{land}	Height above deck at flyover command
H_{ave}	Average wave height
H_s	Significant wave height
I	Identity matrix
I	Integral gain
I_{RPA}	Inertia matrix of RPA
I_{winch}	Equivalent inertia matrix of winch
J_d	Moment of inertia of winch drum
$J_{y,RPA}$	Pitch moment of inertia of RPA
k	Wave number
k_{xx}	Roll Radius of Gyration FP
k_{yy}	Pitch Radius of Gyration FP
k_{zz}	Yaw Radius of Gyration FP
$k_{mooring}$	Linearized mooring stiffness
K	Kernel of frequency dependent added mass and damping
K_C	Keulegan Carpenter number
KG	Vertical position of center of gravity FP w.r.t. keel
L	Characteristic length
L_{fin}	Reference value tether length for pitch control phase
L_t	Unreeled tether length
$\dot{L_t}$	Reel-in speed
$\ddot{L_t}$	Reel-in acceleration
m_{FP}	Displaced mass FP (as tested at MARIN)
m_{RPA}	Mass of RPA
m_t	Mass of tether per unit length
M	Inertia matrix of FP structure
M_{com}	Applied torque at winch
n	Normal vector to discretized panel
N	Filter coefficient

p_{FP}	Position vector FP (3DOF)
p_{RPA}	Position vector RPA (3DOF)
p_{rel}	Relative position vector between FP and RPA (3DOF)
p_{τ}	Exciting force and moment phase
P	Kernel transfer function input nominator
P	Proportional gain
Q	Kernel transfer function input denominator
$\bar{q}$	Dynamic pressure
rx, ry, rz	Attitude Euler angles
ry_{com}	Pitch angle command
ry_{meas}	Measured pitch angle
R_d	Winch drum radius
s	Complex variable Laplace domain
S	Wing area
S_0	Discretized panel area
t	Time variable
T	Draught of FP
T	Wave period
T_p	Wave peak period
T_t	Tether tension
T_z	Wave zero-crossing period
$\mathbb{T}_{21}$	Transformation matrix from reference frame 1 to reference frame 2
u, v, w	Inertial flow velocity variables
ug, vg, wg, pg	Turbulence noise seeds
u_x	Relative flow velocity perpendicular to plate element
$u_{\perp}$	Relative flow velocity vector perpendicular flow to cylinder CL
U_{10}	Average wind speed at 10 meter altitude
v_{app}	Apparent velocity vector
v_{FP}	Velocity vector FP (3DOF)
v_{RPA}	Velocity vector RPA (3DOF)
v_{rel}	Relative velocity vector between FP and RPA (3DOF)
v_{wind}	Wind velocity vector
V	Maximum wave particle velocity amplitude (for KC number)
V_{air}	Airspeed
V_{com}	Relative speed command
V_w	Average wind speed for Monte Carlo simulations

x, y, z	Inertial position variables
$z_{0,ws}$	Wind shear reference altitude

Contents

1 Introduction

The focus of this project is on landing Airborne Wind Energy (AWE) devices on a floating foundation. In this chapter the technology and some of the development challenges will be covered.

Starting with the development of AWE at Ampyx Power, the link will be made between floating structures and AWE. This initial section will provide the necessary context for the research. From there the objective of the research is formulated and the method used to arrive at useful results is elaborated upon. In the final section of this chapter attention is given to the state of the art in AWE as well as related sectors.

1.1 Background

AWE is a group of technologies that capture energy from the wind using airborne devices. By going airborne, the systems are able to reach higher altitude winds, which in general have a higher energy density and smaller gust variations. Another advantage that airborne wind energy has over conventional wind turbines is that most of the load acting on the structure is transferred in tension via a tether to the ground. Compare this to the tower of a wind turbine that is loaded mostly in bending, and therefore requires more structural material. The ratio of material used by a AWE system compared to a conventional wind turbine can be less than 1 to 10 according to (Ampyx Power, 2017). This has a large influence on the overall cost of energy, as the cost of the support structure is significant for wind turbines (IRENA, 2012). It is therefore not surprising that EON identified AWE as a potentially disrupting technology for the energy market (Mann, Gunn, Harrison, Beare, & Lazakis, 2015). And also Google has recognized its potential (NU.nl, 2013).

1.1.1 Ampyx Power

Ampyx Power is one of the frontrunners in the AWE sector. It was founded in 2008 by Richard Ruiterkamp. During his research at the Delft University of Technology (DUT) with Wubbo Ockels, he noted that the increased aerodynamic efficiency of rigid wings could lead to a more cost competitive solution for electrical power generation in comparison to the flexible kite concept that was developed at the university (Ockels, 2001). Together with four co-founders the decision was made to start up Ampyx Power, which would develop the rigid wing technology. Ampyx has since then transformed into a company with approximately 50 employees. In 2009, Ampyx Power demonstrated their principle by generating electricity with a tethered aircraft (AP0). In 2012, another important milestone was reached: AP1 generated electrical power while flying completely autonomous for one hour. In 2015 the AP2 prototype added autonomous launching and landing capabilities; the backup pilot on the ground was only there as a safety precaution.

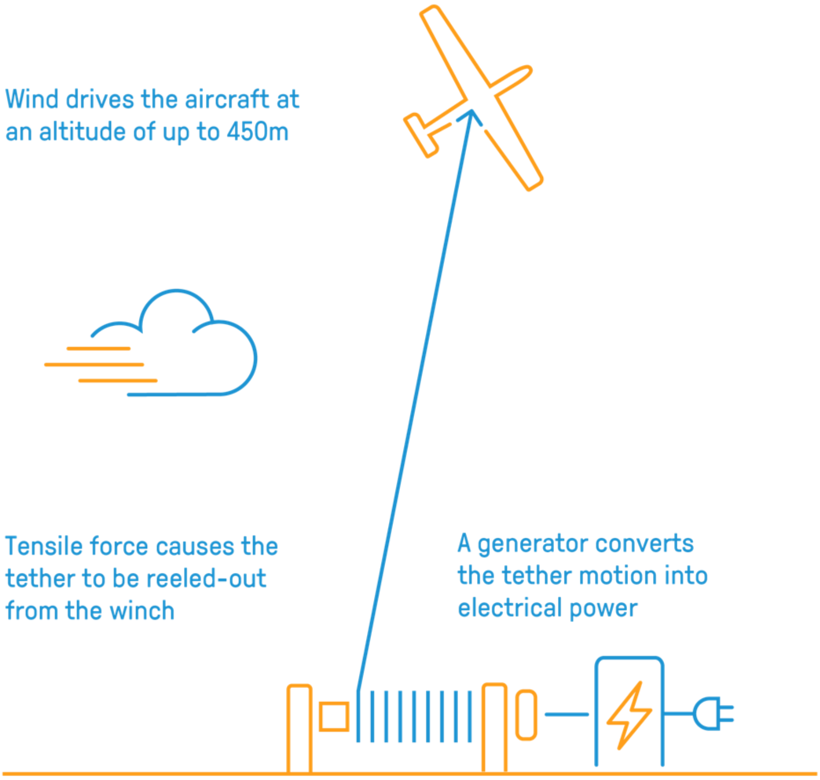

Figure 1, Schematic overview of Ampyx Power airborne wind energy system (Ampyx Power, 2017)

The AWE system that is being developed by Ampyx Power is classified as a rigid wing concept that makes use of ground-based traction power generation (Schmehl, Diehl, & Ahrens, 2011). The method is visualized schematically in Figure 1. The aircraft, which is also called RPA (Remote Piloted Aircraft), exerts large tensile loads on the tether during crosswind flight. While the tether is reeled-out from the torque-controlled winch, electrical power is produced by the generator. When the tether is unreeled close to its maximum length, the RPA autonomously flies back with little resistance to its starting position at a lower altitude closer to the winch, this is called the reel-in phase. During the reel-in phase, a small portion of the energy that is produced during the reel-out phase is used to drive the winch. However, the net energy output is significant over the complete cycle. The intermittent nature of the power output can be solved, either by using power storage methods like batteries, or by having a multitude of systems flying out of phase of each other, thereby levelling out the combined power output. The latter has the preference of Ampyx Power.

Currently, most of the employees at Ampyx Power are working on the AP3 prototype (Figure 3) that is due for testing in 2018. Production on this 12 meter span, 250 kW (wind turbine equivalent[1]) producing prototype is now in progress. The goal of AP3 is validating the scaling of the technology as well as further developing the autonomous processes. Furthermore, a new launch and land method will be tested that requires a smaller footprint.

Due to the operational limits of the system (upper and lower wind speeds) and maintenance requirements, the RPA is required to land regularly during its operational lifetime. Every landing procedure shall be completed autonomously. The proposed method makes use of the tether and a damping cylinder to reduce the horizontal velocity of the RPA. The RPA transitions from crosswind flight to an approach from the downwind position. The RPA then flies towards the Launch and Land Apparatus (LLA), while the winch keeps the tether under tension. When the RPA flies over the LLA, the winch in not being reeled out and the horizontal velocity is damped, as is visible in the schematic overview of the touchdown in Figure 2 (orange guide moving with the RPA).

For AP3 the shape of the approach path is limited due to cable sag, which results in an approach path shaped as an S-curve, as optimized by (Koenemann, Williams, Sieberling, & Diehl, 2017).

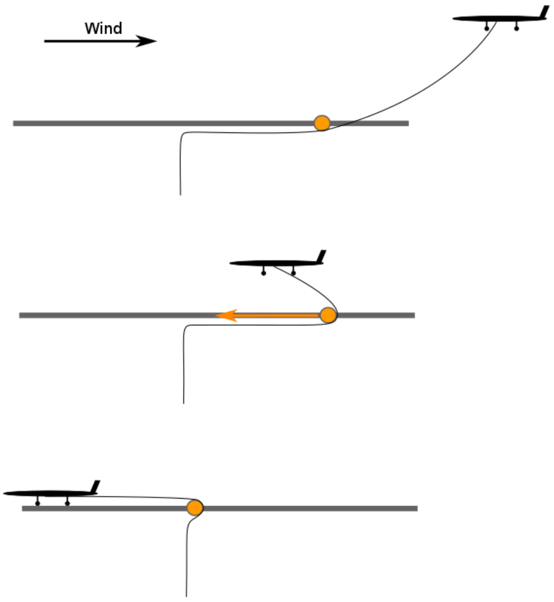

Figure 2, Landing procedure: First approach, then arrest and finally deceleration

---

[1] The power output is expressed in wind turbine equivalent watts; a 250kW Ampyx system would produce the same amount of energy over a year as a wind turbine of rated power 250kW. This does not mean that the ground-based generator is rated at 250kW.

AP3 will be the last pre-commercial prototype before commercial scale is reached with AP4. AP4 will be the full-scale 2 MW demonstration plant, and it is expected to be ready in 2020. Based on an up-scaled version of AP3, the aircraft will have a span of approximately 35 meter and weigh about 3500 kg. However, it should be noted that the conceptual design of AP4 is still in progress. The relevant expected dimensions of the AP4 system as used in this research are shown in Table 1. It is assumed that cable sag will not be as significant for an AP4 landing, and after consultation with engineers at Ampyx Power it is assumed that a linear approach path will be flown with this RPA during landing.

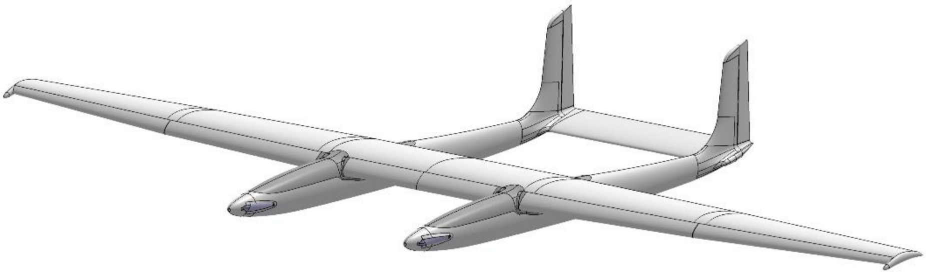

Figure 3, Impression of AP3 concept

The AP4 demonstration plant would be made suitable for offshore use as well. To reach this ambitious goal Ampyx Power has signed a cooperation agreement with E.ON in April 2017. Apart from additional investments, E.ON will realize a testing location for AP3 and AP4 in Ireland. And after successful testing allow for repowering of their decommissioned offshore wind turbine foundations in the North Sea. That will be the last step before the technology can be moved towards deeper water and floating foundations; a move that Ampyx Power is investigating together with partners in the Sea Air Farm (SAF) project.

Table 1, AP4 (RPA and LLA) dimensions

	Symbol	Design	Unit
Mass of RPA	m_{RPA}	3500	kg
Wing span	b	35	m
Chord length (average)	$\bar{c}$	4	m
Pitch moment of inertia	$J_{y,RPA}$	10	m
Tether mass per unit length	m_t	0.4	kg/m
Winch - Drum moment of inertia	J_d	500	kgm^2
Winch - Drum radius	R_d	1	m

1.1.2 SAF project

To smoothen the transition towards a deep water offshore application, TKIWoZ has granted subsidy to investigate the challenges and opportunities of offshore AWES (Ampyx Power, 2016). In collaboration with ECN, MARIN and Mocean Offshore, Ampyx Power is now looking into floating foundation structures and economic viability of offshore AWES. The offshore site that is taken as a reference for the design is Buchan Deep, of the coast of Aberdeen, not coincidentally also the location of Statoil's Hywind Scotland Pilot Park (4C Offshore, 2017a).

During the project Mocean Offshore is responsible for the design and numerical analyses of a floating foundation for an AP4 sized system. This design will be tested with a scale model at the MARIN basin facilities. During these tests the motion response of the floater with and without a tether force acting on the floater is examined. ECN is responsible for the validation of Ampyx Power's numeric (CFD) models, the calculation of the expected levelized cost of energy (LCOE) and the development of an operations and maintenance strategy in collaboration with Ampyx Power.

The floating platform (FP) as designed by Mocean Offshore will be a semi-submersible with three columns, arranged in an equidistant triangle. The reason is that this type of platform has relatively low motion amplitudes and accelerations due to its small water plane area and large displacement. Furthermore, especially high frequency waves will have little effect on the motion of the platform, which is expected to be beneficial for landing an RPA on top of it. A 3D impression of the FP is shown in Figure 4.

The plate at the bottom of the platform (keel plate) increases the added mass of the structure significantly, especially in heave motion. This increased added mass reduces the natural frequency of the platform. Turbulent flows around the edges of this plate dissipate energy and thereby damp the motions of the platform. Depending on whether maximum motion amplitude or frequency of motion is critical for the RPA a decision could be made to add a hole in the plate, which is expected to reduce added mass but increase damping due to additional plate edge length. The dimensions of the platform have been summarized in Table 2. The dimensions that have been realized for the experiments at MARIN have also been listed. In the numerical model of this thesis the dimensions as used in the experiments are used.

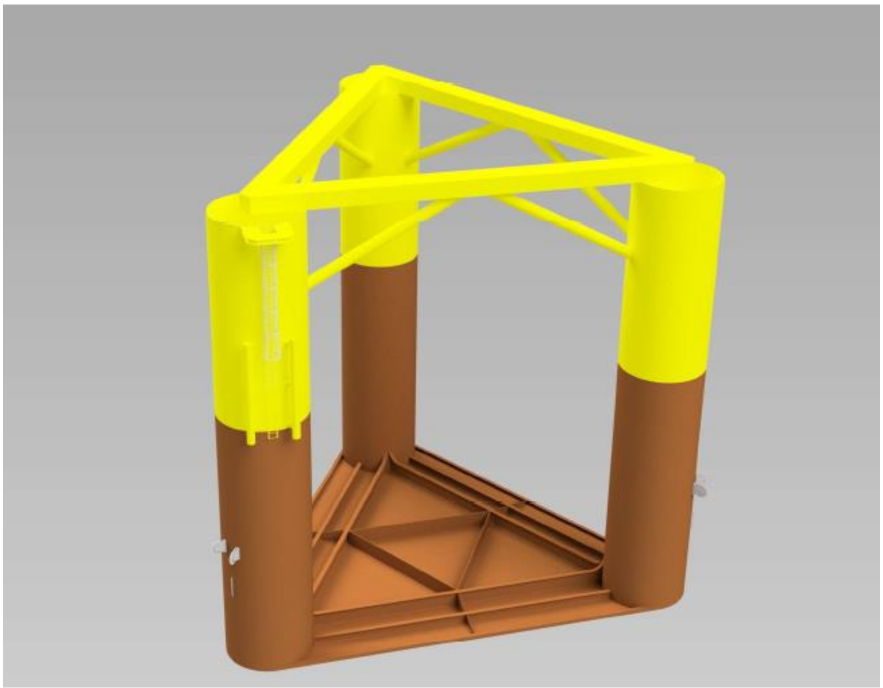

Figure 4, Impression of FP design

Table 2, Semi-submersible (FP) dimensions

	Symbol	Design	Experiment	Unit
Column diameter	D	5.3	5.3	m
Distance between columns (center to center)	dy	24	24	m
Draft	T	16	16	m
Freeboard	FB	12	12	m
Displacement mass (as tested at MARIN)	m_{FP}	1100	1177	tonnes
Vertical position center of gravity w.r.t. keel	KG	9.91	9.01	m
Roll radius of gyration	k_{xx}	15.08	14.6	m
Pitch radius of gyration	k_{yy}	15.27	14.8	m
Yaw radius of gyration	k_{zz}	12.97	13.2	m
Transverse metacentric height	GM_T	4.27	4.25	m
Longitudinal metacentric height	GM_L	4.27	4.29	m

1.2 Objectives and method

The design of the floater as described in the previous section was based on fuzzy requirements: The FP was required to have minimal motions at minimal cost (follows from amount of material and structural complexity). The type of motion, or whether accelerations or amplitudes are critical was still unknown during the initial phase of the SAF project. These constraints on the motion do not follow from cross-wind flight, which does have a large influence on the requirements for the hydrostatic stability and mooring configuration. Instead, the hydrodynamic limitations on the platform are defined by the landing performance of the RPA.

At this point it is impossible to define the actual motion limits for landing in terms of maximum position, velocity or acceleration amplitudes for the FP in specific sea states. The design of both the RPA and ground system of an AP4-sized system needs to be at a more advanced state, preferably with onshore flight tests completed. However, based on preliminary data on AP4 shown in the previous section it is possible to define qualitatively what the approximate effect of platform motions is in comparison to for example wind disturbances due to turbulence. This is done by comparing the uncertainty in relative landing velocity and position. The effect could be small, as the RPA would be able to adjust accurately to the motions of the platform in real time. Then another design iteration of the FP could result in a lower cost. The opposite would naturally result in a more costly design in the next design iteration.

The objective of this research is to determine the relative magnitude of the effect of platform motions on the landing performance. The method used in this research can be extended to more advanced numerical models at a later stage of the design to obtain actual motion limits. The result shall provide a handle for the continued development of a floating airborne wind energy systems.

1.2.1 Method

The approach that is used consists of the development of two numerical models for time domain simulations. The first is used to obtain a database of FP motions responses in a range of sea states. The second is a model that can simulate the final approach of the RPA, and should allow for a moving endpoint. By running this model in several Monte Carlo simulations with varying initial conditions, wind conditions and floater motions, sufficient statistical data can be gathered to compare the effects on landing uncertainty. Note that this approach is only possible if the tether load does not affect the floater motions during the landing approach significantly, this will be confirmed in the next chapter with a short calculation.

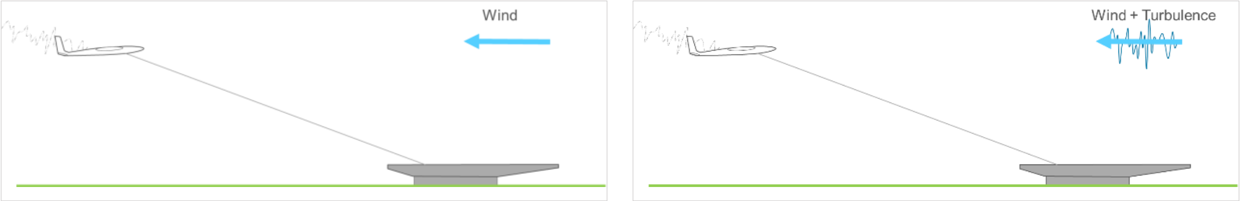

Figure 5, Simulation cases for landing without platform motions: Case 1 (left) - Constant wind speed; Case 2 (right) - Wind turbulence included

A measure of landing uncertainty is the standard deviation of three important parameters at the end of the approach: the relative horizontal speed, the relative height of the RPA above LLA/deck and the relative pitch angle. Combined these parameters provide a good estimation of uncertainty in landing impact, without requiring the modelling of the more complex snap load during the arresting phase of the landing. Although there are also limits to roll, yaw and lateral motion during landing, simulations of Ampyx Power with a 6DOF model of AP3 indicate that these motions are more precisely controlled and therefore less critical for the landing.

The simulations are divided over 5 different cases, each with increased complexity. In Figure 5 the onshore cases (no FP motions) are visualized. The first case will serve as a baseline, and only includes the uncertainties following from varying initials conditions, this case is also used to compare two different starting altitudes. Case 2 is used to determine the effect of wind turbulence on the landing uncertainty. After comparing two different wind turbulence models (Dryden and Von Kármán), the decision to use only the Von Kármán model in further analyses is verified.

The schematic visualizations of the offshore cases are shown in Figure 6, in these cases the effect of floater motions is investigated. Cases 3 and 4 are exactly the same as respectively cases 1 and 2, with the difference that the landing platform (end point) is moving harmonically. This allows for an investigation of the effect of motion amplitude and frequency. In the final case, case 5, the database of FP motions is used as input for the landing simulations. Based on the metocean data at a location of the east coast of Scotland, expected variations in landing approach are determined for low, medium and high wind speeds and compared to previously generated data.

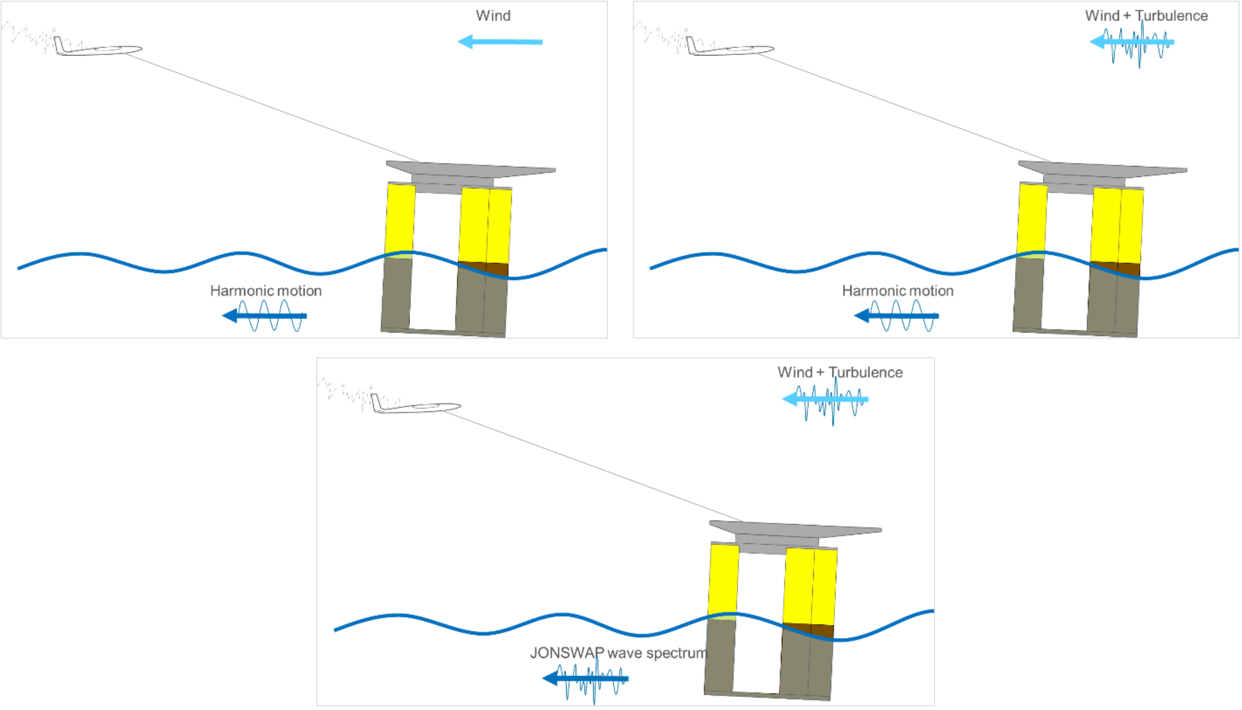

Figure 6, Simulation cases for landing with platform motions: Case 3 (top left) - Constant wind speed on harmonic FP motions; Case 4 (top right) Wind turbulence included and harmonic FP motions; Case 5 (bottom) - Wind turbulence included and simulated FP motions in JONSWAP spectrum

Only the landing approach is investigated in this research and not the arrest and touchdown of the RPA. The most important reason for this is that the time between the RPA flying over the pulley (start of arrest) and touchdown on deck is only a fraction of a second (at low wind speeds this time is shorter than at high wind speeds, but momentum of RPA is larger). Combined with the large inertia of the platform the effect of the landing on platform motions is relatively small in this timeframe. When one assumes conservatively that all momentum of the RPA is transferred to the floating platform in a time span of 0.4-0.67s (10m/$\dot{L_t}$), the horizontal deflection and pitch deflection of the platform at touchdown would be respectively 0.016 meter and 3.2°. This seems like a significant difference in pitch angle, but note that the horizontal damper connected to the pulley would dissipate most of the kinetic energy of the RPA. If 60% of the energy is dissipated by the damper, the resulting angle is just 1.2° at touchdown. This angle can be accounted for by incorporating it in the controller, as in the final phase of the approach the glide path controller switches to pitch angle control. This angle is therefore not considered critical or even significant for the landing performance. By not considering this phase of the landing the numerical model can be greatly simplified, allowing for more simulations in the same amount of time.

1.3 State of the art

In the following section the latest developments in airborne wind energy, floating wind turbines and offshore aerial vehicle landings are covered.

Airborne Wind Energy Systems

In 1980, Miles L. Loyd proposed and analyzed AWE systems in crosswind flight for the first time (Loyd, 1980). In the 1990's Wubbo Ockels brought more attention to the technology at DUT, this indirectly led to the commercial spinoff of both Ampyx Power and more recently Kitepower. Although there are similarities between the companies, they focus on different markets with different products. Where Ampyx Power is developing a rigid wing for utility scale (on-grid) operation, Kitepower has developed a 100kW system with a flexible wing (kite) and easy transportability in a 20ft container, which makes it perfect for off-grid use.

But not just in the Netherlands AWE is developed, in Figure 7 an overview is given of all companies that contribute to the development of AWE globally. Most of these companies came together in Freiburg, Germany in October 2017 for the Airborne Wind Energy Conference (AWEC) 2017, this provided interesting insights on the state of the technology (Diehl, Leuthold, & Schmehl, 2017).

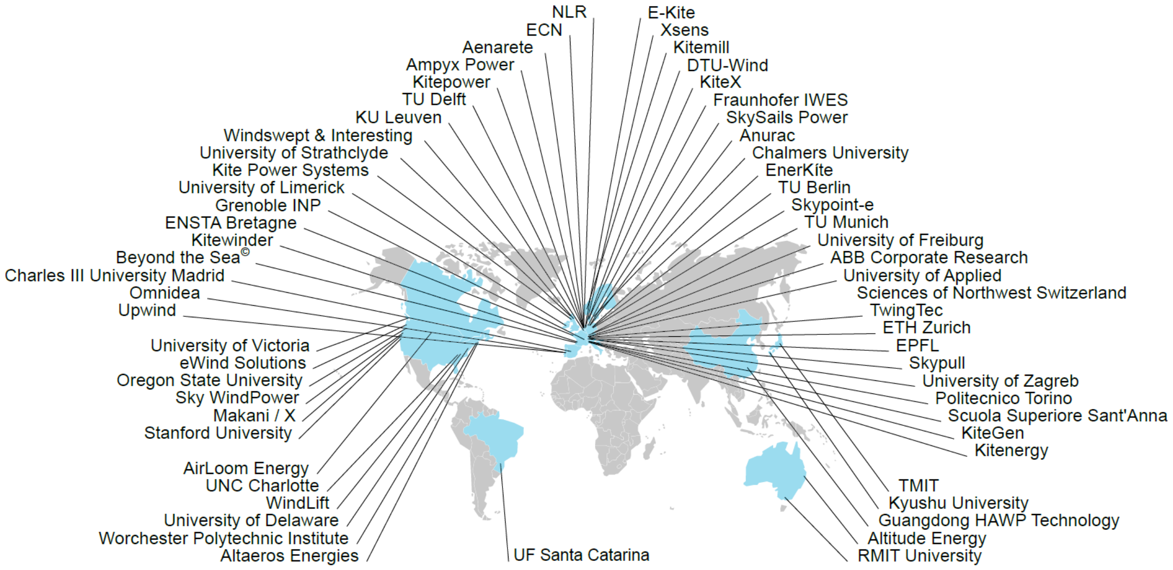

Figure 7: Airborne Wind Energy developers (Diehl et al., 2017; Schmehl, 2017)

Most companies at AWEC can be divided between developers of off-grid power generation systems and developers of on-grid power generation (utility scale) systems. Companies with a focus on utility scale systems have in recent years converged towards rigid wing designs. One of these companies is Makani/X, they recently tested a 600 kW prototype, the M600 with a span of 28 meters (Felker, 2017). Makani noted the opportunities for AWE at deep water offshore locations, as well as other remote location like islands, where the installation of conventional wind turbines would be cumbersome. The system that Makani is developing is a drag type AWES, meaning that the aircraft has turbines connected to the wing that generate the power onboard. Refer to (Schmehl, Diehl, & Ahrens, 2011) for an overview of the technological diversifications within the sector.

TwingTec will focus in the near future predominantly on off-grid markets, but they have the ambition to contribute to the global energy market with multi megawatt systems as well. A roadmap towards an offshore 2.5 MW system was discussed during the conference and in Windtech International an artist impression of TwingTec's vision of an offshore wind farm was shown earlier this year (Luchsinger, 2017; Luchsinger et al., 2017).

Enerkite is an interesting player due to their take-off and landing methods. By means of rotating a mast and increasing tether lengths at the same time, the kite can be reeled out towards a safe altitude for power generation. For landing the same process is used in reverse. Successful initial experiments of this method with a rigid wing prototype were shown at the conference (Rieck, Ranneberg, Candade, Bormann, & Skutnik, 2017). In 2010 Ampyx Power considered a similar method as Enerkite for launching and landing the aircraft, as be seen in the thesis of Bontekoe (Bontekoe, 2010). But during the development of AP3 the linear take-off and landing method, as described in section 1.1.1, was selected.

Fagiano has looked into this linear approach to take-off and landing, and recently performed the first successful experiments with the linear take-off method (Fagiano, Nguyen-Van, Rager, Schnez, & Ohler, 2016; Fagiano, Nguyen-Van, & Schnez, 2017).

Another interesting development that is mostly taking place in academic environments is the dual kite system on a single tether (Zanon, Gros, Andersson, & Diehl, 2013). Although this system is still far from commercialization, it shows considerable benefits over the technologies currently in development, as higher altitudes can be reached due to lower tether drag. However, practical challenges for this method like take-off and landing are even higher than for the systems that are closer to commercialization.

Henrik Stiesdal, wind energy pioneer in the 1970's and 1980's and former CTO of Siemens Wind Power, contributed to AWEC by sharing his views on AWE from the perspective of conventional wind energy developers (Stiesdal, 2017). He recognized the complexity of the technology, but stressed that operational reliability and robustness demands are much higher than in any other, apparently similar industries. On top of that, challenges of technical, environmental and regulatory nature are more severe for AWE than they were for conventional wind turbines. To benefit from the opportunities that AWE has to offer these challenges should be met head on.

As mentioned, most companies recognize the opportunities of the application of AWE on floating foundations. Cherubini recently created an open-source 6DOF coupled simulation model of a floating AWES in crosswind flight (Cherubini, Vertechy, & Fontana, 2016). The numerical model includes a single catenary mooring line, a floating platform, tether and an aircraft in steady state crosswind flight. Cherubini focused on heave motion only (1DOF) of multiple platform shapes, and noted that in future works pitch, surge and irregular seas should be taken into account.

Floating wind energy concepts

A sector that has many similarities with deep water AWE is of course that of floating conventional wind turbines (FWT). The requirements for these floating platforms are similar, as the goal is the have the lowest cost design that still complies with the acceptable motion limits. And due to their relatively small size compared to floating platforms used in the oil and gas industry, similar methods in the development of numerical models for simulations can be used in deep water AWE developments as well.

More importantly FWT are a step ahead in their development, as several concepts have been deployed offshore. This can result in valuable experience in deep water maintenance, risk based inspection planning and installation methods, which are directly transferrable to deep water AWES.

Statoil is one of the pioneers in the industry with the Hywind project. In 2009 they deployed their first prototype with a turbine of 2.3 MW of the coast of Norway. In October this year (2017), Statoil commissioned the first floating wind farm at Buchan Deep. The 30 MW pilot park consists of five 6 MW turbines, on spar foundations with a draft of 80 meter (4C Offshore, 2017a). The assembled systems were towed from Norway, where the turbines were connected to the foundations, to the final site near Peterhead, Scotland.

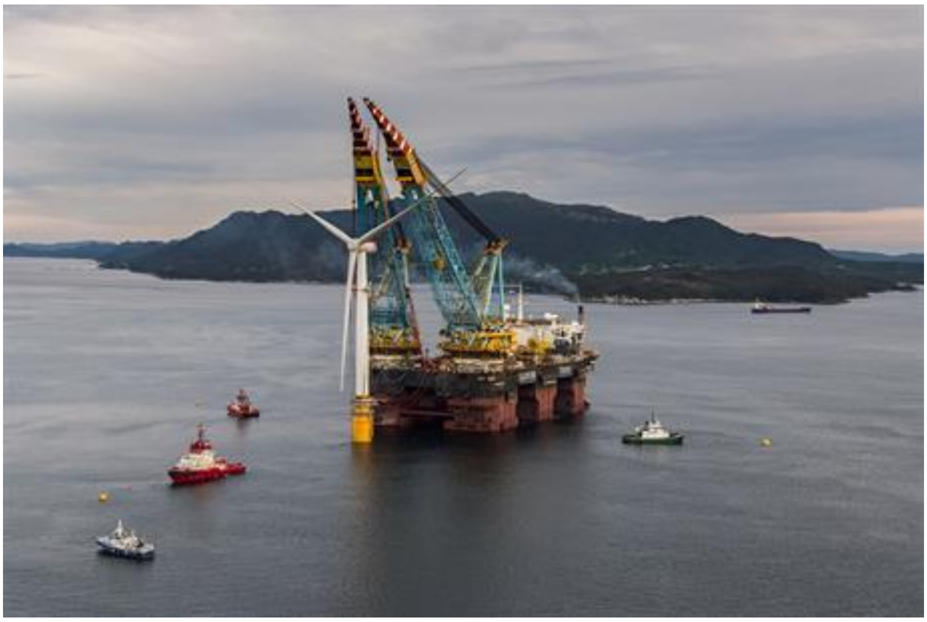

Figure 8, Hywind: Mating of offshore wind turbine with foundation in Norway with Saipem 7000
(Weston, 2017)

Principle Power approached the development of FWT in a similar way, starting with the deployment of a single 2 MW Windfloat prototype of the coast of Portugal in 2011. And now moving on to the developing a relatively small wind farm with larger turbines. The WindFloat Atlantic offshore wind farm with three 8.0 MW turbines is expected to be commissioned in 2018 (4C Offshore, 2017b). The type of platform that Principle Power has designed is very different from the Hywind spar design. The Windfloats are semisubmersible structures with three columns, which makes it similar to both the design of Mocean Offshore for the SAF project and to FWT concepts currently in development at GustoMSC, Fukushima Forward and DeepCWind (ReNEWS, 2017).

Landing aerial vehicles on floating platforms

For many years, the method of choice for auto-landing on aircraft carriers was based on the Instrument Landing System (ILS) (Felux, Dautermann, & Becker, 2013). ILS uses a combination of radio signals (and often in combination with high-intensity lightning arrays) to indicate the desired glide path in line with the runway. But nowadays, a shift towards augmented GPS based systems is occurring. Normal (non-encrypted) GPS signals have a limited accuracy of about 5 meter. However, one could improve the accuracy by placing another GPS receiver on another location (airfield/ship). Because the position errors are more or less equal for both locations as long as they obtain their signals from the same satellites, the relative position of the two objects can be determined with high accuracy (in best cases up to 10cm). This is a major benefit that augmented GPS based systems like GBAS, LAAS and JPALS have over ILS that has a position accuracy of several meters. Furthermore, a single device can be used onshore for an entire airfield, and not one on every runway. For aircraft carriers specifically, the SB-JPALS system is developed, which stands for Sea Based – Joint Precision Approach and Landing System and it will be used on the F-35C and F-35B aircraft (GPS World staff, 2016).

DARPA is currently developing a system for launching and landing small UAV’s; the DARPA SideArm project (DARPA, 2017). During take-off the small UAV that is suspended from a rails is catapulted forward. During landing, the UAV flies underneath the rails, and the system traps a hook that is extended from the back of the vehicle. Horizontal velocity is dissipated along the rails, the upward swing of the aircraft is accounted for with a net. The system has a relatively small footprint, which allows for easy installation on deck. This method has similarities to the take-off and landing method of Ampyx Power, but the largest difference is that a tether is already connected to the underside of the RPA. It makes sense to use this tether as a tool for landing, and not include other structural elements (like a hook) on the RPA.

The last project that is worth mentioning in this section involves landing reusable rockets on floating barges. This is the SpaceX project, and the floating barges are called Autonomous Spaceport Drone Ships (ASDS). SpaceX has delivered payloads into earth orbit using its Falcon rockets and Dragon spacecraft. To reduce cost, the launch systems are reusable. These systems return to earth and land vertically on an ASDS, as shown in Figure 9. At this point in time, sixteen landings have been attempted on the ASDS’s, five of which failed.

Figure 9, First stage of SpaceX Falcon 9 successfully landed on the ASDS 'Of Course I Still Love You'

(SpaceX, 2016)

2 Hydrodynamics

For the determination of the landing performance decrease due to floater motions, landing approaches will be simulated with floater motions that accurately correspond to offshore conditions. As explained in the introduction, case 5 of the landing approach simulations uses time signals of floater motions as input. To produce these time signals, a numerical model of the FP that captures the hydrodynamics is required.

The goal of this chapter is to explain the conventions, methods and assumptions that have been used to develop the hydrodynamic, numerical model. Special attention will be given to the incorporation of nonlinear drag effects as well as the calibration and validation of the numerical model with experiments at MARIN's test basin.

Mocean Offshore also developed a numerical model to determine motions of the floating platform as part of their design process. However, the numerical model they developed was a simplified representation based on Morison equations only. The motion responses they found were on the conservative side, compared to experiments at MARIN. An update of the responses was not performed, as the update would not affect the design of the platform. For the purpose of this study a numerical model that accurately represents the motions of the platform is required. This will lead to more reliable results when it comes to the relative effect of platform motions on the landing performance. Furthermore, the development of the numerical model in Simulink® allows Ampyx Power to investigate limiting wave conditions at a later stage of the AP4 design process, and could even provide a basis for a coupled numerical model for cross-wind flight.

2.1 Approach and assumptions

The approach that is taken to develop a numerical, hydrodynamic model is a combination of the panel method and non-linear empirical drag formulations in a time-domain analysis. The model is validated with experimental tests.

The panel method is a common numerical modelling technique based on 3-D potential theory for semi-submersible structures (Journée, Massie, & Huijsmans, 2015). By solving the potential function, the hydrodynamic properties of the FP like added mass, damping and wave-induced loads can be found in the frequency domain. The software package that has been used is ANSYS® Aqwa™ (ANSYS Inc., 2012). The properties that have been obtained with Aqwa™ are exported to a package that can calculate the time-domain response in a stochastic sea-state using the frequency domain data; in this case an adjusted version of the Marine Systems Simulator (MSS) in Matlab®/Simulink® (Fossen & Perez, 2004). However, the size and shape of the FP does introduce a problem; the hydrodynamic damping is no longer mainly caused by wave radiation, which can be derived with potential theory, but instead by viscous effects. That is why a numerical model based solely on the panel method is not sufficient.

An alternative that is capable of capturing the viscous effects, leading to more accurate results would be a Computational Fluid Dynamics (CFD) model. However, the purpose of the model is producing FP motion responses in the time-domain for a multitude of stochastic sea states, each with a duration of approximately three hours. The amount of computational effort required to produce this using CFD is not available in the project.

The viscous effects should therefore be taken into account in another way. This is where the customizability of the MSS becomes an advantage, as additional subsystems that calculate viscous loads can easily be incorporated in the Simulink® model. This holds for both the viscous loads as well as for the mooring loads. To calculate the viscous loads, the structure is discretized into cylindrical and plate elements. The drag on each element is calculated using the local flow velocity, projected area, water density and a drag coefficient. The determination of viscous loads is discussed in more detail in section 2.3.2.

The numerical model is validated by scale model testing in a wave basin at MARIN. The length scaling is 1:25, and because surface waves are gravity driven, the Froude number will be equal for a full-scale version.

Assumptions in hydrodynamic model

Several assumptions are inherent to the chosen method. In this section the assumptions that have been made to obtain a functioning numerical model are discussed.

Rigid body with point mass; meaning that no hydro-elastic effects are taken into account. This follows from the use of the diffraction software, and it is not expected to have a large effect on the motions of the structure. In fact, the floater will be designed in such a way that structural deflections are very small. Large deflections often go hand in hand with higher stresses, and this is undesirable for a structure that will need to have a long fatigue life.

Linear waves; breaking waves, spray and slamming are not taken into account. In storm conditions, the waves can approach their deep-water breaking limit. At this point, the waves can no longer be represented by a superposition of sinusoidal wave components. These nonlinearities cannot be accurately represented in the hydrodynamic model; a more complex method like CFD is required. On top of that, the assumption is made that the wave does not reach the top structure on the floater, and that the lower keel plate remains fully submerged. The main purpose of this hydrodynamic model is to obtain reliable motion data of the floater in irregular seas, the nonlinear wave effects mentioned here are more relevant for the design of the floater in extreme conditions (determination of freeboard, safe stowage of RPA in survival condition, etc.), which is beyond the scope of this project.

Deep-water assumption (DWA); leads to a simplification of the dispersion relationship that relates the wavenumber k (or wavelength) to the wave frequency ω (or wave period).

$$\omega^2 = k \cdot g \cdot \tanh(kh) \xrightarrow{DWA} \omega^2 = k \cdot g$$

This is valid for water depths that are more than half the wavelength according to DNV-RP-C205 (DNV, 2007). This is the case for wave periods up to 11.3 seconds at a water depth of 100 meter. The bulk of the conditions that are examined will have peak wave periods smaller than 11 seconds. In Figure 10, a comparison is made between the wave particle velocities with and without the DWA at wave periods of 11 and 14 seconds. At a period of 11 seconds, there is no significant difference, especially when considering that the draft of the floating platform is just 16 meters. At a period of 14 seconds, the difference is visible, but still relatively small. And as mentioned before, wave periods larger than 11 seconds are not common.

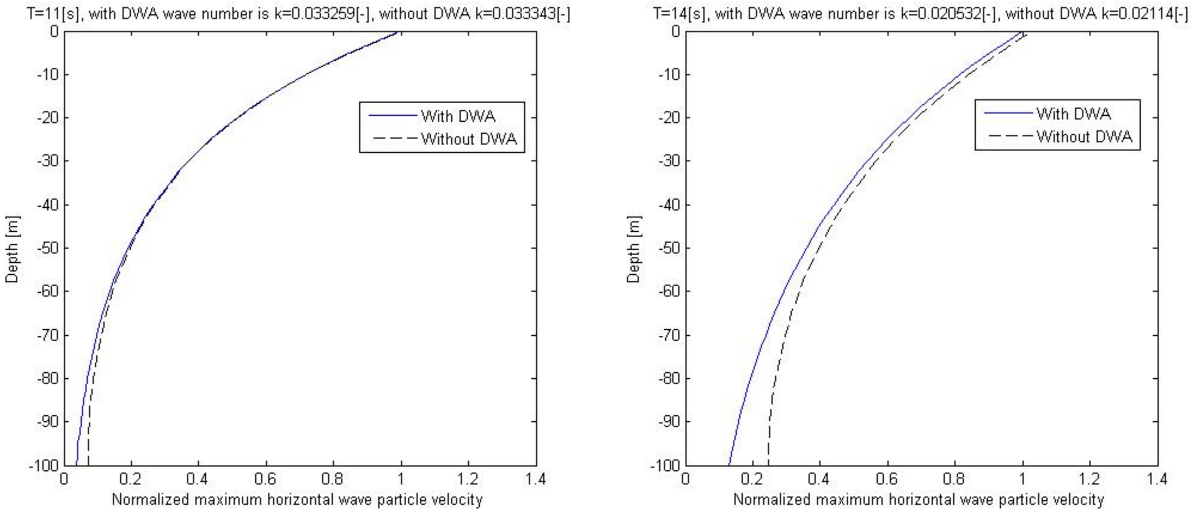

Figure 10, Effect of deep-water assumption on horizontal wave particle velocity amplitude (normalized)

JONSWAP wave spectrum; for the stochastic sea state analyses a JONSWAP wave spectrum is used, with a peakedness factor (γ) of 3.3. This wave spectrum is the result of the JOint North Sea WAve Project, and it is commonly used in offshore projects that are located in the North Sea. Due to a lack of data on the wave frequency spectrum at the Buchan Deep location, this conventional approach is assumed acceptable. When more measurement data is available, the analysis can be updated.

Simplified viscous effects; not all effects caused by viscosity are fully captured by the hydrodynamic model. The viscous effects can be divided over the several load contributions, for each contribution is mentioned to what extend it is included in the hydrodynamic model:

- Viscous drag on cylindrical columns: Is taken into account using drag formulations with a variable drag coefficient (dependent on KC number) using the undisturbed flow field. In this way the nonlinearity was conserved, at the expense of some computational speed. Skin friction parallel to the columns was assumed negligible.
- Viscous drag on keel plate: Is approximated only perpendicular to the plate (no skin friction), using a constant drag coefficient and again using the undisturbed flow field. The drag coefficient should be an acceptable representation for the loads resulting from the flow disturbances caused by the keel plate and stiffeners. On this particular shape little literature is available, that is why first a drag coefficient of 2.0 is assumed based on (DNV, 2007). After the experiments are performed, the drag coefficient can be updated.
- Vortex induced load: Around cylindrical objects in constant flow, vortex shedding can occur. Vortex shedding induces loads on the structure perpendicular to the flow direction. In combination with resonance of the structure, its effect can be significant. This load is not considered in the hydrodynamic model, because the flow around the columns is assumed non-uniform and oscillating, as it is to a greater extend defined by waves than by current. If vortex shedding occurs in this type of flow, the duration will be short, therefore the structure does not build up resonance motion. It is therefore not included in the analysis.
- The difference in Reynolds number between the numerical analyses and the experiments at MARIN is expected to have negligible effect on the floater motions. The Reynolds number for the scale model is a factor 125 smaller than that of the full-scale design in the same conditions, but the actual Reynolds number is constantly varying in an oscillating flow.

No wind loads; the effect from constant wind and wind gusts on the unsubmerged part of the FP is assumed negligible. The top structure of the FP has a relatively small projected area in the horizontal wind directions, therefore wind loads are not assumed to have a great impact on the motions of the FP.

Tether load neglected during landing approach; only significant during crosswind flight. Although some tension should be on the tether to keep it out of the water. The tether tension is orders of magnitude smaller than the hydrodynamic loads. For example, a step in tether tension of 40kN (which is larger than the maximum change of tension during the approach), leads to a change in position and orientation of the FP after two seconds of just 3.5 cm and 0.3°.

Simplified mooring; the mooring configuration is modelled as linear springs acting as a restoring contribution in surge, sway and yaw motion. The reason for this assumption is the level of uncertainty on the mooring configuration, and the state of the design. The effect will most likely be that nonlinearities in surge, sway and yaw are not fully captured, but also increased vertical loads as a result of horizontal deflection are not taken into account. On top of that the mooring lines could have an additional damping contribution. The effect on the motions can be significant and future analyses should be performed with a more accurate representation of the mooring configuration (e.g. using discretized mooring lines and a catenary calculation).

2.2 Conventions

Use has been made of several different reference frames. The conventions for these frames is covered in this section. In Figure 11, the conventions of forward (FWD), aft (AFT), portside (PS) and starboard (SB) in a schematic top view of the FP.

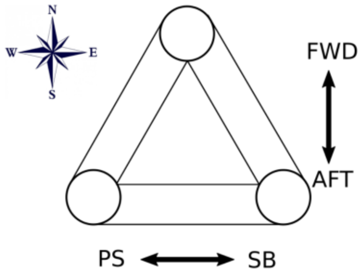

Figure 11, Conventions for FP (top view)

Four reference frames are of interest: the Aqwa^{TM} body-fixed frame (or the Local System Axis (ANSYS Inc., 2012)), in which the frequency-domain analysis is performed; the MSS body-fixed frame (f) and MSS North-East-Down (NED) frame (n), in which the time-domain analyses are performed; and the MARIN body-fixed reference frame, in which the experimental results are presented. The position of the origin and directions of the axes and rotations of these reference frames is presented in Table 3.

Table 3, Reference frame conventions

	Aqwa^{TM} body-fixed frame	MSS body-fixed frame (f)	MSS NED frame (n)	MARIN body-fixed frame
Origin X=0	LCG	LCG	LCG-x_0*	LCG
Origin Y=0	TCG	TCG	TCG-y_0*	TCG
Origin Z=0	VCG	VCG	VCG-z_0*	VCG
Positive X-direction	FWD	FWD	North	FWD
Positive Y-direction	PS	SB	East	PS
Positive Z-direction	Up	Down	Down	Up
Rotations positive	Right hand rule	Right hand rule	Right hand rule	Right hand rule

* Initial condition defined for simulation

The origin of all body-fixed reference frames is at the center of gravity of the structure, only the direction of the y and z axes are switched in the MARIN and Aqwa^{TM} frames. The reason why the down positive conventions are maintained in the MSS model is that the same NED (earth-fixed) reference frame is used in the aerodynamic analyses with the RPA. The origin of the MSS NED frame (n) is the equilibrium position of the FP.

In all reference frames the wave direction is defined as 0° when it moves in the positive x-direction, and 90° when it moves in the positive y-direction.

2.3 Equations of motion

The equation of motion is crucial for hydrodynamic analyses:

$$\left(\boldsymbol{M} + \boldsymbol{A}(\omega)\right)\ddot{\boldsymbol{\xi}}^f(t) + \boldsymbol{B}(\omega)\dot{\boldsymbol{\xi}}^f(t) + \boldsymbol{G}\boldsymbol{\xi}^n(t) = {\boldsymbol{\tau}_{exc}}^f(t) \tag{2.1}$$

In this equation $\boldsymbol{\xi}$ indicates position and orientation of the structure in six degrees of freedom, while $\dot{\boldsymbol{\xi}}$ and $\ddot{\boldsymbol{\xi}}$ are respectively the velocities and accelerations of the structure. Superscripts ‘f’ and ‘n’ indicate in what reference frame the variables are defined (with ‘f’ for MSS body fixed, and ‘n’ for MSS NED). $\boldsymbol{M}$ represents the inertia of the structure, $\boldsymbol{A}(\omega)$ is the frequency dependent added mass, $\boldsymbol{B}(\omega)$ is the frequency dependent damping, $\boldsymbol{G}$ is the stiffness/restoring matrix, , and finally $\boldsymbol{\tau}_{exc}(t)$ stands for all exciting forces and moments acting on the structure. $\boldsymbol{\tau}_{exc}(t)$ is the sum of wave loads acting on the structure and other external forces, e.g. as a result of mooring:

$${\boldsymbol{\tau}_{exc}}^f = {\boldsymbol{\tau}_{wave\_1st}}^f + {\boldsymbol{\tau}_{wave\_2nd}}^f + {\boldsymbol{\tau}_{nl\_drag}}^f + {\boldsymbol{\tau}_{moor}}^n \tag{2.2}$$

The 1st and 2nd order wave loads (${\boldsymbol{\tau}_{wave\_1st}}^f, {\boldsymbol{\tau}_{wave\_2nd}}^f$) are determined by lookup tables based on the frequency, phase and amplitude of the individual components of the wave field at the position of the FP. The lookup tables are basically the Response Amplitude Operators (RAO’s) that have been defined with Aqwa^{TM}, in section 2.3.1 the derivation of the RAO’s is touched upon. The non-linear drag component (${\boldsymbol{\tau}_{nl\_drag}}^f$), is calculated at each time-step, using the formulations given in section 2.3.2. The mooring loads (${\boldsymbol{\tau}_{moor}}^{n}$) are linearized, and depend on the surge, sway and yaw displacements. More information on the mooring is given in section 2.3.3.

The inertia, added mass, damping and stiffness are assumed linear, and these properties define the structure's hydrodynamics. From the geometry and mass distribution of the FP, the inertia and restoring matrices can be determined. Both have entries only on the diagonal of the matrix due to the symmetry of the structure. The inertia matrix diagonals are defined as follows:

$$\begin{gathered}
M_{11} = M_{22} = M_{33} = \rho\nabla \\
M_{44} = \rho\nabla \cdot {k_{xx}}^{2} \\
M_{55} = \rho\nabla \cdot {k_{yy}}^{2} \\
M_{66} = \rho\nabla \cdot {k_{zz}}^{2}
\end{gathered} \tag{2.3}$$

Where ρ is the density of water in kgm^{-3}, ∇ is the displacement in m^{3}, and k_{xx}-k_{zz} are the radii of gyration for roll, pitch and yaw in meter.

The restoring matrix diagonals that follow from hydrostatics are defined as follows:

$$\begin{gathered}
G_{11} = G_{22} = G_{66} = 0; \\
G_{33} = \rho g \cdot A_{WL} \\
G_{44} = \rho g\nabla \cdot GM_{T} \\
G_{55} = \rho g\nabla \cdot GM_{L}
\end{gathered} \tag{2.4}$$

Where A_{WL} is the water plane area, and GM_{T} and GM_{L} are respectively the transversal and longitudinal metacentric heights.

Equation (2.1) holds for steady state responses, in particular to sinusoidal excitations. However, when modelling the response to irregular seas in the time-domain, no steady state response is reached. Therefore a different approach that was proposed by Cummins is considered (Cummins, 1962). This approach includes a convolution term that takes into account fluid memory effects due to wave radiation.

$$(\boldsymbol{M} + \boldsymbol{A})\ddot{\boldsymbol{\xi}}^{f}(t) + \int_{0}^{t} \boldsymbol{K}(t-\tau)\dot{\boldsymbol{\xi}}^{f}(\tau)d\tau + \boldsymbol{G}\boldsymbol{\xi}^{n}(t) = {\boldsymbol{\tau}_{exc}}^{f}(t) \tag{2.5}$$

However, using this approach in a numerical model makes the analysis computationally demanding. For this reason, the fluid memory effects are modelled using a parametric state space representation.

The kernel $\boldsymbol{K}$ in the convolution term is a matrix of retardation functions. The relationship between the kernel and the frequency dependent added mass and damping was found by (Ogilvie, 1964) (Note: $\boldsymbol{B}(\infty) = 0$, and is therefore not included in the relationship):

$$\boldsymbol{A}(\omega) = \boldsymbol{A}(\infty) - \frac{1}{\omega}\int_0^\infty \boldsymbol{K}(t)\sin\omega t\, dt \tag{2.6}$$

$$\boldsymbol{B}(\omega) = \int_0^\infty \boldsymbol{K}(t)\cos\omega t\, dt \tag{2.7}$$

This lead to the following non-parametric representations of the kernel in time-domain and frequency-domain respectively:

$$\boldsymbol{K}(t) = \frac{2}{\pi}\int_0^\infty \boldsymbol{B}(\omega)\cos\omega t\, d\omega \tag{2.8}$$

$$\boldsymbol{K}(j\omega) = \boldsymbol{B}(\omega) + j\omega[\boldsymbol{A}(\omega) - \boldsymbol{A}(\infty)] \tag{2.9}$$

Now because the convolution is a dynamic linear operation it can be represented by a state space model:

$$\boldsymbol{\mu}_r = \int_0^\infty \boldsymbol{K}(t-\tau)\dot{\boldsymbol{\xi}}^f(\tau)d\tau \;\Leftrightarrow\; \begin{matrix}\dot{\boldsymbol{x}} = \boldsymbol{A}_c\boldsymbol{x} + \boldsymbol{B}_c\dot{\boldsymbol{\xi}}^f \\ \boldsymbol{\mu}_r = \boldsymbol{C}_c\boldsymbol{x}\end{matrix} \tag{2.10}$$

Which can be rewritten in the Laplace domain:

$$\boldsymbol{\mu}_r = \boldsymbol{K}(s)\dot{\boldsymbol{\xi}}^f = \frac{\boldsymbol{C}_c\boldsymbol{B}_c}{(sI - \boldsymbol{A}_c)}\dot{\boldsymbol{\xi}}^f \tag{2.11}$$

$\boldsymbol{K}(s)$ is a matrix of transfer functions that is used in the simulation model (in Simulink®).

$$\boldsymbol{K}(s) = \begin{bmatrix} \frac{P_{11}(s)}{Q_{11}(s)} & \cdots & \frac{P_{16}(s)}{Q_{16}(s)} \\ \vdots & \ddots & \vdots \\ \frac{P_{61}(s)}{Q_{61}(s)} & \cdots & \frac{P_{66}(s)}{Q_{66}(s)} \end{bmatrix} \tag{2.12}$$

Where:

$$\frac{P_{ij}(s)}{Q_{ij}(s)} = \frac{b_m s^m + b_{m-1}s^{m-1} + \cdots + b_0}{s^n + q_{n-1}s^{n-1} + \cdots + q_0} \tag{2.13}$$

The transfer functions are obtained by LS (least squares) fitting them to from the discrete data frequency domain model of the kernel ($\boldsymbol{K}(j\omega)$). Minimum order of the transfer functions is 2, and order is increased until an acceptable fit is found. Special attention is given to the region around the natural frequencies. In Figure 12 an example is given of a transfer function fit to the added mass and damping data for yaw motion. In the left two subplots the 4th order fit to the kernel is shown, and on the right the corresponding fit to the added mass and damping data points is visualized.

After the kernel ($\boldsymbol{K}(s)$) is determined, the matrices $\boldsymbol{A}_c, \boldsymbol{B}_c$ and $\boldsymbol{C}_c$ can be derived using the built-in Matlab® function '*tf2ss()*' that transforms transfer functions to state space models. These state space models are used in the fluid memory block of the Marine Systems Simulator that is used for the time-domain analyses (Fossen & Perez, 2004).

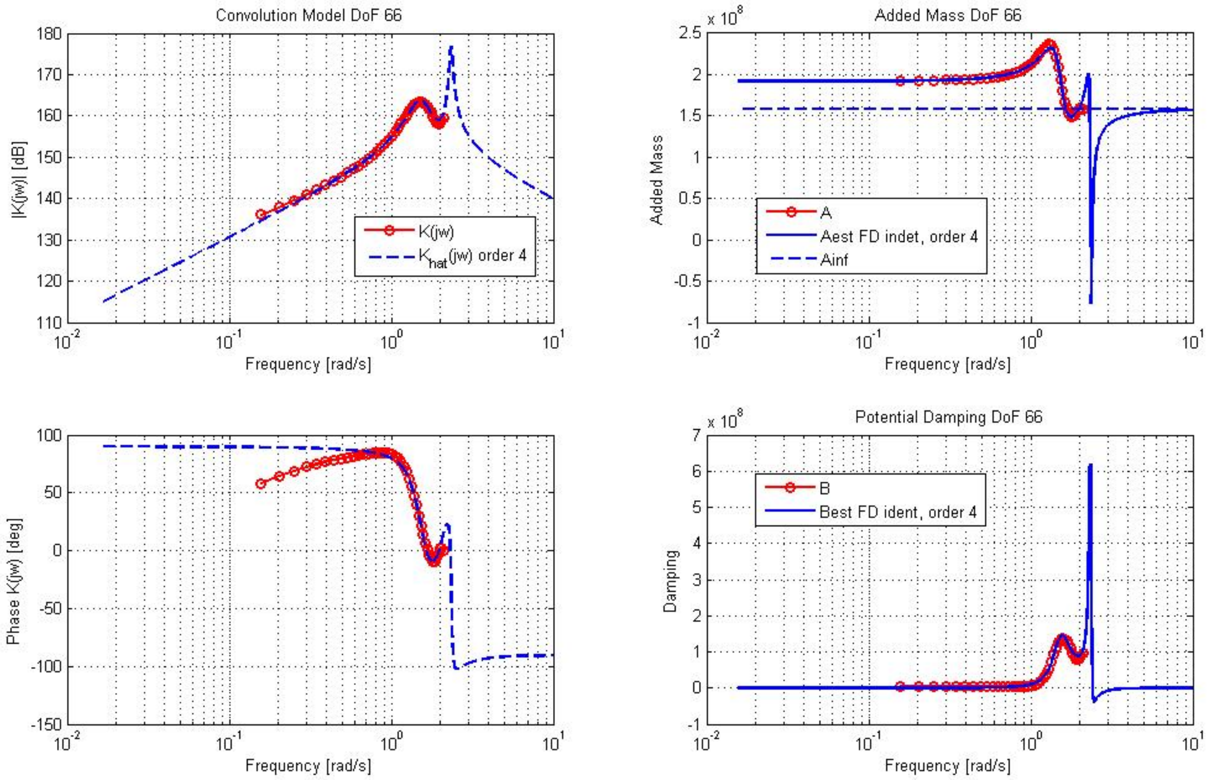

Figure 12, Example of fitting transfer function to Kernel derived from added mass and damping matrix data for yaw motion

It is important that the correct frequency dependent damping and added mass matrices, as well as the correct exciting loads are at the basis of this time-domain model. In the following section, the panel method and in particular the input and results from the Aqwa™ analysis is discussed. Which is followed by a section that reviews the incorporation of viscous effects in the Simulink® model.

2.3.1 Panel method and potential theory

The panel method is used to determine the hydrodynamic properties of the platform in the frequency domain. This includes the frequency dependent added mass and the radiation part of the damping matrices, as well as the 1st and 2nd order wave loads.

Preliminary to the hydrodynamic analysis a hydrostatic analysis is performed, which results in a restoring matrix that correspond to equation (2.4). The analysis is based on potential theory; a flow that is represented by velocity potentials is non-viscous, incompressible, continuous and homogeneous (Journée et al., 2015). The linear fluid velocity potential (Φ) can be written as a product of a space-dependent term (ϕ) and a time-dependent term ($e^{-i\omega t}$).

$$\Phi(x,y,z;t) = \phi(x,y,z) \cdot e^{-i\omega t} \tag{2.14}$$

Pressure p and flow velocities u, v and w can be derived from the velocity potential Φ using the following relations:

$$p = -\rho \frac{\partial \Phi}{\partial t} - \rho g z - \frac{1}{2}\rho\left(\vec{\nabla}\Phi\right)^2 \tag{2.15}$$

$$u = \frac{\partial \Phi}{\partial x}; v = \frac{\partial \Phi}{\partial y}; w = \frac{\partial \Phi}{\partial z} \tag{2.16}$$

Forces and moments acting on the body can be determined by integrating the pressure over the body surface.

The linear fluid velocity potential can be seen as a superposition of three potentials: the undisturbed incoming wave potential Φ_0, the radiation potentials for each of the six body motions $\sum_{j=1}^{6} \Phi_j$, and the diffraction potential Φ_7.

$$\Phi(x,y,z;t) = \Phi_0 + \sum_{j=1}^{6} \Phi_j + \Phi_7 \tag{2.17}$$

The undisturbed incoming wave potential Φ_0 in deep water describes the flow that results from the undisturbed surface waves alone. Note that these surface waves are a sum of N linear (sinusoidal) wave components, defined by their direction ψ_i, wavenumber k_i, wave frequency ω_i, phase angle shift θ_i and wave amplitude ζ_{a_i}.

$$\Phi_0(x,y,z;t) = \sum_{i=1}^{N} \frac{\zeta_{a_i} \cdot g}{\omega_i} e^{k_i z} \sin(k_i(\sin\psi_i\, y + \cos\psi_i\, x) - \omega_i t + \theta_i) \tag{2.18}$$

The wave frequency ω and wave number k are related to each other according to the deep water dispersion relationship:

$$\omega^2 = kg \tag{2.19}$$

Because the potential flows can be super positioned to obtain the total flow, only the wave potentials for a range of wave directions, and wave frequencies need to be calculated.

These can later be combined to obtain an irregular wave pattern. The surface elevation of the irregular wave pattern is represented by the following equation:

$$\zeta(x,y;t) = \sum_{i=1}^{N} \zeta_{a_i} \cdot \cos(k_i(\sin\psi_i\, y + \cos\psi_i\, x) - \omega_i t + \theta_i) \tag{2.20}$$

The loads on the floating body that are caused by the undisturbed wave potentials are called Froude-Krylov forces and moments.

The wave particle velocities that can be derived from the undisturbed wave potential will also be used in the time-domain analysis to calculate additional viscous forces; however, this is not part of potential theory, and will therefore be discussed in the next section (section 2.3.2).

The wave disturbances due to the presence of a body are represented by radiation and diffraction potentials. The two can be distinguished as follows; radiation potentials result from the motions in six degrees of freedom of the floating body in still water, while the diffraction potentials are a result of the diffraction of incoming waves by the body (fixed or floating). The diffraction potential has most influence on the wave-induced loads, whereas the radiation potentials have a larger influence on the damping.

Several boundary conditions need to be considered before solving the radiation and diffraction potentials:

- Continuity condition or Laplace equation: The fluid is homogeneous and incompressible.
- Seabed boundary condition: Water does not penetrate the seabed, vertical flow velocity is equal to zero at seabed (assuming horizontal seabed).
- Free surface boundary condition: The pressure at the free surface of the fluid is equal to the atmospheric pressure.
- Kinematic boundary condition at body surface: Water does not penetrate body surface, normal flow velocity to the body surface is therefore equal to zero.
- Radiation condition: When distance R from the body becomes large, the potential approaches zero.

The radiation and diffraction potentials are solved numerically using Green’s integral theorem, which allows for the transformation of the three-dimensional potential equation to a surface integral equation. This surface integral equation is called Green’s identity and represents a distribution of sources and dipoles on the surface. The source and dipole strengths are the unknowns which have to be solved to obtain the radiation and diffraction potentials. To solve the potential the body surface is discretized in panels, for each panel the source or dipole strength is solved by making use of the abovementioned boundary conditions.

From the space dependent term of the radiation potentials the added mass a_{kj} and damping coefficients b_{kj} can be determined:

$$a_{kj} = -Re\left[\rho \iint_{S_0} \phi_j n_k \cdot dS_0\right] \tag{2.21}$$

$$b_{kj} = -Im\left[\rho\omega \iint_{S_0} \phi_j n_k \cdot dS_0\right] \tag{2.22}$$

ANSYS® Aqwa^{TM} and other diffraction software packages can determine the hydrodynamic properties of fixed or floating structures in waves upon these principles.

Aqwa^{TM} model input

The structure described in the introduction section 1.1.2 is reproduced for Aqwa^{TM} using the DesignModeller^{TM} suite. In order to obtain a usable mesh, the keel plate thickness has been increased to 0.8m, which is the height of the stiffeners on the plate. It was expected that these stiffeners would trap the water on top of the keel plate (as per scenario A in Figure 13), which would justify the increase of keel thickness in the model. In future analyses the keel plate should be modelled using elements of zero thickness (Lee & Newman, 2005), because from experiment follows that the added mass has been overestimated for pitch and roll, see section 2.4.

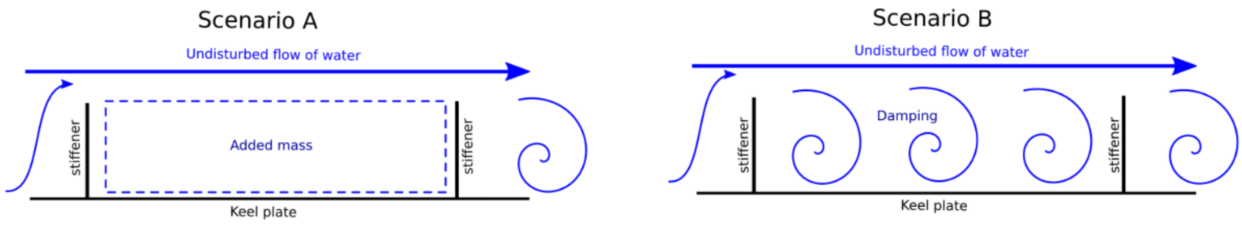

Figure 13, Possible flow scenarios at the keel plate of the FP, with scenario A being an added mass dominant scenario because of trapped water, and scenario B a damping dominant scenario due to increased turbulence/eddies

A mesh is created from the geometry, with a maximum element size set to 1m, which limits the minimum allowed period to approximately 2 seconds. A larger element size would not capture the shape of the structure correctly. The meshed structure is shown in Figure 14.

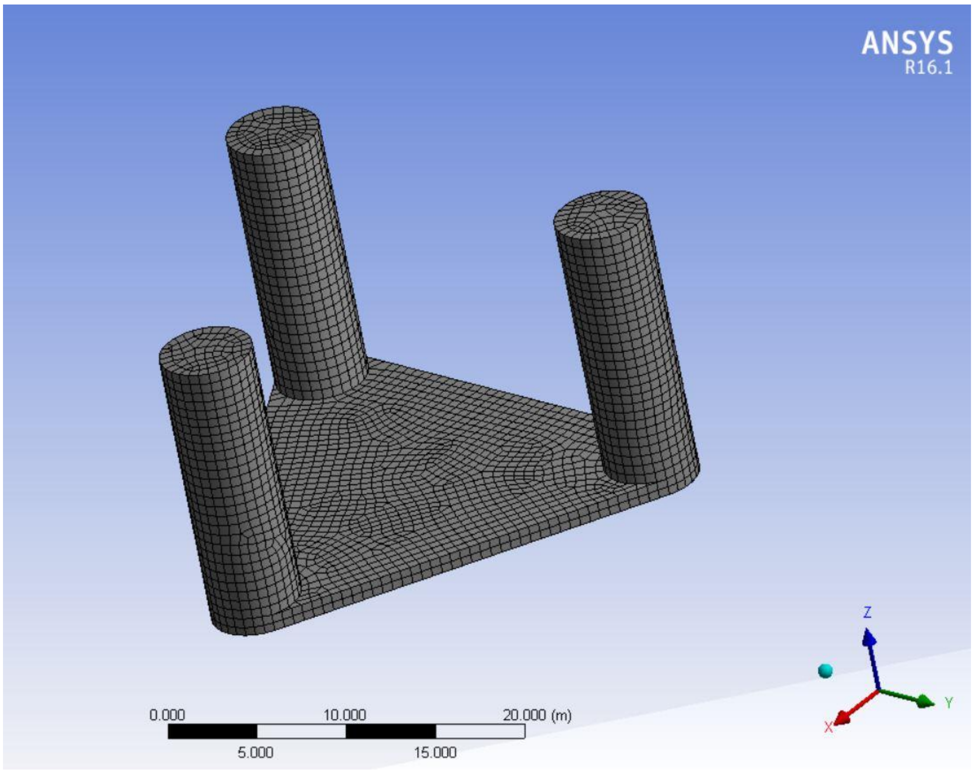

Figure 14, Visualization of grid in Aqwa^{TM} (ANSYS® 16.1 Workbench)

Wave directions ranging from -180° to 180° with steps of 10° are required to be analyzed, because the output of the analysis should later be imported into the time-domain model, which has its own conventions. Forty frequencies are analyzed, in order to obtain a good resolution for the RAO's. The inertia properties of the FP have been included in a point mass.

The Aqwa^{TM} workbench creates with this data a .DAT file that is imported to Aqwa^{TM} GS. In the Aqwa^{TM} GS environment, the solver finds the hydrodynamic properties of the FP based on potential theory.

2.3.2 Viscous effects

As mentioned in the beginning of this chapter, the relatively small size and particular shape of the FP result in a numerical model where viscous effects cannot be neglected. In this section the methods in which the viscosity is taken into account in the time-domain analyses is discussed. First the loads on the columns (cylindrical elements) is discussed, and then the loads on the keel plate (plate elements).

In Figure 15 a visualization of the drag elements can be found. It shows that a larger amount of discretizations is used for the columns. This is done to capture the vertical variation in flow velocity (as seen in Figure 10) accurately, whereas the variation in flow velocity with respect to the horizontal position is smaller.

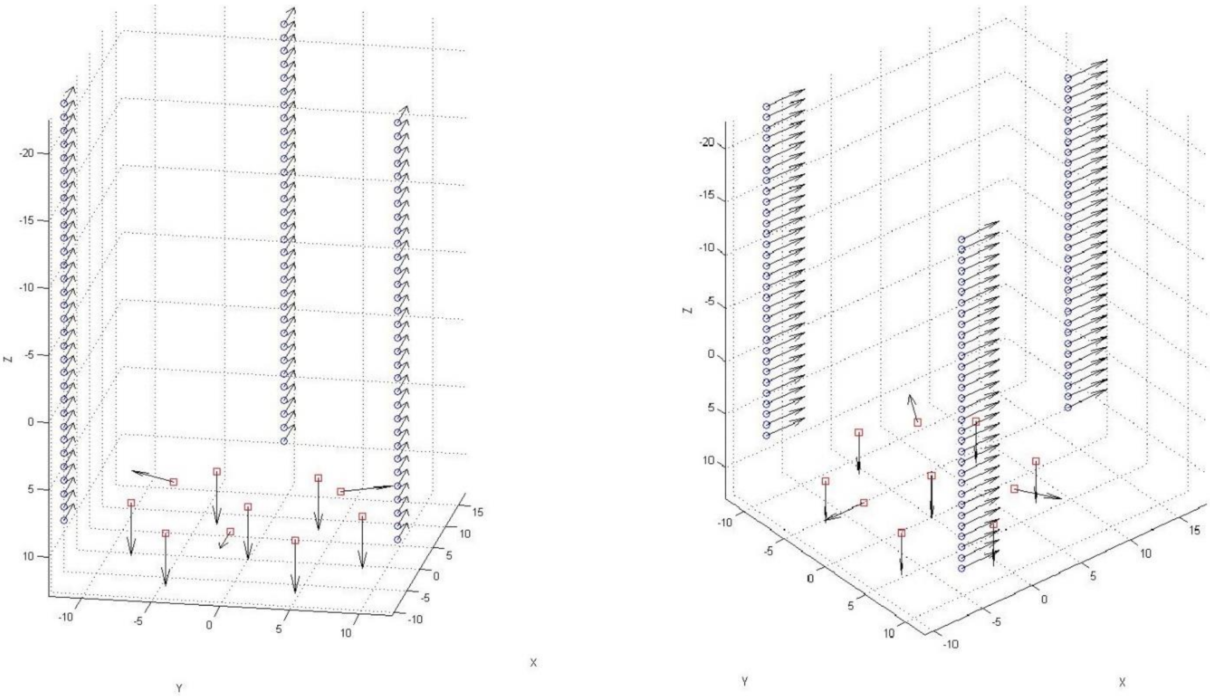

Figure 15, Visualization of non-linear drag elements; rounds indicate cylindrical element centers, squares indicate plate element centers and the arrows show the positive x-direction of each element

Cylindrical elements

Important to note is that the cylindrical columns of the semi-submersible have a relatively small diameter compared to the wavelengths. E.g. the wavelength of a wave with a period of 10 seconds is 156m according to the deep-water dispersion relationship ($\lambda = (g/2\pi)T^2$), while the column diameter is just 5.3m. In Figure 16, a graph from DNV-RP-C205 is shown with the different wave regimes; the red lines indicate the region in which this design falls. It is obvious that not a single wave force regime is responsible for most of the forces. That is why on top of the diffraction and radiation based forces, viscous damping and viscous wave excitation on the columns is taken into account. This is a similar method of modelling a small semi-submersible as described by (Huijs, De Bruijn, & Savenije, 2014).

The columns are discretized, and at each discretization, the relative flow velocity is calculated. To calculate the flow velocity, use is made of the undisturbed wave potential. The position of the discretization element is transformed to the global reference frame, where the undisturbed flow velocity is found by differentiating the flow potential. Wheeler stretching is also taken into account, to have a better representation of flow velocity around the still water level. This results in a flow velocity vector, which is then transformed back to the local reference frame. The relative velocity of the local element with respect of the global reference frame due to body motions is subtracted from the undisturbed flow velocity vector. That is how the relative flow velocity ($\boldsymbol{u}_{\perp,i}$) perpendicular to the centerline of the cylindrical elements is found.

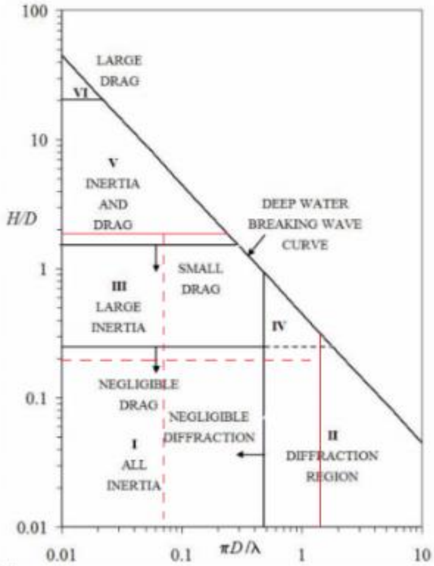

Figure 7-1
Different wave force regimes (Chakrabarti, 1987). *D* = characteristic dimension, *H* = wave height, *λ* = wave length.

Figure 16, Wave force regimes as defined in (DNV 2007)

The following equation is used to calculate the local drag force on the cylinder:

$$\boldsymbol{F}_{D,i,cyl} = \frac{1}{2} \cdot \rho \cdot C_d(K_C) \cdot D \cdot dz \cdot \boldsymbol{u}_{\perp,i} \left|\boldsymbol{u}_{\perp,i}\right| \tag{2.23}$$

This is the drag component of the Morison equation (Journée et al., 2015). The added mass/inertia part of the Morison equation is already accounted for by the frequency dependent added mass matrix that was determined by with the Aqwa$^{\text{TM}}$ analysis.

It is important not to overestimate these drag loads, as they damp the motion of the FP (overestimation of drag would thus lead to underestimation of motions). That is why the drag coefficient has been made dependent on the Keulegan-Carpenter (KC) number, according to (DNV, 2007). The KC number is defined as:

$$K_C = \frac{V \cdot T}{L} \approx \frac{\zeta_a \cdot \omega_p \cdot T_p}{D} = \frac{\pi \cdot H_s}{D} \tag{2.24}$$

Where for the period of oscillation T the peak period of the wave spectrum (T_p) is taken. V is the amplitude of the flow velocity oscillation, which is in this case assumed to be the significant wave particle velocity amplitude ($V = \max\left(\frac{\partial \Phi}{\partial x}\right) = \zeta_a \cdot \omega_p$). That is why the KC number can be defined as a function of significant wave height (H_s) and section diameter (D).

The characteristic length L is the column diameter of 5.3 meter. The KC number remains constant when Froude scaling is used, which allows for a better comparison of the full scale hydrodynamics with the model tests. More information on the scaling will be given in section MARIN test setup.

In case of the decay tests, there will be no waves acting on the structure, that is why a different (equivalent) KC number will be used ($K_{C,eq}$).

$$K_{C,eq} = \frac{V \cdot T}{L} = f(x) = \begin{cases} \dfrac{2 \cdot \delta_{ii,ini}}{D}, & Surge\ (ii = 11), Sway\ (ii = 22) and\ Heave\ (ii = 33) \\ \dfrac{2 \cdot \delta_{ii,ini} \cdot k_{ii}}{D}, & Roll\ (ii = 44), Pitch\ (ii = 55)\ and\ Yaw\ (ii = 66) \end{cases}$$

This is a constant approximation of the KC number, where $\delta_{ii,ini}$ is the initial deflection of the decay variable. For rotation the initial angle of deflection in radians ($\delta_{44-66,ini}$) is multiplied with the radius of rotation (k_{ii}). Again the column diameter is used as the characteristic length. To take into account the decay (reducing amplitude) of the motion the factor π is omitted, it is therefore expected that this equivalent KC number is representative for a larger section of the decay, instead of just the first oscillation.

The relation between KC number, cylinder surface roughness (Δ) and drag coefficient (C_D) is the following:

$$C_D = C_{DS}(\Delta) \cdot \psi(K_C) \tag{2.25}$$

Where C_{DS} is defined as a function of the surface roughness as

$$C_{DS}(\Delta) = \begin{cases} 0.65 & ; \Delta < 10^{-4}\ (smooth) \\ (29 + 4 \cdot \log_{10}(\Delta))/20) & ; 10^{-4} < \Delta < 10^{-2} \\ 1.05 & ; \Delta > 10^{-2}\ (rough) \end{cases} \tag{2.26}$$

For now the cylinder is always assumed to be smooth.

The wake amplification factor $\psi(K_C)$ is

$$\psi(K_C) = \begin{cases} C_\pi + 0.10(K_C - 12) & ; 2 < K_C < 12 \\ C_\pi - 1.00 & ; 0.75 < K_C < 2 \\ C_\pi - 1.00 - 2.00(K_C - 0.75) & ;\ K_C < 0.75 \end{cases} \tag{2.27}$$

Where

$$C_\pi = 1.50 - 0.024 \cdot \left(\frac{12}{C_{DS}} - 10\right) \tag{2.28}$$

Now the force on the discretized element should of course only be taken into account when the element is submerged. That is why the load is multiplied with a submergence factor, which is the fraction of the element that is submerged (fully submerged = 1; not submerged = 0). Based on the location of the element and the local water surface elevation, the fraction of the element that is submerged is determined.

Finally, the drag load acting on each element is added and transformed to loads in the floater's frame of reference, which can then be added to $\boldsymbol{\tau}_{exc}{}^{f}$ in the equation of motion (equation (2.5)). For the transformation to moments, the position of the element with respect to the FP's center of gravity ($\boldsymbol{x}_i{}^{f}$) has to be taken into account, as well as the transformation matrix ($\mathbb{T}_{fc_i}$) that follows from the orientation of the element 'c$_i$' w.r.t. the orientation of the platform 'f'.

$$\boldsymbol{\tau}_{nl\_drag,cyl}{}^{f} = \sum_{i=1}^{n} \left[\mathbb{T}_{fc_i} \cdot \boldsymbol{F}_{D,i,cyl} \; ; \; \boldsymbol{x}_i{}^{f} \times \left(\mathbb{T}_{fc_i} \cdot \boldsymbol{F}_{D,i,cyl} \right) \right] \tag{2.29}$$

Plate elements

An approach similar to that of the columns has been used for the keel plate elements. But one of the most important differences is that only the flow velocity perpendicular to the plate ($u_{x,i}$) is taken into account. This is in line with the local x-axes of the elements that have been shown in Figure 15.

The keel plate has been discretized into 10 sections. The 7 sections that result in a vertical force on the structure, are shown in Figure 17. Section 7 has no effect on the pitch and roll motions, while section 1-6 do. Sections 8-10 represent the stiffeners, the drag forces resulting from these stiffeners act in the horizontal plane. Note that the center points of all plate elements, and the directions in which their respective drag force acts are displayed in Figure 15. The horizontal distance from the center of the FP and the surface area of each section is listed in Table 4. Total surface area of the sections is 452 m^2.

Table 4, Amount, surface area and distance from center for non-linear drag plate elements

	#	dA [m^2]	Horizontal distance from center [m]
Keel plate – center (section 7)	1	109.8	0
Keel plate – between columns (sections 1-6)	6	49.56	8.36
Vertical stiffener	3	14.96	6.93

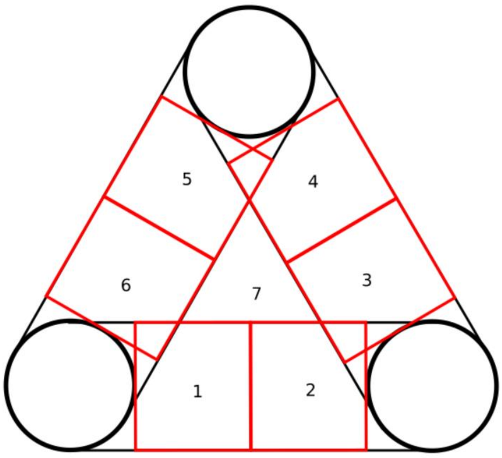

Figure 17, Non-linear drag elements of keel plate (without stiffener plates). Not to scale

An important difference from the cylindrical elements is the drag coefficient, which is assumed constant, and it is initially set to 1.9, in compliance with case 8 ('thin plate normal to flow') of table E-1 in (DNV, 2007). However, it should be noted that the plate is triangular instead of square, which leads to a higher ratio of edge-length over surface area. This could result in increased damping, because turbulence mostly forms at the edges of a plate. That is why the drag coefficient will be adjusted when experimental data is available.

Finally, instead of using the diameter (D) and length of element (dz), the projected area (dA) is used directly. This results in the following formulation for the force vector (which only has a non-zero value in the x-direction)

$$\boldsymbol{F}_{D,i,plate} = \left[\frac{1}{2} \cdot \rho \cdot C_{d,plate} \cdot dA \cdot u_{x,i}\left|u_{x,i}\right|; 0; 0\right] \tag{2.30}$$

Just as with the cylindrical elements the load needs to be transformed to the FP body frame; again the formulation is similar:

$$\boldsymbol{\tau}_{nl\_drag,plate}{}^{f} = \sum_{i=1}^{n}\left[\mathbb{T}_{fc_i} \cdot \boldsymbol{F}_{D,i,plate}\,;\, \boldsymbol{x}_i{}^{f} \times \left(\mathbb{T}_{fc_i} \cdot \boldsymbol{F}_{D,i,plate}\right)\right] \tag{2.31}$$

2.3.3 Mooring

In this numerical model the mooring loads are influencing the motions in the horizontal plane, as well as the yaw motion. The mooring configuration is designed by Mocean Offshore and is built up from six chains hanging in a catenary from the FP to the seabed; at each column two chains are connected. During the experiment at MARIN the mooring is mimicked by a soft-mooring configuration, at each column linear springs are connected that act only in the horizontal plane. The decision was made early in the project to use the same approach for the numerical model for three reasons:

1. The design of the mooring configuration was still in development, therefore large uncertainty about the mooring was still present for the numerical model.
2. The mooring configuration is site-specific, meaning that if the decision was made to switch to another location the mooring configuration would need to change as well.
3. More advanced mooring load calculations could not be validated by experiment at MARIN

The formulation for the mooring loads is therefore simply the following:

$$\boldsymbol{\tau}_{moor}{}^{n} = \begin{bmatrix} k_{mooring,11} \cdot \xi_1 \\ k_{mooring,22} \cdot \xi_2 \\ 0 \\ 0 \\ 0 \\ k_{mooring,66} \cdot \xi_6 \end{bmatrix}^{n} \tag{2.32}$$

The mooring stiffness coefficients ($k_{mooring,11}$-$k_{mooring,66}$) are set equal to those measured in the test basin at MARIN. In that way the added mass can be more accurately compared in the validation. The linear stiffness coefficients realized during the experiment also matched those derived from the first numerical analyses by Mocean. For surge and sway the stiffness was set to 20 kN/m, and for yaw the stiffness is 15700 kNm/rad.

Future development in mooring load

The calculation of mooring loads is an important part of the hydrodynamic model that can gain from additional attention in future developments. Two options should be considered:

The first option is creating a lookup table with mooring loads based on a static catenary. For a range of displacements from the equilibrium positions the resulting forces at the end of the mooring lines could be calculated. These forces, which also act in vertical direction could be summarized in a lookup table.

A more advanced option would be to discretize the mooring chains, and assign a mass, a drag coefficient and an added mass coefficient to each element, and calculating to local load on each element. This would add a significant amount of degrees of freedom to the model that would need to be solved, but it would give a more accurate result. Also because this approach would take into account the dynamics of the mooring chains. There are software packages available that use this method to incorporate mooring lines, so it would be worthwhile to investigate these packages before adjusting the Simulink® model.

2.4 Validation

In this section a comparison is made between the numerical model and the experiment. First an overview is given of the test setup in the basin. Then the decay tests are covered, and a comparison of RAO's is made. Finally an example of a motion time signal is investigated.

2.4.1 MARIN test setup

A two-week test campaign was performed at the concept basin of MARIN. In Figure 18 two photos of the scale model are shown. Most tests will be performed in a soft-mooring configuration. The connection points of the soft-mooring are at each of the cylinders at the waterline. At each of these connection points a tension-meter is installed. At the forward column a wave probe is connected, that can measure the wave run-up. Two cameras are installed at the basin, and by using the checkered patterns on the model, the submergence of the other columns can be determined as well. A single square in the checkered pattern corresponds to a 1x1 meter square in full-scale. The motions in 6 DOF are measured using an optical tracking system (KRYPTON) that comprises of visual sensors and three LED lights positioned in a triangle on the model. This results in a higher accuracy in comparison with integrating accelerometer measurements. One accelerometer is installed at the top of the forward column.

Figure 18, Photos of scale model as tested in the concept basin at MARIN

The tank layout in Figure 19 shows a top view of the basin with the model in its starting position with 0° heading. Waves are generated at the right (outside the figure), and therefore have a direction of 180°. At the platform (to the right of the model) the measurement data is collected. This is also where the cameras are located. What becomes clear from this tank layout is that the basin is quite narrow. It is expected that reflecting waves from the walls will influence the motions.

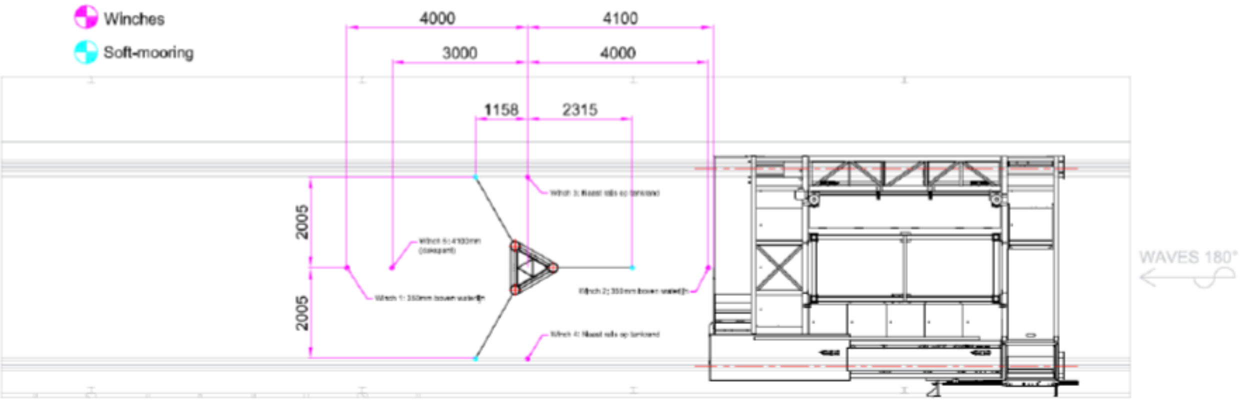

Figure 19, Tank layout top view with model at 0° heading and with waves coming from 180° w.r.t. body axes

To obtain a complete picture of the hydrodynamic behavior of the FP several different tests are performed, each with a different goal:

1. GM determination: by sliding weights the transversal and longitudinal metacentric height are verified. Results have been listed in Table 2;
2. Mooring stiffness determination: restoring force in mooring lines is measured for a range of deflections, the stiffness can be derived from the gradient;
3. Decay tests: for each degree of freedom the response to an initial deflection is measured. From this response the natural frequencies and damping ratios can be determined, which in turn can be used to determine the added mass and damping values at the natural frequency. More on this in section 2.4.2;
4. White noise tests: wave spectra with constant spectral density for the periods ranging from 6 s to 25 s are generated in the basin and then FP response is measured. The first wave spectrum has a significant wave height of 2 meter, and the second 4 meter. From the response of the FP, the motion RAO's can be determined;
5. JONSWAP sea state tests without tether force: Similar to previous tests (4.) but now with a JONSWAP spectrum instead of a white noise spectrum. The two operational conditions that are examined are at a significant wave height of 2 and 5 meter, and peak periods of 6 and 8 seconds. The survival condition is performed with a significant wave height of 10m and a peak period of 12.5 seconds. These tests are performed to obtain statistical properties of the FP response in conditions it is likely to encounter during its lifetime;
6. *JONSWAP sea state tests with tether force;*
7. *Towing tests.*

Tests 6 and 7 are not relevant to this analysis as they focus on the interaction between the RPA in crosswind flight and the FP, and the installation (tow-out) of the platform. Especially tests 3 and 4 are relevant for the validation of the numerical model.

Scaling

The model test is scaled using Froude scaling laws, as surface waves are gravity driven. The Froude number (Fr) is kept constant, this means that the ratio between inertia forces (F_i) and gravity forces (F_g) is kept constant as well (S. Steen, 2017).

$$Fr = \frac{U}{\sqrt{gL}} \tag{2.33}$$

$$\frac{F_i}{F_g} \propto \frac{\rho U^2 L^2}{\rho g L^3} = \frac{U^2}{gL} = Fr^2 \tag{2.34}$$

The conversion factors that have been used by MARIN to scale all variables is shown in the table in Figure 20.

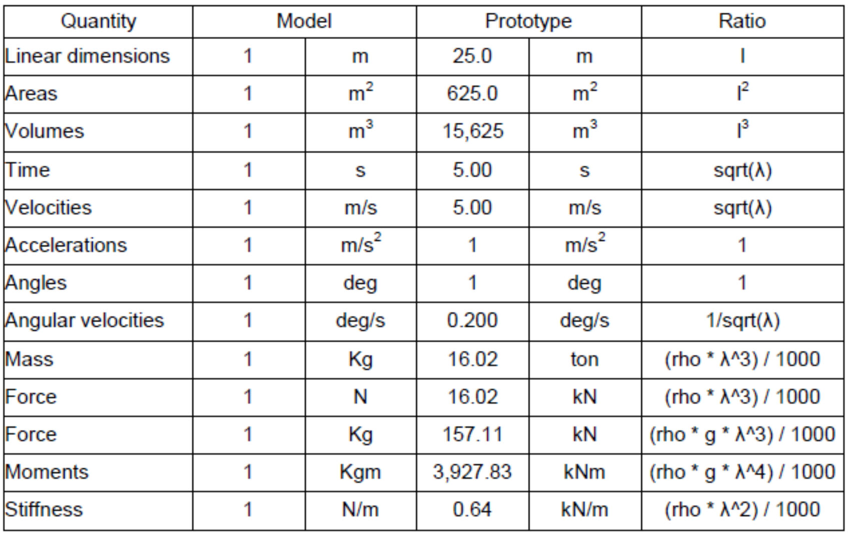

Quantity	Model		Prototype		Ratio
Linear dimensions	1	m	25.0	m	l
Areas	1	m^2	625.0	m^2	l^2
Volumes	1	m^3	15,625	m^3	l^3
Time	1	s	5.00	s	sqrt(λ)
Velocities	1	m/s	5.00	m/s	sqrt(λ)
Accelerations	1	m/s^2	1	m/s^2	1
Angles	1	deg	1	deg	1
Angular velocities	1	deg/s	0.200	deg/s	1/sqrt(λ)
Mass	1	Kg	16.02	ton	(rho * λ^3) / 1000
Force	1	N	16.02	kN	(rho * λ^3) / 1000
Force	1	Kg	157.11	kN	(rho * g * λ^3) / 1000
Moments	1	Kgm	3,927.83	kNm	(rho * g * λ^4) / 1000
Stiffness	1	N/m	0.64	kN/m	(rho * λ^2) / 1000

Figure 20, Conversion factors for Froude scaling as used by MARIN (Lindeboom, 2017)

What should be noted is that it is impossible to maintain the ratio between inertia forces and viscous forces in this test setup. However, for now it is assumed that the viscous forces are not significantly different between the model and the prototype. Tests at an intermediate or full scale should be performed to verify this assumption at a later stage of the development.

2.4.2 Decay tests

In Figure 21 the results of the decay tests from both experiment (E) and simulation (O, A1, A2, B) are plotted. Several approaches have used for the simulation and these will be covered soon, but first the experimental results are discussed.

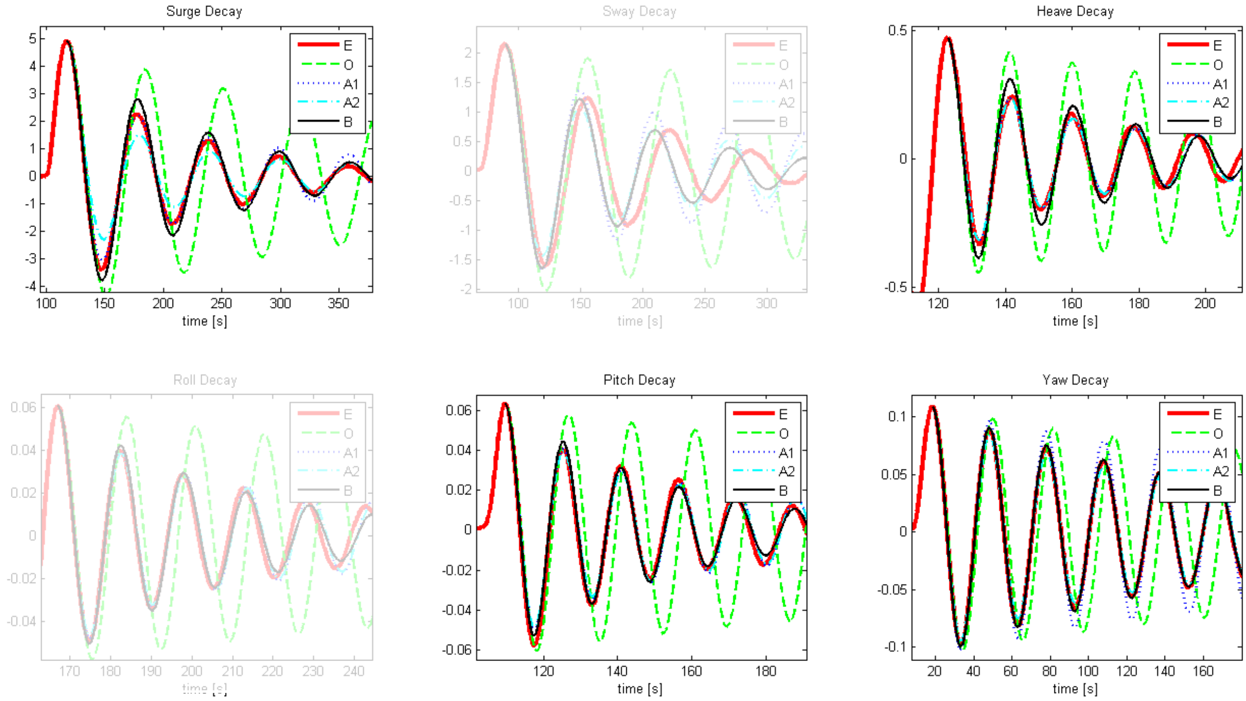

Figure 21, Decay tests results, E=results from experiment, O=original model, A1=tuned model using approach A1, A2=tuned model using approach A2, B=tuned model using approach B. Vertical axes for Surge, Sway and Heave motions indicate deflection in meter, and for Roll, Pitch and Yaw deflection in radians. In the appendix larger versions of these figures can be found.

The thick red line indicates the responses during the experiments. By measuring the deflections at the peaks (both positive and negative), the damping ratio can be determined. Peak 1 is the first positive peak, peak 2 is the first negative peak, peak 3 is the second positive peak etc. The formulation of kappa is given by equation (2.35).

$$\kappa_{ii} = \frac{1}{2\pi} \ln \left(\frac{\xi_{i;peak1} - \xi_{i;peak2}}{\xi_{i;peak3} - \xi_{i;peak4}} \right) \tag{2.35}$$

Instead of using peaks 1-4 it is also possible to use peaks 2-5 or 3-6. If there is a significant difference between these derived damping ratios (with the damping ratio decreasing in time), it can be assumed that the damping is not linear. This is in fact the case for the surge (11), heave (33) and pitch (55) decays measured at MARIN, see damping ratio values in Table 5.

The increase of damping ratio in sway (22) is expected to occur due to wall effects in the basin. There is also a significant difference between the natural periods in surge and sway, which is not expected due to the geometric symmetry of the FP. It is therefore assumed that the sway decays are not reliable. Although the differences between roll and pitch decays are not as pronounced as those between surge and sway, roll decays are also not considered, as they should correspond to the pitch decays.

Another cause of the discrepancy between symmetric (surge, pitch) and asymmetric (sway, roll) motions could be the disturbed flow from one aft column interacting with the other aft column due to inline motion. However, because the deflections during the decay tests are very small, the effect of reflecting waves from the basin walls is expected to have a bigger influence.

Table 5, Damping ratio values from decay experiments in soft-mooring at MARIN, based on different deflection peaks

Motion ii	κ_{ii} peaks 1-4	κ_{ii} peaks 2-5	κ_{ii} peaks 3-6
11	0.117	0.100	0.087
22	*0.088*	*0.090*	*0.094*
33	0.097	0.070	0.050
44	*0.064*	*0.055*	*0.052*
55	0.070	0.054	0.052
66	0.031	0.029	0.031

The natural period of the motions ($T_{z,i}$) is determined by measuring the durations of ten oscillations, and dividing this total duration by ten. The corresponding damped and undamped natural frequency is determined using equation (2.36) and (2.37).

$$\omega_{d,i} = \frac{2\pi}{T_{z,i}} \tag{2.36}$$

$$\omega_{0,i} = \frac{\omega_{d,i}}{\sqrt{1-\kappa_{ii}{}^2}} \tag{2.37}$$

From the undamped natural frequencies ($\omega_{0,i}$) and damping ratios (κ_{ii}) the added mass and damping coefficient at the natural frequencies can be determined using the restoring and inertia matrix, respectively $\boldsymbol{G}$ and $\boldsymbol{M}$ and equations (2.38) (2.39). The relevant values on the diagonals of these matrices have been determined from the FP characteristics listed in Table 2 and hydrostatic calculations.

$$A_{ii} = \frac{G_{ii}}{\omega_{0,i}{}^2} - M_{ii} \tag{2.38}$$

$$B_{ii} = \frac{2 \cdot \kappa_{ii} \cdot G_{ii}}{\omega_{0,i}} \tag{2.39}$$

The natural periods, average damping ratios and derived added mass and damping values are listed in Table 6. The two rightmost columns indicate the added mass and damping values that have been determined using Aqwa$^{\mathrm{TM}}$ at the same frequency. The percentages below the Aqwa$^{\mathrm{TM}}$ added mass and damping values is the ratio between the values derived from experiment and those from Aqwa$^{\mathrm{TM}}$. This shows that the added mass was indeed overestimated by the Aqwa$^{\mathrm{TM}}$ software, which was due to the increased keel plate thickness. That is why the difference is largest for pitch and roll. In heave the difference was deemed acceptable. What is also confirmed that Aqwa$^{\mathrm{TM}}$ is unable to capture the damping that is acting on the FP; less than 1% of the damping is found using potential theory.

Table 6, Decay test results with expected added mass and damping, and values determined with Aqwa$^{\mathrm{TM}}$

ii	T_{zii} Derived from experiment	κ_{ii} Derived from experiment	A_{ii} Derived from experiment	B_{ii} Derived from experiment	A_{ii} (Aqwa$^{\mathrm{TM}}$)	B_{ii} (Aqwa$^{\mathrm{TM}}$)
11	60.2	0.102	6.36E+05	3.87E+04	1.06E+06 (60%)	3.77E+01 (0.10%)
22	*65.8*	*0.090*	*9.97E+05*	*3.77E+04*	*1.06E+06* *(94%)*	*3.77E+01* *(0.10%)*
33	18.4	0.072	4.50E+06	2.80E+05	4.71E+06 (95%)	2.16E+02 (0.08%)
44	*15.3*	*0.057*	*3.89E+07*	*1.36E+07*	*1.07E+08* *(36%)*	*9.78E+02* *(0.01%)*
55	15.5	0.059	4.35E+07	1.44E+07	1.07E+08 (41%)	9.69E+02 (0.01%)
66	29.8	0.030	1.48+08	4.52E+06	1.93E+08 (77%)	4.00E-01 (0.00%)

Decay simulations

In Figure 21 the decays of the numerical model have been showed as well. There are four different numerical responses plotted:

1. O: Original numerical model as described in the previous sections. Added mass, and linear damping is determined with Aqwa$^{\mathrm{TM}}$, the drag coefficient for cylindrical elements is defined by the equivalent KC number (specifically for the decay tests), and the drag coefficient of the plates being set to 2.0 (so slightly higher than the value of 1.9 defined in (DNV, 2007));
2. A1: The discrepancy between the original numerical model and the experiment was obvious. The model has therefore been adjusted. Adjusted version A1, has reduced the added mass matrix by multiplying it with a factor 0.6 for surge and sway, 0.45 for roll and pitch and a factor 0.77 for yaw. The heave added mass has been kept

the same. Note that this action required an update of the state space representation of the frequency dependent added mass and damping. The drag coefficient for the plate has also been significantly increased (although the area was kept constant). The new drag coefficient for the plates is 21. The drag coefficient for the cylinder has been kept the same as in the original numerical model (so KC dependent);

3. A2: This adjusted version is similar to A1, with the exception of the drag coefficient of the cylinders. In this case the drag coefficient for the cylindrical elements has been set to a constant 1.2;
4. B: In the B version of the numerical model the drag coefficients for the non-linear drag elements has been set to 10^{-6} (so negligible). Instead, it was attempted to approximate the damping using linear damping matrix values based on the experimental decay. Now, because the damping values that have been determined by Aqwa^{TM} were a factor 1000 smaller than those derived by experiment, it was decided that instead of scaling the frequency dependent values by a certain factor, simply a constant value would be added. But this leads to an unfortunate side effect: damping no longer reduces to 0 at the high frequency limit. This was a problem when fitting a representative state space model, and the effect of the response at frequencies different from the natural frequencies could be significant.

When comparing the numerical decay responses to the experiment it is clear that changing the added mass results in a good correspondence of natural frequencies. The fact that the heave added mass is slightly higher (5%) does lead to a lower natural frequency in heave for the numerical model, but the difference is not significant and is therefore accepted.

Reducing the added mass in all motions except heave leads to the effect of non-linear drag being more pronounced. However, damping was still not sufficient. Therefore three approaches of increased damping have been investigated as mentioned above. Approach A1, which is closest to the original numerical model, leads to acceptable results, especially for heave and pitch. It should be noted that the drag coefficient of 21 is exceptionally high, and similar drag coefficients have not been found in literature. This could be caused by the ribs/stiffeners on the plate, but more advanced flow simulations/experiments should be performed to confirm this hypothesis. From the decay responses of approach A1 in yaw and beyond the 3rd oscillation in surge it can be concluded that the damping is not fully captured by the drag elements on the columns. That is why in approach A2 the drag coefficient for the columns is increased (to 1.2, which is a common value for cylinders). This has no significant effect on the pitch and heave decays. The effect is positive for the yaw decay; there is good agreement between the experimental yaw decay and approach A2.

However, the surge motion is now overdamped, especially in the first two oscillations, this also indicates that the decay in surge is perhaps more linear than can be achieved using the drag elements. That is why approach B was investigated.

In approach B only linear damping is taken into account. An advantage of this approach is that the damping of surge and yaw could be tuned separately of each other, while in approaches A1 and A2 they are connected, because of the drag elements at the columns. However, the results were as expected; in the first oscillations (with large amplitudes) the damping is underestimated, while at later oscillations the amplitude is smaller (so damping is overestimated). This is especially the case for surge, heave and pitch, and indicates that a significant portion of the damping is nonlinear. The fit to the yaw response is good, as was the case with approach A2, because damping is less pronounced in this degree of freedom.

In general, it can be concluded from the decays that the damping is built up from both a linear and a nonlinear part. This is especially the case for surge, where the experimental response falls between approach A2 and B. To prevent time-consuming tuning towards a numerical model that combines linear and non-linear damping, the decision is made to use approach A1 in further analyses. The reason for this is that it corresponds best to the decays in surge, heave and pitch, which are the only degrees of freedom that are considered in the aerodynamic model later on. The lack of damping in yaw is not considered to be a hindrance.

2.4.3 White noise wave spectra (RAO)

Using the experimental decays, the added mass and damping was adjusted to more accurately represent reality. In this section the response of the system to incoming waves is examined. In this case only waves coming from 180° are considered. In the appendix (B) the RAO's for a heading of 210° are shown as well.

Motion RAO determination from the white noise wave spectra was performed by MARIN. From the time signals of the FP motions in the white noise wave spectrum a response spectrum was derived. By adjusting for the difference of the applied waves from a true white noise spectrum the RAO's are found. This was done for two different significant wave heights of the white noise spectrum; 2 and 4 meters. The resulting motion RAO amplitudes for surge, heave and pitch are plotted in Figure 22.

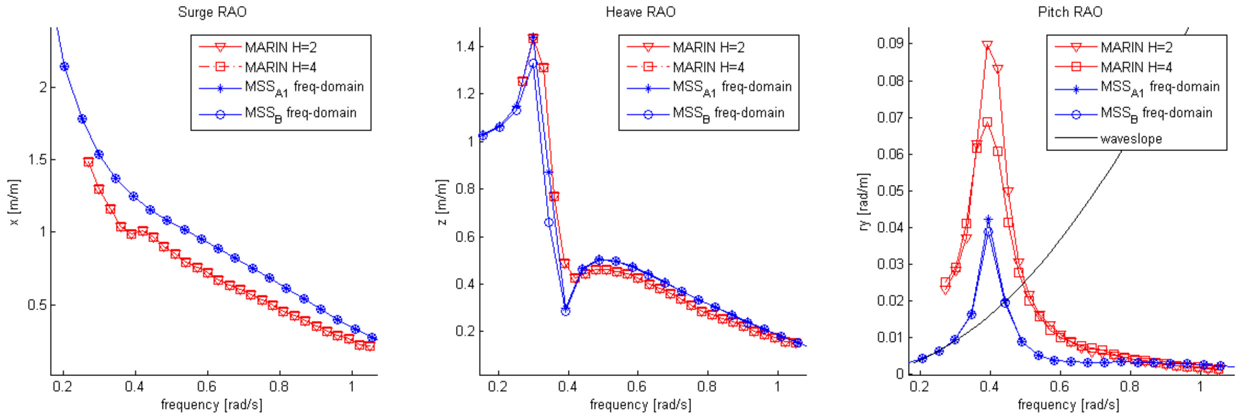

Figure 22, Experimentally (MARIN) and numerically (MSS) determined motion RAO amplitudes for surge, heave and pitch for wave direction=180°

In this figure also the numerically determined motion RAO amplitudes are plotted. These have been determined based on the force RAO's from Aqwa^{TM} in combination with the frequency dependent adjusted added mass, restoring, inertia and damping matrices. The motion RAO's that are determined with Aqwa^{TM} cannot be used as they use both the wrong added mass matrix, as well as the wrong restoring matrices (due to underestimated GM in hydrostatic calculation). First the complex force RAO's ($forceRAO_{ii,complex}(\omega)$) are determined using the frequency (and wave direction) dependent amplitudes ($a_{\tau_{ii,wave_{1st}}}$) and phases ($p_{\tau_{ii,wave_{1st}}}$) as per equation (2.40).

$$\begin{aligned} &forceRAO_{ii,complex}(\omega) \\ &\quad = a_{\tau_{ii,wave_{1st}}} \\ &\quad \cdot \left[\cos\left(p_{\tau_{ii,wave_{1st}}}\right) + i\sin\left(p_{\tau_{ii,wave_{1st}}}\right)\right] \end{aligned} \tag{2.40}$$

Then the complex motion RAO's ($motionRAO_{ii,complex}(\omega)$) can be determined using the restoring (C_{ii}), inertia (M_{ii}) and frequency dependent added mass ($A_{ii}(\omega)$) and damping matrix ($B_{ii}(\omega)$):

$$motionRAO_{ii,complex}(\omega) = \frac{forceRAO_{ii,complex}(\omega)}{C_{ii} - \omega^2 \cdot \left(M_{ii} + A_{ii}(\omega)\right) + i\omega B_{ii}(\omega)} \tag{2.41}$$

Finally, the motion RAO amplitude and phase can be determined from the complex motion RAO's using the '*abs()*' and '*angle()*' functions in Matlab®:

$$\begin{aligned} motionRAO_{ii,amplitude}(\omega) &= \frac{\xi_{ii,a}{}^{n}}{\zeta_a}(\omega) \\ &= \operatorname{abs}\left(motionRAO_{ii,complex}(\omega)\right) \\ motionRAO_{ii,phase}(\omega) &= \operatorname{angle}\left(motionRAO_{ii,complex}(\omega)\right) \end{aligned} \tag{2.42}$$

When using the A1 approach, the damping caused by the drag elements is not captured in this frequency domain method of determining the motion RAO's. That is why the damping matrix of approach B has also been used in one calculation, this has been plotted as MSS_B in the figure. It is assumed that by using approach B a similar motion RAO result is found as you would obtain from the nonlinear drag elements. To some extend this is true, but especially in surge, the nonlinear element are also an exciting force. At the moment only the exciting loads from diffraction and Froude-Krylov components is taken into account. This would explain the consistent difference in surge amplitude visible in the figure, as the drag acts with a phase difference from the Froude-Krylov and diffraction forces.

The heave RAO shows acceptable correspondence for most frequencies between the numerical model and the experiment. However, at a frequency of 0.4 rad/s the numerical response seems to be significantly lower than the experimental value. Although a dip is visible in the experimental response is visible as well, it is much stronger in the numerical data. This could be caused by the method of frequency analysis of the experiment, which could possibly average out abrupt changes in amplitude response.

The pitch RAO is especially interesting. First of all, there is a significant difference in peak response between the two different significant wave heights of the white noise spectra in the experiment. This indicates that nonlinear damping plays an important role in the pitch response. But more importantly, the difference between the experiment and numerical model is suspiciously large. That is why an additional line has been added to the plot. This line indicates the value of wave slope angle over wave amplitude as a function of wave frequency. At low frequencies the pitch response of the floating platform should approach this wave slope angle, as it starts behaving more as a buoy. In the following small section the determination of the low frequency limit of pitch motion is covered.

Pitch low frequency limits

The wave surface elevation of single sinusoidal wave in deep water with a direction of 180°, a phase angle of 0° and at $t=t_0$ can be simplified from equation (2.20) to the following equation:

$$\zeta(x) = \zeta_a \cdot \cos(kx - \omega t_0) \tag{2.43}$$

This expression can be differentiated to find the slope of the wave surface elevation:

$$\frac{d\zeta(x)}{dx} = -k\zeta_a \cdot \sin(kx - \omega t_0) \tag{2.44}$$

At low frequencies the tangent of the pitch angle of the platform should converge to the slope of the wave surface:

$$\max\left(\frac{d\zeta(x)}{dx}\right) = k\zeta_a \approx \tan\left({\xi_{55,a}}^n\right) \tag{2.45}$$

This leads to the following expression of the low frequency limit of the pitch response amplitude:

$$\lim_{\omega\to 0}\left(\frac{{\xi_{55,a}}^n}{\zeta_a}\right) = \frac{\text{atan}(k\zeta_a)}{\zeta_a} \tag{2.46}$$

The expression in equation (2.46) has been used to calculate the wave slope for all frequencies. This shows in Figure 22 that the MARIN data for pitch motion RAO's is higher than expected.

Additional inspection of the experimental data was performed at MARIN, and the discrepancy is expected to be caused by the soft mooring lines. As the difference is largest at the natural frequency, where the pitch and roll are mildly damped, the influence of soft mooring could be significant. The soft mooring was connected at the waterline, this is approximately 7 meters above the center of gravity. A surge or sway deflection therefore results in a pitch or roll moment exercised by the mooring lines. This is an effect that was not captured by the numerical model. This effect of soft mooring interference has been observed in previous tests at MARIN as well. For now it is assumed that the numerical model is fit for purpose.

2.4.4 Hydrodynamic model result

In Figure 23 an example of a motion response in a JONSWAP sea state with a significant wave height of 5.0 meter and a peak period of 10.0 seconds generated with the numerical model is shown. Note that for all simulations with a JONSWAP spectrum a peakedness factor (γ) of 3.3 is used. The numerically determined response is shown in comparison with the response during the MARIN experiment in a JONSWAP sea state with the same parameters (H_s is 5.0 meter and T_p is 10.0 seconds). The sea states are not exactly the same in both simulations, as in the simulation some spreading of the waves is included and of course due to random variations. However, the order of magnitudes of the responses should correspond. This is clearly the case in the figure, and this indicates that the numerical model is successful in producing stochastic time signals that can be used in the landing simulations. The pitch response is for the simulation naturally slightly smaller than that of the experiment, the reason for this difference has been explained in the previous section.

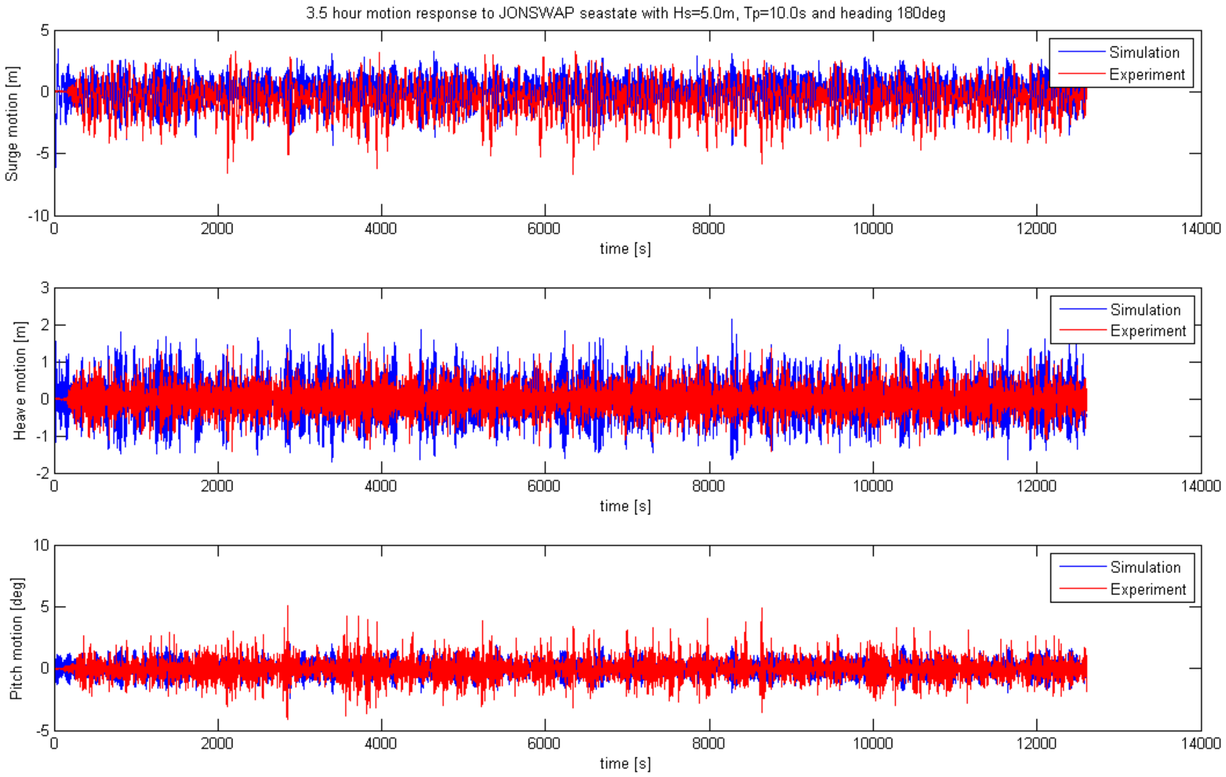

Figure 23, 3.5 hour motions response in JONSWAP sea state, qualitative comparison between experiment and numerical model

3 Aerodynamics

By the end of this chapter the first results of standard deviations from variations in initial conditions and from wind turbulence are covered (case 1 and case 2) in the verification section. These results will serve as a baseline for the analyses with floater motions included, that will be covered in the next chapter. The goal of this chapter is to explain the conventions, methods and assumptions that have been used to develop the numerical model that can be used in Monte-Carlo simulations on the landing approach. Effort will be made to go into detail on the equations of motions that define the system, as well as on the controllers that have been used in the Simulink® model.

Important to take into account is that this model is not a copy of the numerical model of AP3, that has been developed at Ampyx Power. The AP3 numerical model is designed to be as complete as possible, taking into account for example the highly elastic effects of the tether during snap loads. This is done in order to get the best performance out of the RPA and winch controllers before flying and obtain precise design loads for the structure. The increased accuracy is at the expense of calculation speed, which makes it less suitable for the purpose of this study. The numerical model used in this research has been simplified to the point where it still provides useful insights on the landing performance decrease due to floater motions, but also has a high calculation speed. The assumptions that have been made to arrive at such a model are covered in the next section.

3.1 Approach and assumptions

The approach that is taken in the development of a numerical, aerodynamic model is to make an ODE based model with PID controllers in Simulink® that will be used for time-domain analyses. The model represents a tethered aircraft (RPA) in symmetric, unsteady flight with three degrees of freedom: X, Z and RY. The numerical model has been developed such that the calculation time is minimized, which makes it suitable for Monte-Carlo simulation.

The model will be able to simulate the final approach of the RPA, starting at 200 meters from the landing platform. The simulation ends when the RPA is directly above the pulley. Between this point in time and the impact on deck it is expected that control over the RPA with the control surfaces is limited. That is why the spreading of relative height, orientation and velocities at this point will provide a good qualitative indication of the effect of platform motions on the landing performance. This allows for a relatively simple model, as the snapping of the tether during the arrest of the RPA (which is highly dependent on the elasticity of the tether, damping properties of the arresting system and winch control) is not required to be modelled.

In Figure 24 a general overview of the numerical model is shown using a block diagram. In the following sections the content of the blocks will be clarified. But first an elaboration on the most important assumptions in the aerodynamic model will be given. An overview of the Simulink® model is included in appendix (H).

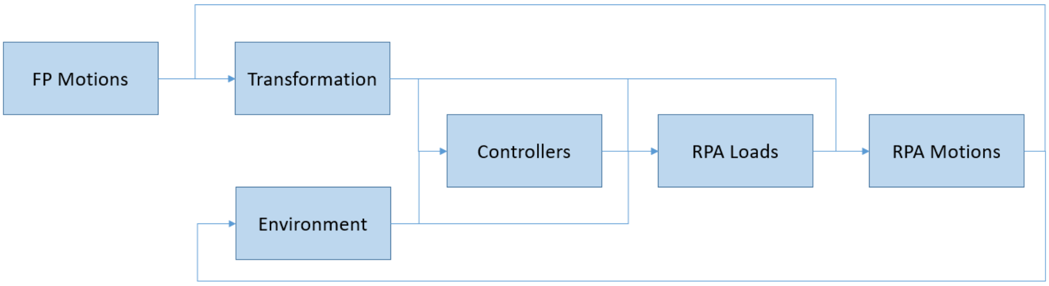

Figure 24, General overview of numerical aerodynamic model

Assumptions in aerodynamic model

In this section the assumptions that have been made to obtain a numerical, aerodynamic model that provides acceptable results are discussed.

Rigid body with point mass; meaning that no aero-elastic effects are taken into account. This assumption is similar to the rigid body assumption in the hydrodynamic model, and again it is not expected to have a large effect on the motions of the structure. An important reason is that the structural design of AP4 has not been defined, and any aero-elastic effect like flutter is highly dependent on the structural characteristics. The incorporation of aero-elasticity would also ask a lot of the computational resources, which is not desirable in this project.

Aerodynamic coefficients from AP3 CFD analyses; preferably validated data on the aerodynamic properties of the offshore RPA was used. Unfortunately is the development of the RPA at a limited level of maturity. Another option would be to use AP2 data, which has been validated during flight tests. However, it was decided in consultation with Ampyx Power that the coefficients obtained with CFD for AP3 would be more representative of a utility-scale RPA than the data from AP2. In this case only the aerodynamic data of AP3 in the landing configuration (flaps down) is considered. The data provides dimensionless coefficients for the aerodynamic forces in the body-axes (including pitching moment) as a function of angle of attack and elevator deflection.

Three degrees of freedom (3DOF); meaning that only symmetric flight is considered. This is one of the most important assumptions in the development of the simulation model, and there are three reasons for it:

- Vertical and longitudinal position and speed have the highest influence on the accelerations during landing. They have therefore the highest relevance to landing performance. For the RPA there will only be small variations in the lateral wind, as it always lands against the prevailing wind direction. Furthermore the numerical simulations of AP3 by Ampyx Power indicate good controllability of the asymmetric motions (Y, RX, and RZ) with respect to the allowed margin of error.
- Only taking into account the symmetric degrees of freedom lowers the complexity of the model significantly. This leads to a shorter development time, as the amount of used control surfaces reduces to just the elevator (flaps remain in landing configuration at all times). The amount of controllers (e.g. roll control, yaw damper, etc.) is also much smaller, and time spent developing and tuning the controllers is therefore greatly reduced.
- Finally, by just examining three degrees of freedom it is possible to develop a numerical model that has a faster calculation speed. This makes the model more suitable for Monte-Carlo simulations.

Simplified tether; yet winch inertia has been taken into account. This is one of the most challenging aspects of modelling any airborne wind energy device. Because the tether will not have significant slack it was decided to represent it with a rigid, straight line. This also means that the rotation of the winch is coupled to the position of the RPA and FP and is no longer an additional degree of freedom. This simplification will be covered in more detail in the section on the equation of motion (section 3.3).

The mass of the tether is taken into account in terms of the gravitational load on the RPA, but this mass does not have its own inertia.

Von Kármán wind turbulence; the choice of wind turbulence spectrum is important as it serves as a benchmark to which the uncertainty from platform motions can be compared. Optimally, wind measurements of sufficient resolution at the offshore site would have been used to determine turbulence parameters. The choice was made to use the Von Kármán wind turbulence spectrum, according to (DoD, 1997). The preference for this turbulence spectrum follows from the fact that it does not require the generation of an entire turbulence field (as was done by (Fechner & Schmehl, 2016)). On top of that provides the Aerospace Toolbox™ in Simulink® a built in block which can be dragged and dropped directly in the Simulink® workspace. Another option would be to use the Dryden turbulence spectrum for which the same advantages hold, but this turbulence spectrum matches the observed gusts not as well as the Von Kármán model (Hoblit, 1988). A comparison of the two models is performed later in this chapter in section 3.5. Furthermore, the Von Kármán turbulence model has also been used before by Ampyx Power in the landing analyses of AP3.

Wind shear effects; the boundary layer of the average wind profile is taken into account as per (DNV, 2007) section 2.3.2.6. The wind shear effects account for the increasing average wind velocity with altitude. This gradient has a significant influence on the airspeed during the approach, at altitudes below 100 meter. The average wind profile (or turbulence model) does not include flow disturbances from the FP.

3.2 Conventions

In Figure 25 the conventions are shown for the RPA in approach. All accelerations will be calculated in the inertial reference frame, which is defined in the figure by superscript 'n' (short for NED). Note that this inertial frame corresponds to the inertial frame used in the hydrodynamic model, only in this model just the X, Z and RY axes are used. The body fixed axes of the floater are indicated by superscript 'f', which corresponds to the axes defined by the MSS body-fixed frame, see Table 3. Please note that the pitch rotation (RY_{FP}) indicated in Figure 25 is negative, this follows from the fact that all reference frames are right-handed.

The aerodynamic loads on the RPA are defined in the body-fixed frame (superscript 'b'), this means that a transformation to the inertial reference frame is required before calculation of the accelerations. Fortunately, this transformation is fairly straightforward and is only dependent on the pitch angle of the RPA, see equation (3.7).

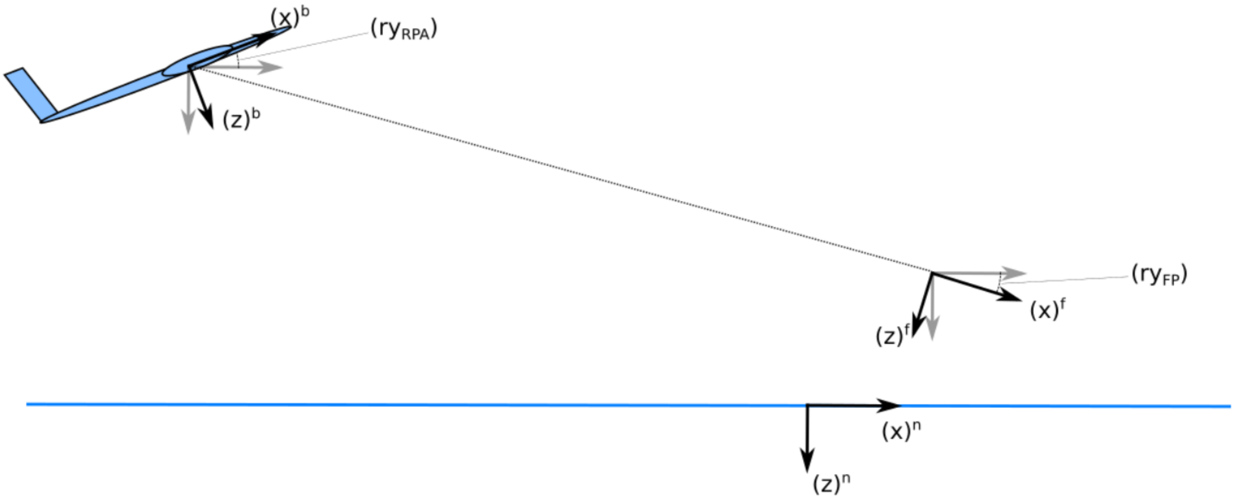

Figure 25, Conventions for RPA body reference frame (^{b}), inertial reference frame (^{n}) and FP reference frame (^{f}) as used in aerodynamic, numerical model

3.3 Equations of motion

The ODE that represents the aerodynamic system is shown in equation (3.1), this is basically an evolution of equation 1.3-1 in (Stevens & Lewis, 1992). Please note that the convention is slightly different from what was used in the hydrodynamic model. The loads ${\boldsymbol{\tau}_g}^n$, ${\boldsymbol{\tau}_a}^n$ and ${\boldsymbol{\tau}_t}^n$ represent respectively the gravitational, aerodynamic and tether loads acting on the RPA in the NED frame of reference (^{n}). This section will be devoted in a large extend to the determination of these loads at each point in time. The usage of the inertial frame of reference (NED frame) makes sense, as no Coriolis effects need to be taken into account.

$$\boldsymbol{I}_{RPA} \cdot {\boldsymbol{a}_{RPA}}^n = {\boldsymbol{\tau}_g}^n + {\boldsymbol{\tau}_a}^n + {\boldsymbol{\tau}_t}^n \tag{3.1}$$

Equations (3.2) and (3.3) show the relation (also in Laplace domain) between the velocities (${\boldsymbol{v}_{RPA}}^n$) and positions (${\boldsymbol{p}_{RPA}}^n$) with respect to the accelerations (${\boldsymbol{a}_{RPA}}^n$) determined in equation (3.1).

$${\boldsymbol{v}_{RPA}}^n = \int_0^t {\boldsymbol{a}_{RPA}}^n dt + {\boldsymbol{v}_{0,RPA}}^n = \frac{{\boldsymbol{a}_{RPA}}^n}{s} + {\boldsymbol{v}_{0,RPA}}^n \tag{3.2}$$

$${\boldsymbol{p}_{RPA}}^n = \int_0^t {\boldsymbol{v}_{RPA}}^n dt + {\boldsymbol{p}_{0,RPA}}^n = \frac{{\boldsymbol{v}_{RPA}}^n}{s} + {\boldsymbol{p}_{0,RPA}}^n \tag{3.3}$$

The acceleration, velocities and positions have been determined for just three degrees of freedom in only one frame of reference:

$${\boldsymbol{a}_{RPA}}^n = \begin{bmatrix} a_{x,RPA} \\ a_{z,RPA} \\ a_{ry,RPA} \end{bmatrix}^n ; \; {\boldsymbol{v}_{RPA}}^n = \begin{bmatrix} v_{x,RPA} \\ v_{z,RPA} \\ v_{ry,RPA} \end{bmatrix}^n ; \; {\boldsymbol{p}_{RPA}}^n = \begin{bmatrix} x_{RPA} \\ z_{RPA} \\ ry_{RPA} \end{bmatrix}^n \tag{3.4}$$

The inertia matrix for the RPA is defined as the following:

$$\boldsymbol{I}_{RPA} = \begin{bmatrix} m_{RPA} & 0 & 0 \\ 0 & m_{RPA} & 0 \\ 0 & 0 & J_{y,RPA} \end{bmatrix} \tag{3.5}$$

Where m_{RPA} is the mass of the RPA in kg, and $J_{y,RPA}$ is the inertia in pitch rotation of the RPA in kgm^2. Note that in this inertia matrix the inertia of the winch is not yet included, while in the beginning of this chapter this was promised. The reason is that the winch inertia is at this point still included in the tether load ($\boldsymbol{\tau}_t{}^n$). Later on in this chapter, equation (3.1) will be altered to indicate this inertia more clearly.

Gravitation loads

The first load acting on the structure is the gravity acting on of the mass of the RPA and tether ($\boldsymbol{\tau}_g{}^n$). Because of the usage of the inertial reference frame the gravity force simply acts in the positive z-direction, the force vector is shown in equation (3.6).

$$\boldsymbol{\tau}_g{}^n = \begin{bmatrix} 0 \\ g\left(m_{RPA} + \frac{1}{2} L_t m_t\right) \\ 0 \end{bmatrix}^n \tag{3.6}$$

In this equation g is the gravitational acceleration (in this case 9.81 ms^{-2}), m_{RPA} is the mass of the RPA as mentioned above and m_t is the mass of the tether per unit length, and L_t is the length of the tether, which is the distance between the platform and the RPA. The mass per meter of the tether is assumed to be 0.4 kg/m, based on a Dyneema tether with a diameter of 4cm.

Aerodynamic loads

The aerodynamic loads are first determined in the RPA body frame, and then transformed to the inertial reference frame using the pitch angle of the RPA at that moment in time (ry) and the following equation:

$$\boldsymbol{\tau}_a{}^n = \mathbb{T}_{nb} \cdot \boldsymbol{\tau}_a{}^b = \begin{bmatrix} \cos ry & \sin ry & 0 \\ -\sin ry & \cos ry & 0 \\ 0 & 0 & 1 \end{bmatrix} \cdot \boldsymbol{\tau}_a{}^b(\alpha, \delta_e, \bar{q}) \tag{3.7}$$

The aerodynamic loads in the body frame are a function of the variables angle of attack (α), elevator deflection (δ_e) and dynamic pressure ($\bar{q}$), as shown in the following equation:

$$\boldsymbol{\tau}_a{}^b(\alpha, \delta_e, \bar{q}) = \begin{bmatrix} \bar{q} \cdot S \cdot C_X(\alpha, \delta_e) \\ \bar{q} \cdot S \cdot C_Z(\alpha, \delta_e) \\ \bar{q} \cdot \bar{c} \cdot S \cdot C_M(\alpha, \delta_e) \end{bmatrix}^b \tag{3.8}$$

Here, S is the wing area, $\bar{c}$ is the mean chord length and C_X, C_Z and C_M are respectively the dimensionless aerodynamic coefficient for the body loads in x, z and pitching directions. These coefficients are determined using the angle of attack and elevator deflection angle in a lookup table. The data for the lookup table was determined for AP3 in landing configuration (flaps down) by CFD analysis, and can be found in the appendix (C) of this document. The C_L-α and C_D-α curves that correspond to these C_X and C_Z coefficients at an elevator deflection of 0° are shown in Figure 26.

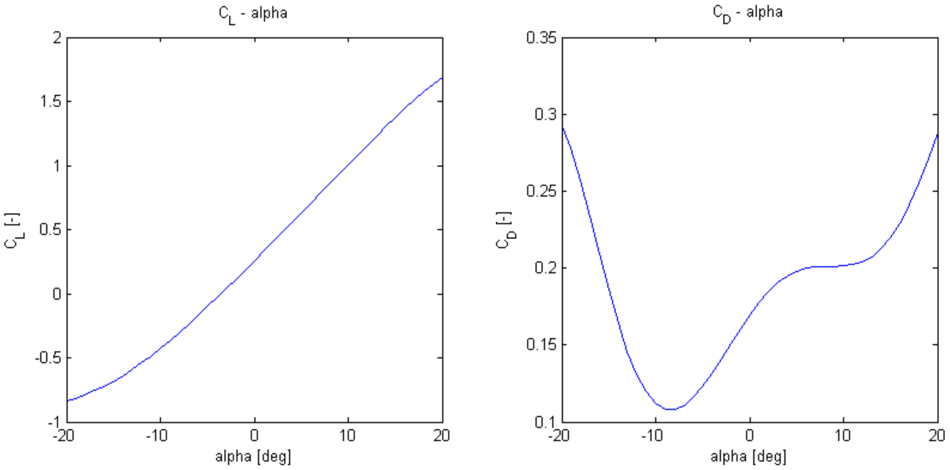

Figure 26, Lift and Drag coefficient as a function of angle of attack at an elevator deflection of 0° in landing configuration

The angle of attack is determined using the arctangent of the apparent vertical velocity and horizontal velocity in the body frame of the RPA, see equation (3.9). This apparent velocity ($\boldsymbol{v}_{app}{}^{b}$) is determined from the actual velocity of the RPA in the body frame ($\boldsymbol{v}_{RPA}{}^{b}$) and the wind velocity ($\boldsymbol{v}_{wind}{}^{b}$) in the same frame of reference. The norm of apparent velocity vector (without the rotational velocity) is the airspeed of the RPA (V_{air}) as shown in equation (3.10).

$$\alpha = \tan^{-1}\left(\frac{v_{z,app}{}^{b}}{v_{x,app}{}^{b}}\right) \tag{3.9}$$

$$V_{air} = \left\|\boldsymbol{v}_{app}{}^{b}\right\| = \left\|\boldsymbol{v}_{RPA}{}^{b} - \boldsymbol{v}_{wind}{}^{b}\right\| \tag{3.10}$$

$$\bar{q} = \frac{1}{2}\rho_a V_{air}{}^{2} \tag{3.11}$$

With the airspeed, the dynamic pressure is determined according to equation (3.11), assuming a constant air density ρ_a of 1.225 kgm^3.

The actual velocity of the RPA in the body frame ($\boldsymbol{v}_{RPA}{}^{b}$) can be derived from the velocity in the inertial frame ($\boldsymbol{v}_{RPA}{}^{n}$) in a similar way the aerodynamic load in the body frame is transferred to a load in the inertial frame: using a transformation matrix ($\mathbb{T}_{bn}$), as shown in equation (3.12). Of course this transformation matrix works in the opposite direction as $\mathbb{T}_{nb}$ in equation (3.7).

$$\boldsymbol{v}_{RPA}{}^{b} = \mathbb{T}_{bn} \cdot \boldsymbol{v}_{RPA}{}^{n} = \begin{bmatrix} \cos ry & -\sin ry & 0 \\ \sin ry & \cos ry & 0 \\ 0 & 0 & 1 \end{bmatrix} \cdot \boldsymbol{v}_{RPA}{}^{n} \tag{3.12}$$

The wind velocity vector is built-up from two components: the average wind velocity at altitude ($\boldsymbol{v}_{windshear}{}^{b}$) according to the DNV wind shear effect, and a randomized turbulence component ($\boldsymbol{v}_{turbulence}{}^{b}$) that has been determined using the Von Kármán wind turbulence spectrum. The latter is already defined in the body frame, but the wind shear component requires a transformation as per equation (3.13).

$$\boldsymbol{v}_{wind}{}^{b} = \mathbb{T}_{bn} \cdot \boldsymbol{v}_{windshear}{}^{n} + \boldsymbol{v}_{turbulence}{}^{b} \tag{3.13}$$

The wind shear component is a function of the altitude of the RPA ($-z_{RPA}{}^{n}$) and the wind velocity (U_{10}) at a certain reference altitude ($z_{0,ws}$), in this case at ten meters above mean sea level. The profile is exponential:

$$\boldsymbol{v}_{windshear}{}^{n} = f\left(z_{RPA}{}^{n}, U_{10}, z_{0,ws}\right) = U_{10} \frac{\ln\left(\frac{-z_{RPA}{}^{n}}{z_{0,ws}}\right)}{\ln\left(\frac{10}{z_{0,ws}}\right)} \tag{3.14}$$

The velocity components following from the Von Kármán wind turbulence model are a function of the altitude and orientation of the RPA ($[z_{RPA}, ry_{RPA}]^{n}$), its actual velocity ($\boldsymbol{v}_{RPA}{}^{b}$), the wind speed at 10 meters altitude and four noise seeds $[ug\ vg\ wg\ pg]$ that are changed in every simulation.

$$\boldsymbol{v}_{turbulence}{}^{b} = f(z_{RPA}{}^{n}, ry_{RPA}{}^{n}, \boldsymbol{v}_{RPA}{}^{b}, U_{10}, [ug\ vg\ wg\ pg]) \tag{3.15}$$

The function block of the Aerospace Toolbox™ is able to produce noise signals that represent the gust velocity in six degrees of freedom. They are derived from the power spectral densities (one for each linear direction) that characterize the von Kármán model. In this numerical model only the gusts in longitudinal direction are used, as at this altitude the vertical gusts are minimal. For more detailed information on the Von Kármán model please refer to (DoD, 1997).

Tether loads

The tether is made from Dyneema, this material has a Young's modulus (E) between 55 and 172 GPa (Matbase, n.d.). With a tether radius of 20mm, small elastic elongations result in very high tensile loads; even with the lowest Young's modulus, a 1cm elongation (δ) on an unreeled tether length (L_t) of 50m results in a change in tension (dT) of 13.8 kN (see equation (3.18)). If the winch would be modelled as a separate degree of freedom and the tether modelled as a nonlinear spring (no compression possible), the time steps of the simulation would need to be very small to get representative results. This would greatly impact the calculation speed.

$$dT = \frac{\delta}{L_t} \cdot EA = \frac{0.01}{50} \cdot [55 \cdot \pi 20^2] = 13.8\,kN \tag{3.16}$$

During the approach it is assumed that the tether sag is minimal, the winch controller will be designed such that this is the case. With this in mind it makes sense to set the unreeled tether length (L_t) equal to the relative distance between the RPA and the FP, see equation (3.17). From this follows that winch rotation does not have to be considered as a different state variable, but it becomes instead a function of the positions of RPA and FP.

$$\|\boldsymbol{p}_{rel}{}^{n}\| = \sqrt{x_{rel}{}^{2} + z_{rel}{}^{2}} = L_t \tag{3.17}$$

The relative position vector ($\boldsymbol{p}_{rel}{}^{n}$) is defined without the relative pitch angle. This angle is not relevant for the control systems loads, it is only relevant at the end of the simulation as limiting factor for landing.

$$\boldsymbol{p}_{rel}{}^{n} = \begin{bmatrix} x_{RPA} - x_{FP} \\ z_{RPA} - z_{FP} \\ 0 \end{bmatrix}^{n} = \begin{bmatrix} x_{rel} \\ z_{rel} \\ 0 \end{bmatrix}^{n} \tag{3.18}$$

The tension in the tether (T) is assumed constant over its length (as the weight of tether was taken into account in the gravity load), and because of the straight line assumption, the tether load vector becomes:

$$\boldsymbol{\tau}_t{}^{n} = T \cdot \frac{\boldsymbol{p}_{rel}{}^{n}}{L_t} \tag{3.19}$$

The tension in the tether follows from the applied torque at the winch (M_{com}), which is a control variable, the drum radius and inertia of the winch (R_d and J_d), and the angular acceleration of the drum ($\dot{\omega}$). This angular acceleration can now be rewritten in terms of relative accelerations and positions, as shown in equations (3.20) and (3.21).

$$\begin{aligned} M_{com} = J_d\dot{\omega} + T \cdot R_d \;\rightarrow\; T &= \frac{M_{com}}{R_d} - \frac{J_d}{R_d{}^{2}}\ddot{L}_t \\ &= \frac{M_{com}}{R_d} - \frac{J_d}{R_d{}^{2}}\|\ddot{\boldsymbol{p}}_{rel}{}^{n}\| \end{aligned} \tag{3.20}$$

$$\|\ddot{\boldsymbol{p}}_{rel}{}^{n}\| = (\boldsymbol{a}_{RPA} - \boldsymbol{a}_{FP})^{nT} \cdot \frac{\boldsymbol{p}_{rel}{}^{n}}{L_t} \tag{3.21}$$

When combining the above two equations with equation (3.19) the following expression is found:

$$\boldsymbol{\tau}_t{}^n = \frac{\boldsymbol{p}_{rel}{}^n}{L_t} \cdot \left(\frac{M_{com}}{R_d} - \frac{J_d}{R_d{}^2} \cdot \left(\frac{\boldsymbol{a}_{RPA}{}^{nT} \boldsymbol{p}_{rel}{}^n}{L_t} - \frac{\boldsymbol{a}_{FP}{}^{nT} \boldsymbol{p}_{rel}{}^n}{L_t} \right) \right) \tag{3.22}$$

Note that the accelerations, velocities and positions of the FP in the inertial reference frame correspond to the conventions used in the previous chapter in the following way (1, 3 and 5 indicate surge, heave and pitch motion):

$$\begin{aligned} \boldsymbol{a}_{FP}{}^n &= \mathbb{T}_{nf} \cdot \ddot{\boldsymbol{\xi}}^f(1,3,5) \\ \boldsymbol{v}_{FP}{}^n &= \mathbb{T}_{nf} \cdot \dot{\boldsymbol{\xi}}^f(1,3,5) \\ \boldsymbol{p}_{FP}{}^n &= \boldsymbol{\xi}^n(1,3,5) \end{aligned} \tag{3.23}$$

Now solving equation (3.1) becomes a bit more tedious, as $\boldsymbol{a}_{RPA}{}^n$ is present on both sides of the equation which would result in an algebraic loop when trying to solve this using ODE's. Therefore equation (3.1) is rewritten such that $\boldsymbol{a}_{RPA}{}^n$ is only present on the left side of the equation, this leads to an additional inertia contribution, which can be concentrated in the term $\boldsymbol{I}_{winch}$. The full derivation of this term is and the new equation of motion is given in equation (3.24) to (3.27).

$$(\boldsymbol{I}_{RPA} + \boldsymbol{I}_{winch}) \cdot \boldsymbol{a}_{RPA}{}^n = \boldsymbol{\tau}_g{}^n + \boldsymbol{\tau}_a{}^n + \boldsymbol{\tau}'_t{}^n \tag{3.24}$$

$$\begin{aligned} \boldsymbol{\tau}'_t{}^n &= \boldsymbol{\tau}_t{}^n + \boldsymbol{I}_{winch} \cdot \boldsymbol{a}_{RPA}{}^n \\ \boldsymbol{\tau}'_t{}^n &= \frac{\boldsymbol{p}_{rel}{}^n}{L_t} \cdot \left(\frac{M_{com}}{R_d} + \frac{J_d}{R_d{}^2} \cdot \left(\frac{\boldsymbol{a}_{FP}{}^{nT} \boldsymbol{p}_{rel}{}^n}{L_t} \right) \right) \end{aligned} \tag{3.25}$$

$$\boldsymbol{I}_{winch} \cdot \boldsymbol{a}_{RPA}{}^n = \frac{J_d}{R_d{}^2} \cdot \frac{\boldsymbol{p}_{rel}{}^n}{L_t} \cdot \frac{\boldsymbol{a}_{RPA}{}^{nT} \boldsymbol{p}_{rel}{}^n}{L_t} \tag{3.26}$$

$$\boldsymbol{I}_{winch} = \frac{J_d}{R_d{}^2 L_t{}^2} \cdot \begin{bmatrix} (x_{rel}{}^n)^2 & x_{rel}{}^n \cdot z_{rel}{}^n & 0 \\ x_{rel}{}^n \cdot z_{rel}{}^n & (z_{rel}{}^n)^2 & 0 \\ 0 & 0 & 0 \end{bmatrix} \tag{3.27}$$

The effect of the winch inertia in comparison to the inertia of the RPA over time is shown in Figure 27, on the left in X-direction and on the right in Z-direction. These inertia loads are determined by multiplying the accelerations with the inertia matrices. From these figures it can be concluded that the winch inertia is indeed significant, in the initial stage the winch inertia in X-direction is approximately equal to 10% of the inertia of the RPA. Closer to the flyover (final two seconds of simulation), the effect becomes significant in the Z-direction (refer to Figure 28 for a plot without adjusted axes). This indicates that it also has an effect on the relative height of the RPA at flyover, it is therefore important to take this winch inertia into account.

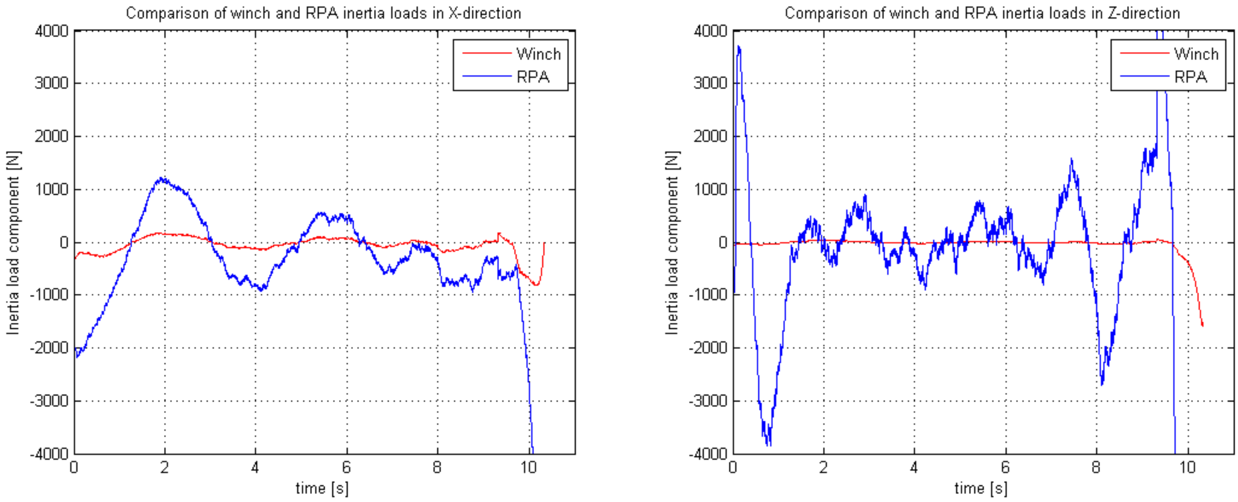

Figure 27, Comparison of winch inertia in relation to RPA inertia (adjusted axes)

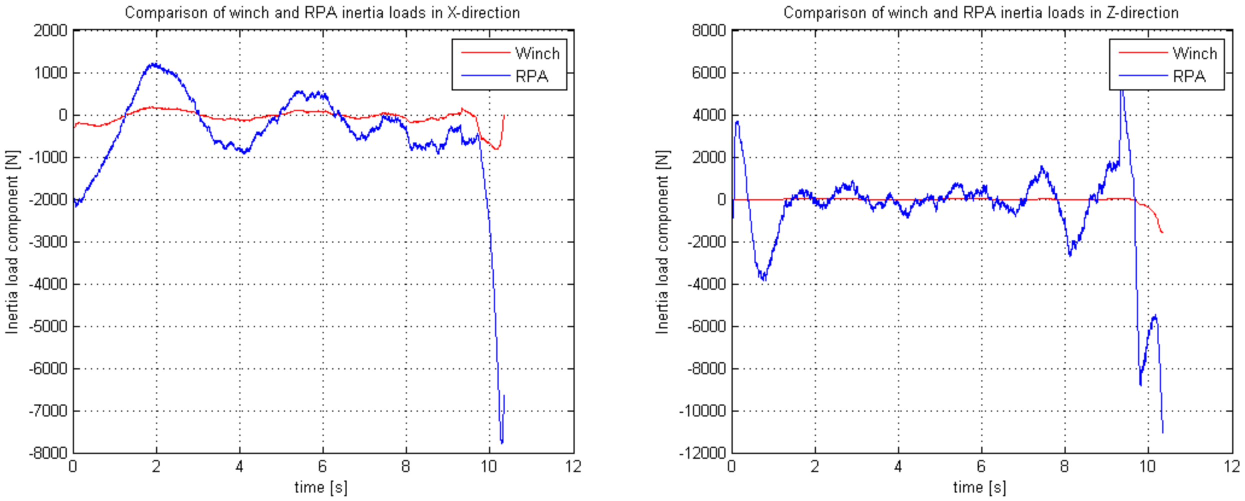

Figure 28, Comparison of winch inertia in relation to RPA inertia

3.4 Controller design

The RPA is controlled in all three degrees of freedom by three different controllers; the pitch controller, the glide path controller and the speed controller. They will be covered in just two sections as the pitch controller is defined to be part of the glide path controller. All controllers are proportional-integral-derivative controllers (PID or three term controller), which is a common control loop feedback mechanism.

3.4.1 Glide path (elevator)

The glide path controller is built up from two parts: a pitch controller and a glide slope coupler. The glide slope coupler calculates a required pitch angle based on the vertical deviation from the required glide slope. The pitch controller calculates the required elevator deflection to reach that pitch angle. The pitch controller can also work individually (without glideslope coupler), to maintain a constant pitch angle.

Pitch controller

The pitch angle controller is a fairly straightforward PID controller with airspeed dependency, meaning that the gains are scheduled based on airspeed. The equations for the pitch PID controller in the Laplace domain are as follows:

$$\varepsilon = ry_{meas} - ry_{com} \tag{3.28}$$

$$\delta_{e,com} = \left(P(V_{air}) + I \cdot \frac{1}{s} + D(V_{air}) \cdot \frac{N}{1 + N\frac{1}{s}} \right) \varepsilon \tag{3.29}$$

The error (ε) is the difference between the measured pitch angle (ry_{meas}) and the pitch angle command (ry_{com}). Equation (3.29) is the formulation of the PID controller, where $P(V_{air})$, I and $D(V_{air})$ are respectively the proportional, integral and differential gain. N is the filter coefficient, which is set to 100.

The gains of the proportional and differential gains are tuned for multiple airspeeds, as the response at lower airspeeds is different from higher airspeeds, where the response is quicker. These tuned gains are saved in a lookup-table, and the result is a scheduled gain with the airspeed as the scheduling variable. In Figure 29 the gains are shown as a function of the airspeed.

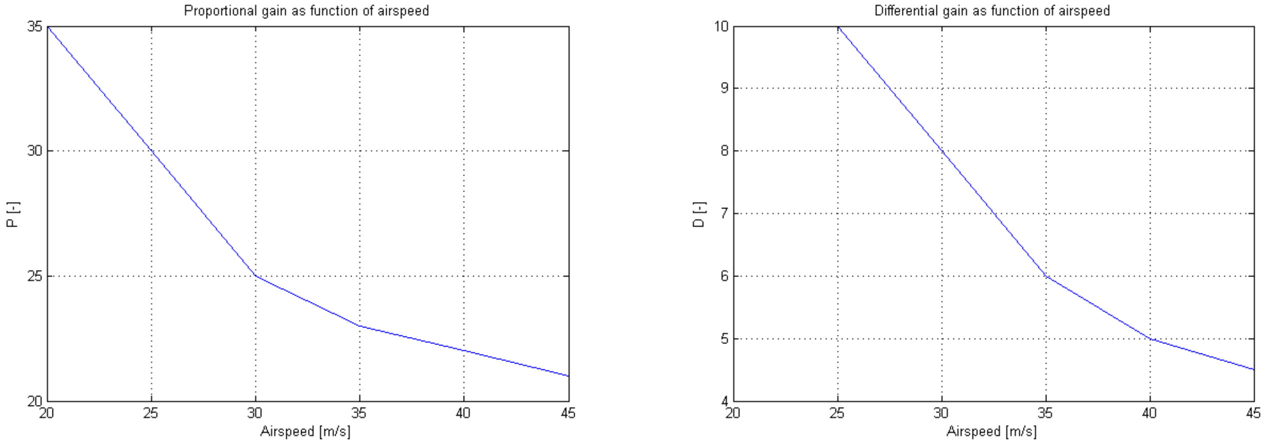

Figure 29, Proportional and differential gains as a function of airspeed (scheduled gains)

The resulting PID controller in Simulink® is shown in Figure 30.

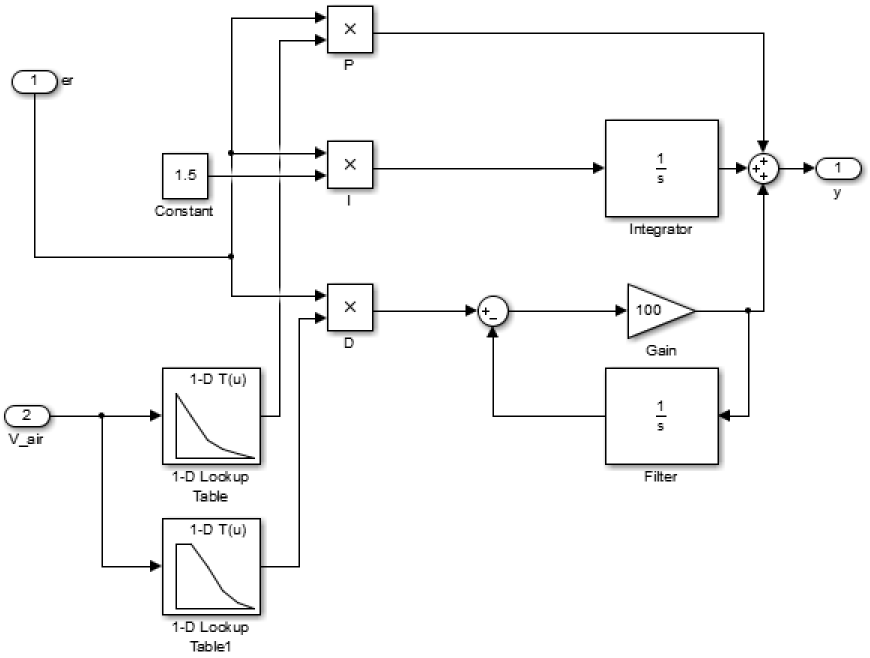

Figure 30, Pitch PID controller as implemented in Simulink®

The actual elevator deflection (δ_e) is not equal to the output of the PID controller ($\delta_{e,com}$), as the elevator servo has a breaking frequency which is set to 10 Hz (or 10π rad/s). This is taken into account with the transfer function shown in equation (3.30). Furthermore, the elevator deflection is limited to maximum values of +20° and -20° using a saturation block.

$$\delta_e = \frac{31.4}{s + 31.4}\delta_{e,com} \tag{3.30}$$

In Figure 31 the pitch response is shown for a step input at approximately 25 m/s airspeed (0 m/s wind speed) on the left and 35 m/s airspeed (20 m/s wind speed) on the right. In the plots the red lines indicate the response, and the blue lines the commanded value. The subplots underneath show the control variable (elevator deflection) over time. Both responses converge quickly to the command value, albeit faster at the high airspeed. On top of that is the overshoot limited, which is also positive. The constant offset from the commanded value, especially at the lower airspeed indicates that the integral gain is too small. However, increasing this integral gain would increase the overshoot significantly. Besides, this error will be accounted for with the glide slope coupler; as this offset is more or less constant, the glide slope coupler will adjust automatically to output to slightly higher commanded pitch angle in order to achieve the correct glide slope (altitude).

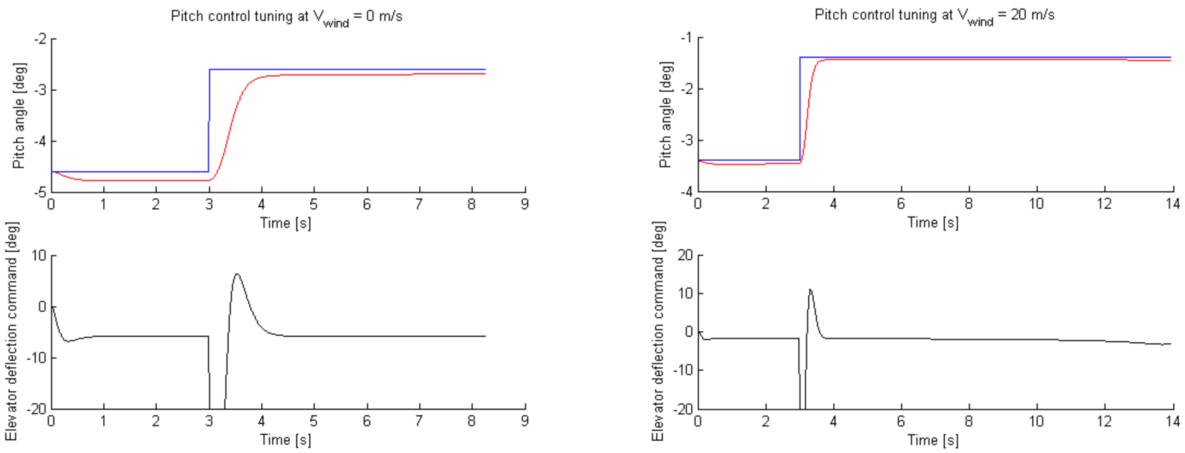

Figure 31, Pitch controller response to step in command value at 0 m/s and 20 m/s wind speed

Glide slope coupler

As mentioned above, ry_{com} is the output of the glide slope coupler, and it is determined based on the vertical deviation (d) from the glide path. The glide slope coupler has two different phases.

The first phase, when the tether length (L_t) is longer than a reference value L_{fin}, is the glide slope control phase. When the tether length is shorter than L_{fin} the controller switches to a pitch control phase; this last section of the flight makes sure that the relative pitch angle with respect to the landing platform is acceptable.

The reference value L_{fin} is determined when the unreeled tether length is equal to 50 meters. At this point the expected distance that is required to adjust the pitch angle sufficiently is calculated; this is the reference value L_{fin}. This distance is dependent on the reel-in speed ($\dot{L_t}$, note that this is a negative value), the airspeed (V_{air}) and the expected relative pitch angle (dry_{fin}) above the pulley without adjustments. The assumptions here are that over the last 50 meters of the approach the speed of the RPA in the inertial frame and the pitch rate of the FP is constant. As the frequency of the FP motion is relatively low it is assumed that this assumption is acceptable.

$$L_{fin} = -dt_{fin} \cdot \dot{L_t}$$
$$dt_{fin} = f_{lookup}(dry_{fin}, V_{air})$$
$$dry_{fin} = v_{ry,FP} \cdot \frac{L_t}{\dot{L_t}} - ry_{rel} \tag{3.31}$$
$$\dot{L_t} = \frac{\boldsymbol{v}_{rel}{}^{nT} \boldsymbol{p}_{rel}{}^{n}}{L_t}$$

The lookup table, which is used to determine the required time to adjust the pitch angle (dt_{fin}), is determined by running simulations with a range of relative pitch angles and airspeeds. The determined length varies from approximately 30 meters (at high reel-in and low airspeed) to just 5 meters (at high wind speeds and small relative angles).

Before the tether length is smaller than L_{fin}, the glide control phase is active. The vertical deviation from the glide slope (d) is determined as follows:

$$d = {z_{rel}}^n - h_{land} - \tan(gs) \cdot {x_{rel}}^n \tag{3.32}$$

Where h_{land} is the optimum height of the RPA above the FP when flying over the pulley (end of simulation), in all simulations this value is set to 2.5 meters. The value gs is the required glide slope angle, and this value is determined from the initial relative altitude. Please note that the Gaussian variations to the initial conditions in the Monte-Carlo analyses are added after the determination of the glide slope angle. They therefore do not change the required glide slope and are in fact initial deviations from the glide slope.

The determination of the vertical deviation (d) is dependent on signals of both the RPA and the FP/winch, therefore a transport delay of 50 milliseconds is imposed on the signal to account for the transfer of data.

The PID controller for the glide slope coupler is not dependent on airspeed, but the tuning of this controller was nevertheless a challenge. Take for example a vertical deviation upwards from the glide slope. To correct for this deviation the RPA would need to pitch its nose down. However, in order to pitch down, first the lift on the tail surface needs to be increased using the elevator deflection. Before the lift of the main wing drops due to a decrease in angle of attack, the additional lift on the tail surface causes the RPA to deviate further from the glide slope. This also holds for a pitch up maneuver to adjust for a downward deviation from the glideslope. This means that the integral gain should not be too high, as this will result in a large overshoot. It is also not possible to compensate for this with the differential gain, as a high differential gain would result in nervous behavior in turbulent wind conditions. This makes it difficult to obtain a stable controller, and it is amplified at large deviations from the glide slope.

The way this was solved was by, instead of taking the deviation value (d) as the variable that needs to be minimized by the PID controller, using the arctangent of the deviation ($\mathrm{atan}(d)$), see Figure 32 for a comparison of the two. This makes sure that the amplifying effect at large deviations was minimized.

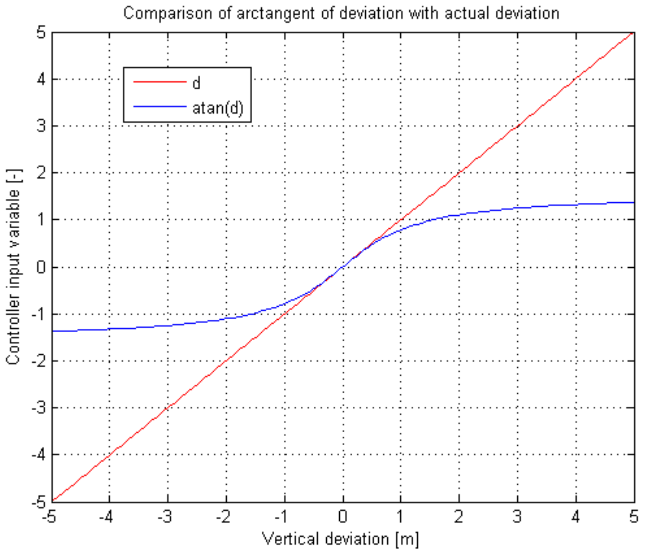

Figure 32, Comparison of vertical deviation and arctangent of the vertical deviation as glide slope coupler controller input

The resulting PID controller that determines the pitch angle command (ry_{com}) is shown in equation (3.33).

$$ry_{com} = \left(P + I \cdot \frac{1}{s} + D \cdot \frac{N}{1 + N\frac{1}{s}} \right) \operatorname{atan}(d) \tag{3.33}$$

The response of the system to a step input is visualized in Figure 33 for 0 and 20 m/s wind speed and for a positive deviation. The red line indicates the actual deviation from the glide slope and the magenta line indicates the arctangent of this value. At 3 seconds the required glide slope is moved down 1m, therefore the deviation increases by a 1m at this point. Clearly visible is first the increase in deviation and then the convergence to 0.

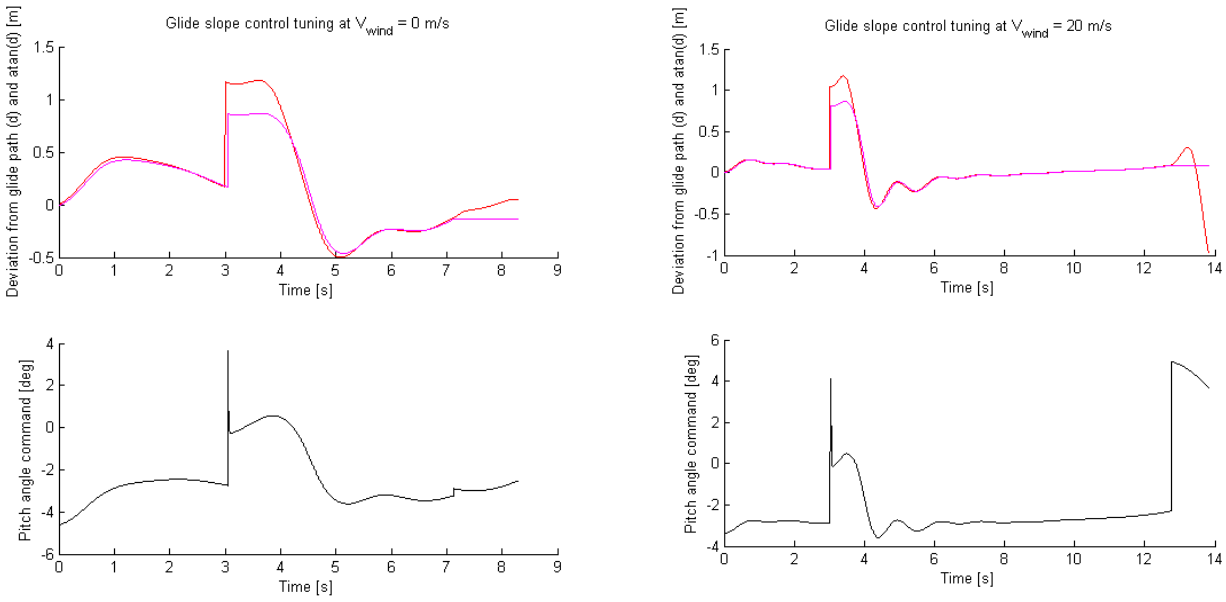

Figure 33, Glide slope controller response to step in command value at 0 m/s and 20 m/s wind speed

Naturally the response is not as fast as with the pitch controller. However the responses converges well to the required values with little overshoot.

When the tether length reduces to less than the specified value of L_{fin} the pitch angle command switches to the pitch angle FP plus a margin of 1°. The RPA will therefore land with is nose slightly up with respect to the FP orientation:

$$ry_{com} = ry_{FP} + \text{deg2rad}(1)$$

This command is also clearly visible in Figure 33, especially at high wind speeds as the relative angle between the RPA and the FP is relatively large.

3.4.2 Speed (winch)

The winch is used to control the relative speed of the RPA with respect to the FP in the inertial frame. The required value (V_{com}) is dependent on the average wind speed (at 10 meter altitude, U_{10}) according to the following relation:

$$V_{com}\ [m/s] = \begin{cases} 25 - U_{10}, & U_{10} < 10 \\ 15, & U_{10} \geq 10 \end{cases} \tag{3.34}$$

Speed controller input (ε) is the error between required reel-in speed ($\dot{L}_{t,com}$), which is based on V_{com} and the actual reel-in speed ($\dot{L_t}$):

$$\varepsilon' = \dot{L}_{t,com} - \dot{L_t} \ = \cos(\alpha_t - gs) \cdot V_{com} - \frac{{\boldsymbol{v}_{rel}}^{nT} {\boldsymbol{p}_{rel}}^{n}}{L_t} \tag{3.35}$$

At the start of the simulation the difference between the reel-in speed and the relative speed in the inertial frame is negligible, as at this point the angle of the tether (α_t) is about the same as the glide slope angle (gs). However, when the RPA comes close to the FP, these two angles start to diverge, and when the RPA is directly above the FP the reel-in speed should approach zero.

Controller output of the controller is the applied torque on the winch (M_{com}), which is used in the determination of $\boldsymbol{\tau}'^{\,n}_{t}$ in equation (3.25). This torque follows from a simple PID controller:

$$M_{com} = \left(P + I \cdot \frac{1}{s} + D \cdot \frac{N}{1 + N\frac{1}{s}} \right) \varepsilon \tag{3.36}$$

At the start of the simulation the torque applied on the winch should keep the system in equilibrium, therefore a value for the integrator at the start of the simulation is derived from the initial velocities, orientation and wind speed.

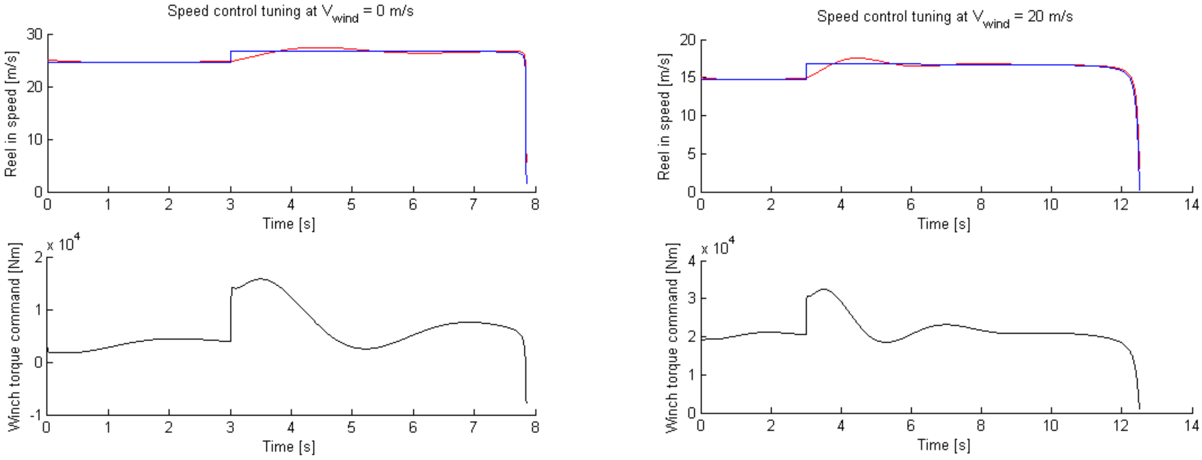

Figure 34, Speed controller response to step in command value at 0 m/s and 20 m/s wind speed

In Figure 34 the response of the system to a step input in commanded reel-in speed is shown. However, due to the large decrease in commanded reel-in speed at the end of the simulation, the response is not very clear. That is why the same plots, but with adjusted axes have been included in Figure 35.

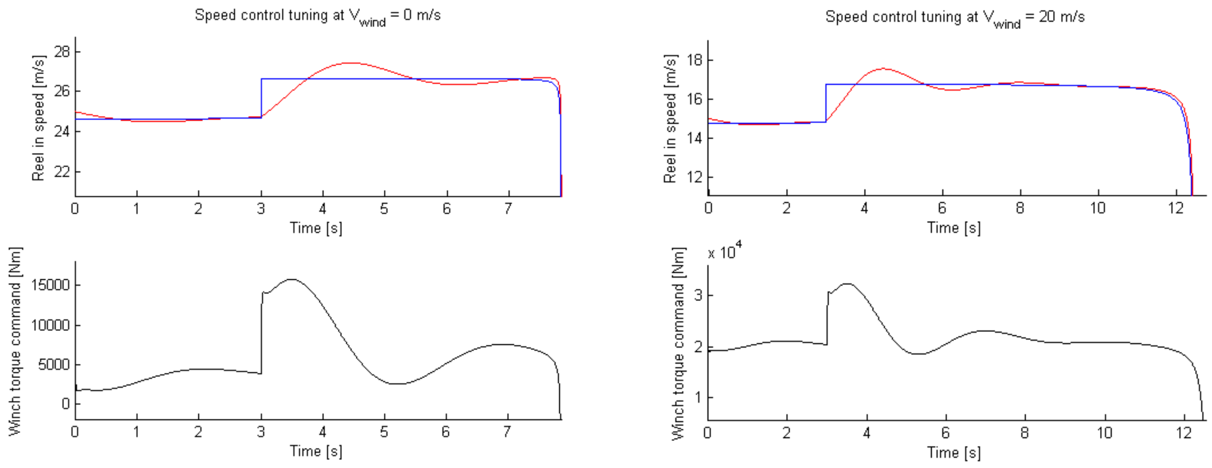

Figure 35, Speed controller response to step in command value at 0 m/s and 20 m/s wind speed (adjusted axes)

Due to the high inertia of the system there is a bit of overshoot and oscillation, but the system converges well to the set value. The torques applied on the winch are also in an acceptable range, they are significantly smaller than the torque on the winch during power production (300kN of tether tension for wind speeds (U_{10}) higher than 8 m/s).

Interesting to note from Figure 34 is that at low wind speeds (especially at 0 m/s) at the end of the simulation the control variable (winch torque command) becomes negative. The winch is thus actively decelerated. At higher wind speeds the wind resistance and lift acting on the RPA is so high that, the winch is decelerated by these forces sufficiently and there is no need for a negative applied torque on the winch.

3.5 Verification

In the final section of this chapter the choice of initial altitude and turbulence model is reviewed. Furthermore, the usage of standard deviations as an indication of landing uncertainty is examined.

3.5.1 Path of RPA during simulation

To give an impression of what a simulated approach looks like, an example is shown in Figure 36 and Figure 37. The approach is at an average wind speed of 15 m/s and a random Von Kármán wind turbulence signal is included. No FP motions are considered.

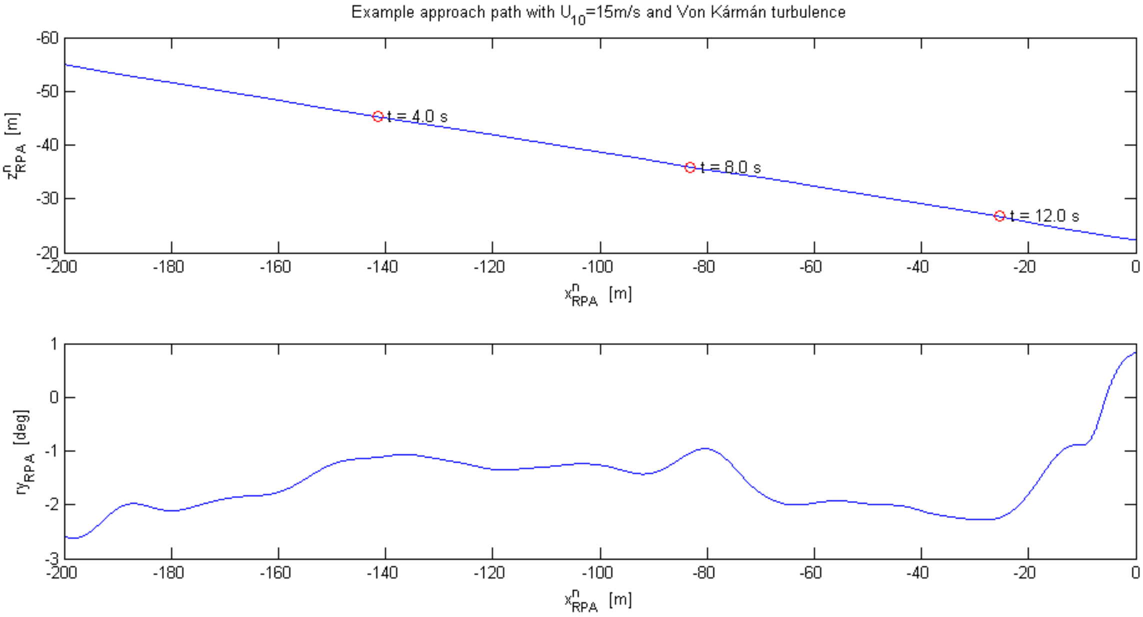

Figure 36, Example of approach path for a landing with 15 m/s wind speed (at 10m altitude), Von Kármán turbulence and no floater motions. Top plot shows approach path, and bottom figure shows corresponding pitch angle of RPA.

In the first figure the altitude and pitch angle are plotted as a function of horizontal position. This shows that the glide path is indeed linear, with a nearly insignificant flare at the end of the approach. This small flare follows from the pitch angle increase that starts about 10 meter before the flyover. Note that the starting positions is at an altitude of 55 meter at 200 meter from the platform, and the flyover at approximately 22.5 meter. That is because the deck is assumed to be at 20 meter above the ground/MSL and a deck clearance (h_{land}) of 2.5 meter at flyover is used in the glide slope controller. Wind disturbances mainly affect the pitch angle, as this is used to respond to a vertical deflection.

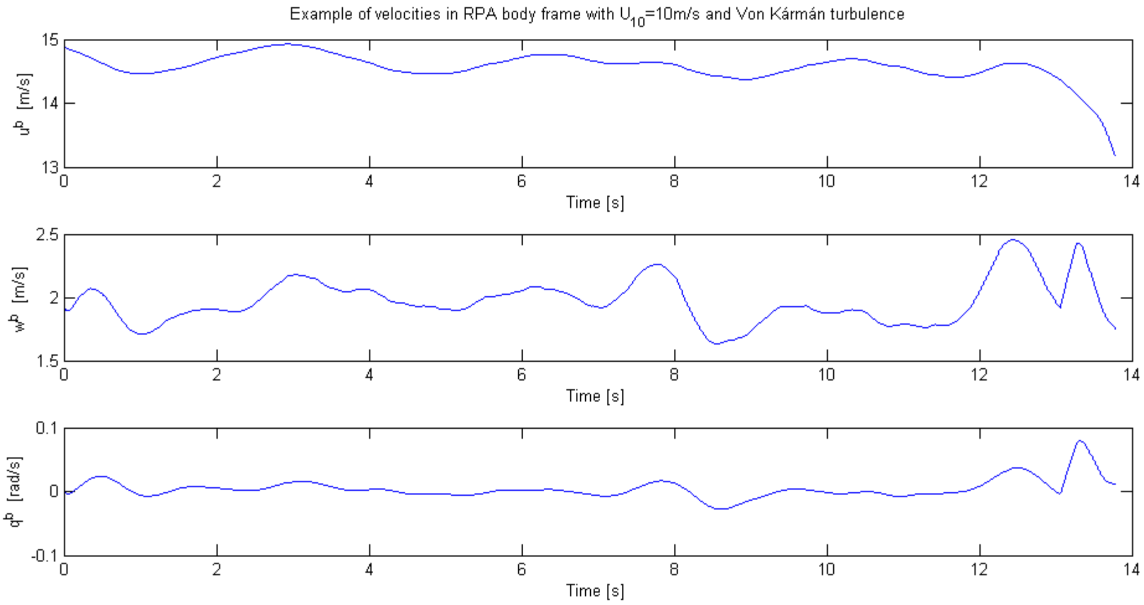

Figure 37, Velocities of RPA in body frame during approach as shown in Figure 36. Top plot shows longitudinal velocity component (u^b) over time, middle plot shows vertical velocity component (w^b) over time and bottom plot shows pitch rate (q^b) over time.

In Figure 37 the velocities in the RPA body frame are shown. It is obvious that the disturbance from turbulence is much more pronounced in these figures, especially vertical velocity is varying randomly due to wind turbulence. In the previous figure it could be noted that this was adjusted for by adjusting the pitch angle. What also stands out is the decrease in horizontal velocity during the final phase of the approach, as at this stage the tether is no longer pulling in line with the flight path. In the bottom graph with the pitch rate, the transition from glide path control to pitch angle control is clearly visible at around 13 seconds, this also affects the vertical velocity slightly, decreasing it by about 0.5 m/s.

This simulation serves as a simple sanity check, it shows that the RPA behaves as expected during the simulations. The numerical model is therefore fit to be used in further analyses.

3.5.2 Without wind turbulence (case 1)

Now Monte-Carlo simulations are performed using the numerical model as a basis. 15000 simulations are run for each case, 2500 at each average wind speed. The variations that have been included in case 1 are only in the initial conditions. The values for the initial conditions are randomly generated from a normal distribution. The standard deviations for initial velocities (both vertical and horizontal) is 0.5 m/s, for the pitch rate it is 1.5 deg/s, the initial altitude 1 meter and the standard deviation for initial pitch angles is 3°.

In Figure 38, Figure 39 and Figure 40 the mean values for respectively the relative horizontal speed, relative height and relative pitch angle at flyover are shown as a function of wind velocity. The red line indicates the values of the simulations with an initial altitude of 55 meter and the blue line those with 45 meter. What is clear from these figures is that the mean values are not constant with wind speed. As a uniform distribution of the average wind speeds (U_{10}) is used as input for the simulations, the complete sets of 15000 simulations will not show a clear normal distribution due to a varying mean. However, the simulation results for each independent, average wind speed separately are normally distributed. An example is shown in the form of a histogram for the relative height of case 1 at an average wind speed of 5 m/s in Figure 41. This verifies the use of the standard deviation at each wind speed as an indication of the uncertainty of important landing parameters, and therefore the landing performance.

The difference in mean values makes sense for the relative horizontal speeds due to different reel-in speeds at different wind speeds. For the relative height this is caused by a controller that is not optimally adjusted for different airspeeds. At low wind speeds the RPA appears to be flying over the pulley at a higher altitude, 0.3 meter above required value of 2.5 meter on average for initial heights of 55 meter. While at higher wind speeds the RPA undershoots the required value by approximately 0.2 meter. This is likely caused by the length of the final pitch up phase, which is over a longer distance at low wind speeds. During this phase there is no specific control over the height of the RPA. The mean value can be evened out, by adjusting the required value, which is currently 2.5 meter, to the average wind speed or even to the expected FP pitch angle.

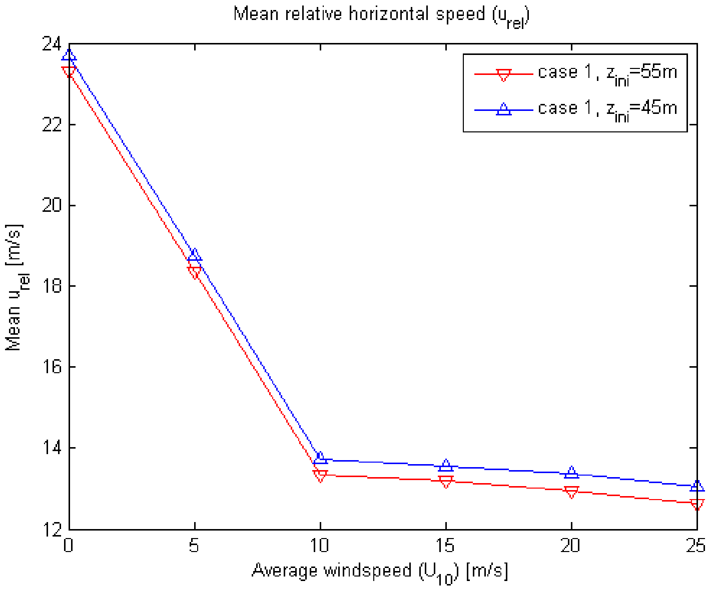

Figure 38, Mean values for relative horizontal speed as function of airspeed in simulations of Case 1, with initial altitudes of 55m and 45m

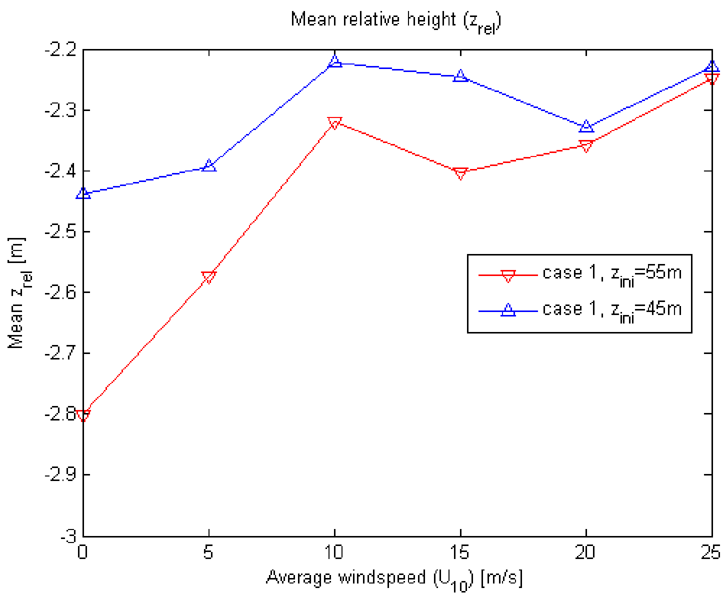

Figure 39, Mean values for relative height as function of airspeed in simulations of Case 1, with initial altitudes of 55 meter and 45 meter

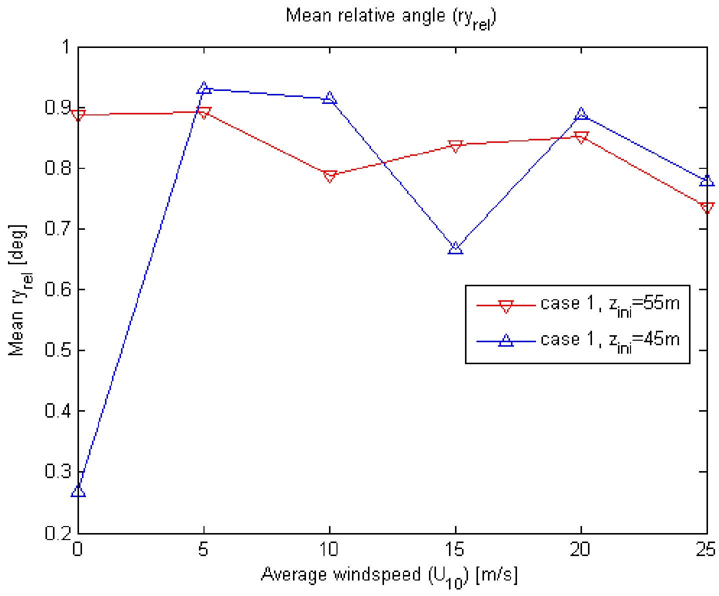

Figure 40, Mean values for relative pitch angle as function of airspeed in simulations of Case 1, with initial altitudes of 55m and 45m

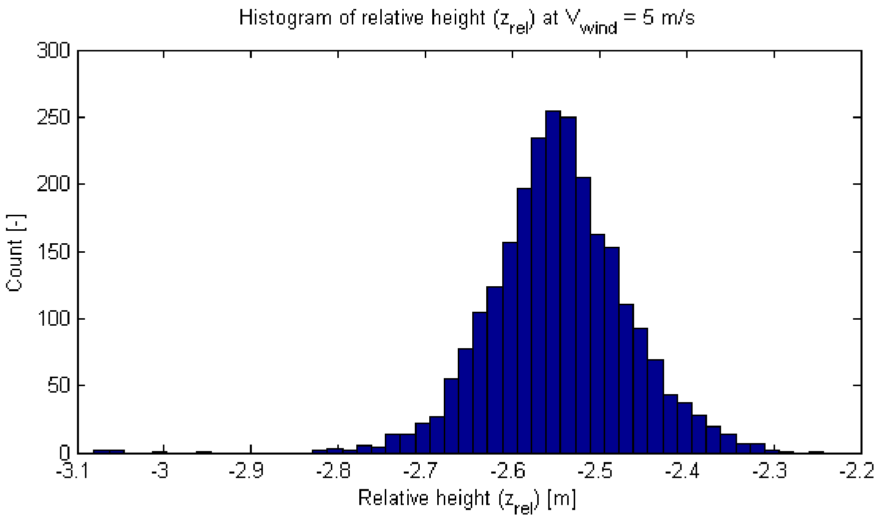

Figure 41, Histogram of relative height at 5 m/s wind speed, indicating normal distribution

In Figure 42, Figure 43 and Figure 44 a comparison of the standard deviations between the simulations with an initial altitude of 55m and those with an initial altitude of 45m is shown. Using a higher initial altitude has preference, as it allows for a less abrupt transition from the cross-wind flight to the approach. Based on the simulations, using an initial altitude of 55m results in no unacceptable decrease in landing performance.

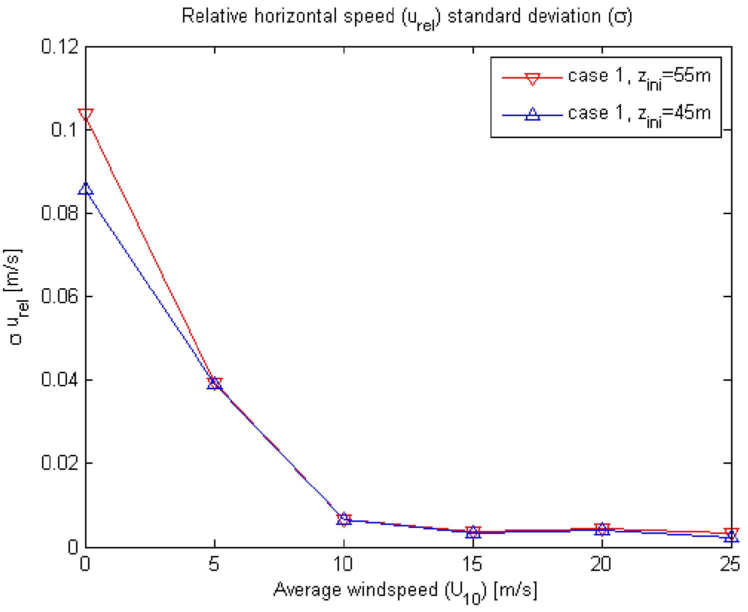

Figure 42, Standard deviation values (σ) for relative horizontal speed as function of airspeed in simulations of Case 1, with initial altitudes of 55m and 45m

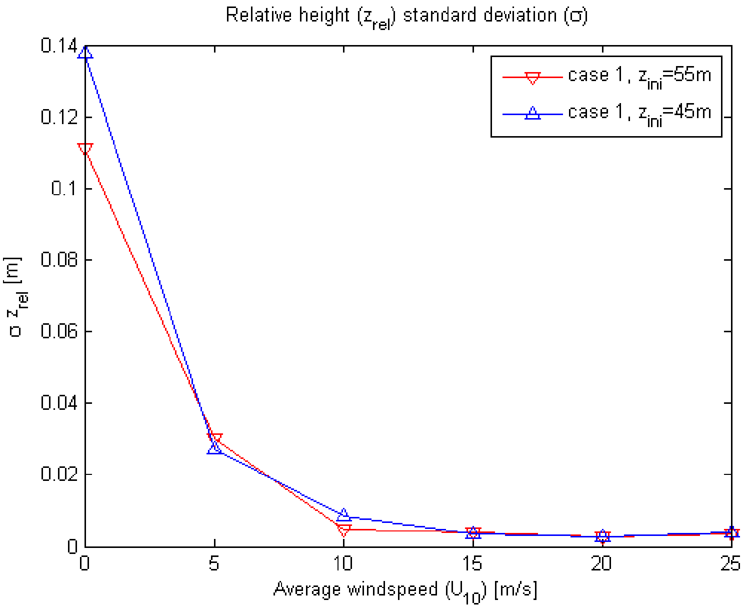

Figure 43, Standard deviation values (σ) for relative height as function of airspeed in simulations of Case 1, with initial altitudes of 55m and 45m

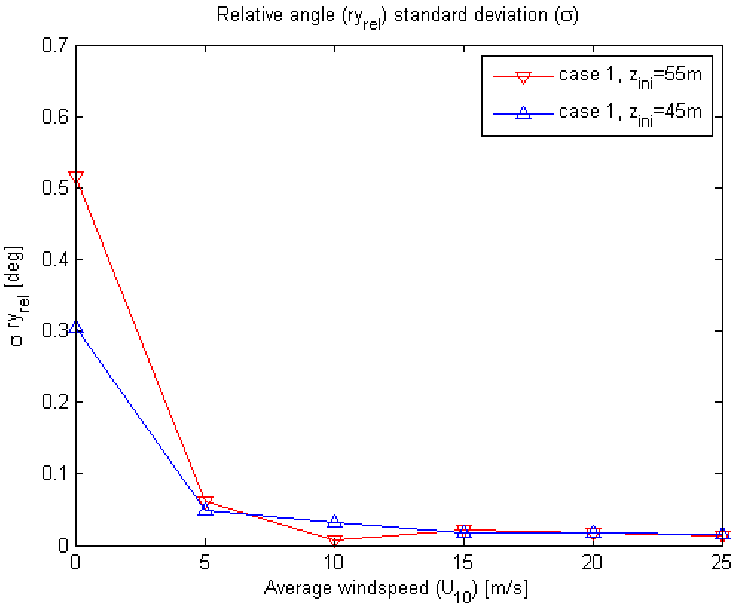

Figure 44, Standard deviation values (σ) for relative pitch angle and relative height as function of airspeed in simulations of Case 1, with initial altitudes of 55m and 45m

3.5.3 With wind turbulence (case 2)

In case 2 the same variations in initial conditions as case 1 were used, but now a wind turbulence signal has been added. 15000 simulations have been run with a Dryden turbulence model, and 15000 with a Von Kármán turbulence model. The mean values of relative horizontal speed and height of these simulations correspond to the simulations without turbulence, as can be seen in Figure 45 and Figure 46.

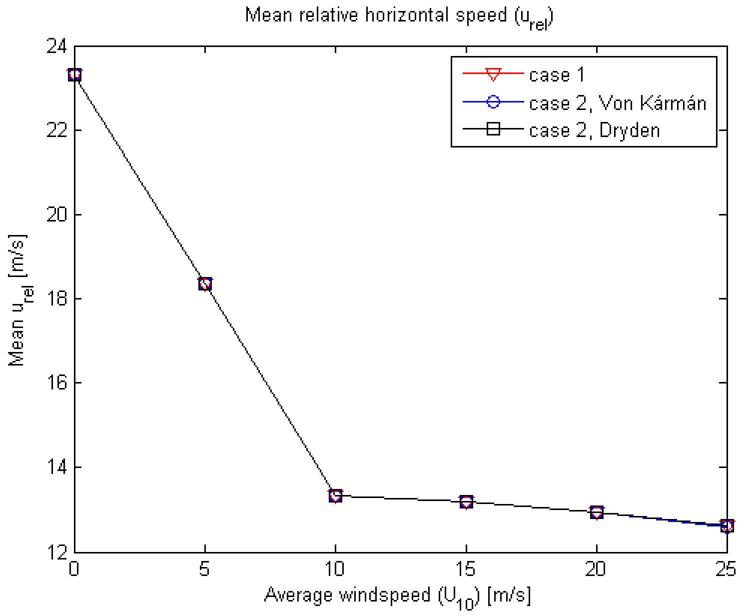

Figure 45, Mean values for relative horizontal speed as function of airspeed in simulations of Case 2, with Dryden and Von Kármán wind turbulence models

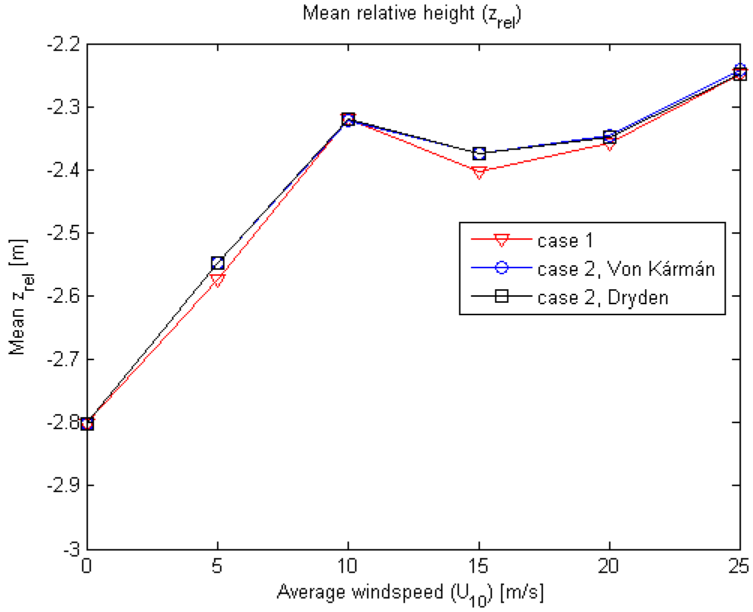

Figure 46, Mean values for relative height as function of airspeed in simulations of Case 2, with Dryden and Von Kármán wind turbulence models

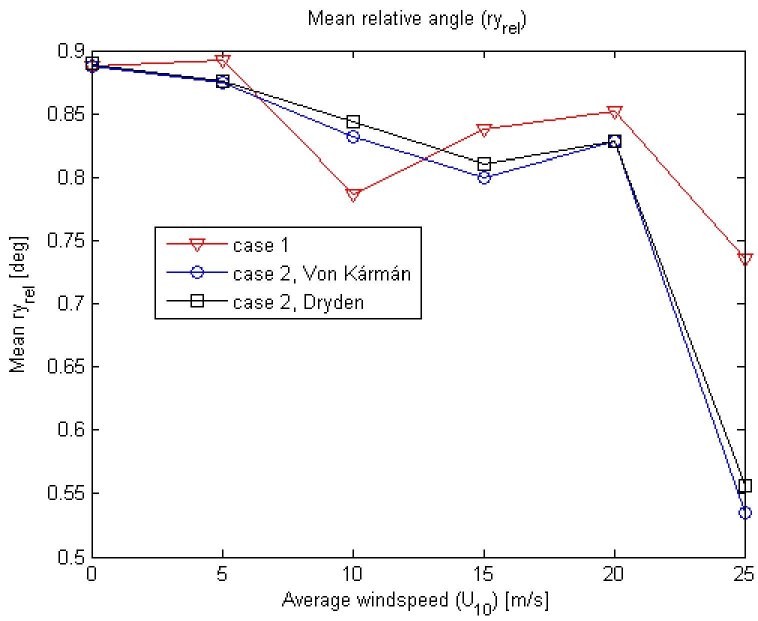

Figure 47, Mean values for relative pitch angle as function of airspeed in simulations of Case 2, with Dryden and Von Kármán wind turbulence models

The corresponding standard deviation results are plotted in Figure 48 and Figure 49, which clearly show the increase of uncertainty with higher wind speeds as expected, and the overlap with the baseline at 0 m/s wind speed, because turbulence is negligible at 0 m/s wind speed. It also shows that the Von Kármán is slightly more conservative than the Dryden turbulence model. Combined with the comment in (DoD, 1997) that the Von Kármán model corresponds better with actual measurement data, the decision was made to use this type of turbulence in further simulations.

The relative pitch angle at landing is highly dependent on the final phase of the approach (pitch-up phase), and specifically the time dt_{fin} (see equation (3.31) in section 3.4.1). It seems by making it dependent on the airspeed of the RPA, this variable is no longer correct in turbulent conditions. The results in Figure 40 and especially Figure 44 indicate that the relative pitch angle is not accurately controlled for all wind speeds and wind turbulence conditions. The implementation of this pitch-up phase will need to be revisited before the pitch angle can serve as a reliable indicator of landing performance. The time dt_{fin} should not only be dependent on airspeed, as this varies significantly due to turbulence, but instead on the reel-in speed and measured average wind speed. Another improvement would be to not just determine the pitch-up time (dt_{fin}) at one point in the approach (50 m before landing), but instead converge to a value based on multiple measurements. The extrapolation would become more accurate. More advanced methods that include for example a Kalman filter or even a FP motion forecasting algorithm could also be examined.

More information on these methods will be provided in the recommendations at the end of this document.

The implementation of a more precise value of dt_{fin} is expected to have a positive effect on the relative pitch angle control at landing, while not significantly influencing the other landing parameters like relative height. In the previous section on the controllers it was already shown that the pitch response is an order of magnitude faster than the speed and height (glide slope) control. Combined with the relatively slow pitch motions of the platform, there is no reason to expect that the pitch angle is the most critical factor for landing on a floating platform. That is why in the remainder of this document only the relative horizontal speed and height at the end of the approach will be discussed.

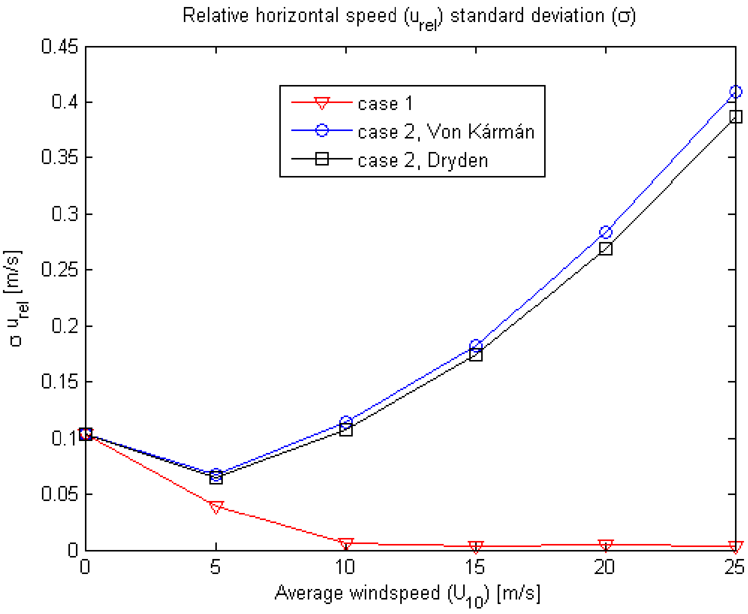

Figure 48, Standard deviation values (σ) for relative horizontal speed as function of airspeed in simulations of Case 2, with Dryden and Von Kármán wind turbulence models

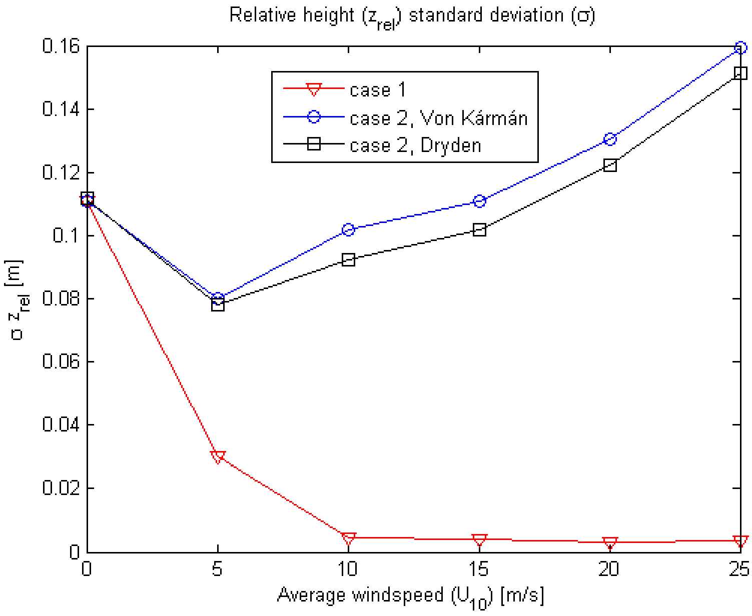

Figure 49, Standard deviation values (σ) for relative height as function of airspeed in simulations of Case 2, with Dryden and Von Kármán wind turbulence models

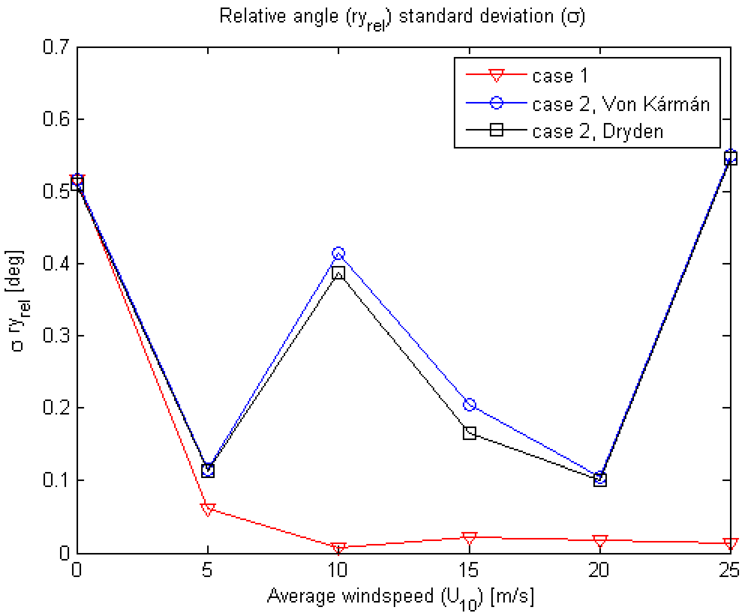

Figure 50, Standard deviation values (σ) for relative pitch angle as function of airspeed in simulations of Case 2, with Dryden and Von Kármán wind turbulence models

4 Landing on moving platform

In this chapter the results of incorporating floater motions into the aerodynamic model are presented. In the first section (section 4.1), harmonic motions are covered to investigate the effect of frequency and amplitude of motions. In the subsequent section (section 4.2), landing uncertainty increases that can be expected for an actual deep-water offshore application are discussed. This is where the models that have been developed in chapter 2 and 3 come together. The section also includes a review of metocean data for the reference location.

4.1 Harmonic motions

As mentioned above, first the harmonic motions are considered. For these conditions a range of twenty different platform motions are considered, both with and without wind turbulence. 15000 approach runs have been simulated with constant wind, and 15000 with Von Kármán wind turbulence.

The twenty platform motions are defined by four different motion amplitudes: 0.5, 1.0, 1.5 and 2.0 meter. The periods of the motions that have been considered are 12, 15, 18, 21 and 25 seconds, which leads to twenty (4x5) motions. As well as varying the wave motions, the average wind speed (U_{10}) has also been varied. This leads to 125 simulations for each combination of average wind speed, motion amplitude and motion period. And each of these 125 simulations starts at a different FP motion phase angle.

The motions of the platform are defined by the following set of equations:

$$\begin{aligned} x_{FP}{}^{n} &= A \cdot \cos\left(\frac{2\pi}{T}t + \theta\right) \\ z_{FP}{}^{n} &= A \cdot \cos\left(\frac{2\pi}{T}t + \frac{\pi}{2} + \theta\right) \\ ry_{FP}{}^{n} &= A \cdot \cos\left(\frac{2\pi}{T}t + \pi + \theta\right) \end{aligned} \tag{4.1}$$

Where A is motion amplitude, either in meter for surge and heave or in degrees for pitch (a platform motion with an amplitude of 0.5 meter therefore has a pitch amplitude of 0.5°), T is the period of the motion, and θ is the phase angle (uniformly distributed between 0 and 2π in 125 steps).

In the following sections the results of these simulations will be covered.

4.1.1 Without wind turbulence (case 3)

In Figure 51 the mean of the horizontal speed and relative height at the end of the approach are shown. From this figure follows that the harmonic motions do not affect the average of the approach simulation results, as expected. It is from here on assumed that this is the case for all other platform motions as well. From this point on, only the standard deviation results of the simulations will be discussed.

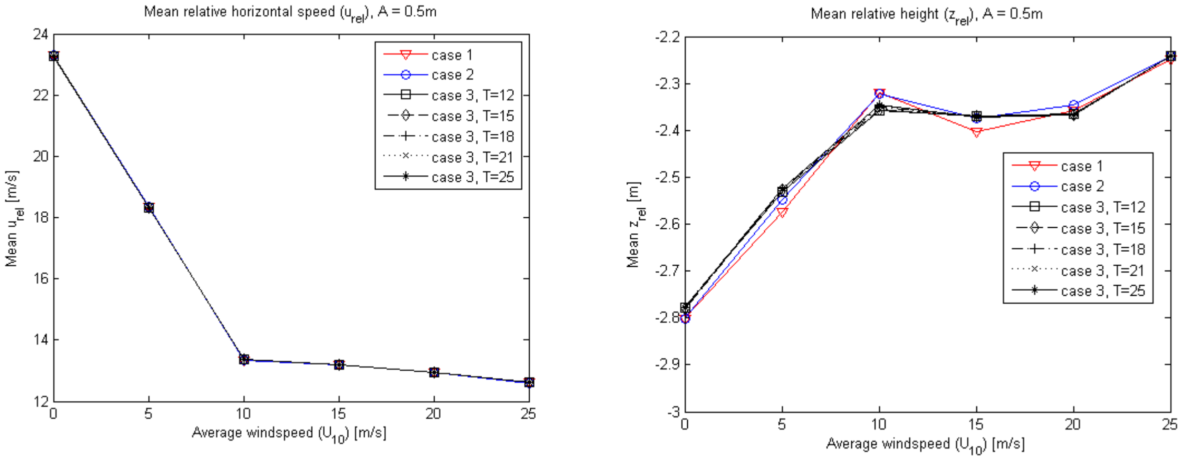

Figure 51, Mean of relative horizontal speed (left) and mean relative height (right) with harmonic platform motions and no wind turbulence

The first standard deviation results of the simulations with platform motions of 0.5 meter are shown in Figure 52. An important point to take from these plots is that the standard deviation increases with smaller periods (or increasing frequency). It seems like this increase is exponential or quadratic, but by plotting the (normalized) standard deviations with respect to frequency instead of period, the relation is found to be linear, see Figure 53. The slope of the linear relationship is dependent on the wind speed (especially for relative height), which can also be concluded from Figure 52. The second important point that can be concluded from the plots is that the standard deviation of the horizontal velocity is more or less constant with airspeed, while it decreases with increasing airspeed for the relative height. The airspeed has a positive effect on the glide slope control, but the effect is not existent in the speed control using the winch torque. This effect is also apparent from the slope of the standard deviations with only Von Kármán wind turbulence (case 2); the slope is smaller for relative height in comparison to the slope for horizontal velocity. This indicates that the glide slope coupler is more capable of adjusting to the variation caused by turbulence than the speed controller.

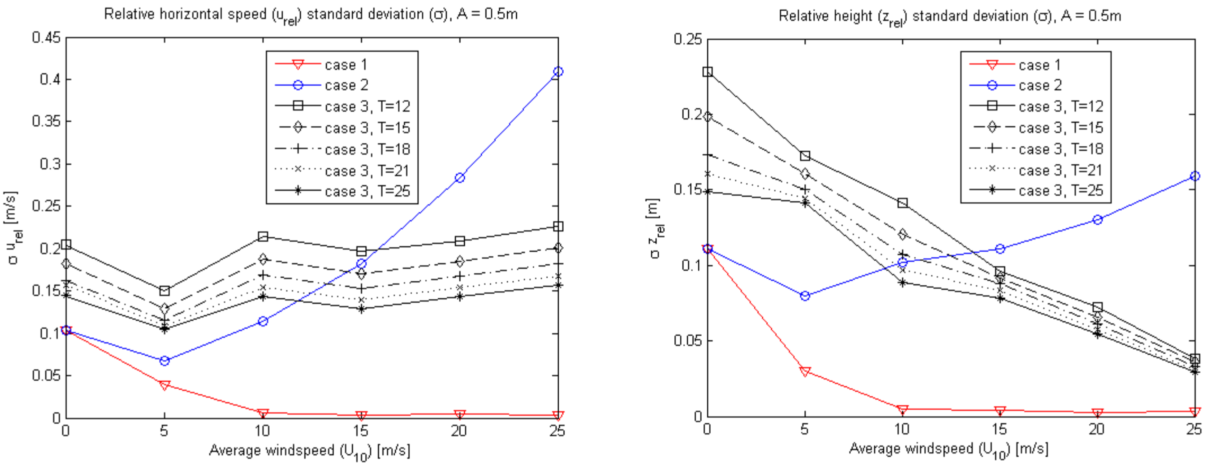

Figure 52, Standard deviation (σ) of relative horizontal speed (left) and standard deviation of relative height (right) at the end of the approach with harmonic platform motions of 0.5m amplitude and no wind turbulence

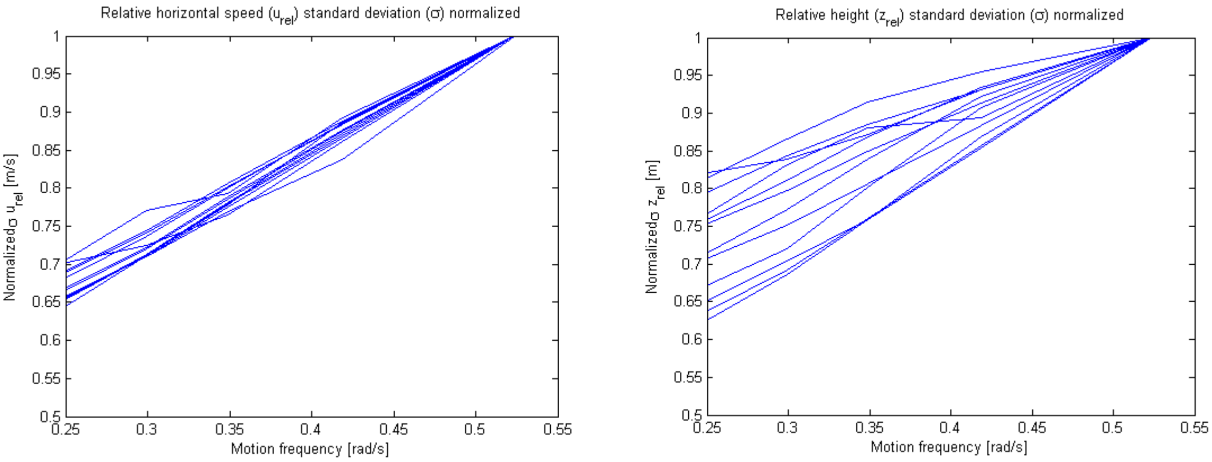

Figure 53, Normalized standard deviation (σ) of relative horizontal speed (left) and of relative height (right) as function of FP motion frequency

The figures of the standard deviation at 1.0 and 2.0 meter motion amplitudes have been included in the appendix (D). In Figure 54, the standard deviations are shown for 1.5 meter motion amplitude. This figure shows that the standard deviation also increases with the amplitude of the motion, as expected. The standard deviations at 1.5 meter motion amplitudes are approximately three times larger than at 0.5 meter, indicating that the increase of standard deviation is linear with motion amplitude. This linear relationship is confirmed by the figures in the appendix.

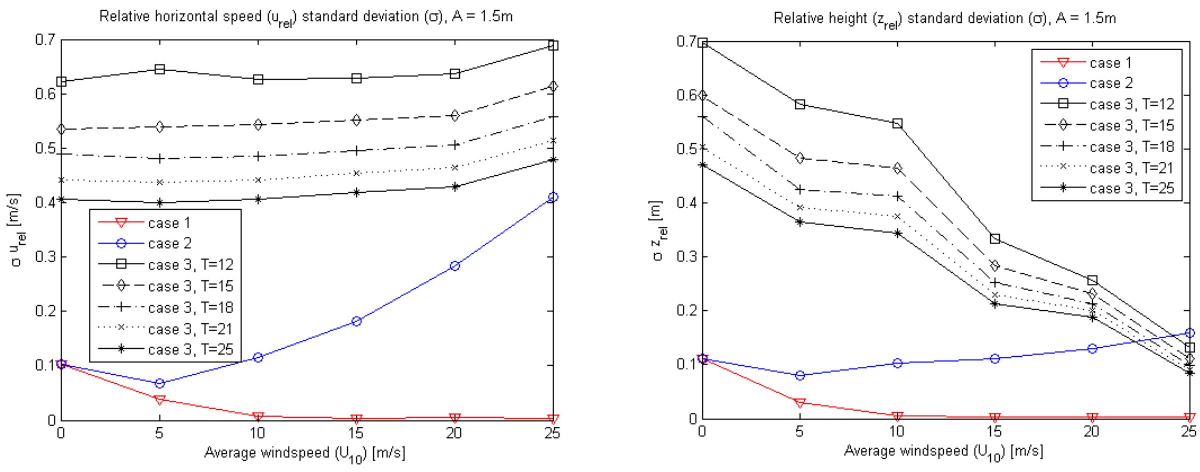

Figure 54, Standard deviation (σ) of relative horizontal speed (left) and standard deviation of relative height (right) at the end of the approach with harmonic platform motions of 1.5m amplitude and no wind turbulence

From these initial analyses with harmonic motions it can thus be concluded that the standard deviation is linearly dependent on both the frequency and the amplitude of the motion. This indicates that the velocity of the platform motions is the driving factor for landing performance.

4.1.2 With wind turbulence (case 4)

Now the combined effect of platform motions and wind turbulence is examined. The same simulations are run as in the previous section, but with Von Kármán turbulence included. The results have been plotted only for motion periods of 15 and 21 seconds and for motion amplitudes of 0.5 and 1.5 meters. In Figure 55 and Figure 56 the magenta lines indicate the resulting standard deviation from platform motions and turbulence combined. For small motion amplitudes the standard deviation converges at high wind speeds to those with turbulence only (case 2, blue line), while at low wind speeds they converge to the standard deviation of only the floater motions (case 3, black lines). At larger floater motions this convergence towards the wind turbulence only case (case 2) is not present, as the standard deviations caused by the floater motions alone are much more significant.

From these simulations it is found the resulting standard deviations of case 4 are not simply the sum of the standard deviations of case 2 and 3. Based on the figures it can be concluded that the standard deviations relate to each other in the following way.

$$\sigma_4{}^2 \approx \sigma_2{}^2 + \sigma_3{}^2$$

This means that the variance (standard deviation squared) of case 4 is approximately equal to the summation of variance of case 2 and case 3.

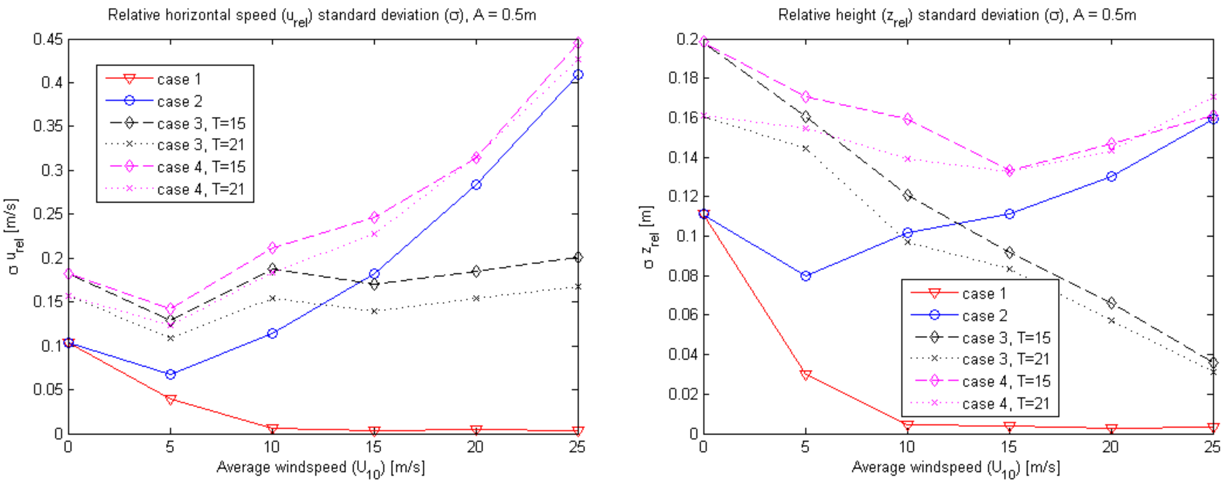

Figure 55, Standard deviation of relative horizontal speed (left) and standard deviation of relative height (right) at the end of the approach with harmonic platform motions of 0.5m amplitude and Von Kármán wind turbulence

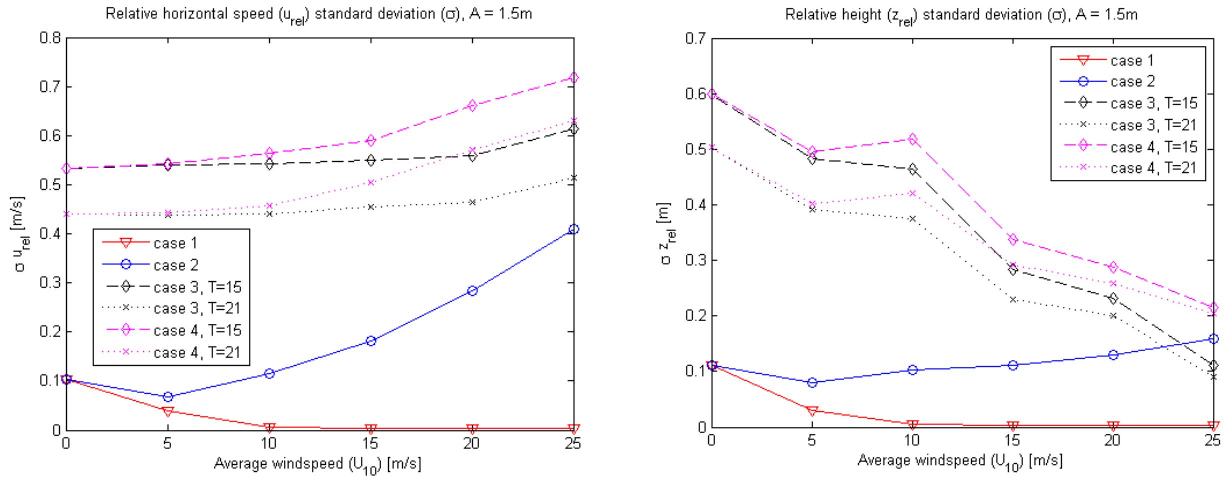

Figure 56, Standard deviation of relative horizontal speed (left) and standard deviation of relative height (right) at the end of the approach with harmonic platform motions of 1.5m amplitude and Von Kármán wind turbulence

From cases 3 and 4 some conclusions can be made on the relationship between floater motion properties (like frequency and amplitude) on the landing performance. However, it does not show what the order of magnitude is of the floater motion induced landing performance decrease. Case 5 is used to give an indication based on the FP design by Mocean and the environmental data at the reference location. This will be covered in the next section.

4.2 Motions from hydrodynamic model

In chapter 2 the development of the numerical model for the FP is covered. This numerical model is used to determine the magnitude of the effect of platform motions on the landing performance. As discussed in chapter 1, the standard deviation of relative horizontal speed and relative height at flyover are used as indicators of the landing performance. In the previous cases (1-4) six different wind speed conditions were investigated (0-25 m/s). For this analysis only three wind speeds will be covered; 5, 15 and 25 m/s, they represent respectively low, medium and high wind conditions. Based on the metocean data for the reference location, a distribution of wave conditions for these specific wind conditions can be determined. This distribution in combination with a database of FP motion time-series is used as input for the Monte-Carlo analysis of case 5.

4.2.1 Metocean data and FP motion database

For the reference location Buchan Deep, which is located of the east coast of Scotland in the North Sea, environmental data was gathered. This metocean data consists of wave and wind measurements over a ten year period with three hour intervals, so approximately 29220 measurement points. In Figure 57 the variation in time of significant wave height and wind velocity is shown, as well as their respective distributions. The variation over time clearly shows seasonal dependency, with high wind and wave conditions occurring mostly in winter. For the installation and maintenance strategies this seasonal dependency should be taken into account, but for this analysis the dependency is neglected; the RPA is assumed to land as often in winter as in summer.

As mentioned in the introduction of this chapter, three different wind conditions will be examined. In the bottom right plot the limits for a measurement point to be considered in one of these wind conditions is shown. For low wind conditions all measurements points with wind speeds (U_{10}) between 2.5 and 7.5 m/s are considered, for medium wind conditions all measurement points with wind speeds between 12.5 and 17.5 m/s are taken into account, and finally for the high wind case the measurement points with wind speeds above 20 m/s are included. The wave conditions of these measurement points have been plotted in a wave scatter in Figure 58. In this wave scatter the peak periods and significant wave height of the measurement points are plotted, the color of the points indicate the respective wind condition. Based on this wave scatter, the combinations of significant wave height and peak period that are collected in a database of FP motions are determined. The black dots in the figure indicate these 24 wave conditions. At each of these 24 combinations of peak period and wave height a simulation of 3.5 hours is run with the numerical model of the floating platform. Refer to Chapter 2 for more details on the development of this numerical model. Using the scatter diagram, the probability of a certain sea state in the database is determined, this is done by counting the amount of measurement points that fall within limits defined by the orange dashed lines around the database points. For low wind conditions it is therefore likely that floater motions in wave conditions with a significant wave height of 1m and a peak period of 7 seconds are selected during the Monte-Carlo analysis, while this will not happen during the high wind conditions.

The approach of determining the distribution for the database points works especially well for the low wind conditions, due to high amount of measurement points and ease of implementation. However, at high wind conditions the amount of measurement points is limited and an approach where a continuous probability distribution is generated first has preference.

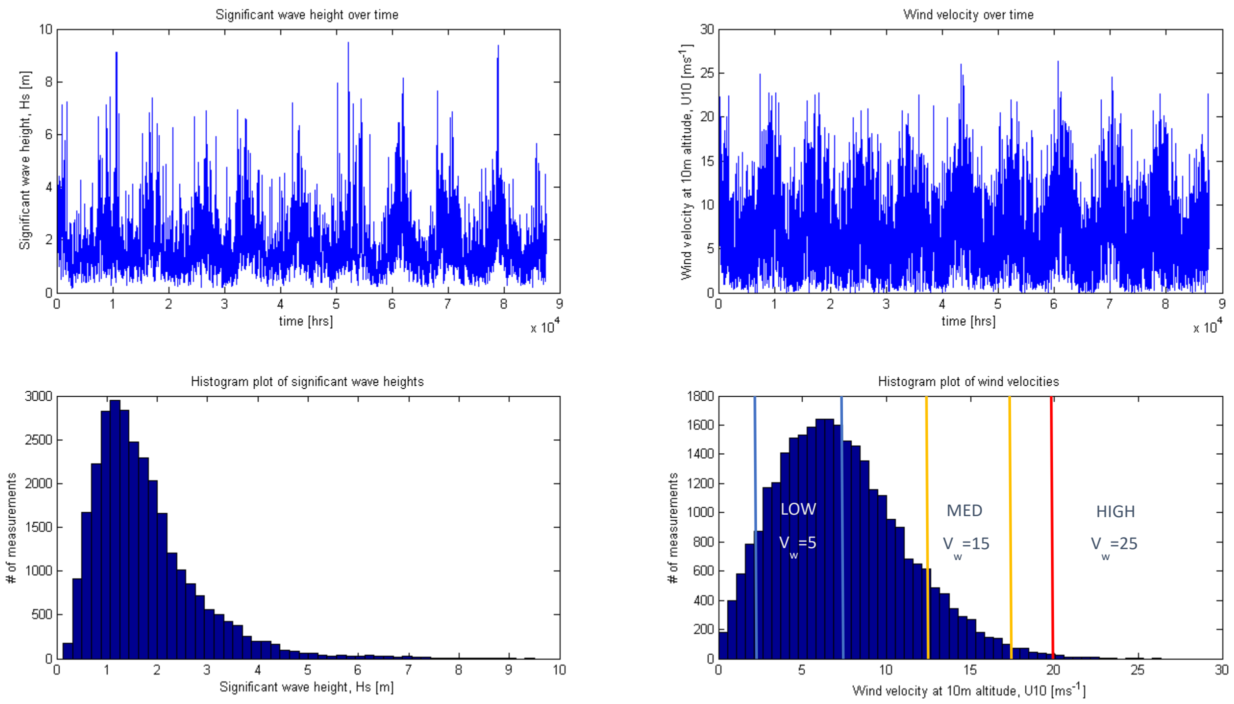

Figure 57, Metocean conditions for 10 years (3hr intervals) at reference location Buchan Deep (Scotland), top left plot shows significant wave height over time, top right plot shows wind velocity (U_{10}) over time, bottom left plot shows distribution of significant wave height in a histogram, bottom right plot shows distribution of wind velocity (U10) in a histogram, with limits for low, medium and high wind conditions indicated.

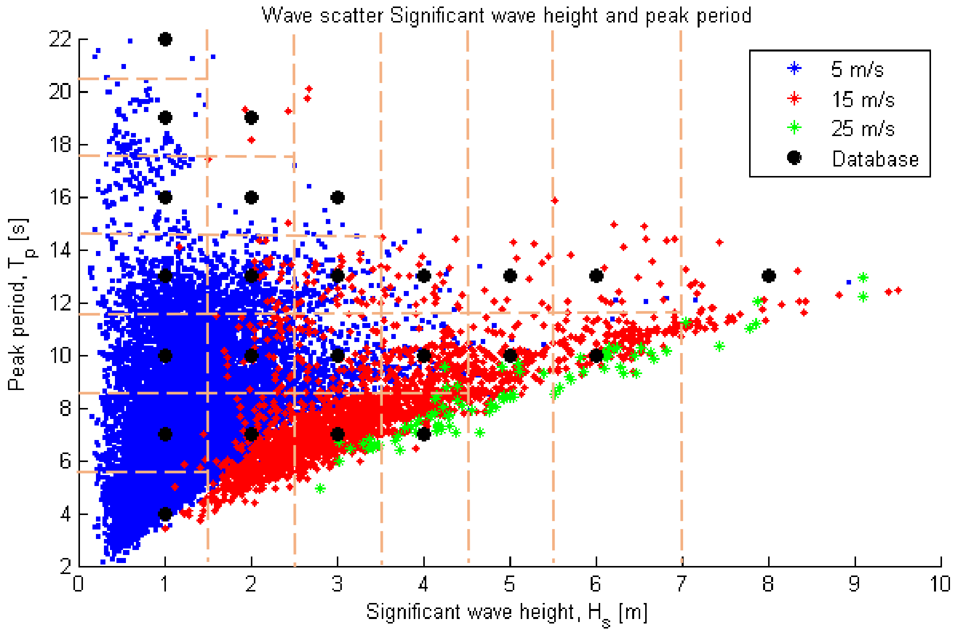

Figure 58, Wave scatter diagram with significant wave height (H_s) and peak period (T_p) of measurement points, combined with database points and respective limits for determination of probabilities of database points

4.2.2 Results (case 5)

For this last case 15000 landing approaches are simulated; 5000 at each wind condition. For each simulation the wave conditions are determined using a random number generator. Depending on the database distribution this random number corresponds to a time signal of 3.5 hours of floater motions. The start time within this signal is also randomly generated; as approaches generally last less than 15 seconds, there would be no point of creating a 3.5 hour time signal. The wind turbulence noise seeds and initial conditions are the same as in case 2 and case 4.

In Figure 59 the results of case 5 (black line) are shown in comparison to case 1 (red line), case 2 (blue line) and case 4 (magenta lines) for the relative horizontal speed at flyover. A couple of things stand out from this graph.

The effect of floater motions at low wind speeds is minimal; the reason is that the horizontal motions of the platform in low wind conditions are in general small. The natural frequency of the structure in surge is approximately 60 seconds, while most wave conditions at low wind speed have a peak period of 4 to 13 seconds. Interesting is that when looking at the surge RAO in section 2.4.3, the slope of the graph is linearly decreasing between frequencies of 0.3 and 1.0 rad/s (≈ 21 and 6.3 seconds) from approximately 1.5 to 0.45 m/m. And because the motion velocity is proportional to the motion amplitude multiplied with the frequency, it can be concluded that the surge velocity response of the structure is independent of frequency for this range of frequencies. The surge velocity is thus in the most wave conditions only dependent on wave amplitude. At relatively small wave amplitudes of 1 and 2 meter, which are dominant at low wind conditions the response in surge is thus minimal, leading to a relatively small influence on landing performance.

Wave heights significantly increase for medium wind conditions, with an average significant wave heights of 3.33 meter. This is clearly visible in the figure as the relative effect of platform motions on the standard deviation of relative horizontal speed is much larger. It should be noted that the effect is still smaller than that of case 4 (harmonic motion) with 0.5 meter amplitude, this might seem counterintuitive as the surge velocity amplitude for the harmonic motions are approximately 0.21 and 0.15 m/s for the periods of respectively 15 and 21 seconds ($v_{x,max} = A \cdot \frac{2\pi}{T}$). And for case 5 this surge velocity amplitude ($v_{x,a,ave}$) is expected to be on average 0.21 m/s, based on the surge RAO.

$$v_{x,a,ave} = \frac{1}{2} H_{ave} \cdot RAO_{surge}(\omega) \cdot \omega \tag{4.2}$$

Where $RAO_{surge}(\omega) \cdot \omega$ is equal to approximately 0.40 ms^{-1}/m and H_{ave} is the mean wave height, which is related to the variance (σ^2) of the wave height Rayleigh distribution and therefore the average significant wave height ($H_{s,ave}$) according to the following relations:

$$\begin{gathered} H_{ave} = \sigma \cdot \sqrt{\frac{\pi}{2}} \\ H_s = 4 \cdot \sqrt{\sigma^2} \\ H_{ave} = \sqrt{\left(\frac{H_{s,ave}}{4}\right)^2} \cdot \sqrt{\frac{\pi}{2}} = \sqrt{\left(\frac{3.33}{4}\right)^2} \cdot \sqrt{\frac{\pi}{2}} = 1.04\, m \end{gathered} \tag{4.3}$$

The reason why the effect on the landing performance is still smaller for case 5, has to do with the nonlinearity added to the hydrodynamic numerical model. The RAO does not represent the response at high wave heights as damping increases, the RAO shown in section 2.4.3 therefore overestimates the surge response at these wave heights. The nonlinearity is most clearly visible in the heave RAO which is smaller for the experiments with a wave height of 4 meter compared to those with 2 meter significant wave height.

The additional standard deviation in relative horizontal speed at high wind speeds is not as pronounced as at medium wind speeds, this was also the case for the harmonic motions. The reason is that turbulence is the largest contributor to the standard deviation.

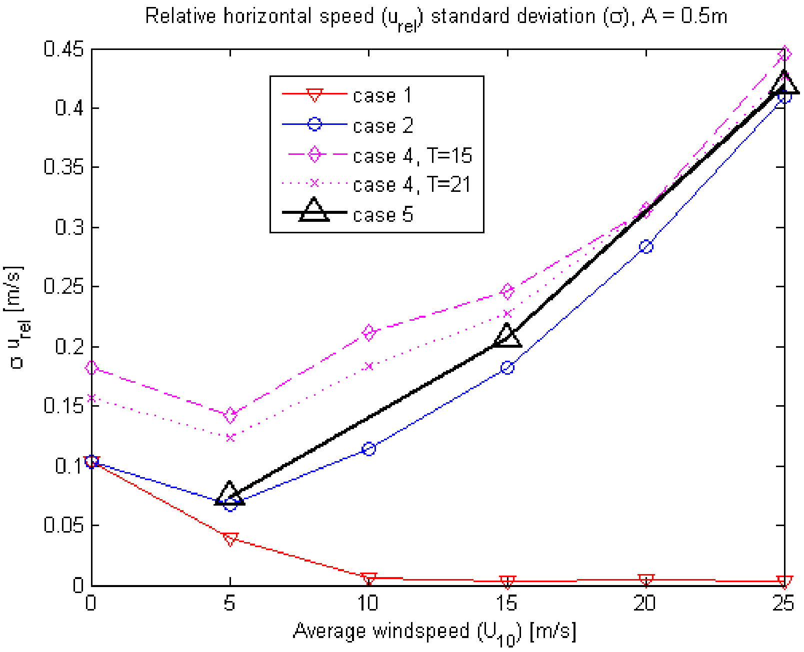

Figure 59, Standard deviation results of case 5 for relative horizontal speed

In Figure 60 the standard deviation of vertical height at flyover is plotted. The effect of these motions on landing performance is more constant over the wind speed regime. The reason is that there is an increase of peak period of the motion with wind speed, which approaches the natural period of the heave motion. This natural period/frequency of heave motion falls unlike the surge natural frequency within the range of applied wave frequencies. The effect is therefore more significant on the landing performance.

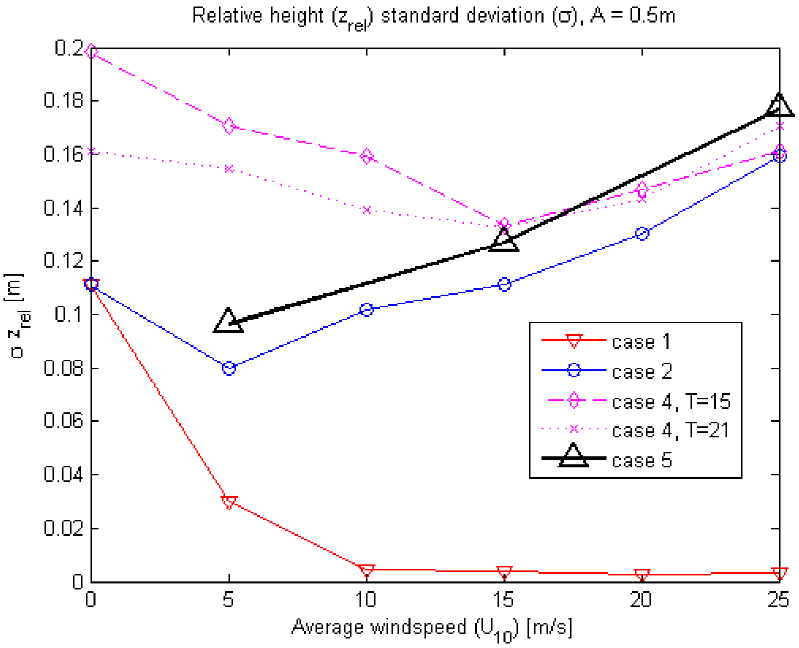

Figure 60, Standard deviation results of case 5 for relative height

In Figure 61 the distribution of relative horizontal speed and relative height are shown for the high wind speed condition of case 5 using a histogram. These figures show that the distribution is either log-normal or skew-normally distributed. The figures confirm the use of the standard deviation value as an indicator for landing performance.

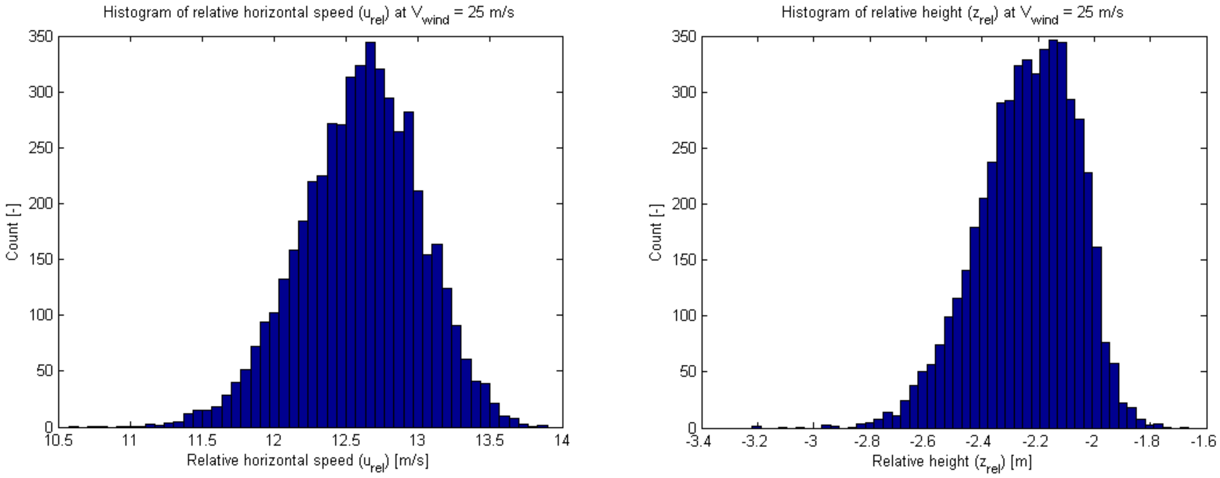

Figure 61, Histogram of relative horizontal velocity and relative height at the end of the approach for case 5 in high wind conditions (25 m/s)

5 Discussion and recommendations

The objective of this research was to determine the relative magnitude of the effect of platform motions on the landing performance. This was achieved by investigating the increase of standard deviation of several parameters that give an indication of landing performance.

5.1 Discussion of results

Based on the results presented in the previous chapter it was found that both frequency and amplitude of platform motions are critical for the landing performance. There is a linear relationship between performance decrease and either FP motion frequency or amplitude, this indicates that landing performance is mainly related to the platform motion velocities.

In general, there are two ways to increase landing performance using the design of the platform.

1. Increase the damping of the platform, which will decrease the motion amplitudes: Damping is kinetic energy dissipation from the floating structure to the surrounding water (or air), either through viscous effects or by wave radiation. For the design by Mocean Offshore viscous effects contribute the most to damping, as the water piercing area is relatively small, leading to little wave radiation. Additional edges and plates connected to the model will dissipate energy by creating turbulence around these elements. The keel plate and the stiffeners connected to it create a significant amount of damping, which could be increased by making a hole in the middle of the plate to increase edge length. However, the keel plate has another positive effect on the floater's motions that does not benefit from a hole in the middle.
2. Increase the (added) mass of the platform, which will decrease the natural frequencies of the motions: Decreasing the natural frequency can be done in one way without increasing the motion amplitude. This is increasing the inertia of the platform. The inertia is a result of both the structural and ballast mass and the added mass. However, increasing the structural or ballast mass (increasing displacement) will probably increase the cost of the structure. The keel plate is the biggest contributor to the added mass in heave. That is why increasing heave damping by making a hole in the plate would not necessarily increase landing performance, as this would reduce the added mass of this plate. More plates could be added on the columns to increase the added mass of the

structure, also in other degrees of freedom. A nice effect of increasing the pitch and roll inertia is that a low natural frequency also results in lower motion amplitudes as the wave slope at lower wave frequencies is smaller.

In Figure 62 both methods of increasing landing performance by adjusting the floater design are schematically represented using an example of a heave RAO.

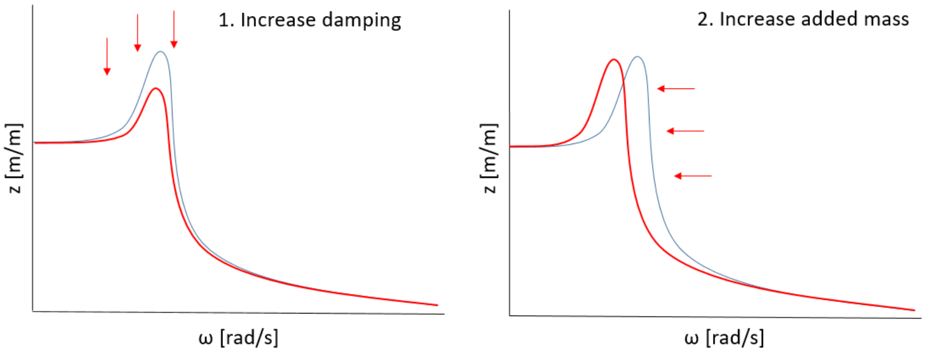

Figure 62, Comparison of methods that would increase landing performance, visualized using schematic heave ROA's

When looking further at the results of the simulations with platform motions based on metocean data and the numerical model, it was found that the current design of the FP by Mocean Offshore leads to a decrease of landing performance. However, the performance decrease is not insurmountable. It could be solved for by adjusting the landing gear and size of landing platform, and thereby increasing for example the acceptable range of landing impact. However, the cost of an increase in strength of landing gear and size of landing platform is hard to predict due to the complex nature of the technology. It should therefore be noted that the effect of floater motions could be reduced by incorporating smarter control systems. More detail will be given on these systems in the recommendations for further research in the next section.

Pitch motion was a critical part of this study. Pitch motion has led to difficulties in the hydrodynamic modelling side, as the experiments at MARIN resulted in significantly larger pitch motions in comparison to the simulations. This problem was caused by the difference between the numerical representation of the soft mooring and the experimental setup. In the future a more advance mooring configuration should be used in both the numerical model as well as in the experiment, to prevent discrepancies and obtain an accurate representation of the deep water AWE system.

On the other hand, pitch control during the final phase of the approach was not optimally incorporated. This led to unreliable results for the standard deviation of relative pitch angle at flyover. The decision was made continue the study with just the relative horizontal speed and relative height as indicators of optimal landing, as the pitch angle is not expected to be the most critical part of landing the RPA safely on floating foundations. The reason for this assumption is that the tuning of the pitch controller showed the capability of fast convergence towards specified pitch angles, the response was orders of magnitudes faster than the pitch motion of a floating platform.

To prevent issues like these in the future development of deep water offshore applications by Ampyx Power the following section is included, it consists of recommendations for further research.

5.2 Recommendations for further research

The recommendations for further research are distributed over different aspects of the development. They are listed here:

RPA model:

- Increase performance of final pitch up phase; this has been discussed extensively in this report. Update is required to get accurate relative pitch angles at landing.
- 6 degrees of freedom; although not considered critical, there are limits to acceptable relative roll and yaw angles as well as to lateral deflections at landing. In the next stage of the development, these should be taken into account to obtain a more complete image of landing constraints.
- Finalize design AP4; before the investigation towards landing on floating platforms is continued, a more detailed design of AP4 should be ready for use in simulations, this includes the control algorithms.
- Include measurement errors, signal delays etc.; in the current model some of the delays are taken into account, but in future analyses a more detailed representation of the sensors and communication systems is required.
- Validate CFD derived aerodynamic coefficients with flight tests; experiments are required to validate the aerodynamic coefficients that have been used in the numerical model. This holds for both AP3 and at a later stage for AP4. At Ampyx Power, research has been performed to determine aerodynamic coefficients based on flight tests with AP2 (Licitra, Williams, Sieberling, & Diehl, 2017).
- Define limits to landing in terms of flyover parameters; when the dimensions of the landing gear and landing platform are known, the limits to landing are most likely defined in terms of impact speed at touchdown and maximum horizontal deflection from mean landing location. To avoid modelling the computationally demanding arrest phase in future simulations, it should be investigated whether these limits can also be

defined by (a combination of) parameters like relative speed and pitch angle at flyover. This would greatly simplify further simulations.

- Include hydrodynamic motion prediction in control algorithm; by correctly predicting the position and velocity of the floating platform before landing, the landing performance could in a perfect case be improved to that of an onshore system. That is why a section with a literature review on hydrodynamic motion prediction methods is included at the end of this chapter.

FP model

- Use plate of zero thickness instead of box in panel method; necessary to obtain added mass of floating structure more accurately. A major flaw in the hydrodynamic model was the modelling of the keel plate. The assumption of a box structure in Aqwa^{TM} enforced a manual adjustment of the added mass in all degrees of freedom except heave. This can be avoided in the future by using plates of zero thickness in panel method tools.
- Use a more advanced representation of mooring configuration; holds for both numerical model and experiment. An accurate representation of the mooring configuration is necessary to accurately determine motions in nearly all degrees of freedom. Compared to this study, it is expected to influence pitch and roll motions especially. The mooring is dependent on location (water depth), and it would make most sense to update the analyses when an actual location for the system is decided upon.
- Confirm that Froude scaling in model tests leads to no significant differences; the difference between model tests and full scale motions is at the moment not expected to be significant. Additional analyses should confirm that the viscous effect at full scale do not differ from the experiment. A possibility is to perform CFD analyses at model scale and full scale to get an impression of the effect without investing in a full scale model test.
- Determine drag and added mass at other frequencies than natural frequencies; the numerical model's drag and added mass has only been validated at the natural frequencies using decay tests. By performing forced oscillation experiments the frequency dependency of added mass and drag could be assessed.
- Expand hydrodynamic database; create more time signals to obtain a database of platform motions with a higher resolution of peak periods and wave heights, and thereby increase the accuracy of the Monte-Carlo simulations.

Metocean data

- Extend metocean data with wave spectra; for this analysis the JONSWAP spectrum with a peakedness factor of 3.3 is used. The wave spectra should be updated based on actual measurement data.
- Update metocean data for possible new location; As the Buchan Deep location is already in use by the Hywind project, it is very unlikely that the first Sea Air Farm will be installed at this location. However, the influence of metocean conditions is large on the landing performance, and accurate metocean data at the new location will be required.
- Define probability distributions based on wave scatters; to determine the probability of FP motion database points instead of using measurement counts. The reason for this has been explained at the end of section 4.2.1.

Other

These recommendations do not concern the landing, but are nevertheless important for the development of deep water offshore systems.

- Review criticality of green water on RPA when stowed in extreme conditions; even in a 'once in a 50 year' storm the RPA should not be damaged by water slamming on the deck of the floating platform, unless it makes sense after a cost trade-off. Possible shelters for stowage of the RPA could also be incorporated in the design of the FP, as long as this is more cost-effective than increasing the FP's size, specifically freeboard. A study to determine countermeasures to green water and their cost should be performed.
- Review effect of corrosion; an offshore environment is a harsh environment, not only because of waves. Corrosion is an important factor to take into account when moving to sea. The effect of corrosion should be taken into account in the design of and offshore RPA, especially in the actuator design and electric components. Corrosion could also influence the operation and maintenance strategy, which is an important cost factor of the system.

Approach to RPA design for floating application

With the abovementioned recommendations in mind, the approach towards transforming an onshore AP4 system towards a floating AWE system can be examined. Two different approaches are presented, both assume that the design of an onshore AP4 system is finished and validated.

The first approach adjusts the design of the RPA based on a design of a FP and a known location:

1. In design/mass budget of RPA take 5-10% margin on components that have been sized based on onshore landing (like size of deck on landing platform and landing gear).
2. Include motion forecasting algorithm to increase landing performance (see next section for an introduction to different options).
3. Use the resulting design as input for Monte Carlo analysis with 6DOF simulations, assume worst case location for metocean conditions. Arresting phase should be included in simulations if no direct relation between parameters at flyover and impact at landing can be made.
4. Optimize design of critical components based on expected maximum loads (e.g. with 6sigma approach) and fatigue loads.
5. Perform additional design iteration (repeat steps 3-4).

This would result in an RPA design that is optimized for a specific location and platform design.

The second approach assumes a constant RPA design, and defines operational limits instead.

1. Use design of RPA for an onshore location or offshore bottom founded structure (monopile refurbishment).
2. Define limits of operation in terms landing parameters (preferably parameters at flyover like combination of relative height, speed and pitch angle, otherwise parameters like impact at touchdown).
3. Define acceptable probability of exceeding limiting landing parameters.
4. Derive operational limitations in terms of environmental conditions using Monte Carlo simulation.
5. Optimize FP design by making a trade-off between down-time cost and cost of structure.
6. Perform additional FP design iteration (repeat steps 4-5).
7. Use weather forecast to safely stow RPA during environmental (wave) conditions outside of operational envelope.

This approach would allow for location specific designs of FP, where the design follows from a trade-off between down-time cost and cost of structure.

A combination of the two methods, where a slightly strengthened version of the onshore AP4 system with FP motion forecasting algorithms serves as input for the second approach, is expected to lead to the most cost competitive design.

Hydrodynamic motion prediction/forecasting

One of the most promising methods of reducing the negative effects of FP motion on the landing performance is predicting and anticipating on the motions of the platform. Perfect FP motion prediction would lead to landing performance equal to that of an onshore system. That is why in this final section of the report attention is given to literature on several different approaches that could be worthwhile for the development of deep water AWE.

The signal that will need to be predicted is a stationary, continuous stochastic signal (Newland, 1993). In consultation with the engineers at Ampyx power, it was decided that only data from the inertial measurement unit (IMU) and the global navigation satellite system (GNSS) onboard the FP and RPA can be considered as input for the predictive algorithm. This decision eliminates methods that require remote wave sensing, like the OWME project (Dannenberg, Hessner, Naaijen, van den Boom, & Reichert, 2010).

Predictive algorithms shall be calculated in real-time onboard the RPA, it is therefore important that the method is computationally not too demanding. Ship motion prediction has been a research subject for a long time; this is because many operations at sea can be executed at lower risk and with more efficiency when the ship motions are known several seconds in advance. Think of helicopter landings, missile launches and more recently, autonomous UAV landings.

Ship motion prediction was first investigated by (Dalzell, 1965), who made use of a Wiener filter. Kaplan et al. noted that the Wiener filter was too complex for practical applications and therefore proposed the Kalman filter method (Kaplan & Sargent, 1970). Since then, much research has been dedicated to the Kalman predictor approach. (Weiss & DeVries, 1977) designed a filter in which ship motion spectra was modelled; they noted that this increased performance with respect to methods that do not consider this. Sidar and Doolin came to a similar conclusion at NASA in 1975 and published their findings in 1983, they also demonstrated the ability to predict heave and pitch motions up to 15 seconds in advance (Sidar & Doolin, 1975, 1983). In 1982 and 1983, Tryantafillou et al. continued with the development of the Kalman filter approach, and focused on the hydrodynamic considerations in the form of linear differential equations with frequency dependent coefficients (Triantafyllou & Athans, 1982; Triantafyllou, Bodson, & Athans, 1983). (Lainiotis, Charalampous, Giannakopoulos, & Katsikas, 1992) focused on deriving a state space model based on sufficient knowledge of the ship dynamics by using an adaptable approach. According to (Yang, Pota, Garratt, & Ugrinovskii, 2008), this method suffers from the dependency on available information. (Ra & Whang, 2006) made use of a robust least squares frequency estimator to predict in the rolling motion of a ship; applying this estimator in combination with a Kalman filter based long term predictor enabled them to predict non-stationary ship rolling motion in real-time. The vertical motions of a floating platform are predicted using a Kalman filter approach for autonomous landing of a quadcopter UAV in the MSc thesis of (Mendes, 2012), thereby showing more recently that the Kalman filter is a practical solution for motion prediction of floating structures.

In 1981, Yumori took a different approach and investigated the Auto Regression Moving Average (ARMA) method to estimate and predict ship heave motions based on the measured motion time series (Yumori, 1981). Regression methods are widely used in the field of econometrics, where time signal prediction has obvious benefits. In 1994 a book on time signal analysis was written by J.D. Hamilton, which provides detailed information on multiple prediction methods, including the Kalman filter and the regression techniques (Hamilton, 1994). In 1998, Broom and Hall extended the ARMA method to incorporate roll and pitch predictions as well, and were able to visualize the predicted motions online (Broome & Hall, 1998). In 2008, Yang et al, used an Auto Regressive model with exogenous input (ARX) in combination with the Bayes Information Criterion which obtains the optimal system order (Yang et al., 2008). (Keke, Nong, & Qing, 2015) Recently noted that an AR model performs well for short-term prediction, but struggles once the prediction horizon is extended to 10 seconds; the alternative they present is an ARMAX model that requires wave input, which is not an option for the application by Ampyx.

Recently a shift is visible in literature towards using machine-learning methods for ship motion prediction. (Lainiotis & Plataniotis, 1993) Showed that even with minimal information on the system dynamics a neural network can perform well. This is beneficial compared to the Kalman filter method, which requires a good match between the actual dynamics and the model. Some of the proposed machine-learning methods require significant computational capabilities, which makes them ill-suited for the application. Examples are the Minor Component Analysis (Zhao, Xu, & Kwan, 2004), but also artificial neural networks that use genetic algorithms as training methods (Khan, Bil, & Marion, 2005). However, (Khan et al., 2005) also showed that an artificial neural network with a Singular Value Decomposition training method was able to obtain a prediction reliably, accurately and quickly; ship motions could be predicted up to 7 seconds in advance in rough seas (sea state 5; 2.5-4m wave height) while requiring less than 0.1 seconds of CPU time. Another promising method is the grey sequential extreme learning machine proposed by (Yin, Zou, Xu, & Wang, 2014). (P. M. H. Van der Steen, 2016) Compares regression techniques (AR and ARMA) with a wavelet neural network (WNN) approach for the application of active motion compensation with a steward platform, and notes that WNN's outperform the regression techniques.

There is a possible pitfall in the use of time history data of the motions as the basis for prediction. The motions are likely to be influenced by the tether tension acting on the FP during power production. This load is greatly reduced during the landing phase, which could lead to errors in the motion prediction. The magnitude of the effect caused by tether tension is significant, as experiments at MARIN proved. It will be interesting to see how this can be accounted for in the prediction algorithm. One could think of lower weight factors on motion signals before transitioning the landing approach or only using motions from this transition point onwards.

There is an additional opportunity for the application of airborne wind energy. When a Sea Air Farm (SAF) is commissioned on a commercial scale, approximately 150 FP's will be arranged in an array. Motion data from surrounding FP's could perhaps improve the landing performance. It should be noted that these FP's will be placed several hundreds of meters apart, it is therefore not expected that individual waves can be predicted for adjacent FP's. More likely is that the surrounding FP's can be used for identifying quiescent periods.

Appendices

A. Decay plots (large)

In this section of the appendix large versions of the decays in Figure 21 are included. Please refer to section 2.4.2 for a description of the legend.

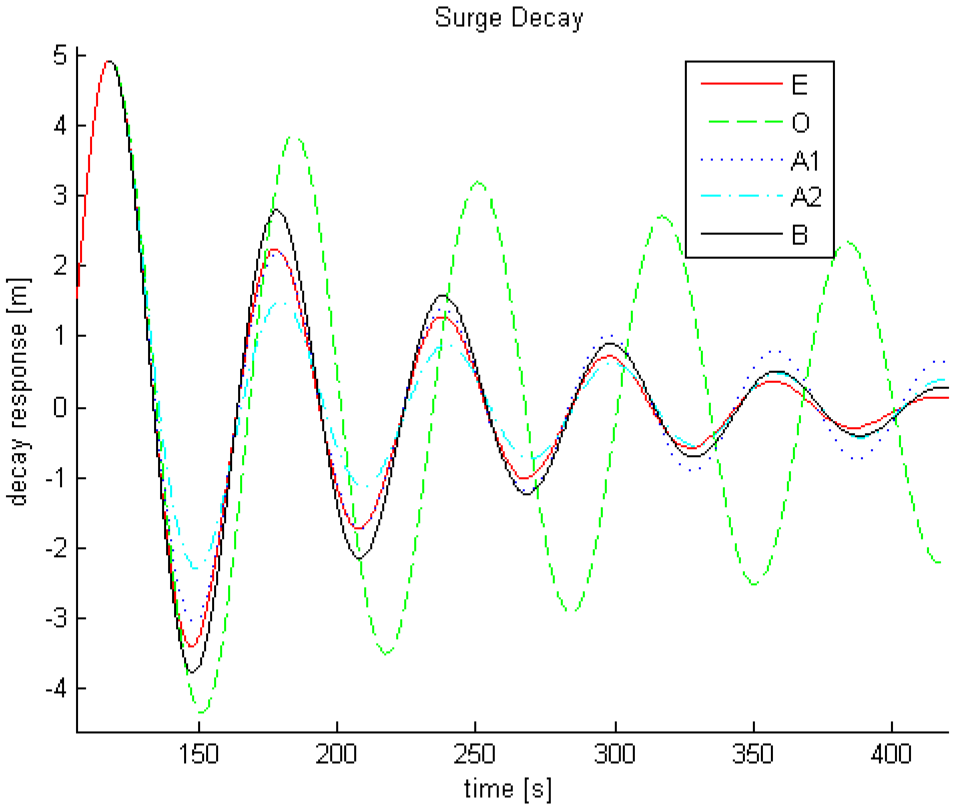

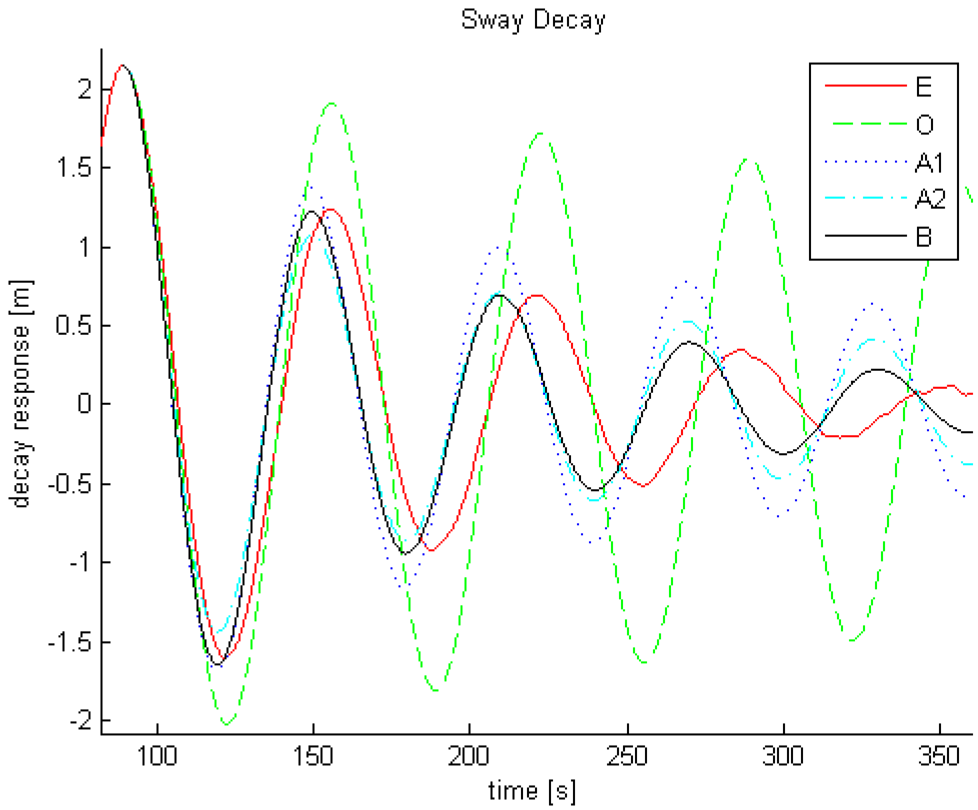

Sway Decay

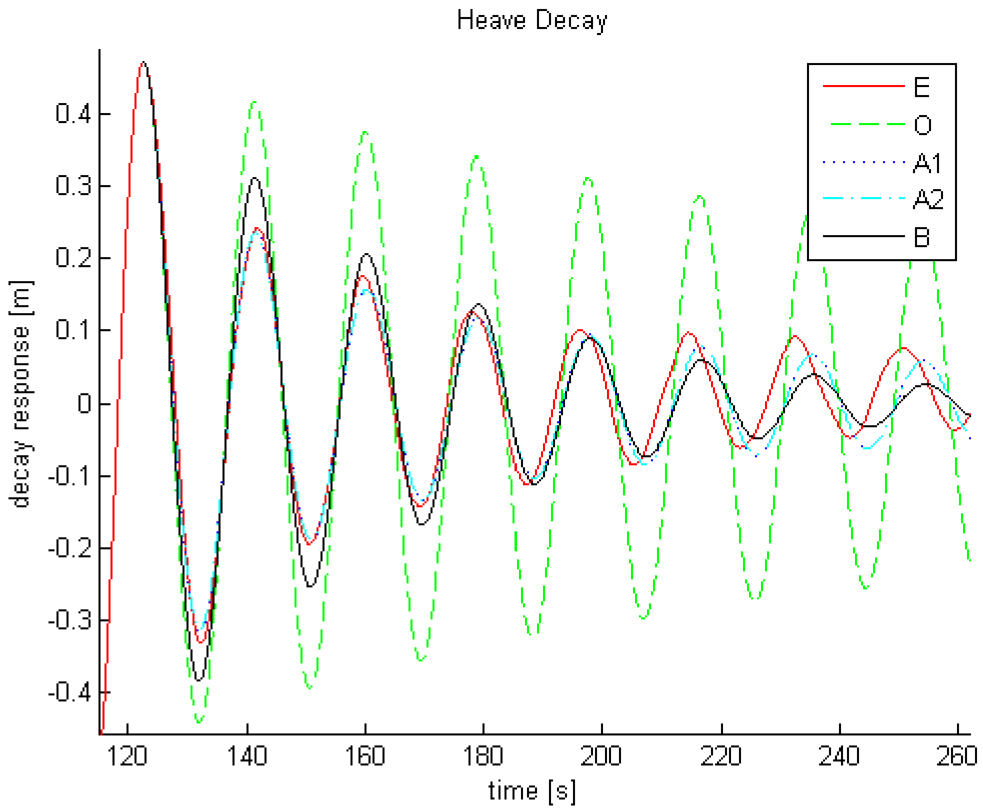

Heave Decay

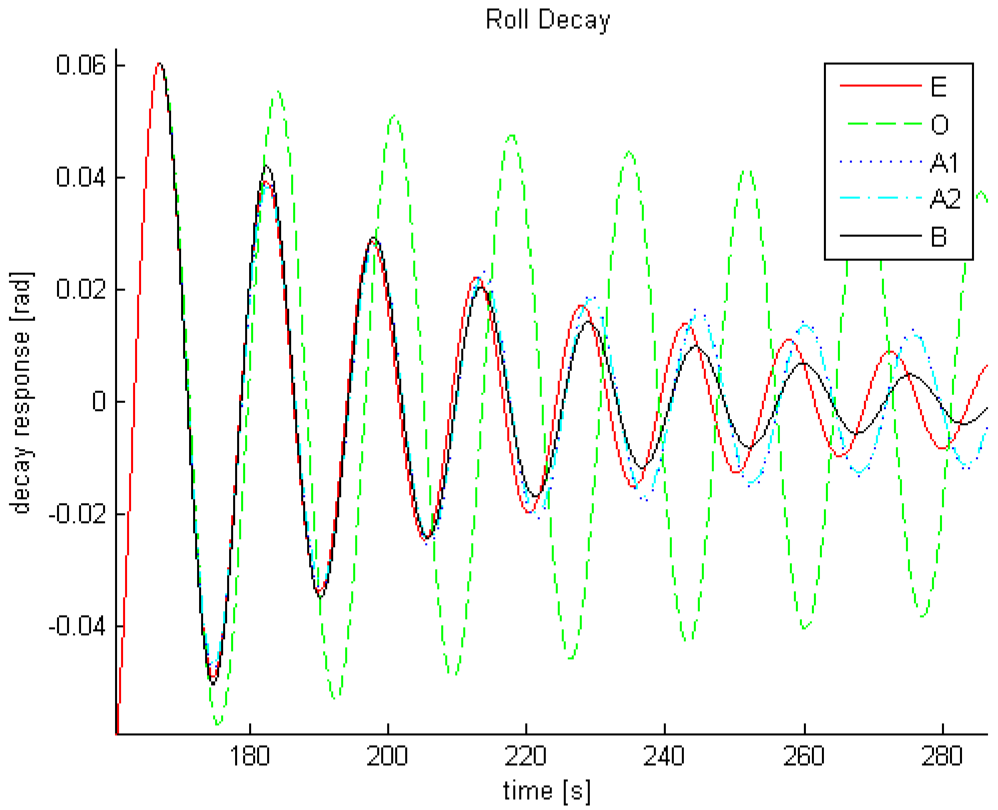
Roll Decay
decay response [rad]
0.06
0.04
0.02
0
-0.02
-0.04
180
200
220
240
260
280
time [s]
E
O
A1
A2
B

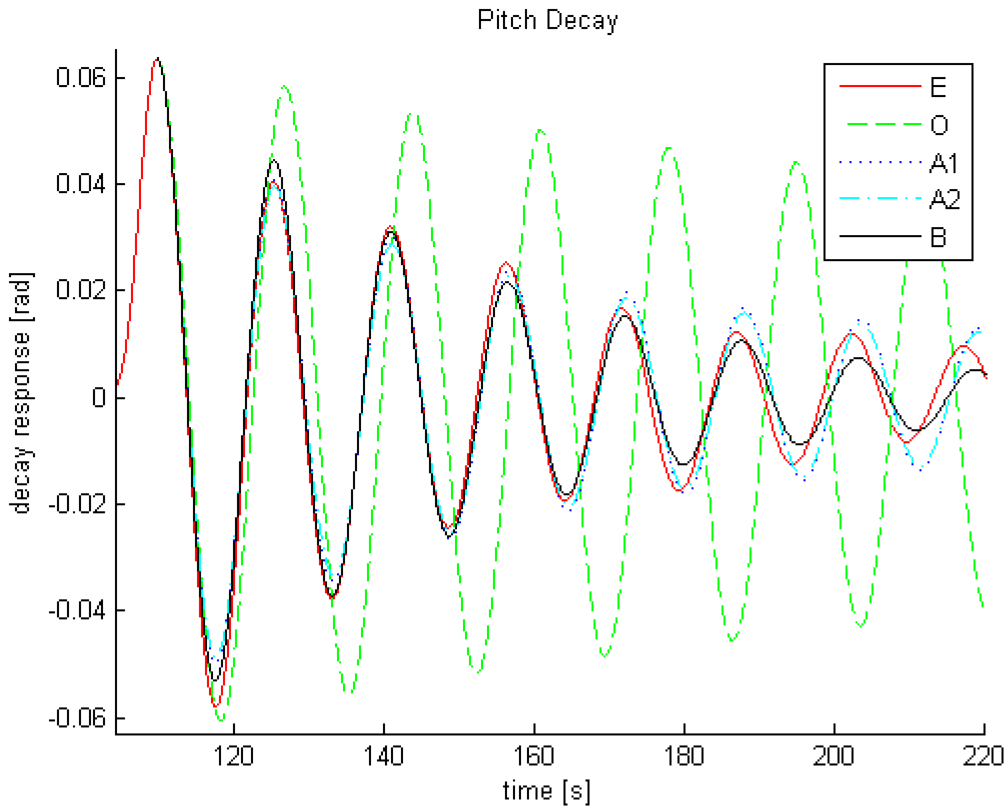
Pitch Decay
decay response [rad]
0.06
0.04
0.02
0
-0.02
-0.04
-0.06
120
140
160
180
200
220
time [s]
E
O
A1
A2
B

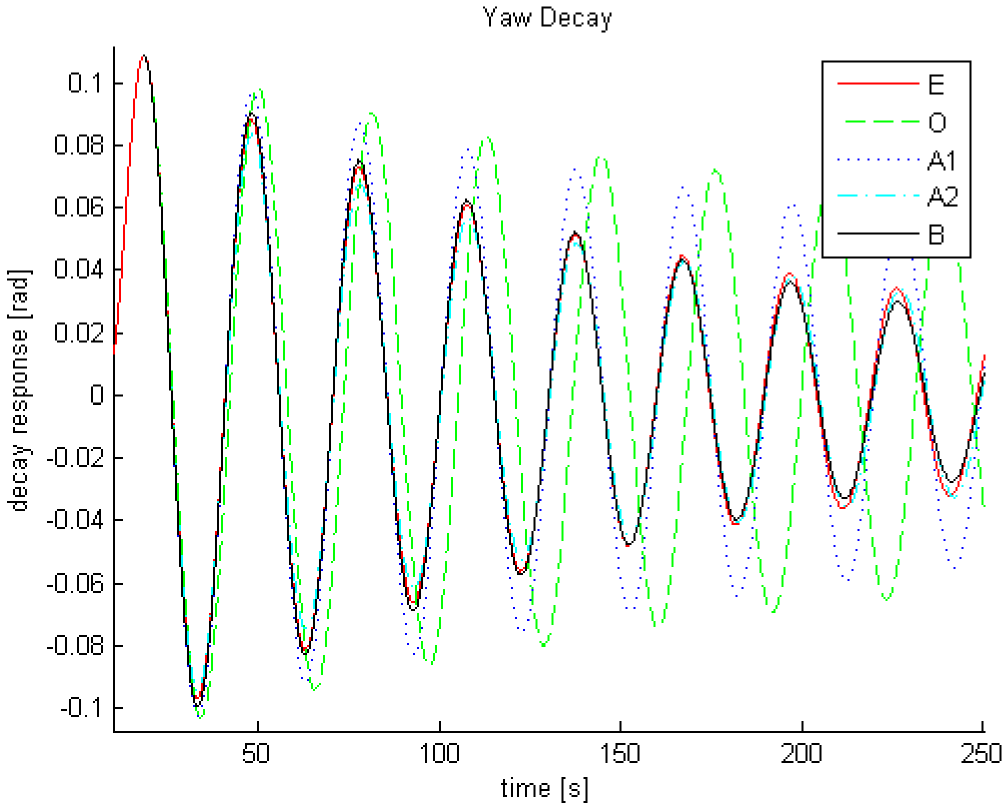
Yaw Decay
decay response [rad]
0.1
0.08
0.06
0.04
0.02
0
-0.02
-0.04
-0.06
-0.08
-0.1
50
100
150
200
250
time [s]
E
O
A1
A2
B

B. RAO amplitudes for wave directions 180 and 210 degrees

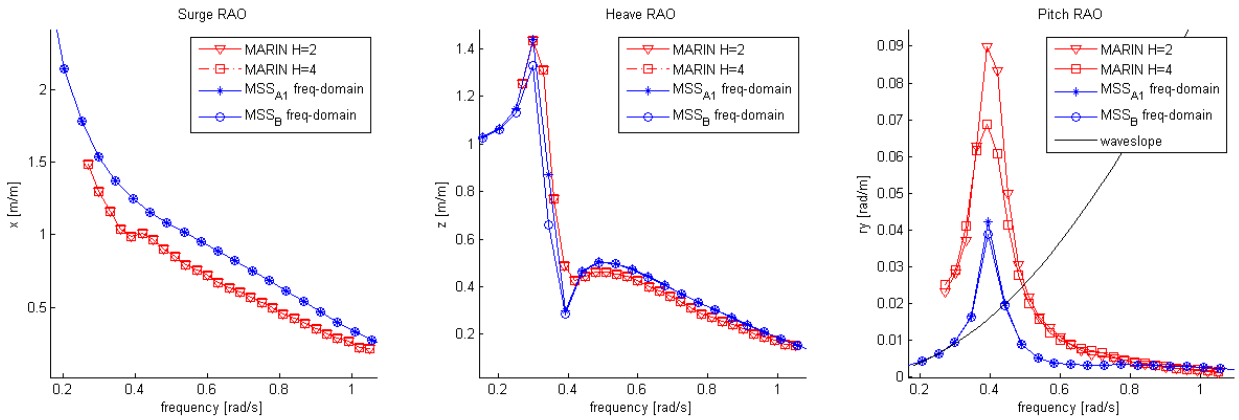

Figure 63, Experimentally (MARIN) and numerically (MSS) determined motion RAO amplitudes for surge, heave and pitch for wave direction=180°

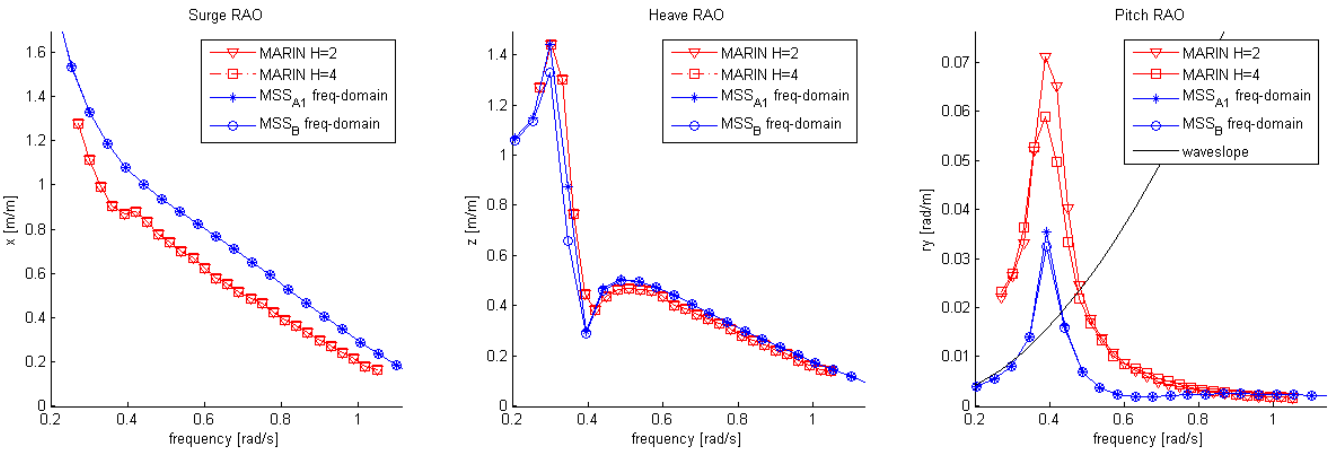

Figure 64, Experimentally (MARIN) and numerically (MSS) determined motion RAO amplitudes for surge, heave and pitch for wave direction=210°

C. Aerodynamic coefficients AP3

Figure 65, Visualization of aerodynamic coefficients (C_X, C_Z, C_M) as a function of elevator deflection (delta) and angle of attack (alpha)

Contact Ampyx Power (info@ampyxpower.com) for disclosure of this data

D. Mean and Standard deviation results (complete)

In this section of the appendix the mean and standard deviation results of relative horizontal speed, relative height and relative pitch angle are shown. No captions have been included, as the figure titles, axis labels and legends should provide sufficient information.

CASE 1

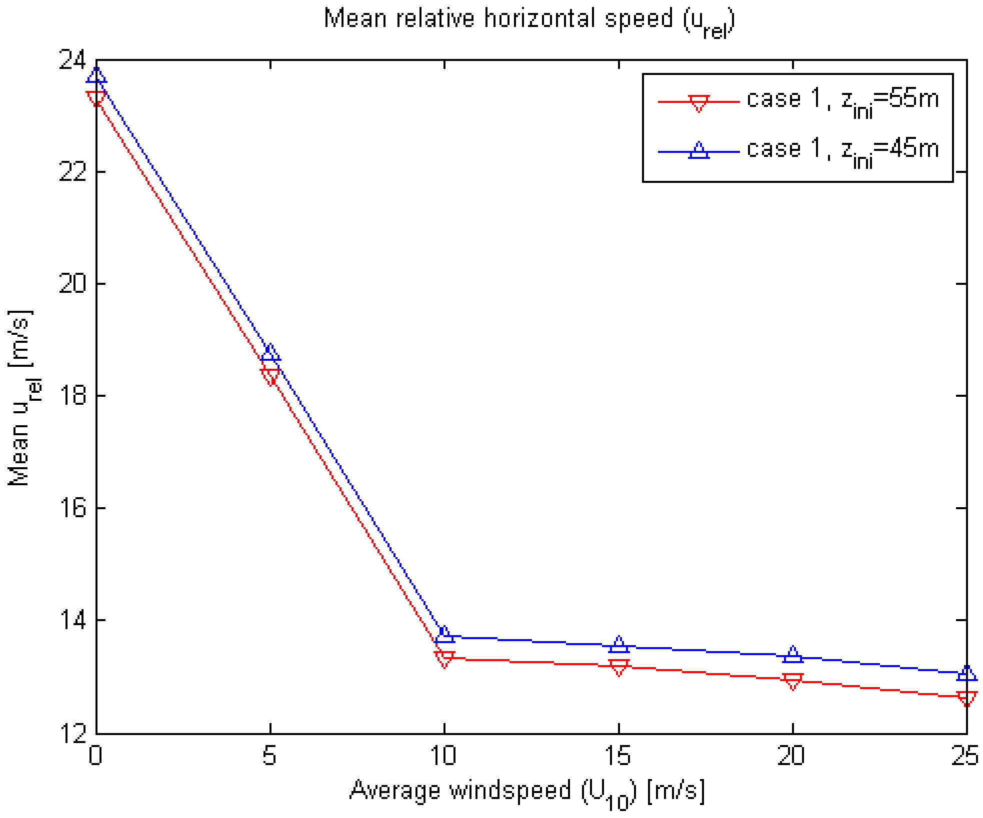

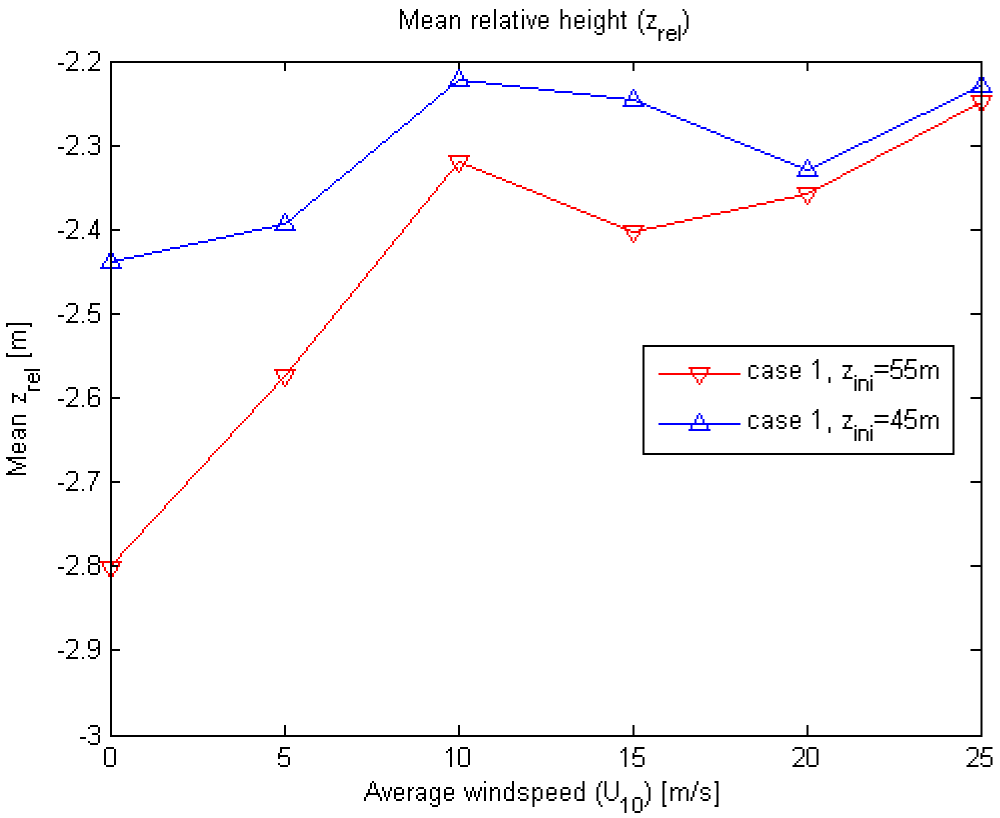
Mean relative height (z_{rel})
Mean z_{rel} [m]
-2.2
-2.3
-2.4
-2.5
-2.6
-2.7
-2.8
-2.9
-3
0
5
10
15
20
25
Average windspeed (U_{10}) [m/s]
case 1, z_{ini}=55m
case 1, z_{ini}=45m

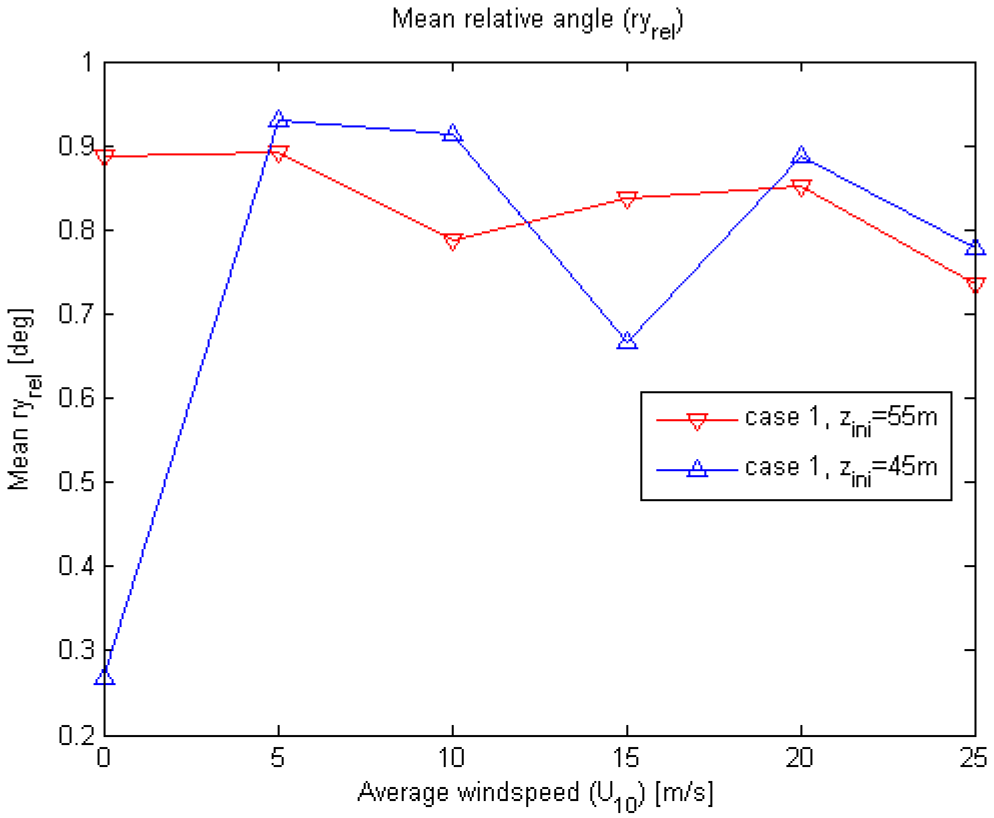
Mean relative angle (ry_{rel})
Mean ry_{rel} [deg]
1
0.9
0.8
0.7
0.6
0.5
0.4
0.3
0.2
0
5
10
15
20
25
Average windspeed (U_{10}) [m/s]
case 1, z_{ini}=55m
case 1, z_{ini}=45m

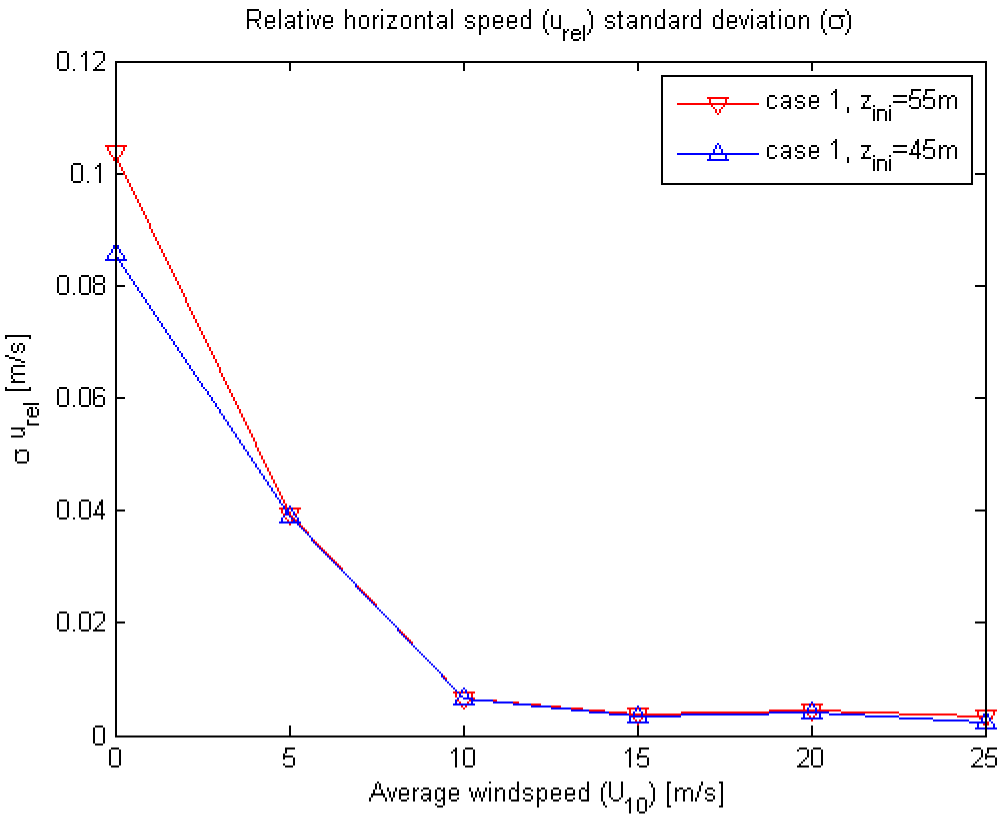
Relative horizontal speed (u_{rel}) standard deviation (σ)
σ u_{rel} [m/s]
Average windspeed (U_{10}) [m/s]
case 1, z_{ini}=55m
case 1, z_{ini}=45m
0.12
0.1
0.08
0.06
0.04
0.02
0
0
5
10
15
20
25

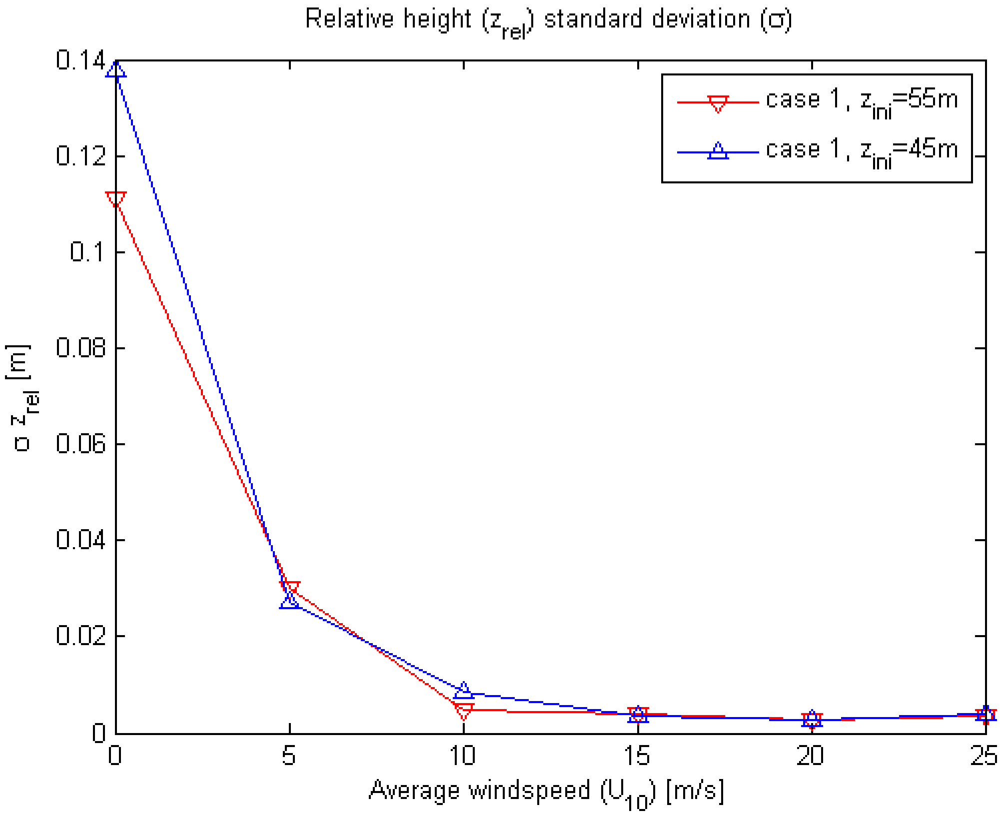
Relative height (z_{rel}) standard deviation (σ)
σ z_{rel} [m]
Average windspeed (U_{10}) [m/s]
case 1, z_{ini}=55m
case 1, z_{ini}=45m
0.14
0.12
0.1
0.08
0.06
0.04
0.02
0
0
5
10
15
20
25

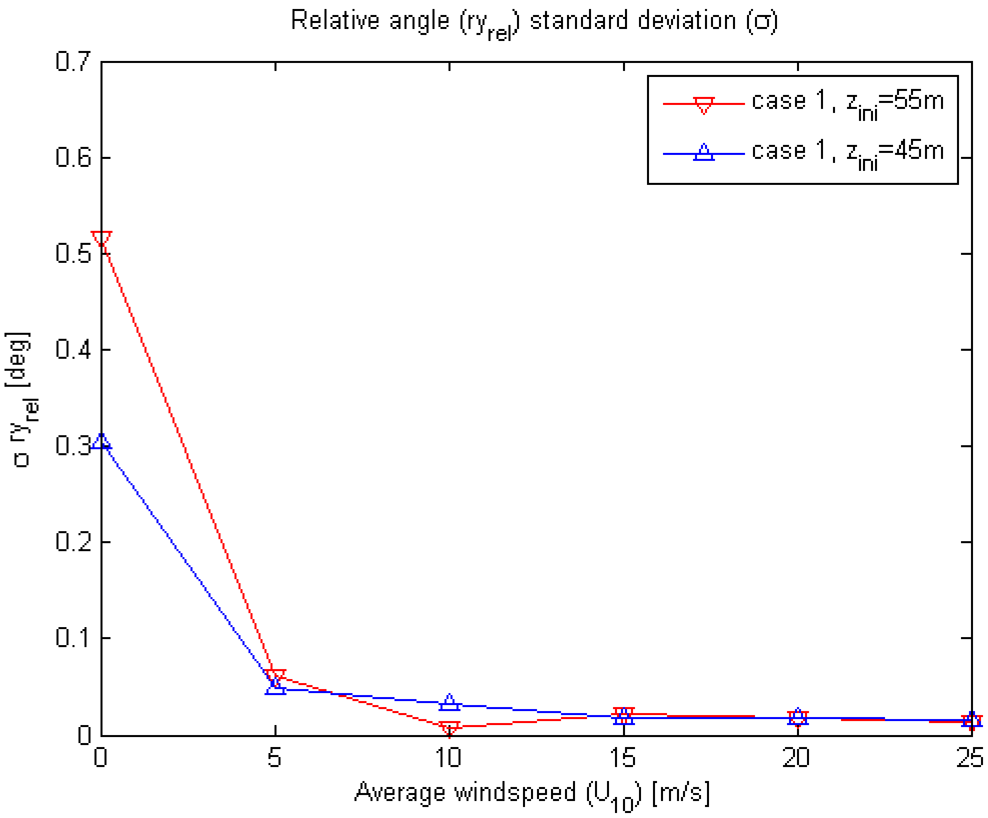
Relative angle (ry_{rel}) standard deviation (σ)
case 1, z_{ini}=55m
case 1, z_{ini}=45m
σ ry_{rel} [deg]
0.7
0.6
0.5
0.4
0.3
0.2
0.1
0
0
5
10
15
20
25
Average windspeed (U_{10}) [m/s]

CASE 2

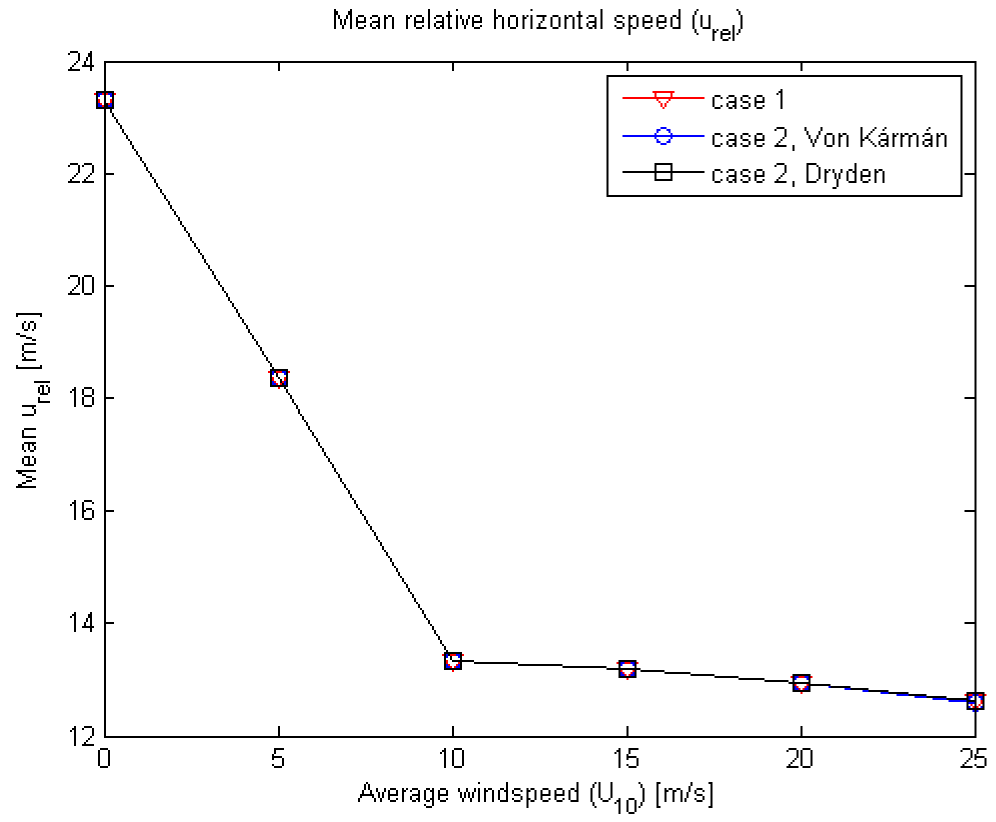
Mean relative horizontal speed (u_{rel})

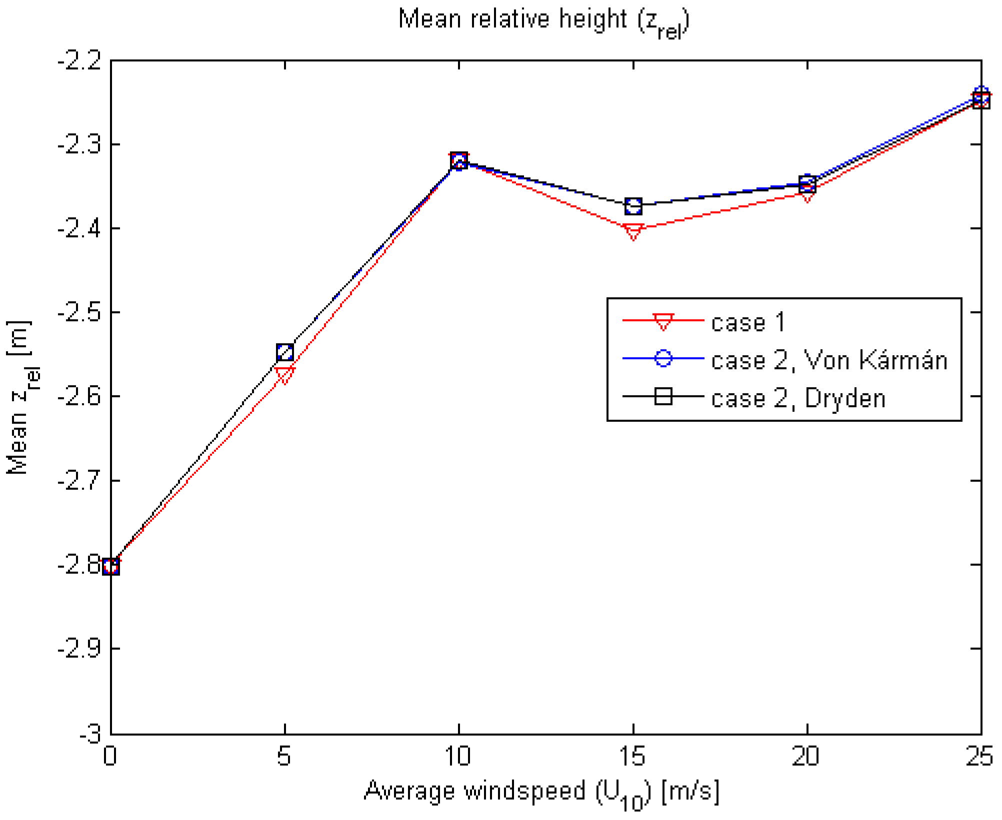
Mean relative height (z_{rel})

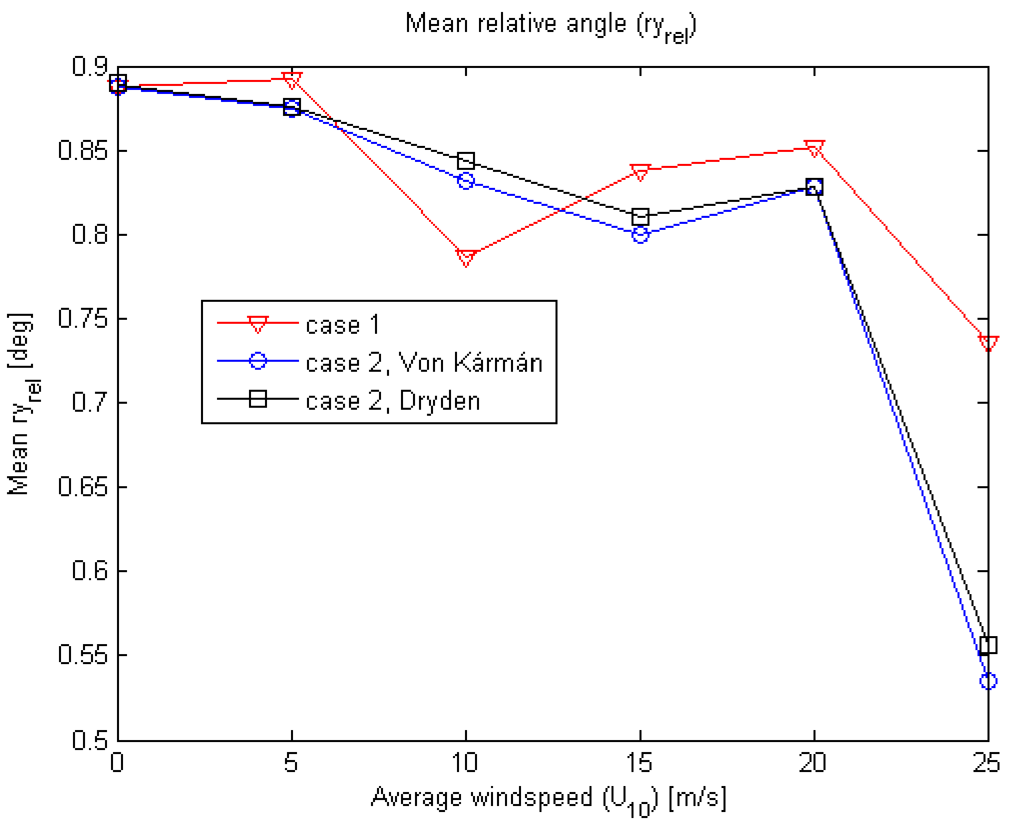
Mean relative angle (ry_{rel})
Mean ry_{rel} [deg]
0.9
0.85
0.8
0.75
0.7
0.65
0.6
0.55
0.5
0
5
10
15
20
25
Average windspeed (U_{10}) [m/s]
case 1
case 2, Von Kármán
case 2, Dryden

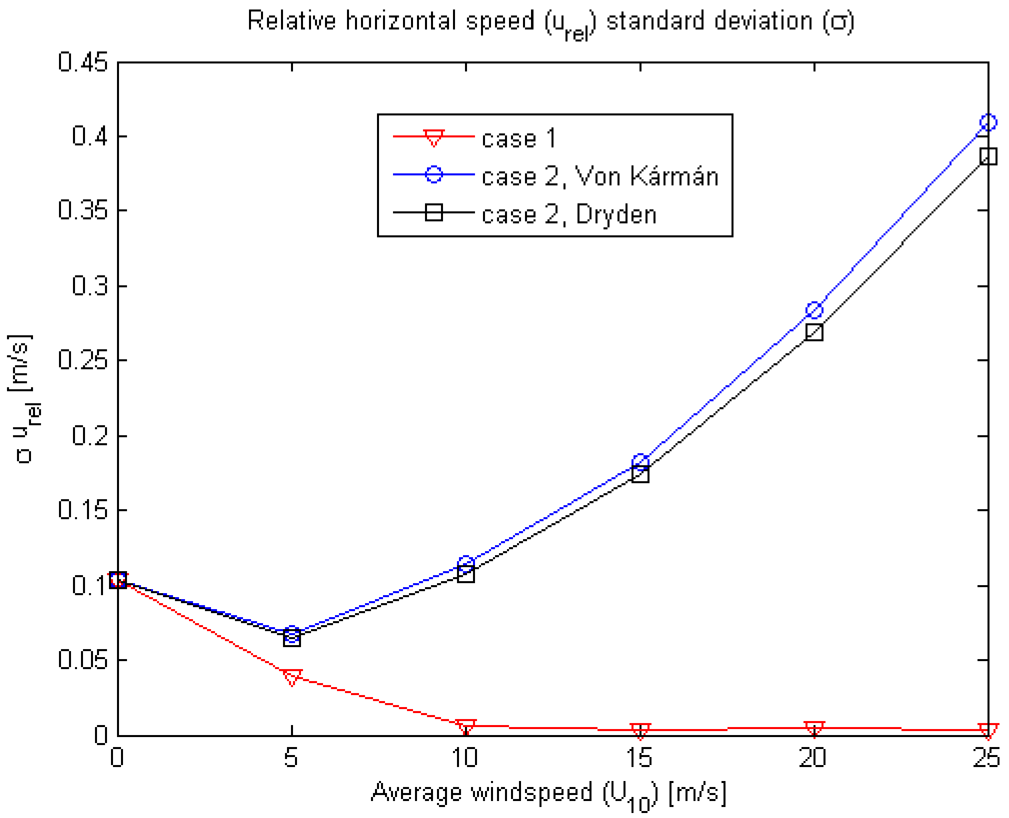
Relative horizontal speed (u_{rel}) standard deviation (σ)
σ u_{rel} [m/s]
0.45
0.4
0.35
0.3
0.25
0.2
0.15
0.1
0.05
0
0
5
10
15
20
25
Average windspeed (U_{10}) [m/s]
case 1
case 2, Von Kármán
case 2, Dryden

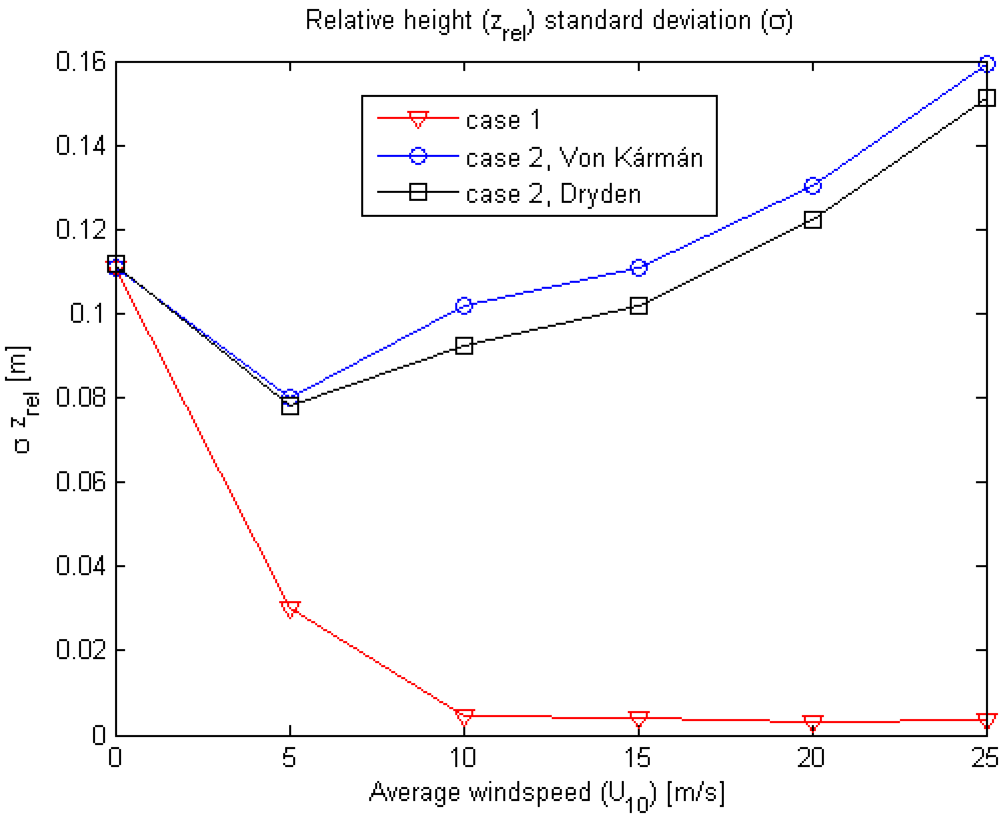
Relative height (z_{rel}) standard deviation (σ)
case 1
case 2, Von Kármán
case 2, Dryden
σ z_{rel} [m]
0.16
0.14
0.12
0.1
0.08
0.06
0.04
0.02
0
0
5
10
15
20
25
Average windspeed (U_{10}) [m/s]

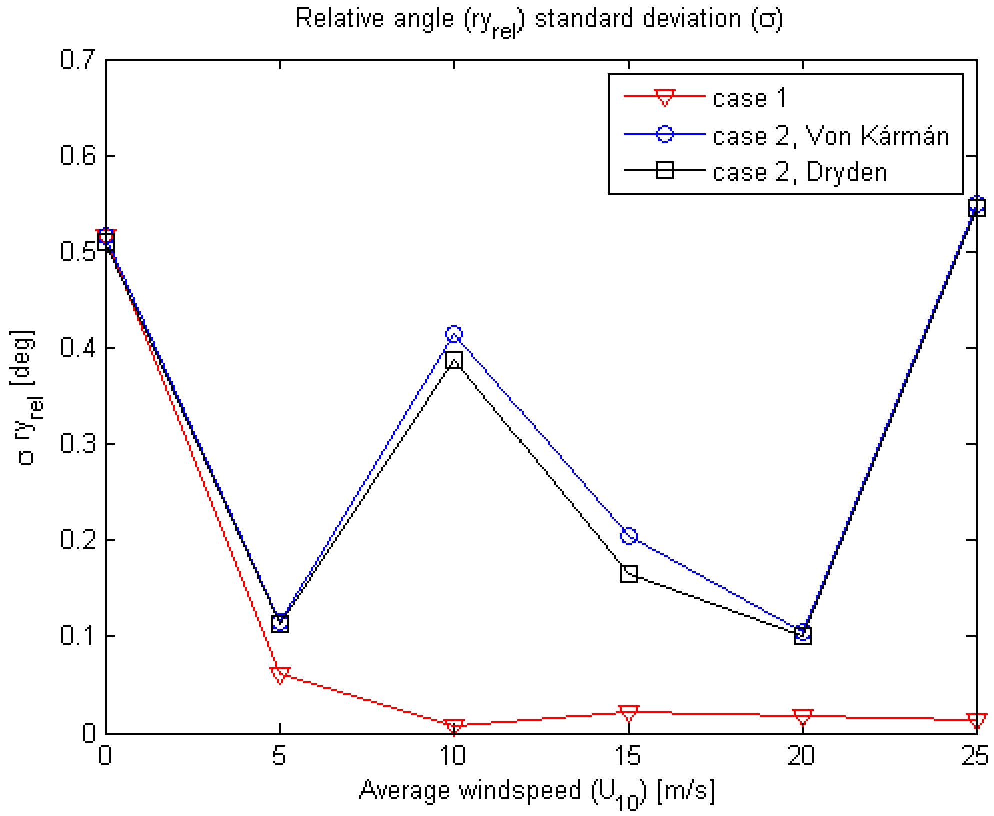
Relative angle (ry_{rel}) standard deviation (σ)
case 1
case 2, Von Kármán
case 2, Dryden
σ ry_{rel} [deg]
0.7
0.6
0.5
0.4
0.3
0.2
0.1
0
0
5
10
15
20
25
Average windspeed (U_{10}) [m/s]

CASE 3

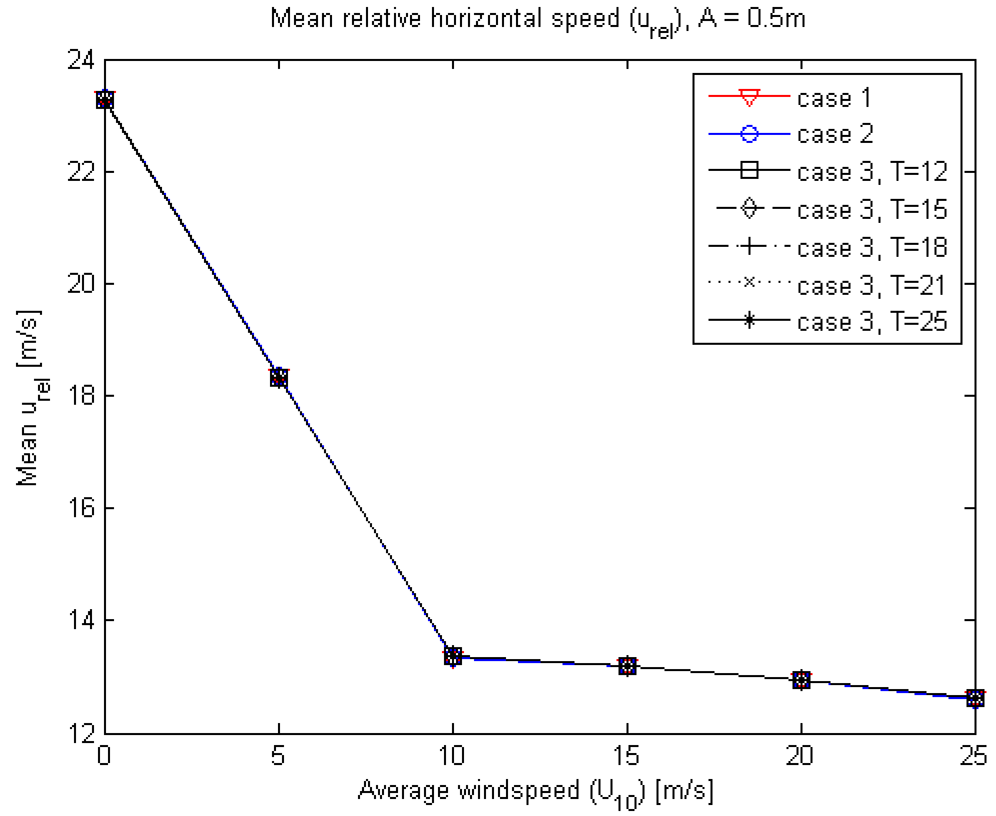
Mean relative horizontal speed (u_{rel}), A = 0.5m
Mean u_{rel} [m/s]
Average windspeed (U_{10}) [m/s]
24
22
20
18
16
14
12
0
5
10
15
20
25
case 1
case 2
case 3, T=12
case 3, T=15
case 3, T=18
case 3, T=21
case 3, T=25

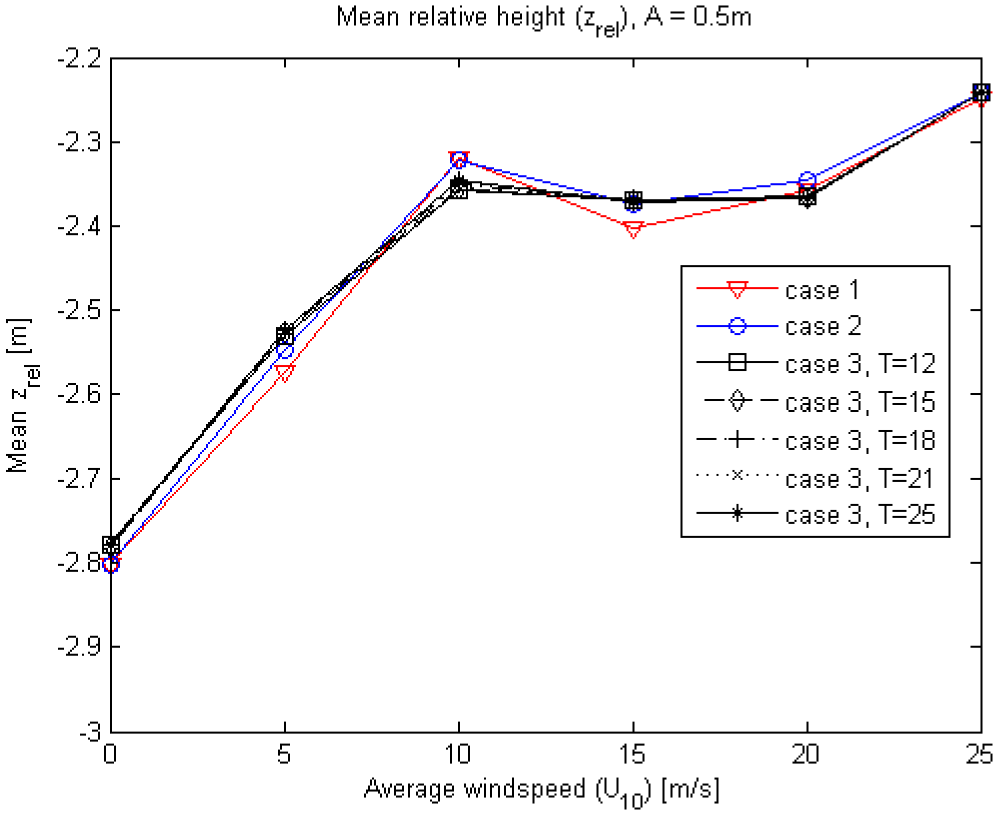
Mean relative height (z_{rel}), A = 0.5m
Mean z_{rel} [m]
Average windspeed (U_{10}) [m/s]
-2.2
-2.3
-2.4
-2.5
-2.6
-2.7
-2.8
-2.9
-3
0
5
10
15
20
25
case 1
case 2
case 3, T=12
case 3, T=15
case 3, T=18
case 3, T=21
case 3, T=25

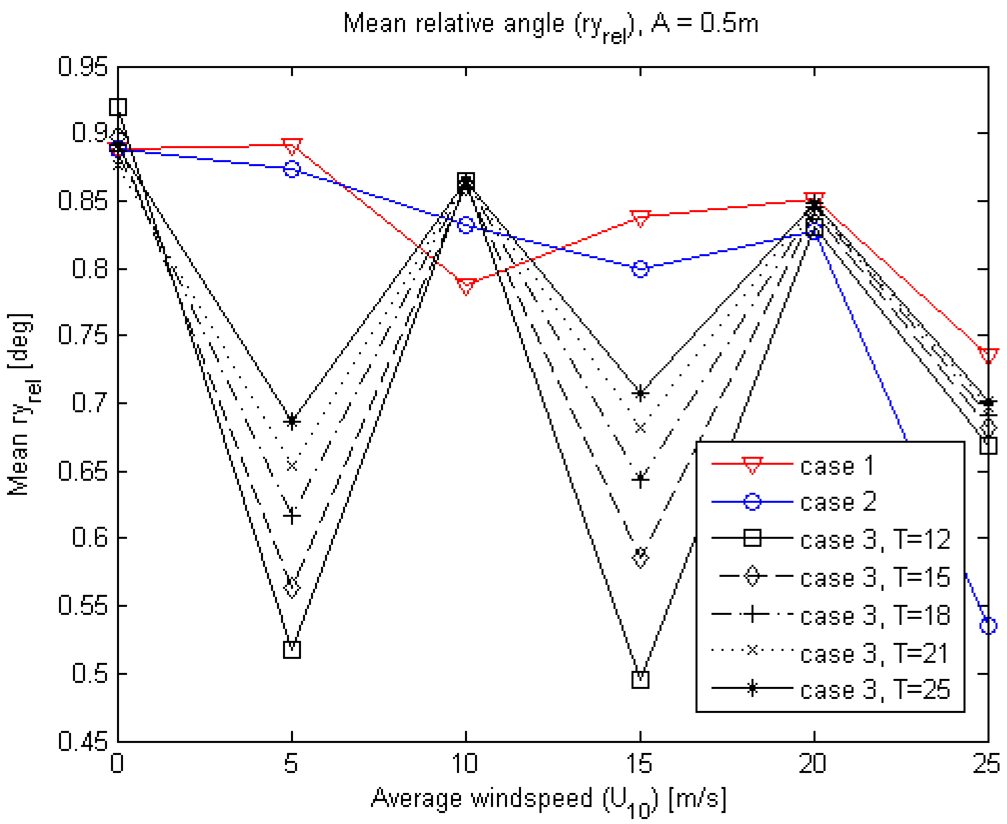
Mean relative angle (ry_{rel}), A = 0.5m
Mean ry_{rel} [deg]
0.95
0.9
0.85
0.8
0.75
0.7
0.65
0.6
0.55
0.5
0.45
0
5
10
15
20
25
Average windspeed (U_{10}) [m/s]
case 1
case 2
case 3, T=12
case 3, T=15
case 3, T=18
case 3, T=21
case 3, T=25

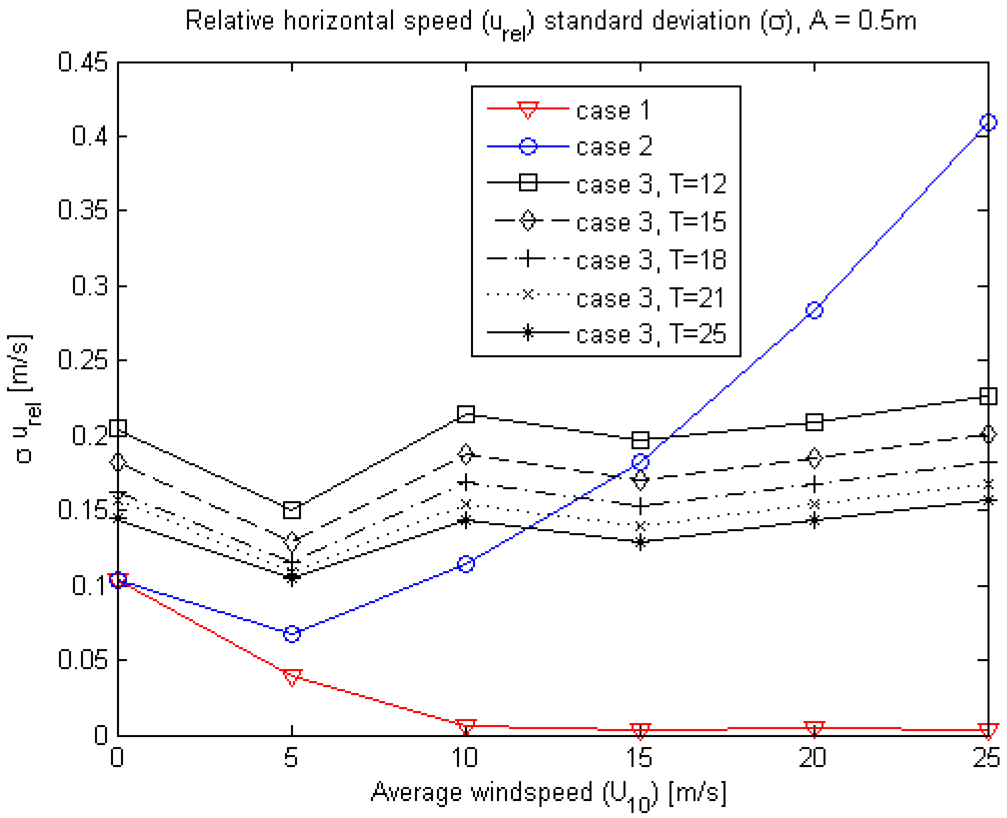
Relative horizontal speed (u_{rel}) standard deviation (σ), A = 0.5m
σ u_{rel} [m/s]
0.45
0.4
0.35
0.3
0.25
0.2
0.15
0.1
0.05
0
0
5
10
15
20
25
Average windspeed (U_{10}) [m/s]
case 1
case 2
case 3, T=12
case 3, T=15
case 3, T=18
case 3, T=21
case 3, T=25

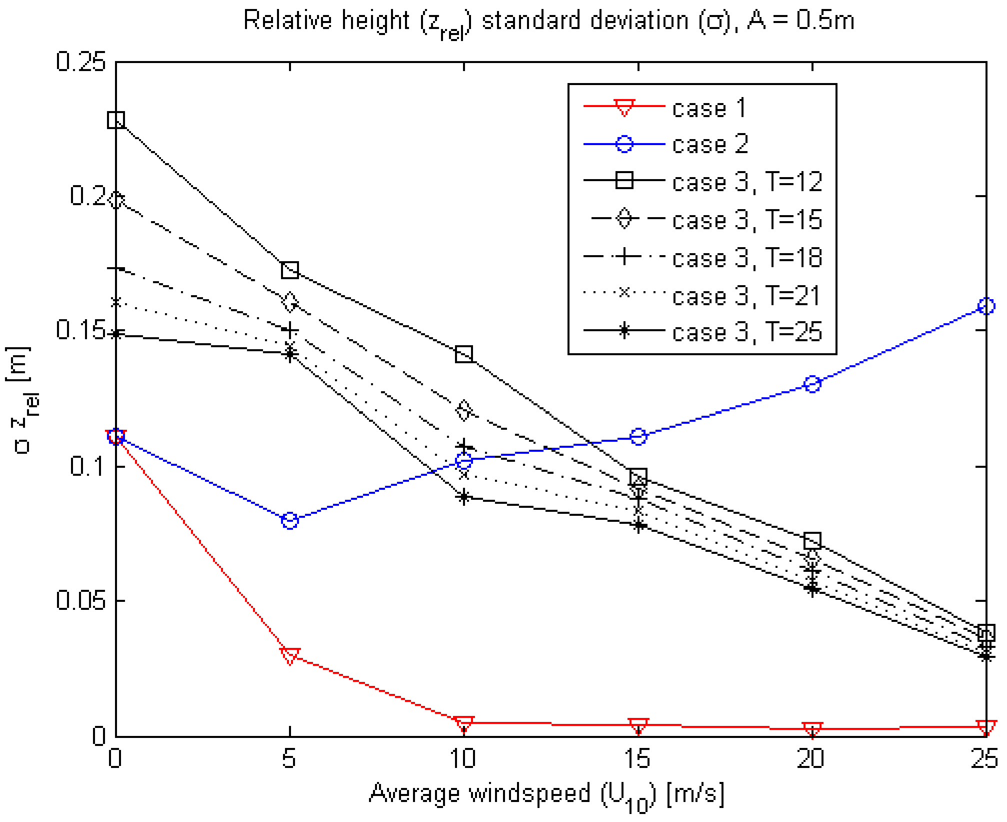
Relative height (z_{rel}) standard deviation (σ), A = 0.5m
σ z_{rel} [m]
0.25
0.2
0.15
0.1
0.05
0
0
5
10
15
20
25
Average windspeed (U_{10}) [m/s]
case 1
case 2
case 3, T=12
case 3, T=15
case 3, T=18
case 3, T=21
case 3, T=25

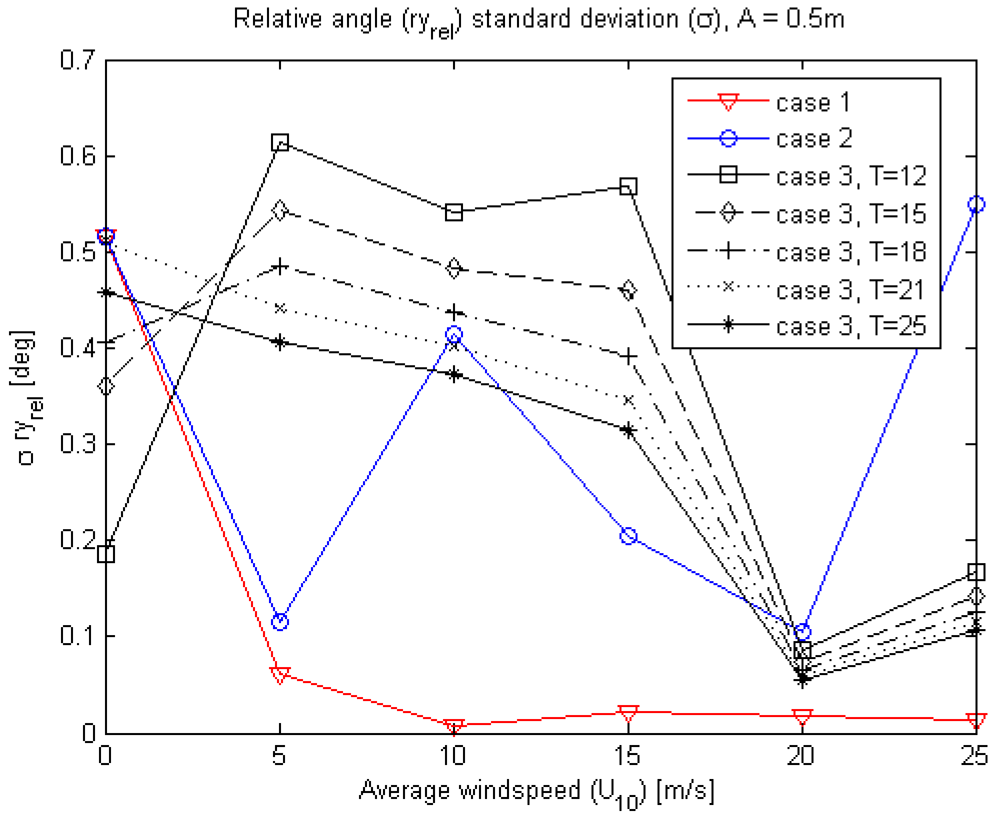
Relative angle (ry_{rel}) standard deviation (σ), A = 0.5m
σ ry_{rel} [deg]
0.7
0.6
0.5
0.4
0.3
0.2
0.1
0
0
5
10
15
20
25
Average windspeed (U_{10}) [m/s]
case 1
case 2
case 3, T=12
case 3, T=15
case 3, T=18
case 3, T=21
case 3, T=25

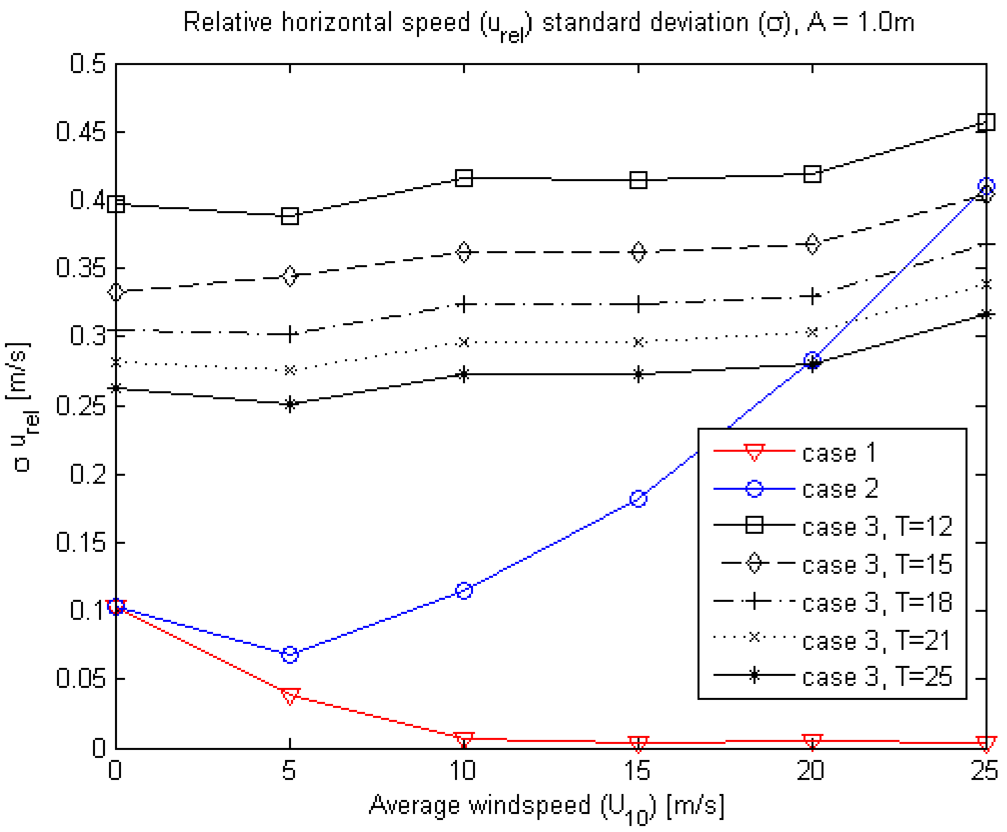
Relative horizontal speed (u_{rel}) standard deviation (σ), A = 1.0m
σ u_{rel} [m/s]
0
0.05
0.1
0.15
0.2
0.25
0.3
0.35
0.4
0.45
0.5
0
5
10
15
20
25
Average windspeed (U_{10}) [m/s]
case 1
case 2
case 3, T=12
case 3, T=15
case 3, T=18
case 3, T=21
case 3, T=25

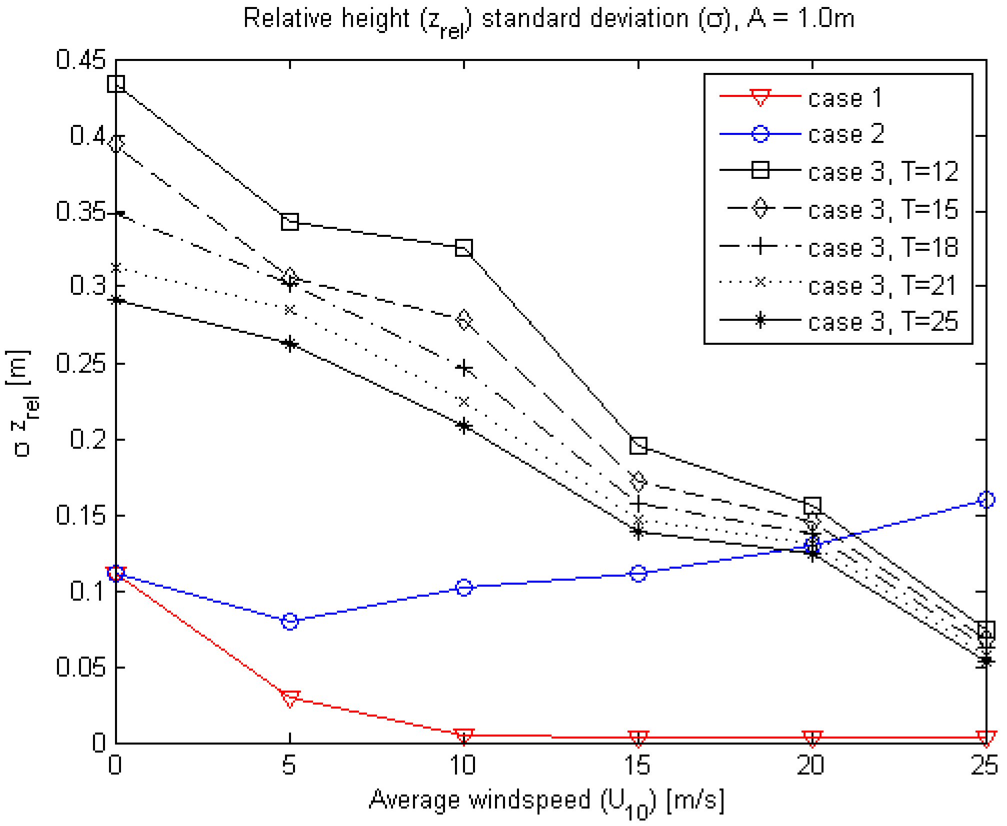
Relative height (z_{rel}) standard deviation (σ), A = 1.0m
σ z_{rel} [m]
0
0.05
0.1
0.15
0.2
0.25
0.3
0.35
0.4
0.45
0
5
10
15
20
25
Average windspeed (U_{10}) [m/s]
case 1
case 2
case 3, T=12
case 3, T=15
case 3, T=18
case 3, T=21
case 3, T=25

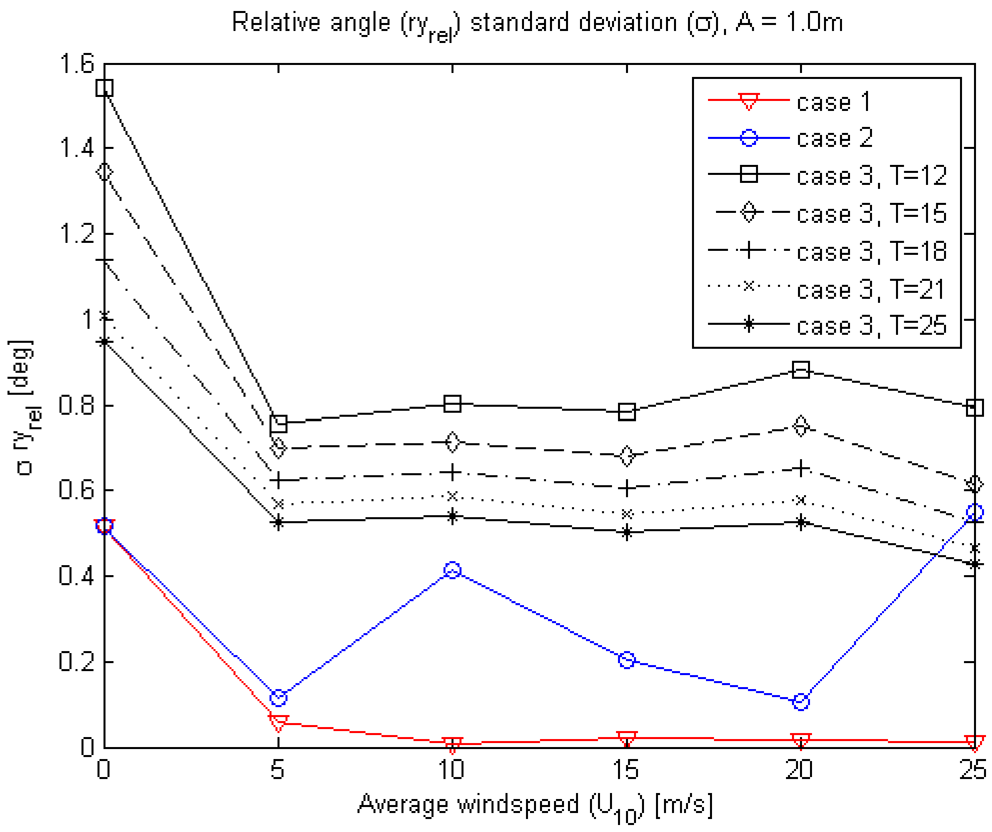
Relative angle (ry_{rel}) standard deviation (σ), A = 1.0m

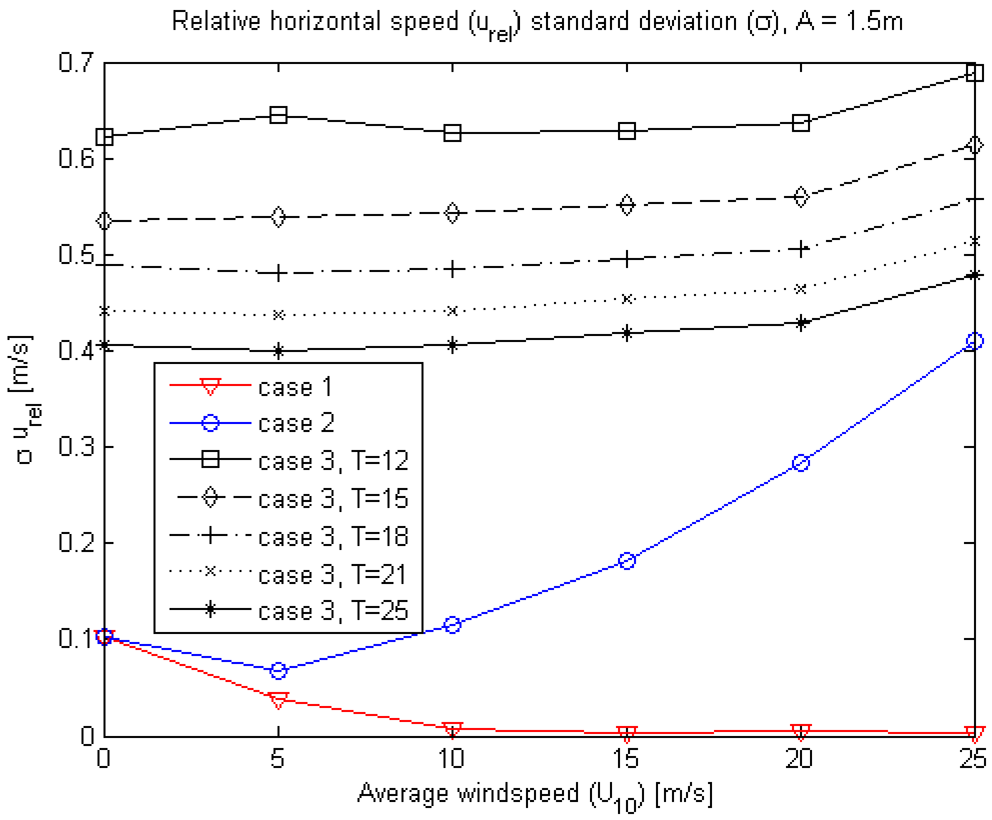
Relative horizontal speed (u_{rel}) standard deviation (σ), A = 1.5m

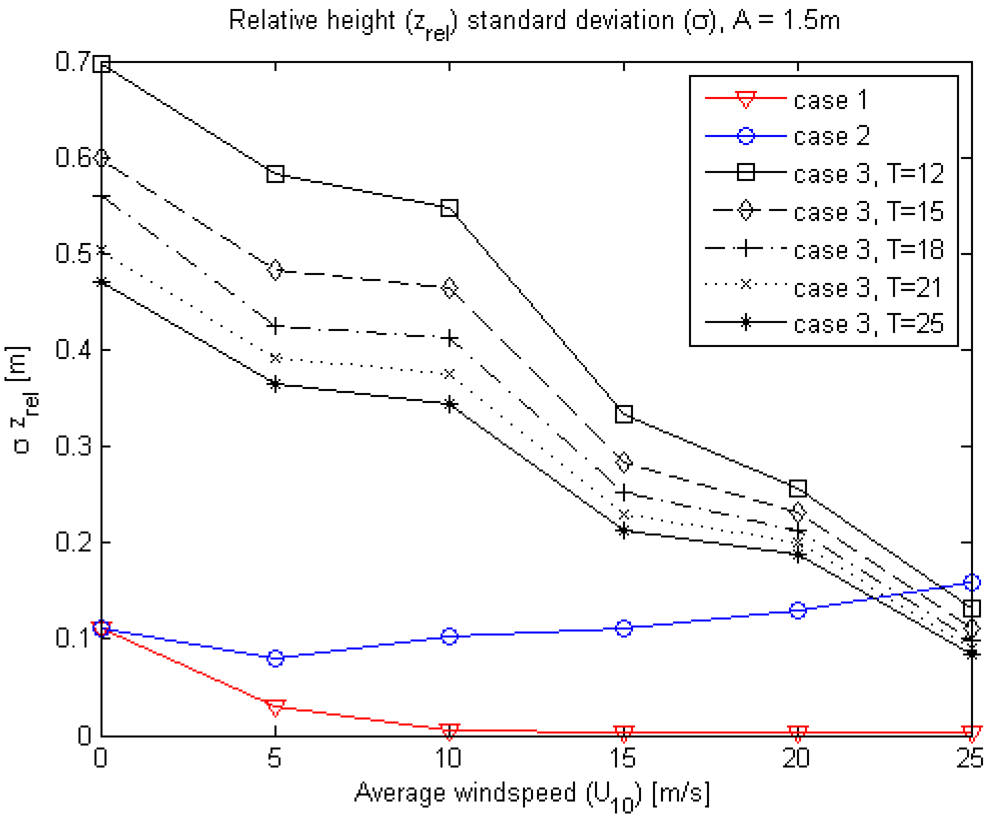
Relative height (z_{rel}) standard deviation (σ), A = 1.5m
σ z_{rel} [m]
0.7
0.6
0.5
0.4
0.3
0.2
0.1
0
0
5
10
15
20
25
Average windspeed (U_{10}) [m/s]
case 1
case 2
case 3, T=12
case 3, T=15
case 3, T=18
case 3, T=21
case 3, T=25

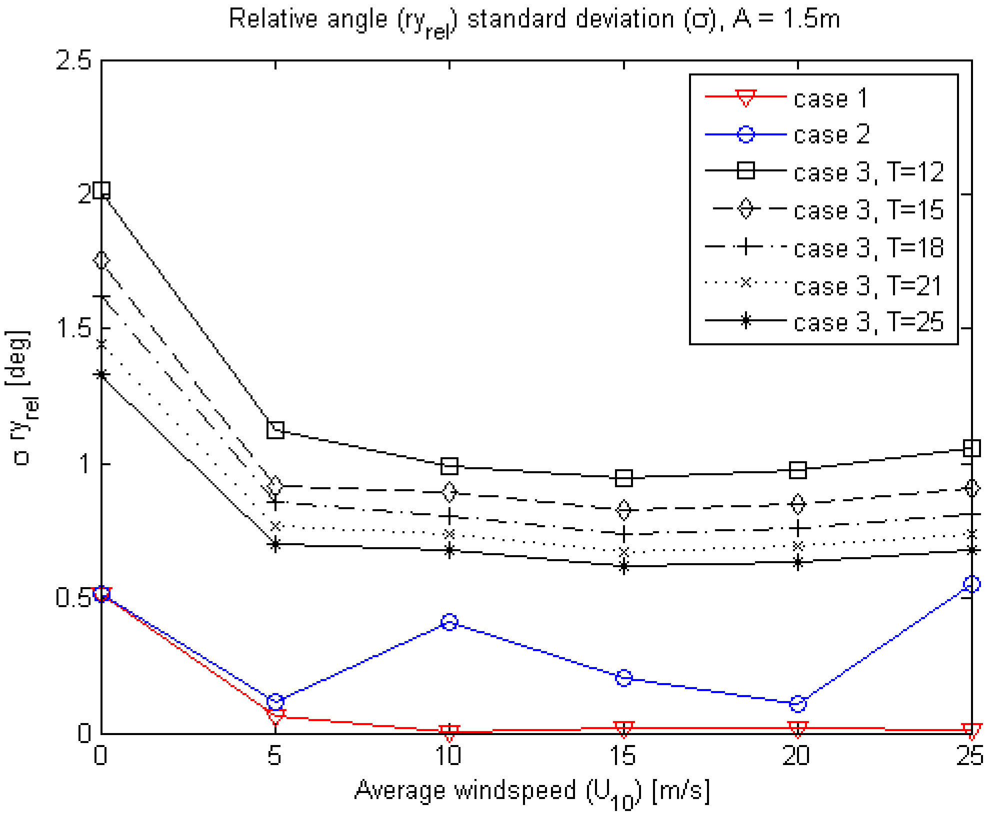
Relative angle (ry_{rel}) standard deviation (σ), A = 1.5m
σ ry_{rel} [deg]
2.5
2
1.5
1
0.5
0
0
5
10
15
20
25
Average windspeed (U_{10}) [m/s]
case 1
case 2
case 3, T=12
case 3, T=15
case 3, T=18
case 3, T=21
case 3, T=25

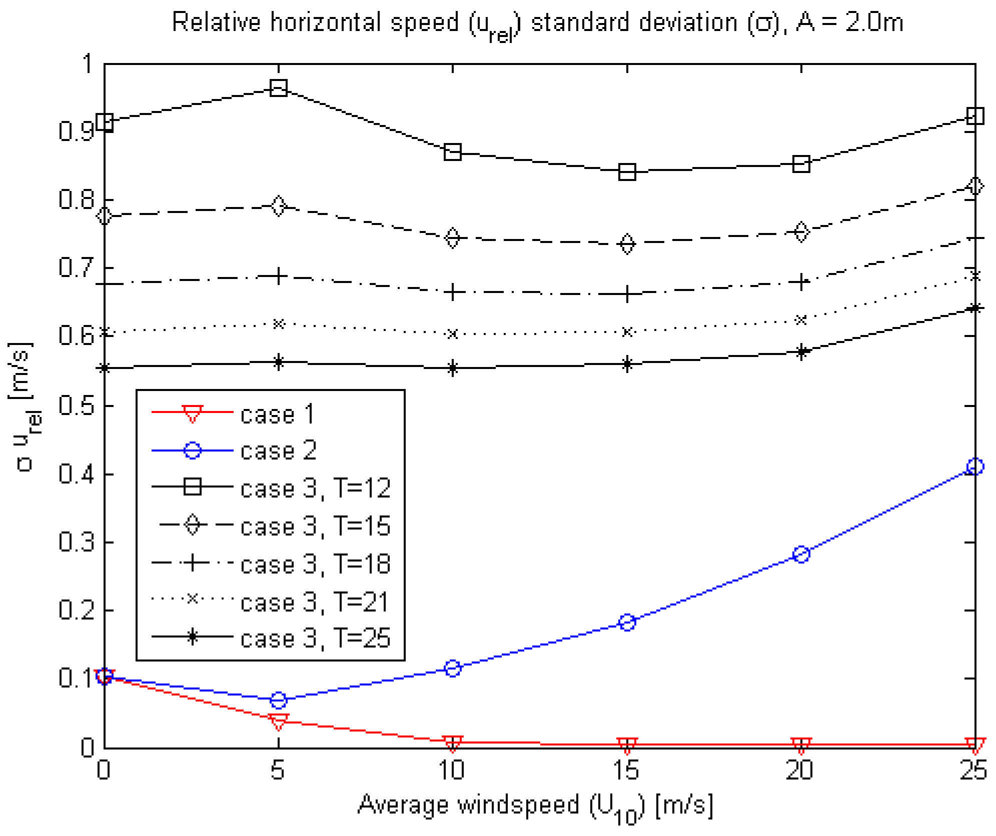
Relative horizontal speed (u_{rel}) standard deviation (σ), A = 2.0m
σ u_{rel} [m/s]
1
0.9
0.8
0.7
0.6
0.5
0.4
0.3
0.2
0.1
0
0
5
10
15
20
25
Average windspeed (U_{10}) [m/s]
case 1
case 2
case 3, T=12
case 3, T=15
case 3, T=18
case 3, T=21
case 3, T=25

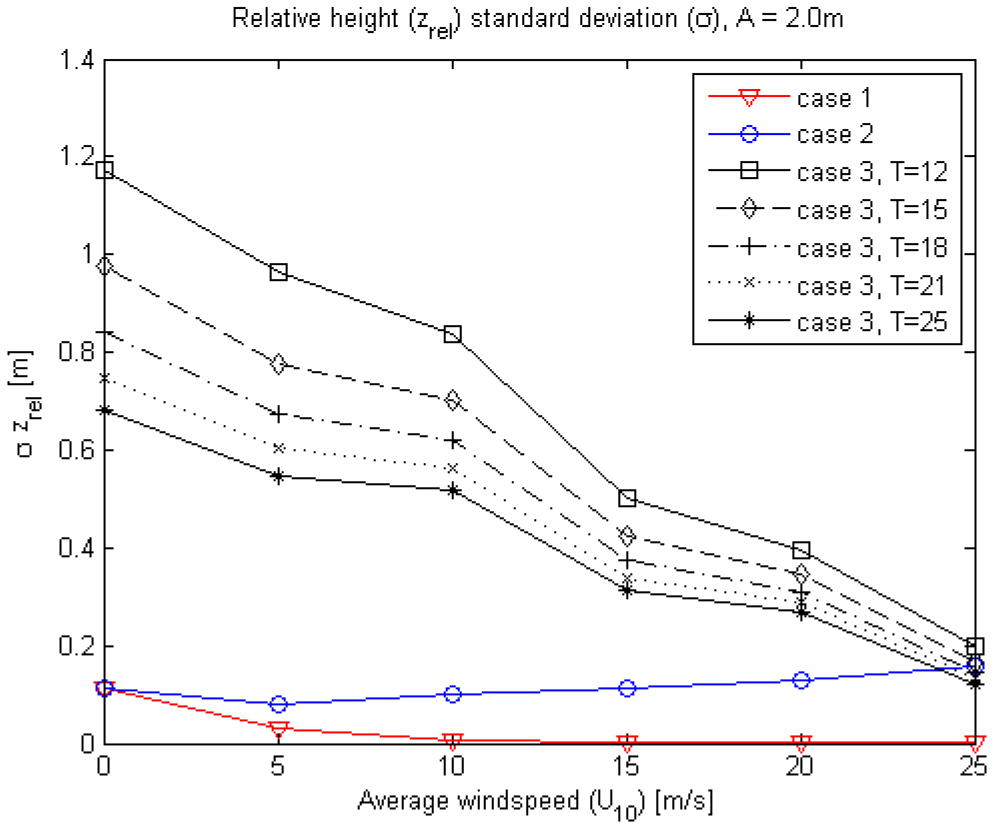
Relative height (z_{rel}) standard deviation (σ), A = 2.0m
σ z_{rel} [m]
1.4
1.2
1
0.8
0.6
0.4
0.2
0
0
5
10
15
20
25
Average windspeed (U_{10}) [m/s]
case 1
case 2
case 3, T=12
case 3, T=15
case 3, T=18
case 3, T=21
case 3, T=25

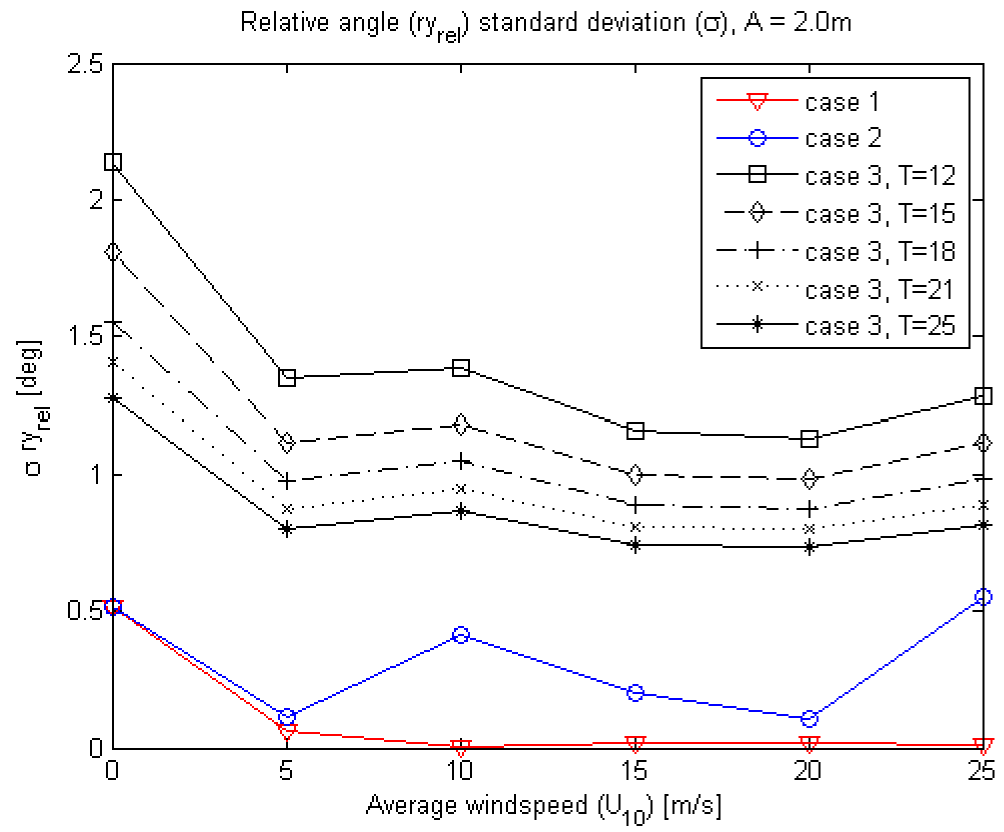
Relative angle (ry_{rel}) standard deviation (σ), A = 2.0m
σ ry_{rel} [deg]
Average windspeed (U_{10}) [m/s]
case 1
case 2
case 3, T=12
case 3, T=15
case 3, T=18
case 3, T=21
case 3, T=25
0
0.5
1
1.5
2
2.5
0
5
10
15
20
25

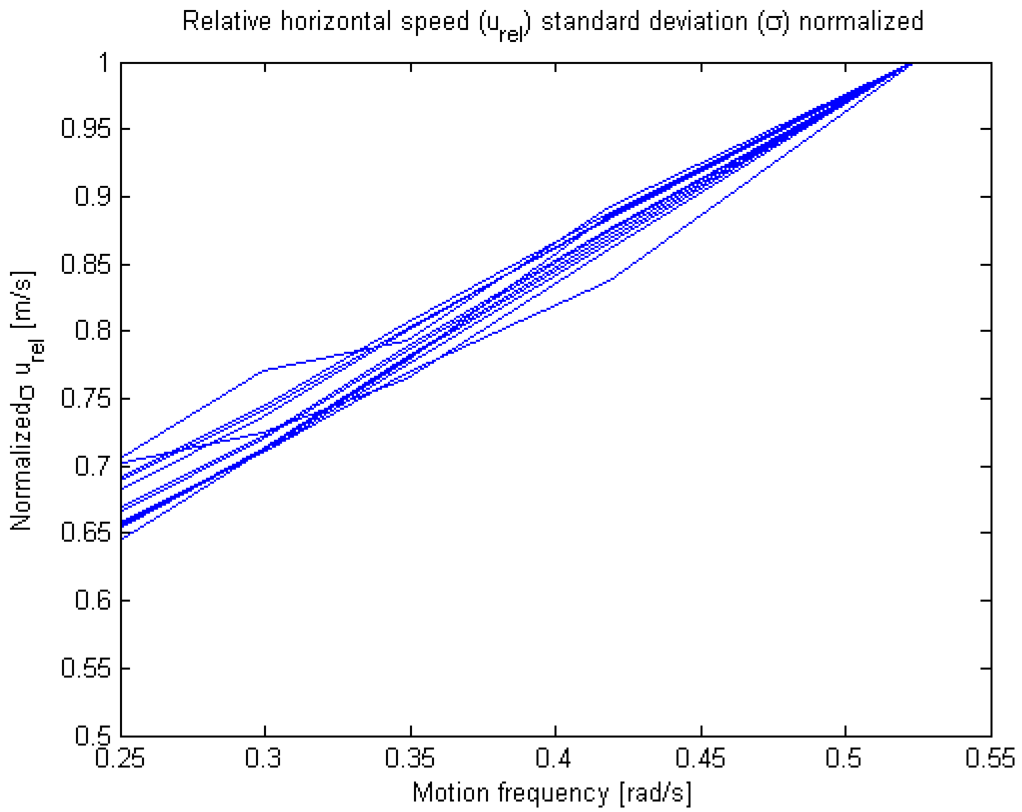
Relative horizontal speed (u_{rel}) standard deviation (σ) normalized
Normalizedσ u_{rel} [m/s]
Motion frequency [rad/s]
0.5
0.55
0.6
0.65
0.7
0.75
0.8
0.85
0.9
0.95
1
0.25
0.3
0.35
0.4
0.45
0.5
0.55

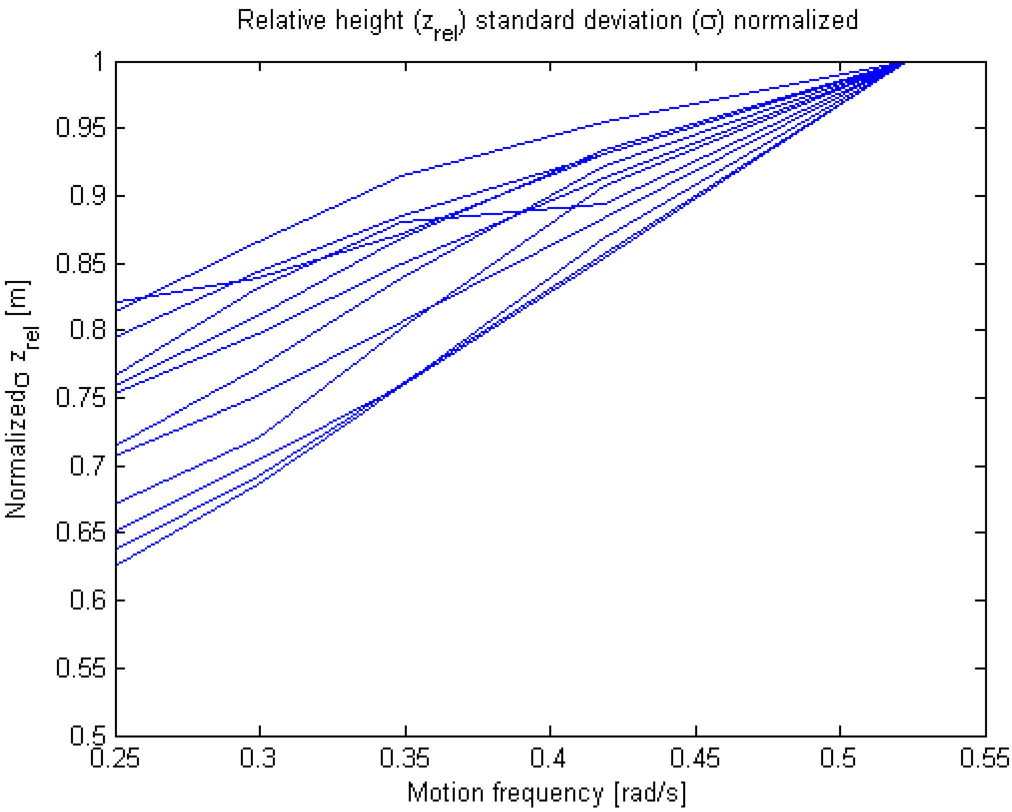
Relative height (z_rel) standard deviation (σ) normalized
Normalizedσ z_rel [m]
Motion frequency [rad/s]
1
0.95
0.9
0.85
0.8
0.75
0.7
0.65
0.6
0.55
0.5
0.25
0.3
0.35
0.4
0.45
0.5
0.55

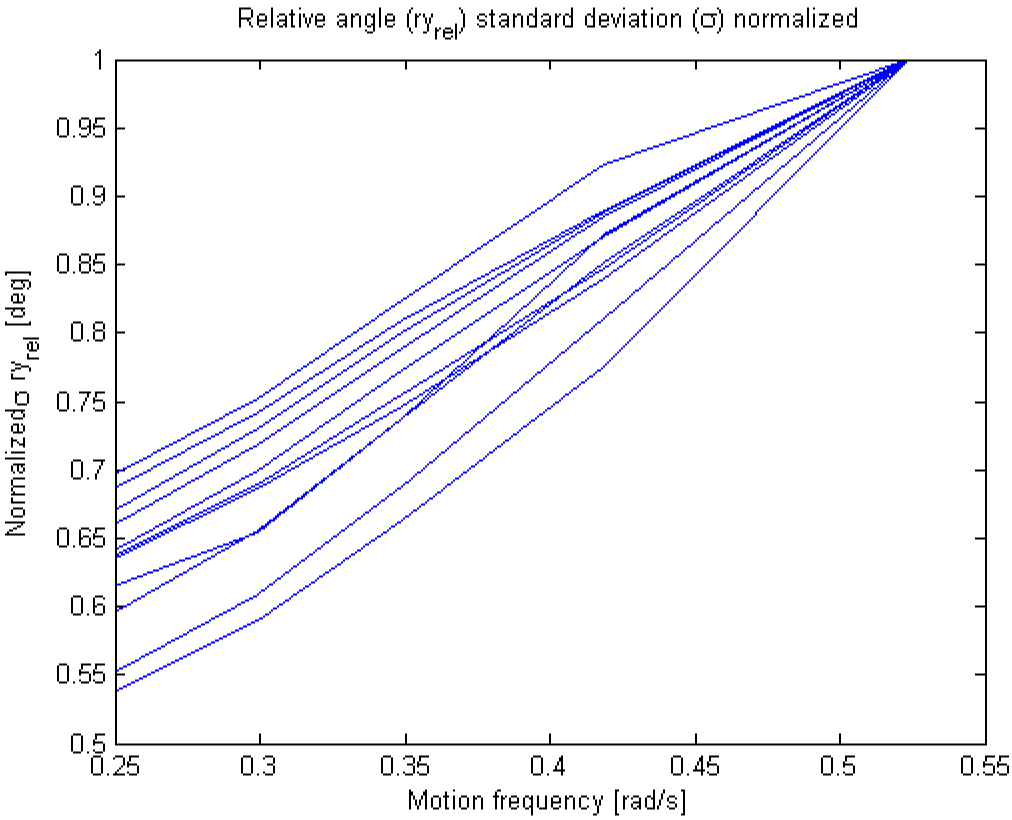
Relative angle (ry_rel) standard deviation (σ) normalized
Normalizedσ ry_rel [deg]
Motion frequency [rad/s]
1
0.95
0.9
0.85
0.8
0.75
0.7
0.65
0.6
0.55
0.5
0.25
0.3
0.35
0.4
0.45
0.5
0.55

CASE 4

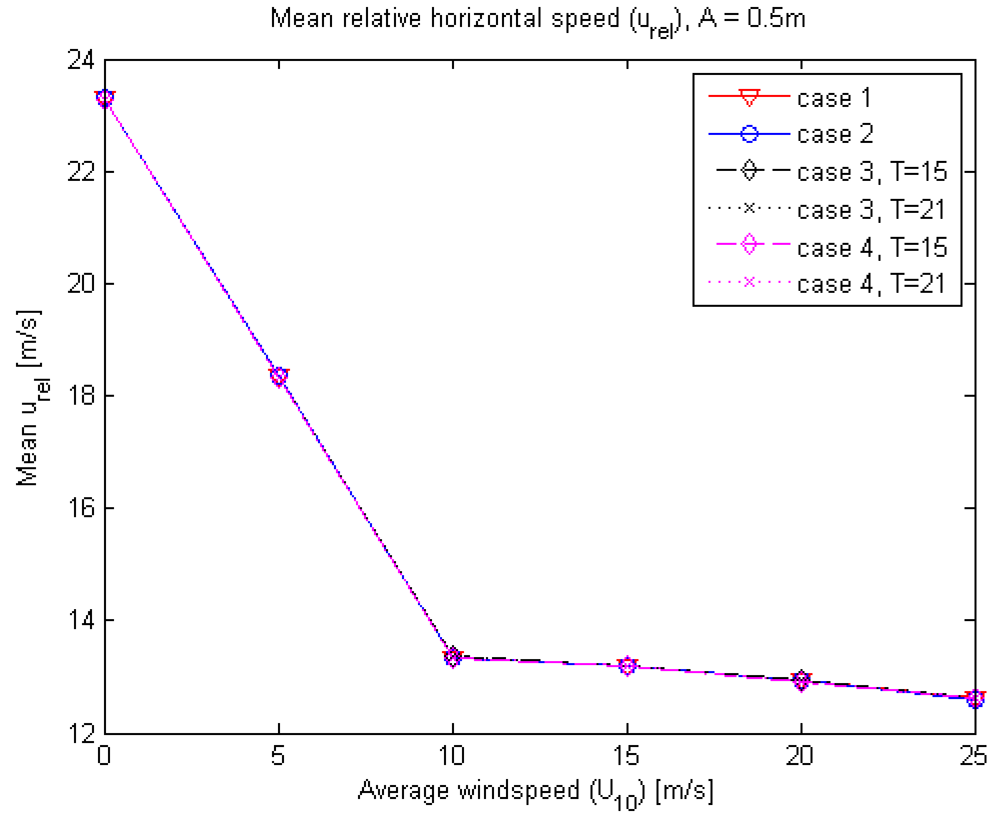
Mean relative horizontal speed (u_{rel}), A = 0.5m
Mean u_{rel} [m/s]
Average windspeed (U_{10}) [m/s]
24
22
20
18
16
14
12
0
5
10
15
20
25
case 1
case 2
case 3, T=15
case 3, T=21
case 4, T=15
case 4, T=21

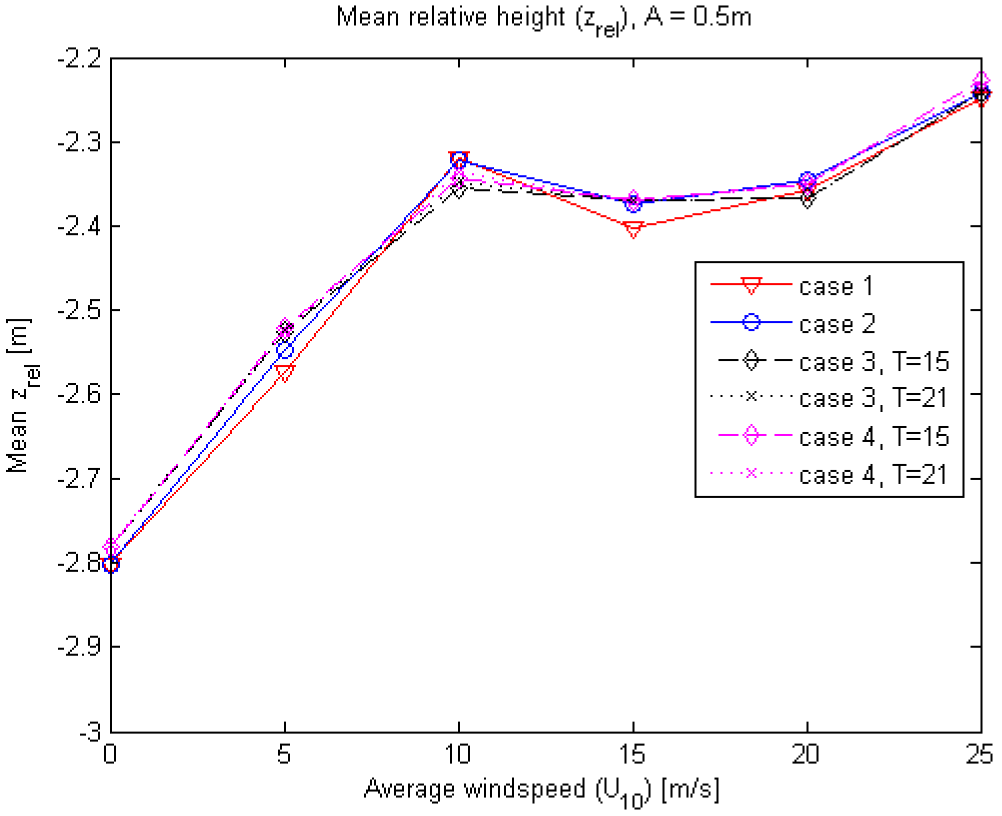
Mean relative height (z_{rel}), A = 0.5m
Mean z_{rel} [m]
Average windspeed (U_{10}) [m/s]
-2.2
-2.3
-2.4
-2.5
-2.6
-2.7
-2.8
-2.9
-3
0
5
10
15
20
25
case 1
case 2
case 3, T=15
case 3, T=21
case 4, T=15
case 4, T=21

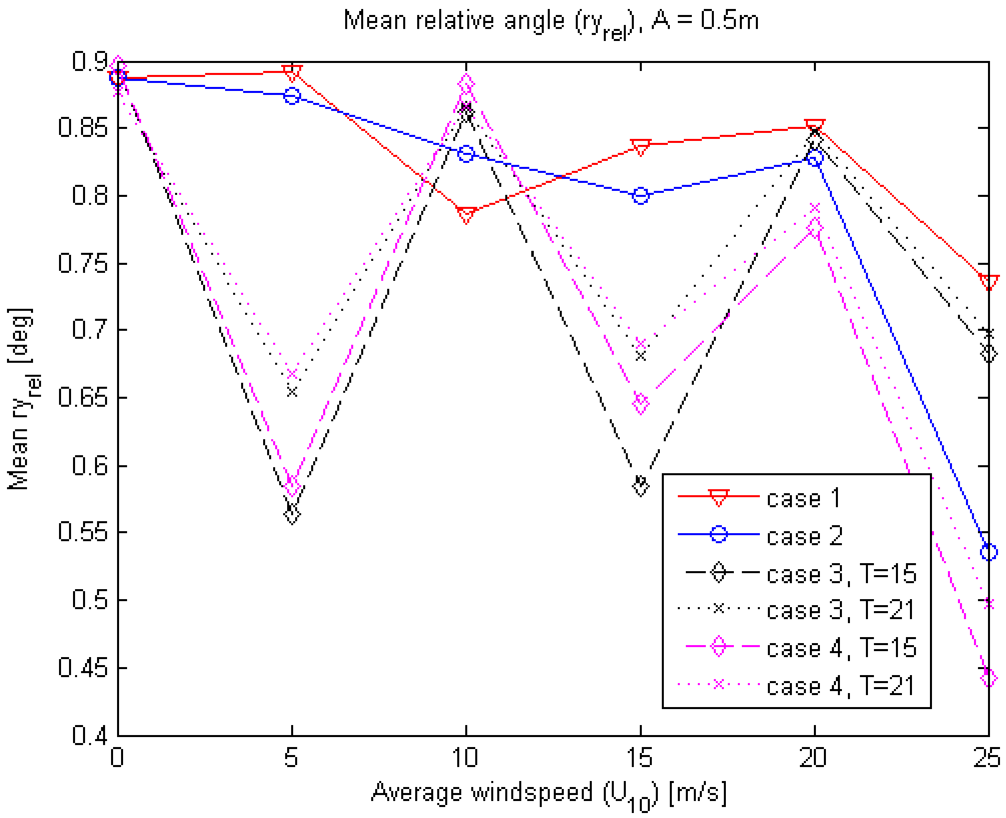
Mean relative angle (ry_{rel}), A = 0.5m
Mean ry_{rel} [deg]
0.9
0.85
0.8
0.75
0.7
0.65
0.6
0.55
0.5
0.45
0.4
0
5
10
15
20
25
Average windspeed (U_{10}) [m/s]
case 1
case 2
case 3, T=15
case 3, T=21
case 4, T=15
case 4, T=21

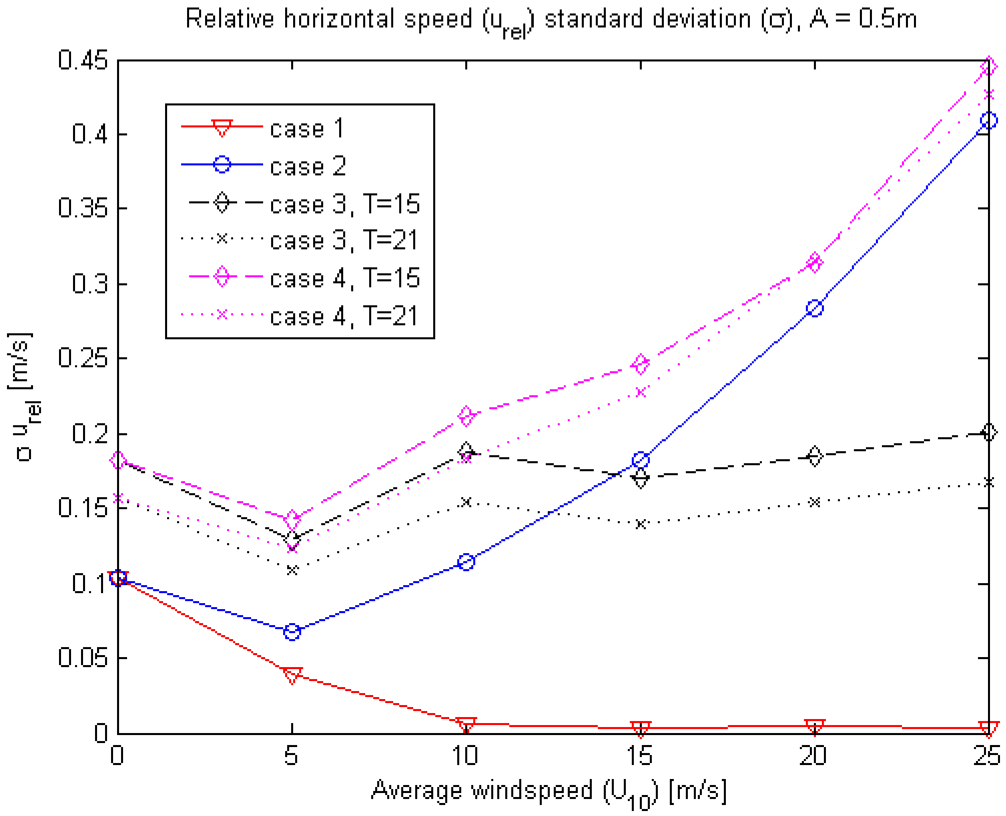
Relative horizontal speed (u_{rel}) standard deviation (σ), A = 0.5m
σ u_{rel} [m/s]
0.45
0.4
0.35
0.3
0.25
0.2
0.15
0.1
0.05
0
0
5
10
15
20
25
Average windspeed (U_{10}) [m/s]
case 1
case 2
case 3, T=15
case 3, T=21
case 4, T=15
case 4, T=21

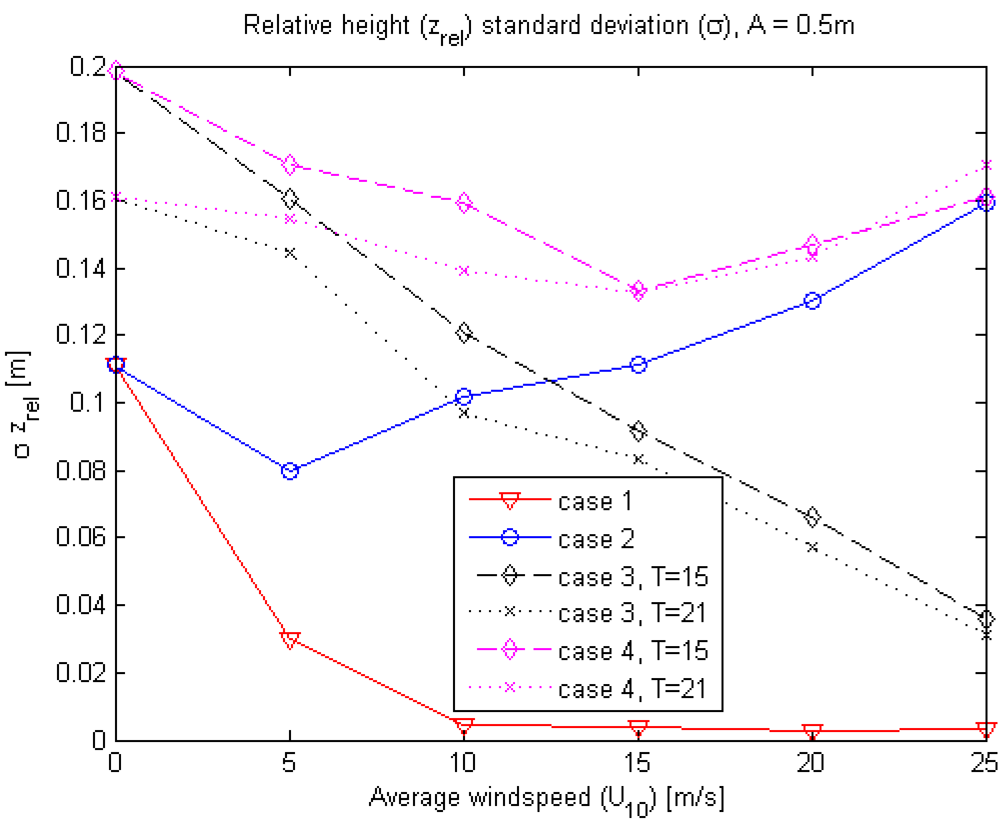
Relative height (z_{rel}) standard deviation (σ), A = 0.5m
σ z_{rel} [m]
0.2
0.18
0.16
0.14
0.12
0.1
0.08
0.06
0.04
0.02
0
0
5
10
15
20
25
Average windspeed (U_{10}) [m/s]
case 1
case 2
case 3, T=15
case 3, T=21
case 4, T=15
case 4, T=21

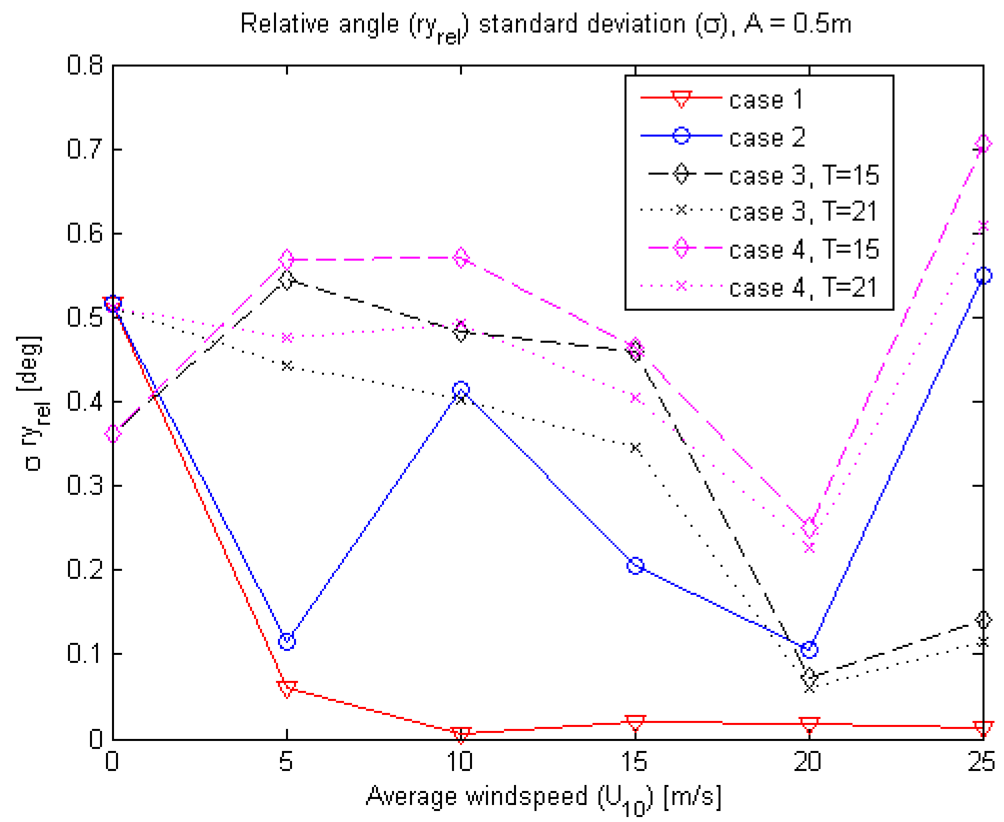
Relative angle (ry_{rel}) standard deviation (σ), A = 0.5m
σ ry_{rel} [deg]
0.8
0.7
0.6
0.5
0.4
0.3
0.2
0.1
0
0
5
10
15
20
25
Average windspeed (U_{10}) [m/s]
case 1
case 2
case 3, T=15
case 3, T=21
case 4, T=15
case 4, T=21

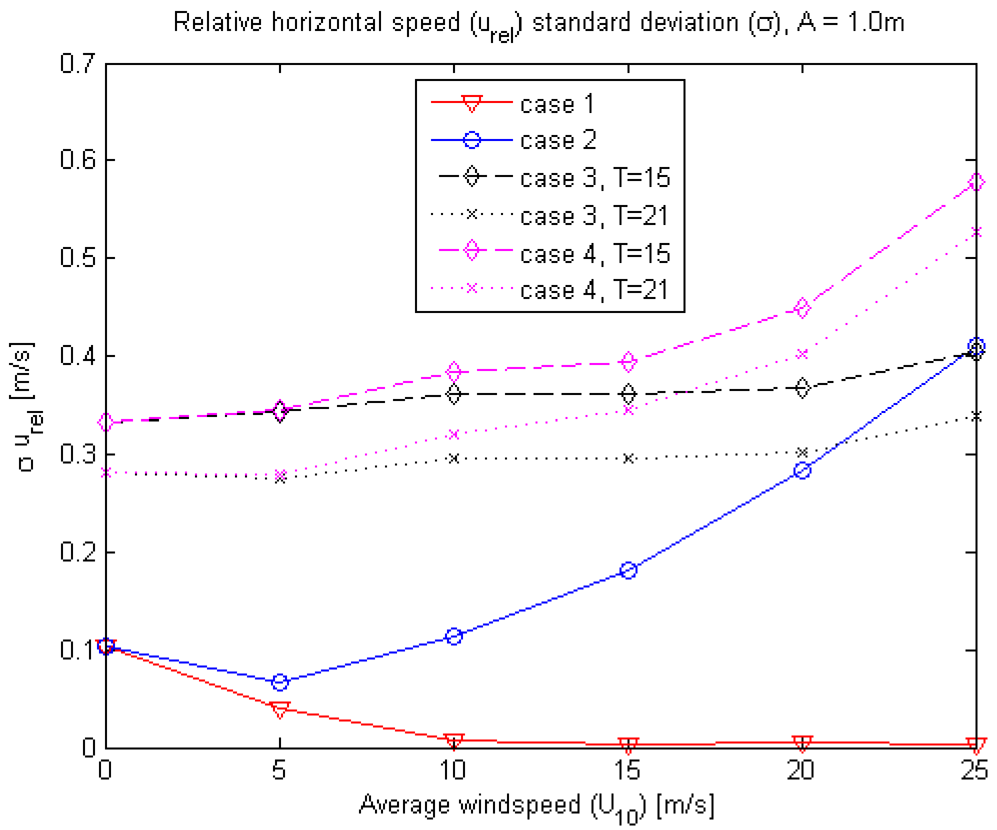
Relative horizontal speed (u_{rel}) standard deviation (σ), A = 1.0m
σ u_{rel} [m/s]
Average windspeed (U_{10}) [m/s]
0
0.1
0.2
0.3
0.4
0.5
0.6
0.7
0
5
10
15
20
25
case 1
case 2
case 3, T=15
case 3, T=21
case 4, T=15
case 4, T=21

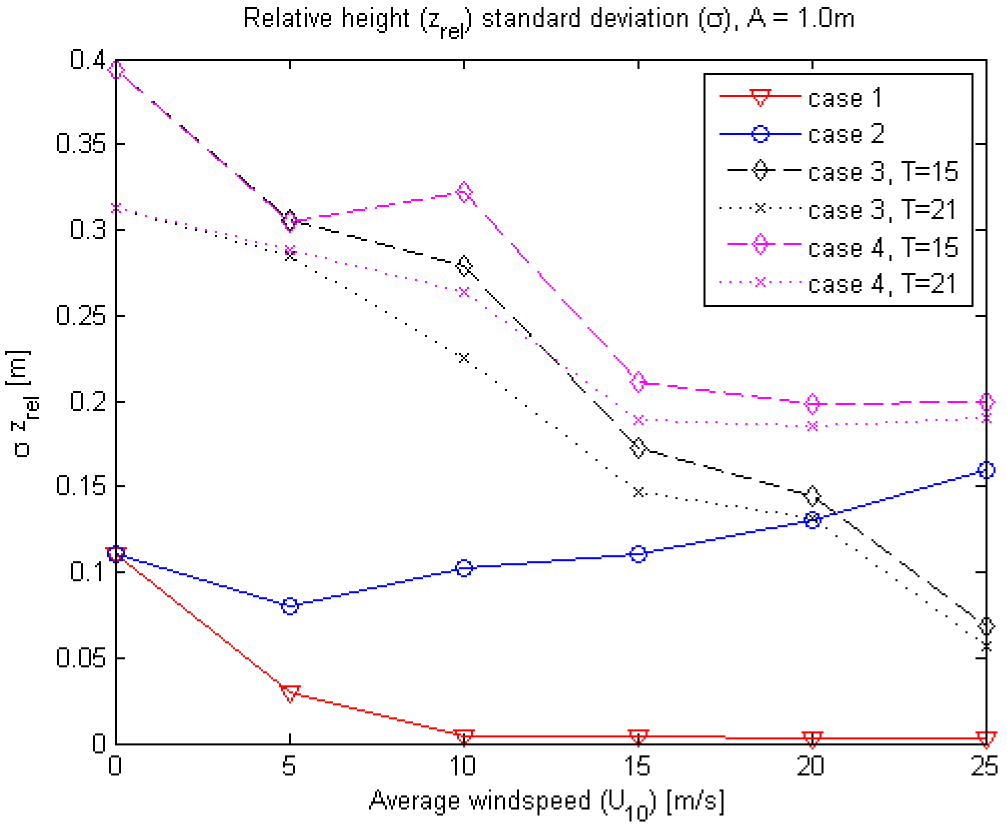
Relative height (z_{rel}) standard deviation (σ), A = 1.0m
σ z_{rel} [m]
Average windspeed (U_{10}) [m/s]
0
0.05
0.1
0.15
0.2
0.25
0.3
0.35
0.4
0
5
10
15
20
25
case 1
case 2
case 3, T=15
case 3, T=21
case 4, T=15
case 4, T=21

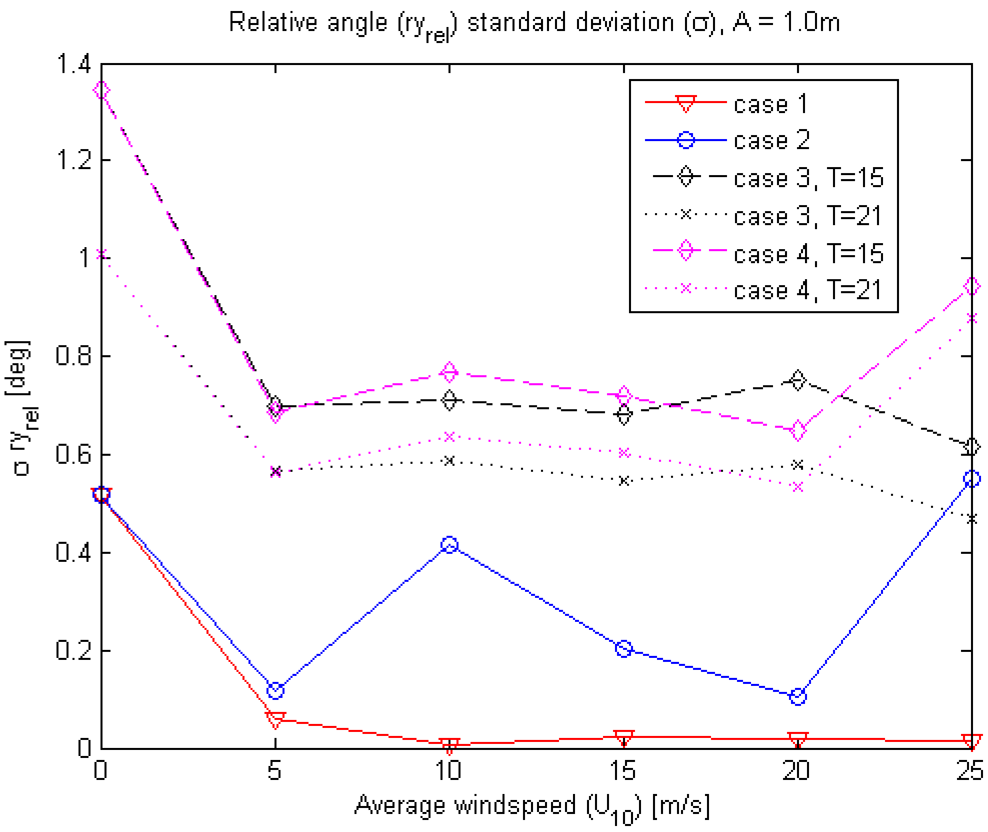
Relative angle (ry_{rel}) standard deviation (σ), A = 1.0m
σ ry_{rel} [deg]
Average windspeed (U_{10}) [m/s]
0
0.2
0.4
0.6
0.8
1
1.2
1.4
0
5
10
15
20
25
case 1
case 2
case 3, T=15
case 3, T=21
case 4, T=15
case 4, T=21

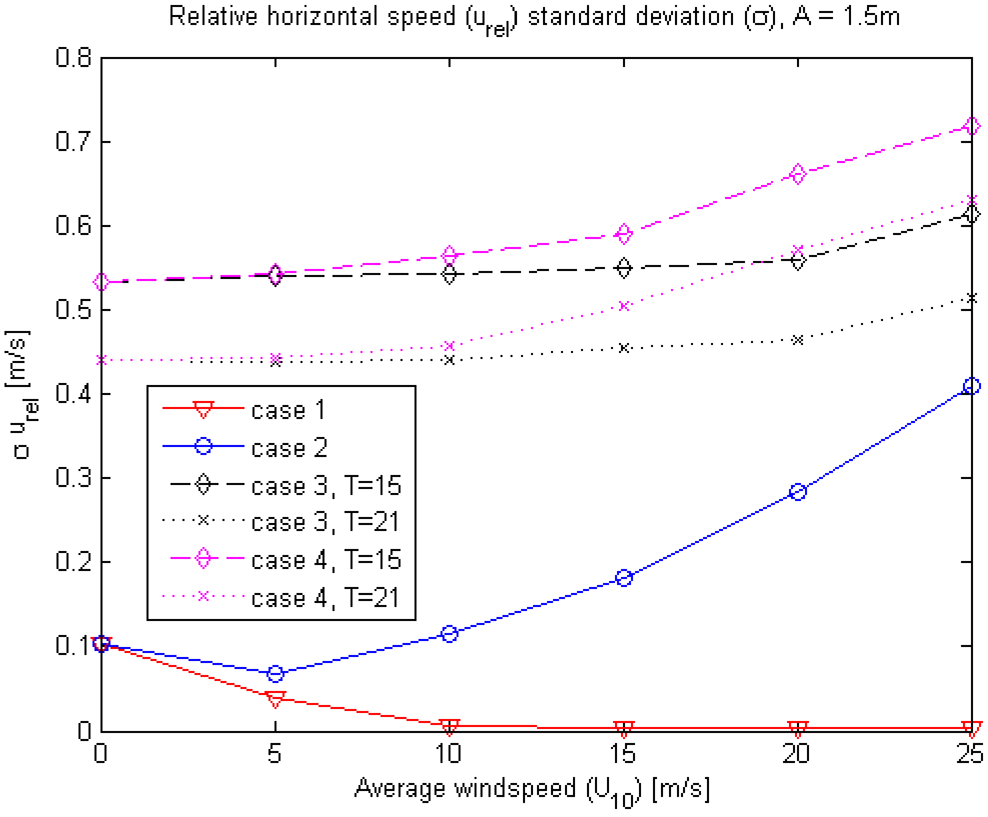
Relative horizontal speed (u_{rel}) standard deviation (σ), A = 1.5m
σ u_{rel} [m/s]
Average windspeed (U_{10}) [m/s]
0
0.1
0.2
0.3
0.4
0.5
0.6
0.7
0.8
0
5
10
15
20
25
case 1
case 2
case 3, T=15
case 3, T=21
case 4, T=15
case 4, T=21

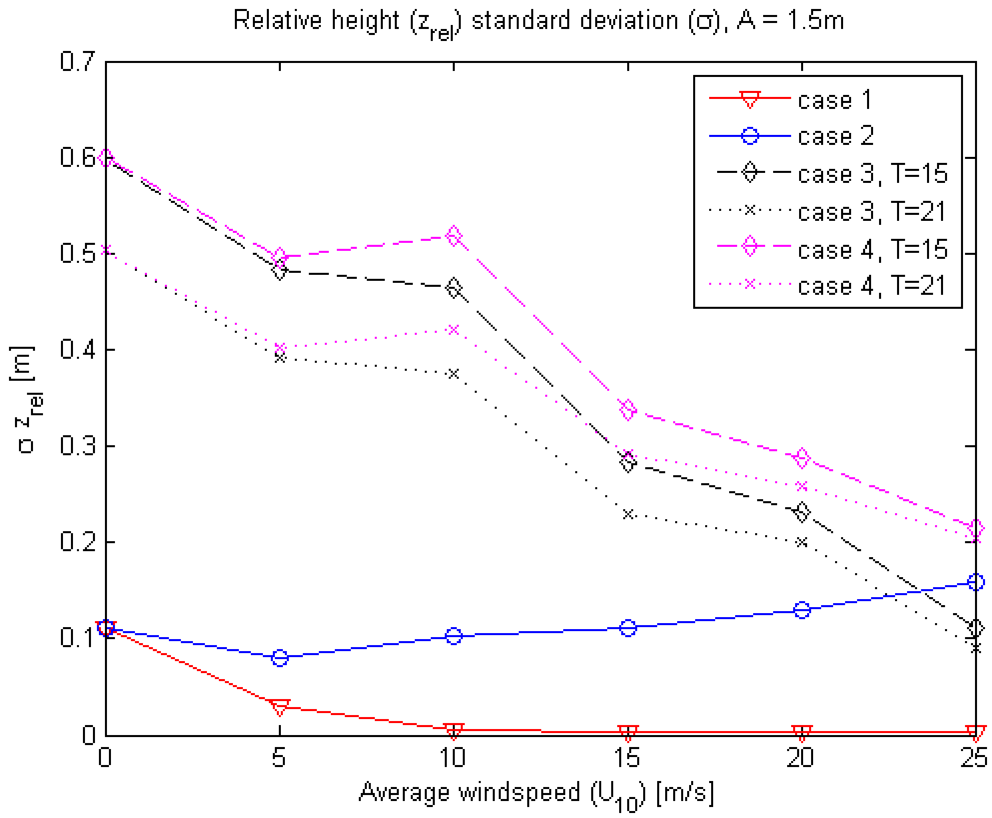
Relative height (z_{rel}) standard deviation (σ), A = 1.5m
0.7
0.6
0.5
0.4
0.3
0.2
0.1
0
σ z_{rel} [m]
0
5
10
15
20
25
Average windspeed (U_{10}) [m/s]
case 1
case 2
case 3, T=15
case 3, T=21
case 4, T=15
case 4, T=21

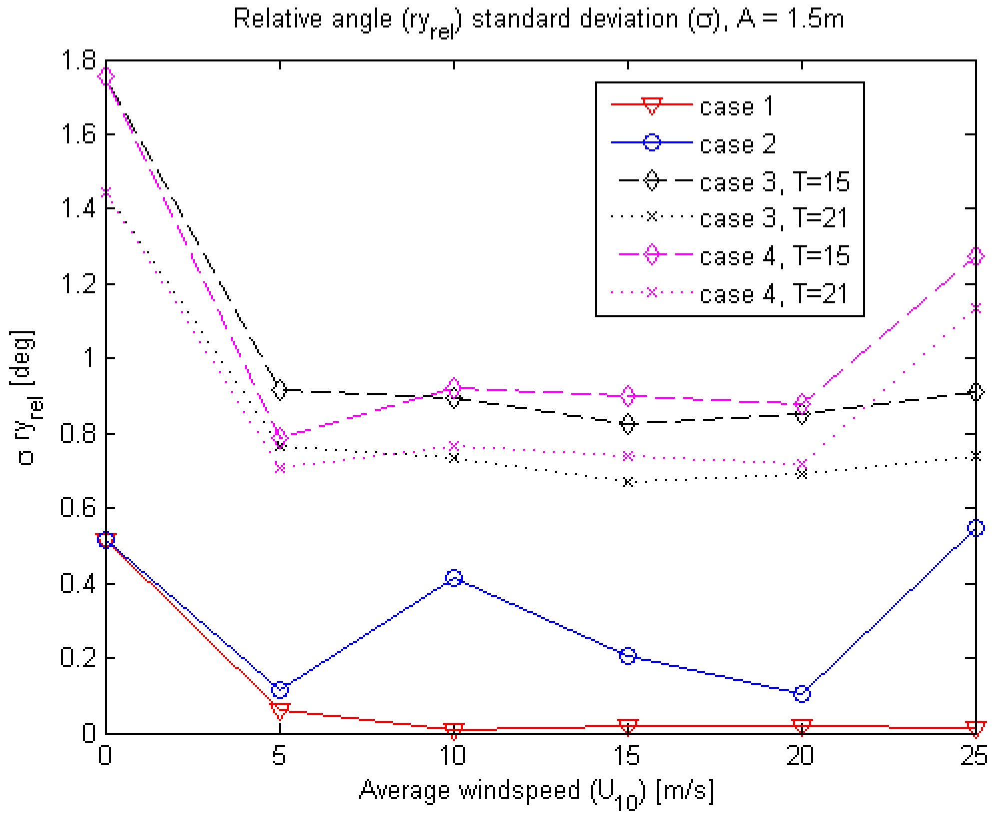
Relative angle (ry_{rel}) standard deviation (σ), A = 1.5m
1.8
1.6
1.4
1.2
1
0.8
0.6
0.4
0.2
0
σ ry_{rel} [deg]
0
5
10
15
20
25
Average windspeed (U_{10}) [m/s]
case 1
case 2
case 3, T=15
case 3, T=21
case 4, T=15
case 4, T=21

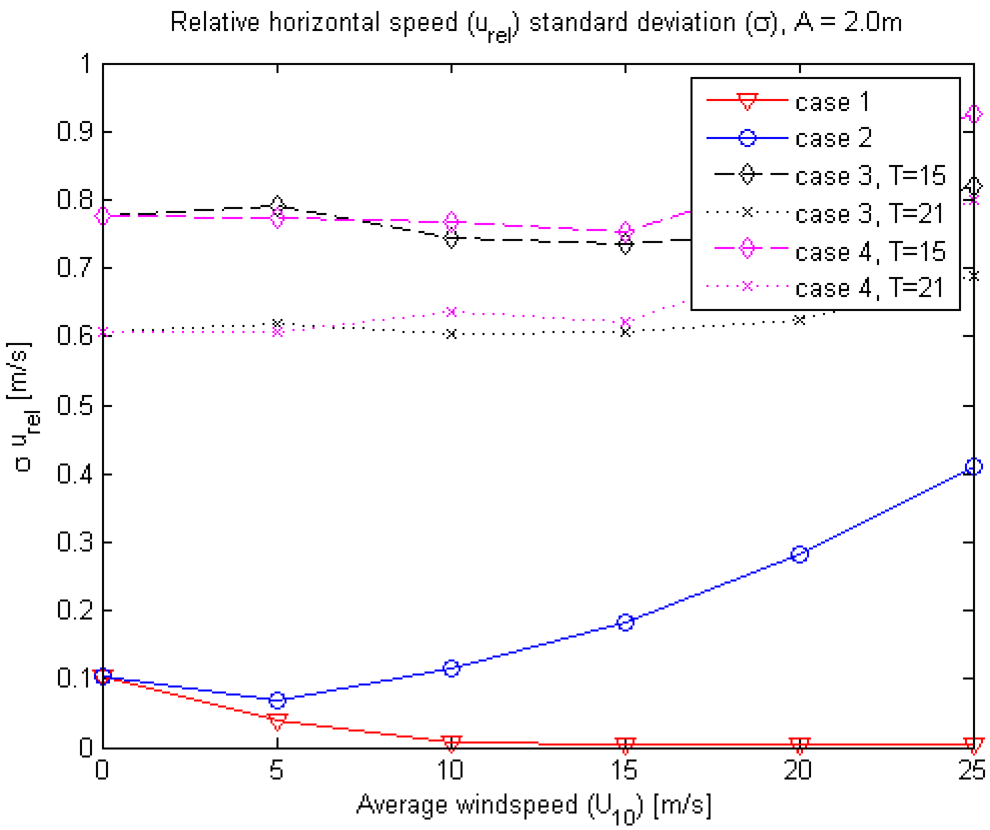

Relative horizontal speed (u_{rel}) standard deviation (σ), A = 2.0m

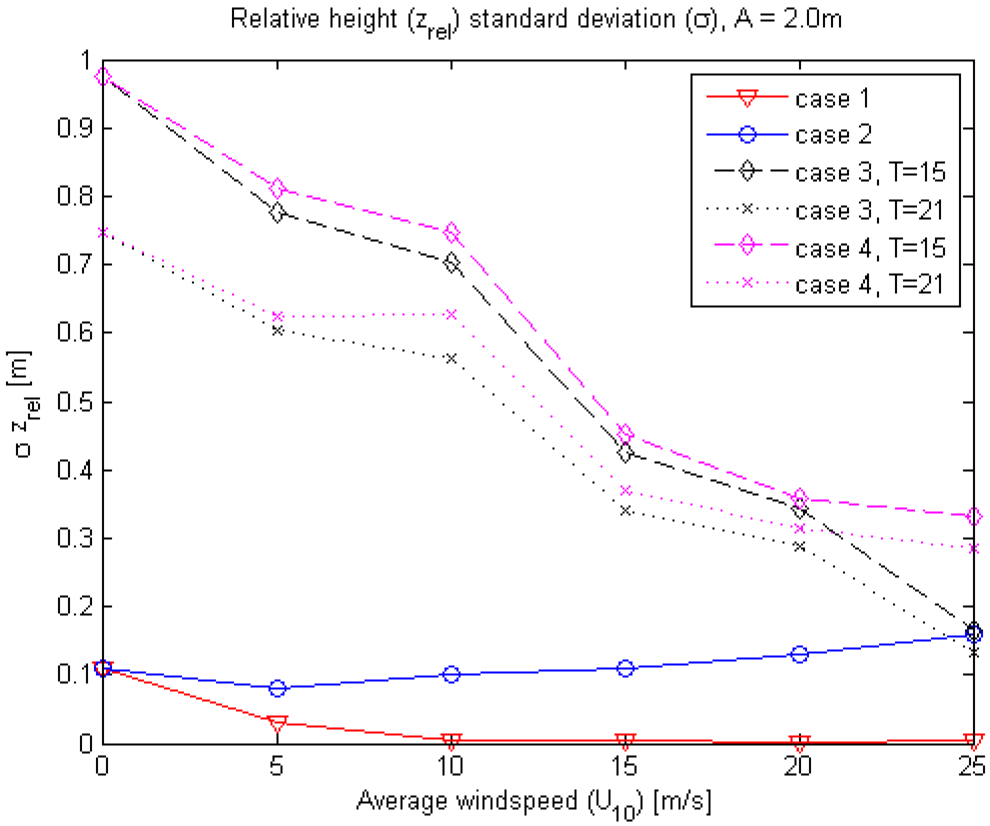

Relative height (z_{rel}) standard deviation (σ), A = 2.0m

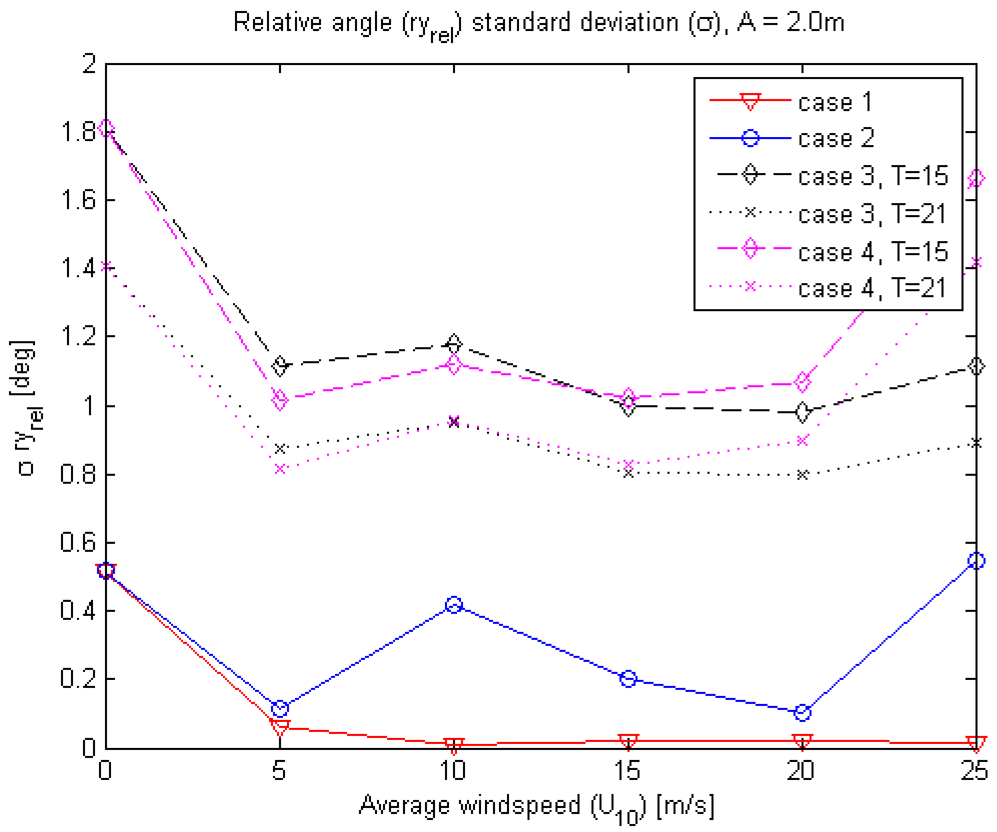
Relative angle (ry_rel) standard deviation (σ), A = 2.0m
σ ry_rel [deg]
2
1.8
1.6
1.4
1.2
1
0.8
0.6
0.4
0.2
0
0
5
10
15
20
25
Average windspeed (U_10) [m/s]
case 1
case 2
case 3, T=15
case 3, T=21
case 4, T=15
case 4, T=21

CASE 5

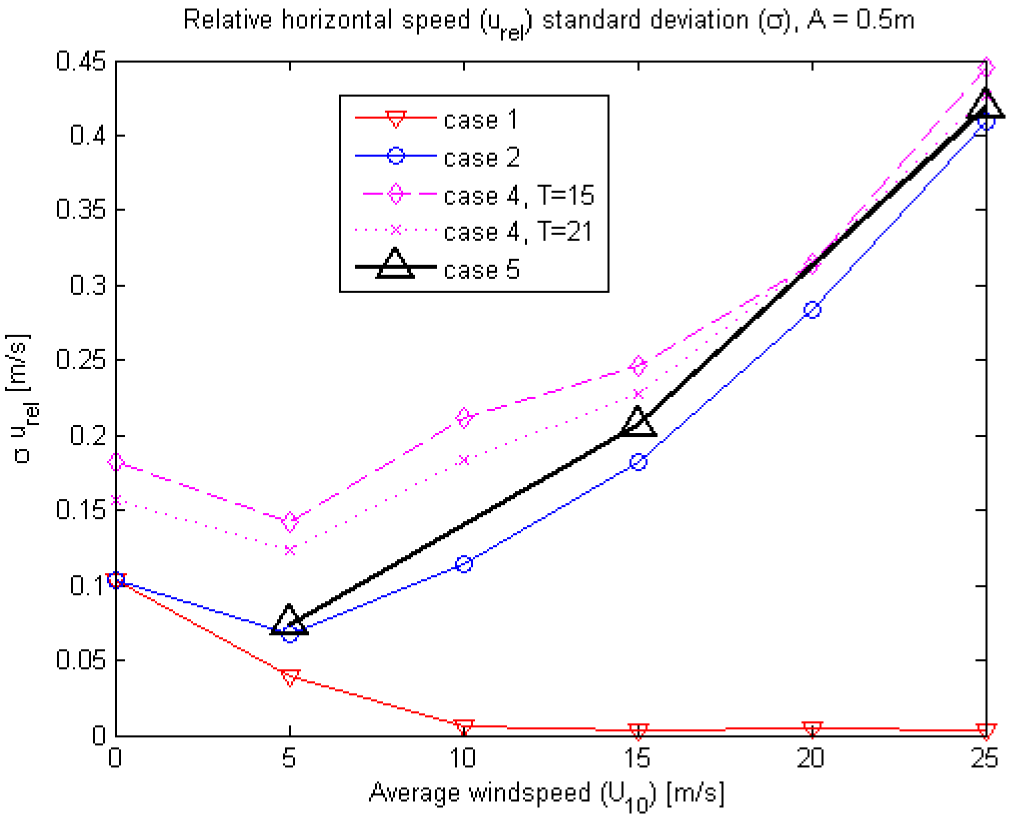
Relative horizontal speed (u_rel) standard deviation (σ), A = 0.5m
σ u_rel [m/s]
0.45
0.4
0.35
0.3
0.25
0.2
0.15
0.1
0.05
0
0
5
10
15
20
25
Average windspeed (U_10) [m/s]
case 1
case 2
case 4, T=15
case 4, T=21
case 5

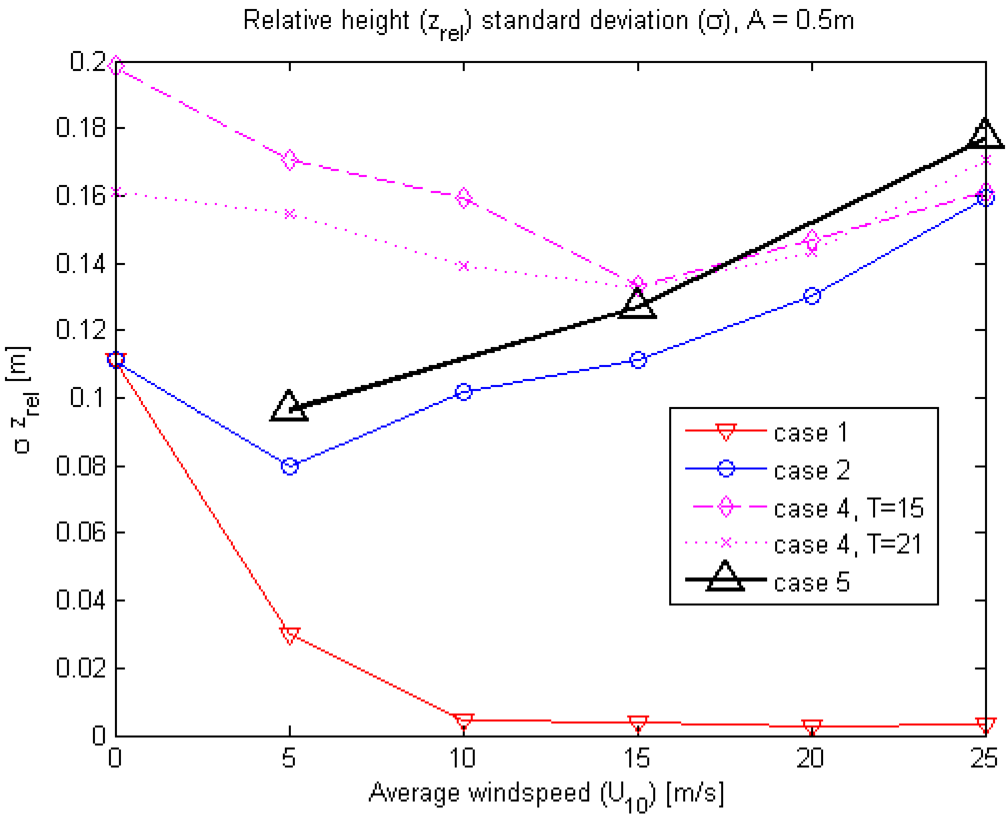

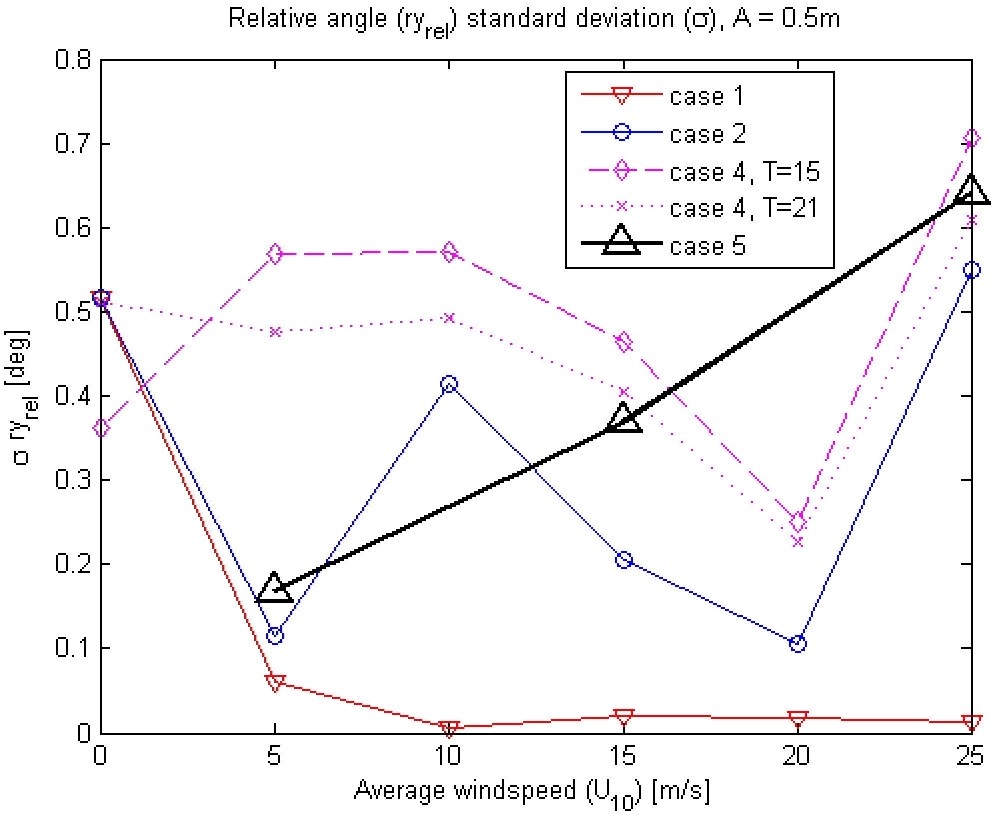

E. ANSYS® Aqwa^{TM} output data description

Load RAO's are the hydrodynamic load amplitudes exerted on the structure by a sinusoidal wave of 1m amplitude and for a range of frequencies. It also indicates the phase lag that the load has with respect to the exciting wave. The loads are divided in the 6 degrees of freedom (surge, sway, heave, roll, pitch and yaw). The hydrodynamic load scales linearly with wave height, thus if the wave height doubles, so does the load on the structure. This output has the largest contribution to the total load on the structure in further calculations.

Wave-Drift Loads result from the second order pressures. These loads scale quadratic with wave amplitude; meaning that if the wave height doubles, then the load quadruples. The magnitude of this load is significantly smaller than that of the linear RAO's and it only acts in the horizontal plane. However, in the analyses the load acts constantly in the direction of wave propagation, meaning that it causes the FP to drift from its initial position. This is not true for the first order loads that are harmonic and oscillate around zero, leading to no average load to act in a certain direction. Wave-drift loads are defined for surge, sway and yaw.

Mass/Inertia matrix is not calculated by Aqwa^{TM} but defined beforehand by mass of structure (which should be equal to the displacement in rest), and the radii of gyration.

Stiffness matrix is based on hydrostatics. It defines the restoring forces and moments for heave, roll and pitch when the structure is moved from its equilibrium position. Restoring forces for surge, sway and yaw follow from the mooring configuration and are therefore not included in this stiffness matrix. Because the stiffness matrix follows from hydrostatics, it is not frequency dependent.

Added mass and Damping matrices, are frequency dependent. They follow from the potential flow analysis. The added mass matrix indicates additional inertia, as can be seen in the equation of motion at the beginning of this chapter. The damping matrix damps out the motions of the FP. Important to note is that the damping that is calculated with potential theory does not include viscous effects, it is calculated based on kinetic energy dissipation by radiation and diffraction of waves. Damping is especially important when wave frequencies are close to the natural frequency of the structure, and an underestimation of damping leads to a significant overestimation of motions. That is why a non-linear viscous approximation in the form of the semi-empirical Morison drag is included in the time-domain analysis.

Natural frequencies, are given for heave, roll and pitch. The natural frequencies are based on the inertia matrix and stiffness matrix.

Motion RAO's, are similar to load RAO's, but they indicate displacements instead of loads. This type of RAO is not used in later analyses and is therefore not discussed further.

Aqwa^{TM} output is in text file format (.LIS files).

F. Marine Systems Simulator (MSS) variable description

MSS developed for addition of control system. Now used for the addition of semi-empirical (non-linear) drag contributions (that are not captured by potential theory) in the time-domain.

Preprocessing of MSS toolbox input (Conversion of Aqwa™ output to MSS input)

The output of Aqwa™, which is a large text file, needs to be transformed to two Matlab® structures of variables: 'vessel' and 'vesselABC'. Only when these two structure are correctly loaded into the Matlab® workspace, the MSS Simulink® model can be run. The transformation to the required format is automated by the script Aqwa2vessel.m, which is an alteration of the script wamit2vessel.m that is supplied with the MSS toolbox, and the script ReadRao.m that was developed in-house at Mocean Offshore. The first structure ('vessel') contains the following variables:

vessel.main is a structure in a structure that contains the main particulars of the FP. These particulars are the **name**, draft (**T**), breadth (**B**), length between perpendiculars (**Lpp**), water density (**rho**), gravitational acceleration (**g**), volume displacement (**nabla**), mass displacement (**m**), location of center of gravity (**CG**), location of center of buoyancy (**CB**), transverse metacentric height (**GM_T**), longitudinal metacentric height (**GM_L**), roll radius of gyration (**k44**), pitch radius of gyration (**k55**), yaw radius of gyration (**k66**).

vessel.freqs is a vector with the frequencies for which the Aqwa™ analysis is performed, with the addition of 0 rad/s and 10 rad/s.

vessel.velocities is a vector containing the velocities that are investigated, in this case it is equal to zero.

vessel.headings is a vector with a length of 36 containing the headings in rad/s, note that these should always be defined from 0 to pi*350/180 with steps of pi*10/180. It is therefore important that the Aqwa™ analysis is run with 37 headings from -180 to 180 degrees.

vessel.MRB contains the mass matrix of the FP. The mass matrix is frequency independent; this is therefore a 6x6 matrix.

vessel.A contains the added mass matrix of the FP, which is frequency dependent. This is a three-dimensional matrix of 6x6x22, where for each of the 22 frequencies an added mass matrix of 6x6 is defined. Note that for the frequencies 0 and 10 rad/s the assumption is made that they are equal to respectively the smallest and the largest calculated frequency. The reason for this is that the zero frequency and infinite frequency added mass are not part of the Aqwa™ output.

vessel.B is similar in form to the added mass matrices described above, but in this case contains the frequency dependent damping matrices that result from radiation/diffraction analysis. The same approach is taken for the 0 rad/s and 10 rad/s frequencies as well.

vessel.C contains the hydrostatic stiffness matrix, or restoring matrix. This is not frequency dependent and is therefore similar in form to the vessel.MRB matrix.

vessel.motionRAO is the variable containing the motion RAO's. This is a structure containing three other variables: w, amp and phase. Where 'w' is a vector with the frequencies, but without 0 rad/s and 10 rad/s. amp and phase are 1x6 cells, as the 6 degrees of freedom are given their own cell. Within these cells a three-dimensional matrix is found defining amplitudes or phases for each frequency, wave direction and velocity. Ten velocities are considered, but as mentioned before only for 0 m/s forward speed the analysis is performed. This means that 9 out of 10 matrices have all zero entries.

vessel.forceRAO is has the same structure as the motion RAO's, but in this case the 'amp' matrix indicates force and moment amplitudes instead of motion amplitudes. Of course, the corresponding phase lags are different from the motion RAO's as well.

vessel.driftfrc in this structure, that contains the vector with frequencies 'w' and amplitudes (amp) in 1x3 cells, the mean wave drift loads are defined. As the wave drift loads only act in surge, sway and yaw only three cells are used, in these cells the same type of three dimensional matrix is found as in 'vessel.forceRAO.amp'. Forces are thus defined for a range of frequencies, wave directions and forwards speeds, where again the only matrix corresponding to 0 m/s forward speed has non-zero values.

vessel.Bv is the final variable in the vessel structure. This is the viscous damping matrix, it is determined based on the added mass and damping matrices using the script viscous.m that is supplied with the MSS toolbox. However, the calculation method in the script is focused on ship-shaped structures; damping in surge, sway and yaw are determined based on skin friction assumptions, which are different for the semi-submersible type structure. The additional viscous roll damping that is calculated in the script is based on increasing the relative damping ratio at the natural roll frequency. In other words, the viscous roll damping is a direct result of an arbitrary increase of the damping ratio and is independent of actual shape of the FP. On top of this, the damping is not added in pitch, which is because of the ship shaped assumption (for ship shaped structures, pitch-damping results mostly from radiating waves instead of viscous effects). This is why the Bv matrix is neglected in the MSS calculation, and other approaches for the calculation of viscous damping are considered.

The ‘vessel’ structure is input for the determination of the ‘vesselABC’ structure. The ‘vesselABC’ structure is the main input for the fluid memory effect calculation. How this structure is determined was covered in Section 2.3.

G. Hydrodynamic model overview

In the following two figures an overview is given of the Simulink^{TM} model used for hydrodynamic time-domain calculations, in the first figure the entire model is shown, in the second figure only the content of the '*6 DOF model' block*. Refer to chapter 2 for more details on the used methods.

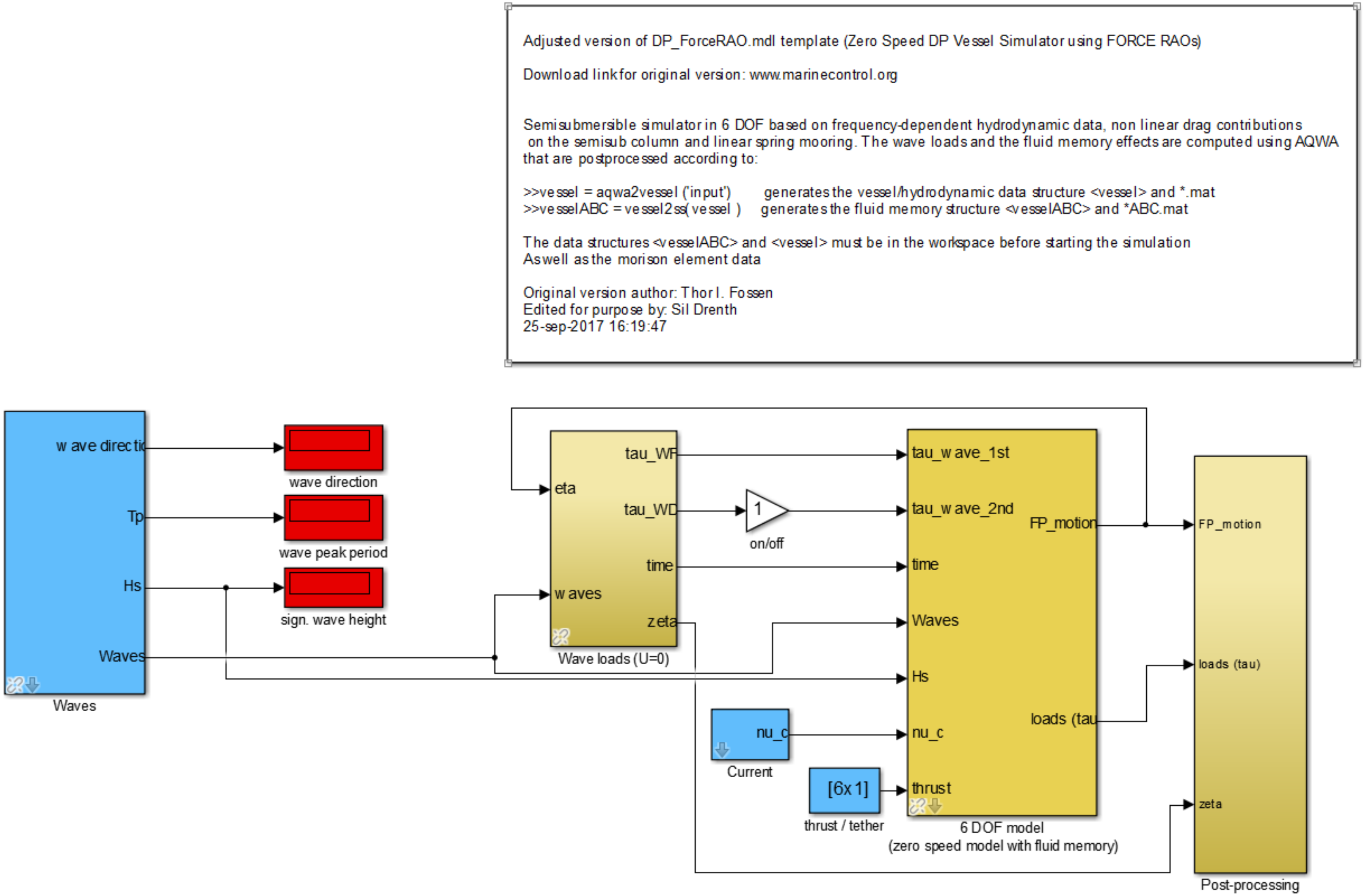

Adjusted version of DP_ForceRAO.mdl template (Zero Speed DP Vessel Simulator using FORCE RAOs)

Download link for original version: www.marinecontrol.org

Semisubmersible simulator in 6 DOF based on frequency-dependent hydrodynamic data, non linear drag contributions on the semisub column and linear spring mooring. The wave loads and the fluid memory effects are computed using AQWA that are postprocessed according to:

```
>>vessel = aqwa2vessel ('input')       generates the vessel/hydrodynamic data structure <vessel> and *.mat
>>vesselABC = vessel2ss( vessel )     generates the fluid memory structure <vesselABC> and *ABC.mat
```

The data structures <vesselABC> and <vessel> must be in the workspace before starting the simulation
Aswell as the morison element data

Original version author: Thor I. Fossen
Edited for purpose by: Sil Drenth
25-sep-2017 16:19:47

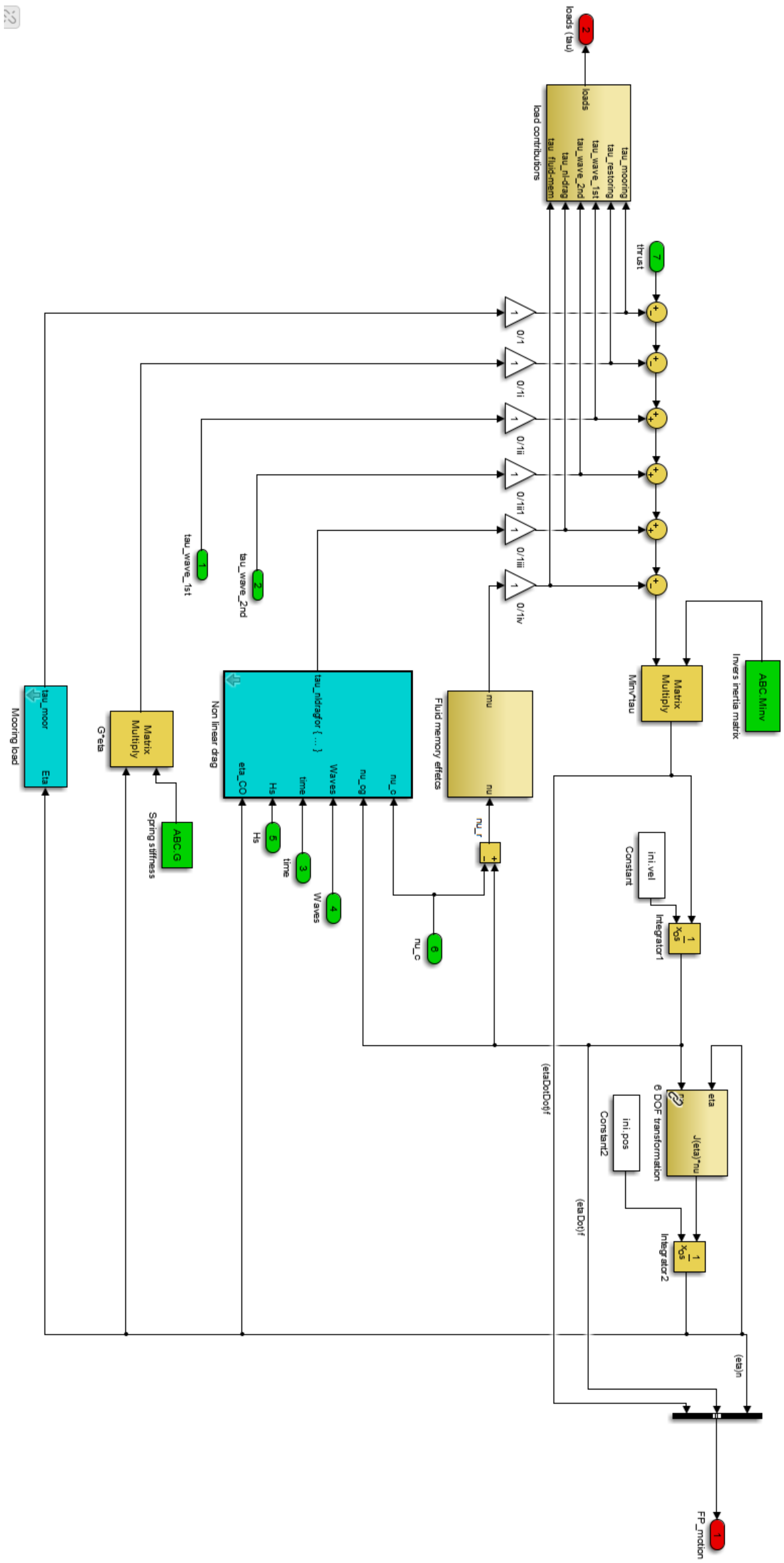
loads (tau)
loads
tau_mooring
tau_restoring
tau_wave_1st
tau_wave_2nd
tau_nl-drag
tau_fluid-mem
load contributions
thrust
0/1
0/1i
0/1ii
0/1iii
0/1iiii
0/1iv
tau_wave_1st
tau_wave_2nd
tau_moor
Eta
Mooring load
Matrix Multiply
G*eta
ABC.G
Spring stiffness
tau_nldragfor {...}
nu_c
nu_cg
Waves
time
Hs
eta_CO
Non linear drag
mu
nu
Fluid memory effects
nu_r
nu_c
Matrix Multiply
Minv*tau
ABC.Minv
Invers inertia matrix
ini.vel
Constant
Integrator1
eta
J(eta)*nu
6 DOF transformation
ini.pos
Constant2
Integrator2
(etaDotDot)f
(etaDot)f
(eta)n
FP_motion

H. Aerodynamic model overview

In the following three figures an overview is given of the Simulink^{TM} model used for aerodynamic time-domain calculations. In the first figure the entire model is shown, in the second figure only the content of the '*Loads to RPA motions*' block, and in the third figure the content of the '*Loads on RPA*' block. Refer to chapter 3 for more details on the used methods.

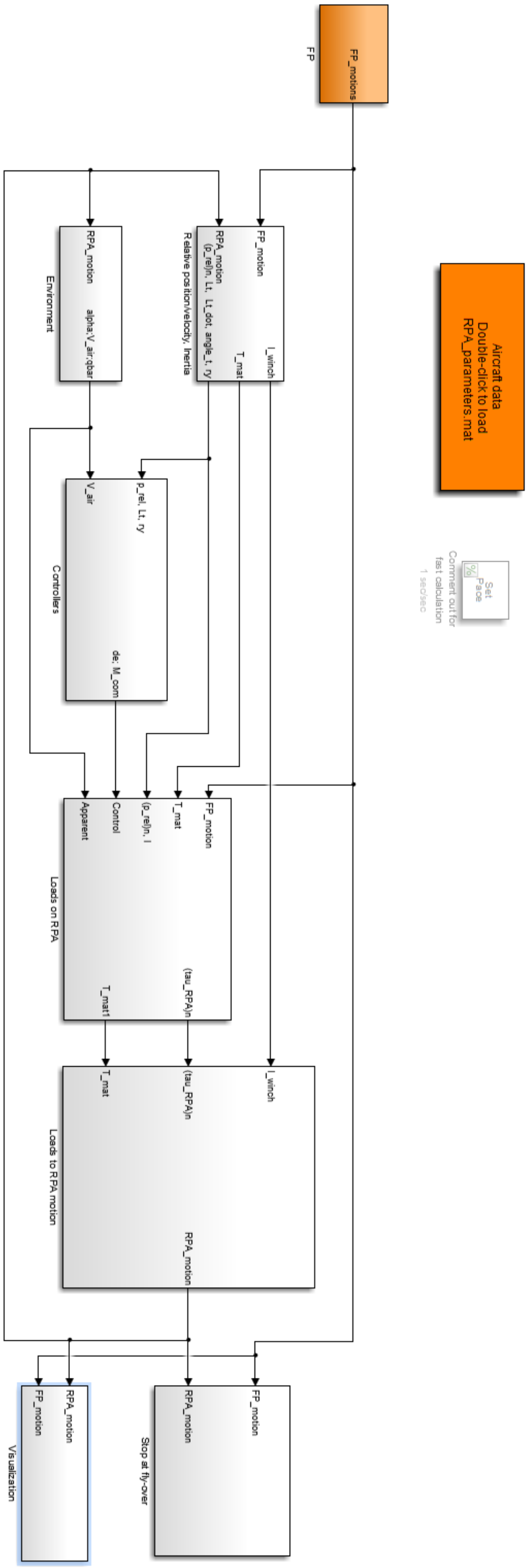
FP_motions
FP
Aircraft data
Double-click to load
RPA_parameters.mat
Set Pace
Comment out for fast calculation
1 sec/sec
FP_motion
l_winch
RPA_motion
(p_rel)n, Lt, Lt_dot, angle_t, ry
T_mat
Relative position/velocity, inertia
RPA_motion
alpha/V_air,qbar
Environment
p_rel, Lt, ry
V_air
de; M_com
Controllers
FP_motion
T_mat
(p_rel)n, l
Control
Apparent
(tau_RPA)n
T_mat1
Loads on RPA
l_winch
(tau_RPA)n
T_mat
RPA_motion
Loads to RPA motion
FP_motion
RPA_motion
Stop at fly-over
RPA_motion
FP_motion
Visualization

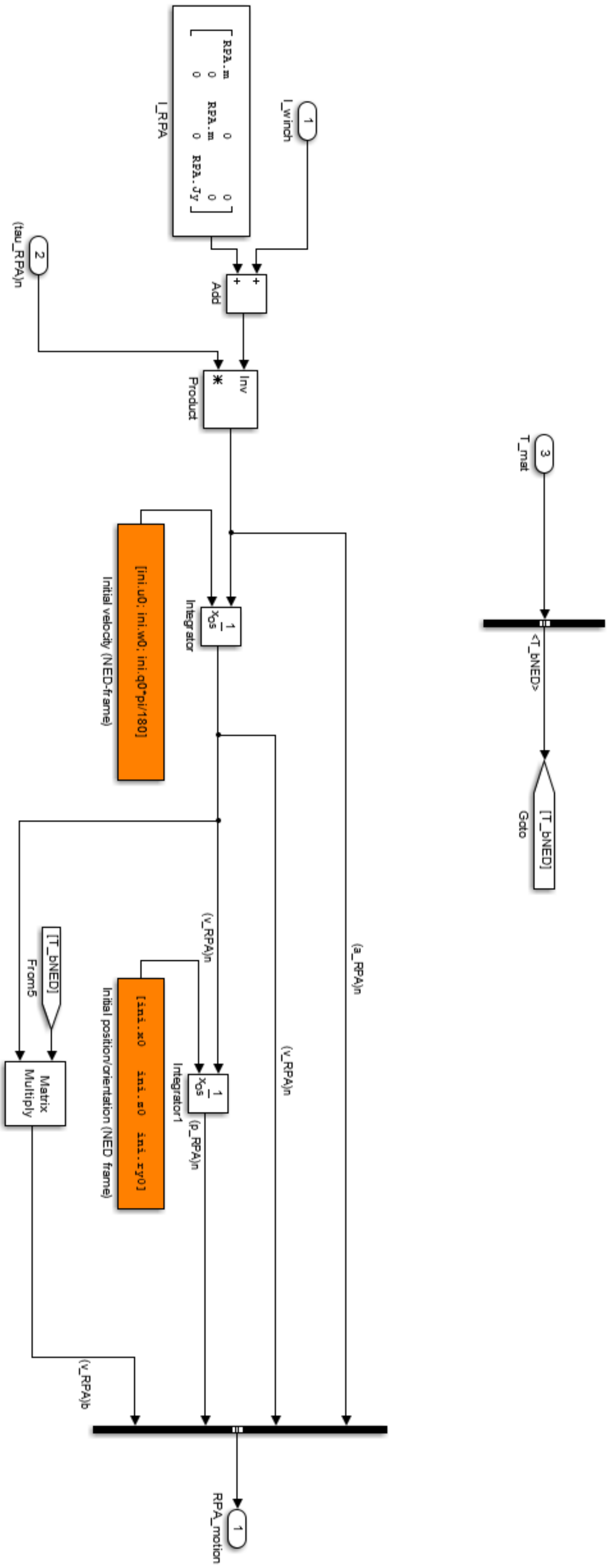
1
I_winch
RPA.m 0 0
0 RPA.m 0
0 0 RPA.Jy
I_RPA
+ +
Add
2
(tau_RPA)n
Inv
*
Product
3
T_mat
<T_bNED>
[T_bNED]
Goto
[ini.u0; ini.w0; ini.q0*pi/180]
Initial velocity (NED-frame)
1/s
xo
Integrator
(a_RPA)n
(v_RPA)n
(v_RPA)n
[ini.x0 ini.z0 ini.ry0]
Initial position/orientation (NED frame)
1/s
xo
Integrator1
(p_RPA)n
[T_bNED]
From5
Matrix Multiply
Divide2
(v_RPA)b
1
RPA_motion

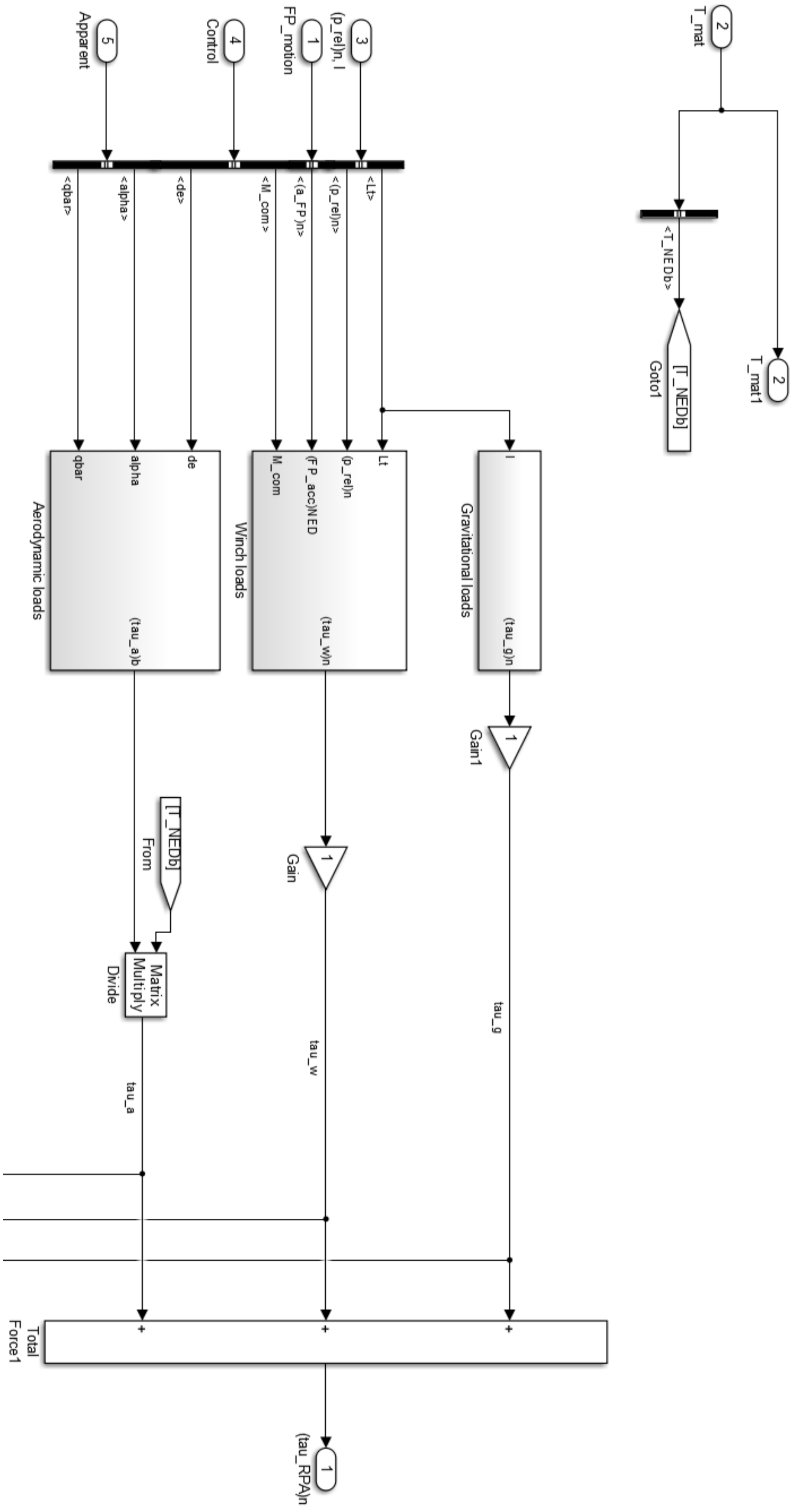
2
T_mat
<T_NEDb>
[T_NEDb]
Goto1
2
T_mat1
3
(p_rel)n, l
1
FP_motion
4
Control
5
Apparent
<Lt>
<(p_rel)n>
<(a_FP)n>
<M_com>
<de>
<alpha>
<qbar>
l
Gravitational loads
(tau_g)n
Lt
(p_rel)n
(FP_acc)NED
M_com
Winch loads
(tau_w)n
de
alpha
qbar
Aerodynamic loads
(tau_a)b
1
Gain1
1
Gain
[T_NEDb]
From
Matrix Multiply
Divide
tau_g
tau_w
tau_a
+
+
+
Total Force1
1
(tau_RPA)n

Bibliography

4C Offshore. (2017a). Hywind Scotland Pilot Park. Retrieved March 16, 2017, from http://www.4coffshore.com/windfarms/hywind-scotland-pilot-park-united-kingdom-uk76.html

4C Offshore. (2017b). WindFloat Atlantic (WFA). Retrieved October 25, 2017, from http://www.4coffshore.com/windfarms/windfloat-atlantic-(wfa)-portugal-pt03.html

Ampyx Power. (2016). Subsidy Granted for Offshore Research Project with ECN, Marin and Mocean | Ampyx Power. Retrieved March 16, 2017, from https://www.ampyxpower.com/2016/08/subsidy-granted-for-offshore-project-with-ecn-marin-and-mocean

Ampyx Power. (2017). Technology – Ampyx Power. Retrieved March 16, 2017, from https://www.ampyxpower.com/technology

ANSYS Inc. (2012). Aqwa Reference Manual. SAS IP Inc.

Bontekoe, E. (2010). *Up! How to Launch and Retrieve a Tethered Aircraft*. Delft University of Technology. Retrieved from https://repository.tudelft.nl/islandora/object/uuid%3A0f79480b-e447-4828-b239-9ec6931bc01f?collection=education

Broome, D. R., & Hall, M. S. (1998). Application of Ship Motion Prediction I. *Transactions - Institute of Marine Engineers*, *110*, 77–93. Retrieved from http://cat.inist.fr/?aModele=afficheN&cpsidt=1587453

Cherubini, A., Vertechy, R., & Fontana, M. (2016). Simplified Model of Offshore Airborne Wind Energy Converters. *Renewable Energy*, *88*, 465–473. https://doi.org/10.1016/j.renene.2015.11.063

Cummins, W. E. (1962). *The Impulse Response Function and Ship Motions*. Washington, D.C.

Dalzell, J. (1965). A Note on Short-Time Prediction of Ship Motions. *Journal of Ship Research*. Retrieved from https://scholar.google.nl/scholar?q=A+note+on+short-time+prediction+of+ship+motions+1965&btnG=&hl=nl&as_sdt=0%2C5

Dannenberg, J., Hessner, K., Naaijen, P., van den Boom, H., & Reichert, K. (2010). The On board Wave and Motion Estimator OWME. *International Society of Offshore and Polar Engineering*, *7*, 424–431.

DARPA. (2017). SideArm Prototype Catches Full-Size Unmanned Aerial System Flying at Full Speed. Retrieved October 25, 2017, from https://www.darpa.mil/news-events/2017-02-06

Diehl, M., Leuthold, R., & Schmehl, R. (2017). Airborne Wind Energy Conference 2017. In *Book of Abstracts*. Freiburg, Germany. https://doi.org/10.4233/uuid:4c361ef1-d2d2-4d14-9868-16541f60edc7

DNV. (2007). Recommended Practice DNV-RP-C205, Environmental Conditions and Environmental Loads. https://doi.org/10.1109/INTLEC.1993.388591

DoD. (1997). *MIL-HDBK-1797 - Flying Qualities of Piloted Aircraft*.

Fagiano, L., Nguyen-Van, E., Rager, F., Schnez, S., & Ohler, C. (2016). A Small-Scale Prototype to Study the Take-Off of Tethered Rigid Aircrafts for Airborne Wind Energy. https://doi.org/10.1109/TMECH.2017.2698405

Fagiano, L., Nguyen-Van, E., & Schnez, S. (2017). Linear Take-Off and Landing of a Rigid Aircraft for Airborne Wind Energy Extraction. In R. Schmehl (Ed.), *Airborne Wind Energy - Advances in Technology Development and Research*. Springer-Verlag.

Fechner, U., & Schmehl, R. (2016). Flight Path Control of Kite Power Systems in a Turbulent Wind Environment. In *2016 American Control Conference (ACC)* (pp. 4083–4088). IEEE. https://doi.org/10.1109/ACC.2016.7525563

Felker, F. (2017). Progress and Challenges in Airborne Wind Energy. In *Airborne Wind Energy Conference 2017*. https://doi.org/10.4233/uuid:056d3dd2-bdd1-4bf1-8331-fe5295ce7003

Felux, M., Dautermann, T., & Becker, H. (2013). GBAS Landing System – Precision Approach Guidance After ILS. *Aircraft Engineering and Aerospace Technology*, *85*(5), 382–388. https://doi.org/10.1108/AEAT-07-2012-0115

Fossen, T. I., & Perez, T. (2004). Marine Systems Simulator (MSS). Retrieved from http://www.marinecontrol.org

GPS World staff. (2016). US Navy Awards Raytheon $255 Million for Precision Landing | GPS World. Retrieved March 20, 2017, from http://gpsworld.com/us-navy-awards-raytheon-255-million-for-precision-landing/

Hamilton, J. D. (1994). *Time series analysis*. Princeton University Press. Retrieved from http://press.princeton.edu/titles/5386.html

Hoblit, F. M. (1988). *Gust Loads on Aircraft: Concepts and Applications*. American Institute of Aeronautics and Astronautics. Retrieved from https://books.google.nl/books/about/Gust_Loads_on_Aircraft.html?id=Z0FR8QkNFtUC&redir_esc=y

Huijs, F., De Bruijn, R., & Savenije, F. (2014). Concept Design Verification of a Semi-Submersible Floating Wind Turbine Using Coupled Simulations. *Energy Procedia*, *53*(C), 2–12. https://doi.org/10.1016/j.egypro.2014.07.210

IRENA. (2012). Renewable Energy Technologies: Cost Analysis Series, Wind Power. *IRENA Working Paper*. https://doi.org/10.1016/B978-0-08-098330-1.00011-9

Journée, J. M. J., Massie, W. W., & Huijsmans, R. H. M. (2015). Offshore Hydromechanics, (3).

Kaplan, P., & Sargent, T. P. (1970). Development and Testing of an Aircraft Carrier Deck Motion Prediction System, *11803*(August 1970).

Keke, L., Nong, C., & Qing, L. (2015). Research and Simulation on the Carrier Deck Motion Adaptive Prediction for ACLS Design. *2014 IEEE Chinese Guidance, Navigation and Control Conference, CGNCC 2014*, 1341–1345. https://doi.org/10.1109/CGNCC.2014.7007391

Khan, A., Bil, C., & Marion, K. E. (2005). Ship Motion Prediction for Launch and Recovery of Air Vehicles. *Proceedings of MTS/IEEE OCEANS, 2005*, *2005*. https://doi.org/10.1109/OCEANS.2005.1640198

Koenemann, J., Williams, P., Sieberling, S., & Diehl, M. (2017). Modeling of an Airborne Wind Energy System for the Optimization of Short Winch Landing Trajectories, (2016), 12450–12456.

Lainiotis, D. G., Charalampous, C., Giannakopoulos, P., & Katsikas, S. (1992). Real Time Ship Motion Estimation. In *OCEANS 92 Proceedings@m_Mastering the Oceans Through Technology* (Vol. 1, pp. 283–287). IEEE. https://doi.org/10.1109/OCEANS.1992.612703

Lainiotis, D. G., & Plataniotis, K. N. (1993). Neural Network Estimators: Application to Ship Position Estimation. *Proceedings of 1994 IEEE International Conference on Neural Networks (ICNN'94)*, *7*, 384–390. https://doi.org/10.1109/ICNN.1994.375037

Lee, C., & Newman, J. N. (2005). Computation of Wave Effects Using the Panel Method. *Numerical Models in Fluid Structure Interaction*, *18*(1), 1–41. https://doi.org/10.2495/978-1-85312-837-0/06

Licitra, G., Williams, P., Sieberling, S., & Diehl, M. (2017). System Identification of a Rigid

Wing Airborne Wind Energy Pumping System. In *Airborne Wind Energy Conference 2017*. https://doi.org/10.4233/uuid:f16704d6-c0da-4405-9276-7db0f7225b61

Lindeboom, R. C. J. (2017). *Soft Mooring Model Tests for the Ampyx Platform*. Wageningen.

Loyd, M. L. (1980). Crosswind Kite Power. *Journal of Energy*, *4*(3), 106–111. https://doi.org/10.2514/3.48021

Luchsinger, R. H. (2017). TwingPower High Altitude Wind Energy System - Windtech International. Retrieved October 25, 2017, from https://www.windtech-international.com/editorial-features/twingpower-high-altitude-wind-energy-system

Luchsinger, R. H., Arreger, D., Bezard, F., Costa, D., Galliot, C., Gohl, F., … Houle, C. (2017). Off-grid, Off-shore and Energy Drones: TwingTec's Roadmap to Wind Energy 2.0. In *Airborne Wind Energy Conference 2017*. https://doi.org/10.4233/uuid:50bc2330-45c0-48f3-bfde-79e7285ae1fb

Mann, S., Gunn, K., Harrison, P. G., Beare, B., & Lazakis, I. (2015). Wind Yield Assessment for Airborne Wind Energy. *EWEA Offshore 2015*.

Matbase. (n.d.). Material properties Dyneema. Retrieved October 25, 2017, from https://www.matbase.com/material-categories/natural-and-synthetic-polymers/polymer-fibers/synthetic-fibers/material-properties-of-dyneema.html#properties

Mendes, S. (2012). *Vision-Based Automatic Landing of a Quadrotor UAV on a Floating Platform*. Delft University of Technology.

Newland, D. E. (1993). *Random vibrations, spectral and wavelet analysis*.

NU.nl. (2013). Google Gaat Stroom Winnen met Zwevende Windturbines. Retrieved March 16, 2017, from http://www.nu.nl/internet/3481206/google-gaat-stroom-winnen-met-zwevende-windturbines.html

Ockels, W. J. (2001). Laddermill, a novel concept to exploit the energy in the airspace. *Aircraft Design*, *4*(2–3), 81–97. https://doi.org/10.1016/S1369-8869(01)00002-7

Ogilvie, T. F. (1964). *Recent Progress Toward the Understanding and Prediction of Ship Motions*. Washington, D.C.

Ra, W. S., & Whang, I. H. (2006). Real-time long-term prediction of ship motion for fire control applications. *Electronics Letters*, *42*(18), 1020. https://doi.org/10.1049/el:20061053

ReNEWS. (2017). *Offshore Technology Yearbook 2017*.

Rieck, B., Ranneberg, M., Candade, A., Bormann, A., & Skutnik, S. (2017). Comparison of Launching & Landing Approaches. In *Airborne Wind Energy Conference 2017*. https://doi.org/10.4233/uuid:746d1263-9685-452a-b26b-d26b6a138c65

Schmehl, R. (2017). *Airborne Wind Energy - Advances in Technology Development and Research*. Springer-Verlag.

Schmehl, R., Diehl, M., & Ahrens, U. (2011). *Airborne Wind Energy 2011*. Springer.

Sidar, M. M., & Doolin, B. F. (1975). On the Feasibility of Real-Time Prediction of Aircraft Carrier Motion at Sea. Moffet Field, California: Ames Research Center, NASA.

Sidar, M. M., & Doolin, B. F. (1983). On the Feasibility of Real-Time Prediction of Aircraft Carrier Motion at Sea. *IEEE Transactions on Automatic Control*, *28*(3), 350–356. https://doi.org/10.1109/TAC.1983.1103227

SpaceX. (2016). CRS-8 Launch and Landing. Retrieved October 25, 2017, from http://www.spacex.com/news/2016/04/09/crs-8-launch-and-landing

Steen, S. (2017). General Modelling and Scaling Laws. *TMR7 Experimental Methods in Marine Hydrodynamics*. NTNU. Retrieved from http://www.ivt.ntnu.no/imt/courses/tmr7/lecture/Scaling_Laws.pdf

Stevens, B. L., & Lewis, F. L. (1992). *Aircraft Control and Simulation*. John Wiley and Sons, Inc.

Stiesdal, H. (2017). Airborne Wind Energy – Challenges and Opportunities Based on Experiences from the Conventional Wind Industry. In *Airborne Wind Energy Conference 2017*. https://doi.org/10.4233/uuid:7908247b-583f-49e3-8f17-b276f16a82ec

Triantafyllou, M. S., & Athans, M. (1982). Real Time Estimation of The Heaving and Pitching Motions of a Ship Using a Kalman Filter.

Triantafyllou, M. S., Bodson, M., & Athans, M. (1983). Real Time Estimation of Ship Motions Using Kalman Filtering Techniques, (1).

Van der Steen, P. M. H. (2016). *Ship Motion Prediction for the Ampelmann System*. Delft University of Technology. Retrieved from http://repository.tudelft.nl/islandora/object/uuid:71021f4c-4bb1-4297-ada1-1a70428e9a54?collection=education

Weiss, I., & DeVries, T. (1977). Ship Motion Measurement Filter Design. *IEEE Journal of*

Oceanic Engineering, *2*(4). https://doi.org/10.1109/JOE.1977.1145359

Weston, D. (2017). Hywind Turbines Complete Foundation Installation | Windpower Offshore. Retrieved October 25, 2017, from https://www.windpoweroffshore.com/article/1437693/hywind-turbines-complete-foundation-installation

Yang, X., Pota, H., Garratt, M., & Ugrinovskii, V. (2008). Ship Motion Prediction for Maritime Flight Operations. *Proceedings of the 17th World Congress The International Federation of Automatic Control*, 12407–12412.

Yin, J. C., Zou, Z. J., Xu, F., & Wang, N. N. (2014). Online Ship Roll Motion Prediction Based on Grey Sequential Extreme Learning Machine. *Neurocomputing*, *129*, 168–174. https://doi.org/10.1016/j.neucom.2013.09.043

Yumori, I. (1981). Real Time Prediction of Ship Response to Ocean Waves Using Time Series Analysis. In *OCEANS 81* (pp. 1082–1089). IEEE. https://doi.org/10.1109/OCEANS.1981.1151574

Zanon, M., Gros, S., Andersson, J., & Diehl, M. (2013). Airborne Wind Energy Based on Dual Airfoils. *IEEE Transactions on Control Systems Technology*, *21*(4), 1215–1222. https://doi.org/10.1109/TCST.2013.2257781

Zhao, X., Xu, R., & Kwan, C. (2004). Ship-motion prediction: algorithms and simulation results. *2004 IEEE International Conference on Acoustics, Speech, and Signal Processing*, *5*(June), V-125-8. https://doi.org/10.1109/ICASSP.2004.1327063